Extreme Mechanics-Driven Nanomanufacturing of Low-Dimensional Material-Based Three-Dimensional Architectures

A

Dissertation

Presented to

the faculty of the School of Engineering and Applied Science

University of Virginia

in partial fulfillment

of the requirements for the degree

Doctor of Philosophy

in Mechanical and Aerospace Engineering

by

Qingchang Liu

August 2020

APPROVAL SHEET

This
Dissertation
is submitted in partial fulfillment of the requirements
for the degree of
Doctor of Philosophy

Author: Qingchang Liu

This Dissertation has been read and approved by the examing committee:

Advisor: Baoxing Xu

Advisor:

Committee Member: Xiaodong (Chris) Li

Committee Member: Gaurav Giri

Committee Member: Osman Eser Ozbulut

Committee Member: Liheng Cai

Committee Member:

Committee Member:

Accepted for the School of Engineering and Applied Science:

Craig H. Benson, School of Engineering and Applied Science

August 2020

Abstract

Low-dimensional materials, such as one-dimensional (1-D) carbon nanotubes (CNTs) or two-dimensional (2-D) graphene, have attracted tremendous attention over the past few years for their exceptional electronic, mechanical and thermal properties underpinned by their extremely large specific surface area. However, a single piece of them is too delicate to be useful in most applications, for example, high-performance electrodes in energy storage, filters for wastewater/gas treatments in environmental systems, and lightweight structures. Crumpling and assembling them into three-dimensional (3-D) porous architectures, if achieved, will inherit the structural merits and unique properties of 1 and 2-D nanomaterials due to excellent aggregation-resistant properties and can also serve as building blocks to construct even large-scale bulk forms with unprecedented functions.

In this PhD dissertation, the fundamental deformation mechanism of 1 or 2-D nanomaterials that will be expected to experience large deformation and severe instability in the crumpling and assembling process will be ascertained to establish systematical mechanics models. Moreover, the proposed theoretical framework in mechanics will be used to guide a low-cost and high-throughput liquid evaporation-assisted manufacturing approach that can be readily realized by utilizing aerosol processing, dynamic spraying or 3-D printing techniques to build such a 1 and/or 2-D nanomaterial-based 3-D porous superstructure. More importantly, to highlight the leading role of mechanics in the explored manufacturing approach, we define underpinned mechanics mechanism as extreme mechanics.

Specifically, in Chapter 2 an energy-based theoretical framework is established to describe the liquid evaporation-driven deformation and self-folding of a single 1-D nanofiber and 2-D nanofilm suspended in a free-standing liquid droplet. The effect of cross-section shape of 1-D nanofiber and geometry shape and surface wettability of 2-D nanofilm on the folding process and final folded patterns are investigated. Comprehensive molecular dynamics simulation are performed and validate the theoretical predictions on both the energy variations and final folded morphology.

When there are multiple 2-D sheets suspended in a free-standing liquid droplet, the energy competition between self-folding of individual sheets and assembly of different sheets is elucidated by a rotational spring-mechanical slider network mechanics model in Chapter 3. A computational simulation method to unveil the synthesis mechanism and deformation of 2-D sheets during liquid evaporation is developed. The effect of overall pressure, the total area of graphene, graphene shape, number, and size distribution on the overall size, surface morphologies, and accessible areas of particles is discussed.

By mixing 1-D materials with 2-D materials in a free-standing liquid droplet, the assembling of CNTs-encapsulated, crumpled graphene assembled hybrid particles are obtained by liquid evaporation in Chapter 4. A theoretical framework is established to predict the overall size, surface morphologies, and inner structures of the particles. Molecular dynamics simulation is implemented to validate the theoretical predictions and illustrate details of the synthesis process. The effect of CNTs sizes and mass fraction on the morphologies and properties of assembled particles are investigated.

In Chapter 5, the crumpling and assembling of multiple 2-D sheets in the liquid droplet on a substrate by liquid evaporation is studied. The importance of curvature evolution of liquid surface and substrate properties on the assembling process of 2-D sheets is emphasized. A mechanics model incorporating the profile evolution of liquid droplet with the influence of substrate, comprehensive molecular dynamics simulation, and liquid evaporation experiments are conducted to explain the synergistic effect of liquid and substrate on the morphologies and properties of assembled particles.

The mechanics theories, manufacturing techniques, modeling skills, and characterization methods established in this thesis will provide a fundamental understanding of mechanics in large deformation, instability, and self-assembly of low-dimensional materials in liquid environments, and will also transform applications of the evaporation-assisted technique in the manufacturing of 3-D superstructures of a broad scope of nanomaterials such as lipid membranes, nanowires, nanotubes, nanofibers, and nanoparticles, to meet emerging needs in high-performance composites, filters, batteries, and sensors.

Table of Contents

List of Figures

Acknowledgements

Firstly, I would like to express my sincere and heartful gratitude to my advisor Professor Baoxing Xu for his insightful academic guidance, persuasive encouragement, and keen academic intuition. He has always been an example of demonstrating how a self-motivated person could devote himself to his career with joy and passion. His enthusiastic and rigorous attitude would continue to inspire and encourage me in my future career. I feel so fortunate to work with Prof. Xu in the pursuit of my education and research.

Secondly, I would show my appreciation to my committee members, Professor Xiaodong (Chris) Li, Professor Gaurav Giri, Professor Osman E. Ozbulut and Professor Liheng Cai, for their time to read my thesis and papers, for their kindness to serve in my thesis proposal and defense, and for their inspiring sharing and patient discussion to support my research.

Thirdly, I would thank the current and former members in Professor Xu’ s research group for their long-term supports, invaluable discussions, eternal friendship, encouragements, and suggestions, including Prof. Zongzhan Gao, Dr. Weizhu Yang, Dr. Yuan Gao, Mr. Yue Zhang, Mr. Haozhe Zhang, Mr. Mengtian Yin, Ms. Xuemei Xiao, Mr. Dashun Liu, Mr. Yize Dong, and Ms. Songwei Li.

Last but not least, I would like to express my deepest gratitude to my parents and family, thanks for raising me and supporting me to pursue my career. Thanks to my parents Honglu Liu and Yunzhi Han and my sister Qingfang Liu who always love me unconditionally, and support me constantly for my choices. Here, I give my special thanks to my beloved wife, Fujuan Tong, thanks for the understanding, continuous support, and encouragement. She is my peaceful harbor, my happy place, and my everything.

Chapter 1 Introduction and Motivation

1.1 Advantages of Low-Dimensional Materials in Functional Devices

Low-dimensional materials, such as 1-D nanotubes, nanowires [1] and 2-D graphene, boron nitride [2] (**Figure. 1.1**), have attracted tremendous attention over the past few years for their exceptional electronic[3-9], mechanical[10-13] and thermal[14-16] properties underpinned by their extremely high specific surface area, often demonstrated at the single strip/layer level[17]. For example, the surface area of graphene can be as high as 2630 m^2/g [18] due to its single-atomic layer structure.

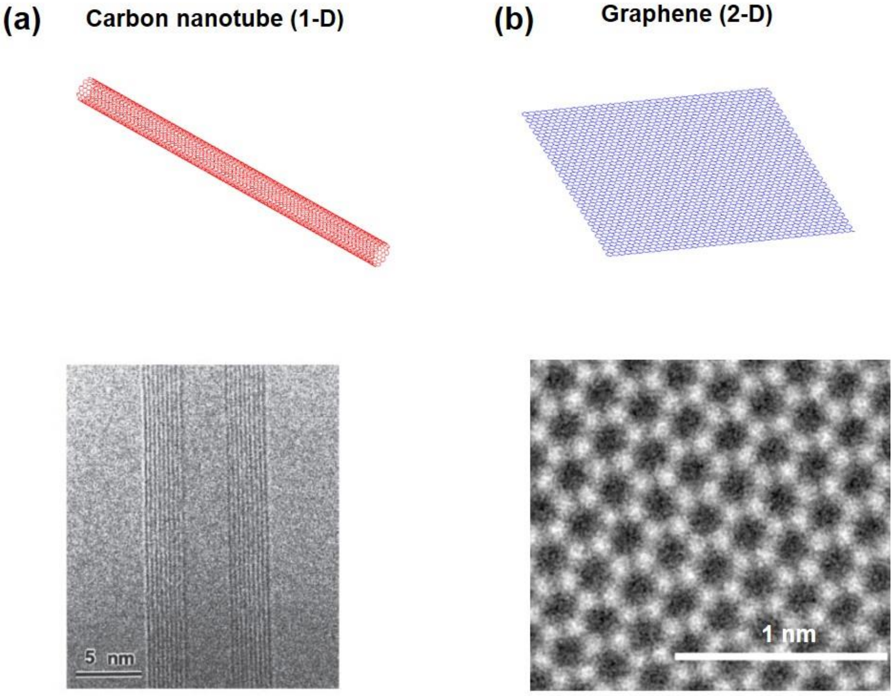

Figure 1.1. The atomistic model and transmission electron microscopy (TEM) images of representative low-dimensional materials. (a) 1-D carbon nanotube[1]. **(b)** 2-D graphene[2].

However, a single strip/sheet of low-dimensional materials would be too delicate to be used in functional devices and a bulk form of these 1-D/2-D materials, either as powders or a monolith is necessary for most applications such as high-performance electrodes in energy storage[19-21], filters for wastewater/gas treatments in environmental systems[22-24], and lightweight structures to undertake mechanical loading[25, 26]. As a result, a significant thrust in recent years is to assemble these low-dimensional materials into bulk, 3-D forms in the hope that the excellent properties at the single strip/layer level can be scaled up as much as possible[27]. As a result, crumpling and assembling them into 3-D porous architectures not only possess a high surface area and high free volume but also provide a spatial network accessible to foreign atoms and molecules (**Figure 1.2**). For example, unlike a tight restacking of flat graphene sheets, ~60% of the accessible surface area ($>1500\ \mathrm{m^2/g}$) is maintained in the crumpled graphene sheets[28]. The crumpled graphene-assembled structures can even maintain 45% of its original surface area under mechanical compression of 55 MPa, while the regular flat graphene sheets turn into chunks with a drastic reduction of surface area by 84%[21]. The excellent inherence of large surface areas and robust deformation resistance in crumpled graphene 3-D structures have been leveraged in supercapacitors and show 5 times higher of energy density than that of flat graphene sheet powder and a stable specific capacitance with the increase of mass loading[29]. The 3-D porous spaces have been employed as a scaffold to enhance the sensitivity of sensors[30] and catalytic[31] performance with an interlocking and interactions with host matrixes in Li-metal batteries[32] and manufacturing of 1 or 2-D material-reinforced composites and enhance overall physical and mechanical properties[33]. Therefore, the crumpled 1 and/or 2-D material-based 3-D porous superstructures, if achieved, will inherit the structural merits and also serve as building blocks

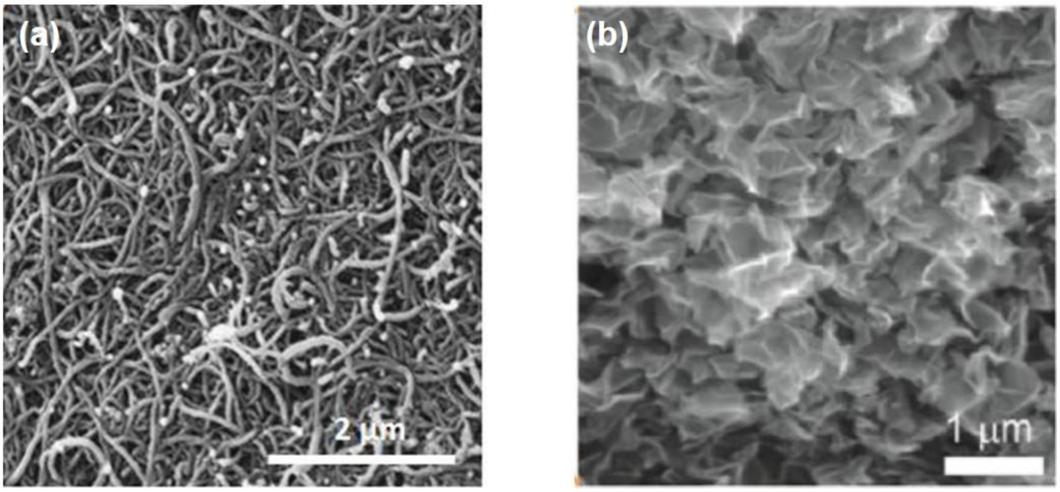

Figure 1.2. SEM images of crumpled (a) CNTs[24] **and (b) Graphene**[21].

to construct even large-scale bulk forms with unprecedented functions.

1.2 Challenges in the Manufacturing of Low-Dimensional Materials-Based Architectures

The major issue in the manufacturing of low-dimensional materials-based architectures is that the low-dimensional materials tend to aggregate/restack due to strong van der Waals attraction between them such as restacking of 2-D flat graphene sheets, which not only results in a tremendous reduction of their accessible area and poor mass/ion transport[34] but also degrades with processing and/or application environments such as mechanical loadings, hence adversely affecting their properties and subsequent applications[35].

Developing a low-cost and high-throughput technique to build such 1 and/or 2-D material-based 3-D porous superstructures is the most paramount challenge in manufacturing. Several manufacturing techniques have been developed to obtain the 1-D/2-D materials-based 3-D structures including mechanical folding by applying an external mechanical loading[25], and chemical folding by decorating functional groups[36] or defects[37]. For example, releasing pre-strain applied to the substrate prior has been designed to achieve wrinkled graphene patterns [38] and has also been used to pop up 3-D graphene porous structures [39]. Similar to this mechanical controlling means, thermally generated strain [40], hydrogenation [41], and irradiation to surface atoms [42] have been developed to regulate 2-D structures of graphene into various geometrical configurations. These manufacturing techniques are currently challenged by mass production of low-dimensional materials-based 3-D structures with a low cost to meet requirements for broad applications.

1.3 Opportunities for Liquid Evaporation in the Manufacturing of Low-Dimensional Materials-Based Architectures

The liquid evaporation-assisted manufacturing technique is considered to provide a facile route to address this challenge[43] (**Figure 1.3**). In this technique, 1 or 2-D materials will experience large deformation and severe instability under evaporation-induced compression to create spacing when assembled, which is highly desirable to minimize restacking and retain the large surface areas of 1 or 2-D material in the assembled 3-D structures. This conversion

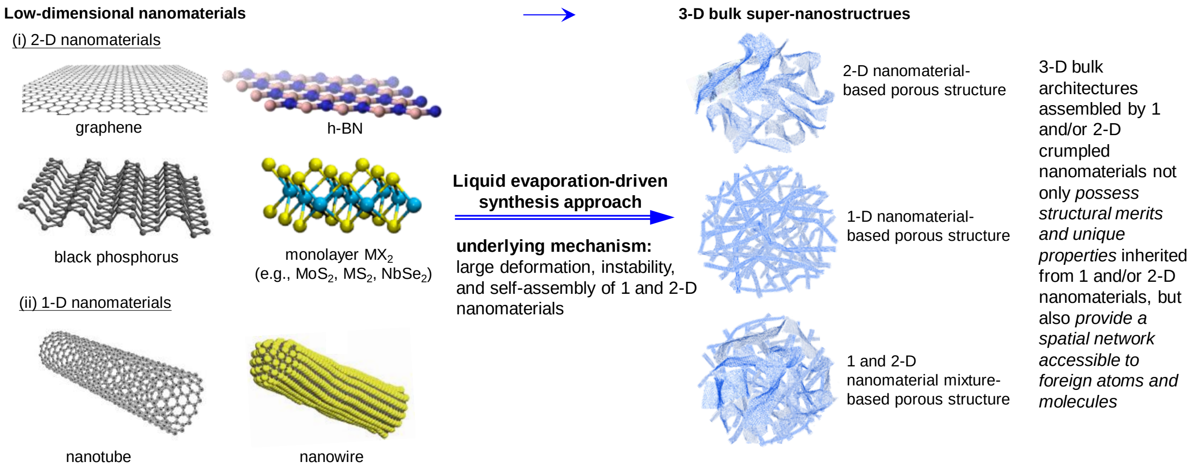

Figure 1.3. Liquid evaporation-driven synthesis of 1 and/or 2-D materials-based 3-D bulk scaffolds.

from 1 or 2-D materials to 3-D porous structures is a mechanical deformation process associated with dynamic interactions and mutual coordination of deformation between solid and liquid during liquid evaporation, and is underpinned by mechanics.

Figure 1.4a depicts the schematic illustration of a typical experimental setup of the aerosol-assisted, evaporation-driven manufacturing technique [44-48]. The aerosol droplets with suspended low-dimensional materials are first nebulized from a bulk dispersion and then sent through a pre-heated furnace via a carrier gas. At the end of the flight path, evaporation of the aerosol droplets is complete and dried particles are collected. By adjusting the concentration of low-dimensional materials and/or the furnace temperature, the size and morphology of assembled particles can be tuned [27, 47, 49-52]. More importantly, 2-D sheets such as those made of graphene, are usually hard to disperse in solvents due to their strong tendency to restack. However, for their crumpled version, the uneven surface morphology, coupled with strain-hardening property leads to unusual aggregation-resistant properties, allowing them to be processed in nearly arbitrary solvents without the need for dispersing agents [53]. Crumpled graphene balls were found to self-disperse in lubricant oil for improved tribological performance and wear protection [54]. The scalable surface areas in crumpled graphene balls have exhibited more scalable performance in ultracapacitors [21, 55, 56]. Their uneven surface morphology and aggregation-resistant packing behavior have been leveraged to reduce the reflection of light for solar heating and distillation purposes [44]. The 3-D porous spaces have also been employed as a scaffold to enhance the sensitivity of sensors [57] and catalytic

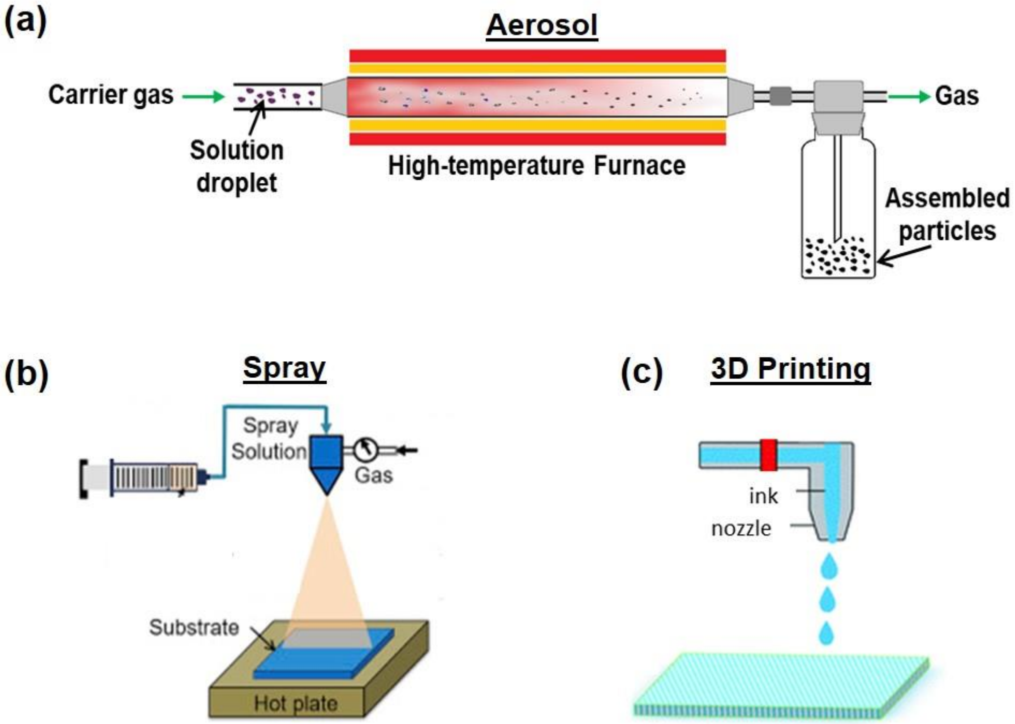

Figure 1.4. Schematics of typical experimental technique for the liquid evaporation-driven manufacturing of low-dimensional materials. (a) Aerosol-assisted evaporation. **(b)** Mechanical spray painting. **(c)** 3D printing.

performance [31] with rapid diffusion of atoms/ions and mass transfer. In addition, the 3-D spatial networks facilitate the interlocking and interactions with host matrixes in Li metal batteries [32] and manufacturing of 2-D material-reinforced composites and enhance overall physical and mechanical properties [33, 58]. Crumpled graphene balls can also act as breathable shells to encapsulate and protect expandable particles from reactive environments, which has been leveraged for applications in energy storage devices such as Li-ion battery [45, 46, 49, 59, 60]. Recently, the liquid evaporation-driven manufacturing technique has been applied in the crumpling and assembly of other 2-D materials such as MoS_2 flakes [61]. In addition to the evaporation of free-standing liquid droplets, the evaporation of droplet on a substrate in the mechanical spray painting (**Figure 1.4b**) and 3D printing (**Figure 1.4c**) also provide facile methods to fabricate low-dimensional materials-based 3-D structures with versatile morphologies and properties [30, 62, 63].

1.4 Innovations of Present Research

In fundamental, this liquid evaporation manufacturing technique is similar to self-assembly of nanoparticles in the synthesis of colloidal crystal, nevertheless, nanoparticles are commonly rigid and only aggregation is expected by inter-particle attraction to achieve dense-packed assembly of nanoparticles[64, 65]. Besides, in comparison with other techniques such as mechanical patterning[66, 67], chemical doping[68, 69] or growth[70], the deformation, crumpling and self-assembly of 1 or 2-D materials can be simultaneously achieved by one-step evaporation of liquid without the need of complex loading conditions or modification to material compositions. Moreover, the 3-D porous structures in size, geometric shape and porosity can be easily regulated by controlling manufacturing and/or material parameters (e.g. surface wettability, concentration), thus satisfying mass production in a low-cost manner. Besides, this liquid evaporation-assisted manufacturing technique remains open to be directed by applying external conditions (e.g. electric, magnetic field).

At the root of this technique, the evaporation in our manufacturing setup is usually conducted at the temperature of <200 ℃, far below the temperature of either melting graphene or CNTs or triggering their chemical reaction with liquid and is a physical process of drying. Besides, the elementary steps rely critically on the large deformation, instability, and self-assembly of 1 and 2-D materials with dynamically-constrained boundary conditions during liquid evaporation. The complexity and multiplicity of these deformation mechanisms are strongly underpinned by mechanics. The traditional solid mechanics models that focus on small deformation or capturing only one mechanism are not sufficient. The self-assembly mechanics that focuses on aggregation among rigid nanoparticles in colloid science is limited to understanding the large deformation and instability of 1 and 2-D materials. The theoretical developments of mechanics schemes will be essential to guide well-defined on-demand 3-D porous superstructures with a precisely controlled process. They must seamlessly combine the principles of solid mechanics and surface wettability engineering together, and fully incorporate solid-liquid interactions, deformation of solids. More importantly, unlike the traditional role of mechanics in manufacturing where the emphasis is placed on analysis for optimization of material choices or process selections, mechanics in the proposed evaporation-assisted manufacturing of the 3-D porous structures is a central driving factor. The elucidation of mechanical interactions among deformable solids and liquid molecules is also expected to open new opportunities for emerging unconventional concepts and strategies in flexible and smart manufacturing in the future.

1.5 Outline of the Dissertation

Through the present thesis, the following problems are thoroughly investigated and explored: (1) The mechanics mechanism of the liquid evaporation-driven crumpling and assembly of 1-D and 2-D materials; (2) The large scale molecule dynamics simulation technique to elucidate the details of the synthesis process; (3) The characterization methods to explore the structures and properties of the as-fabricated structures; (4) The applications of 1-D and/or 2-D materials-based structures in the functional devices and composite materials. The thesis consists of six chapters:

In Chapter 1, an introduction of the low-dimensional materials, the current challenges in the manufacturing of low-dimensional materials-based three-dimensional architectures, the liquid evaporation-driven manufacturing technique, the current research finds, mechanisms, and methods, is briefly overviewed.

In Chapter 2, by introducing a unified energy criterion and implementing molecular dynamics simulations, we systematically investigated the liquid evaporation-driven self-folding of a single 1-D/2-D material suspended in a free-standing liquid droplet. The 3-D profile of the liquid droplet is extracted to precisely capture the surface energy of the liquid. The final folded pattern is examined after complete liquid evaporation. The critical elastocapillary length, wet-capillary length, and self-folding lengths that determine the self-folding by liquid evaporation and the ultimate formation of a stable folded pattern are obtained, respectively.

In Chapter 3, by combining the theoretical analysis, computational simulations, and experimental validations, we elucidate the mechanism of crumpling and assembling of multiple 2-D deformable materials suspended in a free-standing liquid droplet. An equivalent pressure model is first developed to unify the driving forces of crumpling and assembling 2-D materials including capillary force, carrier gas pressure, vapor pressure, vapor recoil pressure and capillary flow-induced shear force. Then, a rotational spring-mechanical slider mechanics model is proposed to describe mechanical deformation and self-folding of individual 2-D sheets and their assembly during evaporation. The resultant energies are derived to quantitatively elucidate the energy competition between crumpling and assembling of 2-D materials. The morphologies and sizes of assembled 3-D particles are predicated theoretically by minimizing the ultimate energy state after the complete evaporation of liquid. The extension of the proposed theory that takes into account the numbers, size distribution, and geometric shapes of 2-D sheets in the droplet is further discussed.

In Chapter 4, by combining the theoretical analysis with computational simulation, we uncover the mechanism of crumpling and assembling of hybrid 1-D and 2-D deformable materials suspended in a free-standing liquid droplet. A diffusion model of 1-D (CNTs) and 2-D (graphene) materials in the liquid solution at both equilibrium and liquid evaporation stage is first established to determine the coordination of CNT and graphene. The specific surface areas, electrical conductivity, and elastic modulus of the as-fabricated particles are characterized by the contact area and compression test.

In Chapter 5, with theoretical analysis and coarse-grained simulations, the mechanism of crumpling and assembling of multiple 2-D materials suspended in a sessile liquid droplet is elucidated. The contact line evolution during liquid evaporation is unified by an evaporation route model. Then the influence of the substrate is considered by establishing a linear spring-mechanical slider model. The morphologies of assembled particles as functions of evaporation routes and substrate properties can be predicted by the theory and show remarkable agreement with the simulation results. Liquid evaporation experiments are conducted to validate the theoretical predictions and simulation results.

In Chapter 6, the major findings are summarized and future work in the relevant fields is discussed.

Chapter 2 Liquid Evaporation-driven Crumpling of a Single 1-D/2-D Material

2.1 Overview of the Chapter

In this chapter, we develop a quantitative theory of the liquid evaporation-driven deformation and self-folding of a single 1-D nanofiber and 2-D nanofilm suspended in a free-standing liquid droplet. The theoretical model is established through a unified energy-based criterion by taking into account the deformation energy of the nanofibers/nanofilm, and interactive energy of solid in folded parts, and surface energy of the liquids. We firstly present the details of the theoretical framework by considering the evolution of the solid-liquid system energy with liquid evaporation. The folded patterns and sizes of 1-D nanofiber with a focus on racket-like, spiral and helical patterns and 2-D nanofilm with a focus on racket-like, spiral, and cone-like patterns are exemplified and determined based on the minimization of total energy after the complete evaporation of liquid. To validate the theoretical model, comprehensive molecular dynamics simulations are performed. The bead-spring CG model and force fields are discussed in the nanofibers and are confirmed by full atomistic MD simulations. The full-atom model of graphene and water are selected as representative for the nanofilm. The quantitative comparison between MD calculations and theoretical predictions are conducted including energy variations and critical folding parameters during evaporation and configurations and sizes of ultimate self-folded patterns after complete evaporation of liquid. A remarkable agreement between them is found. The extension of the proposed theory to the nanofibers with hollow structures is discussed, where the effect of the local buckling deformation on folding energies and patterns is included. In addition, we discuss the elongation effect of nanofibers and capillary-flow induced variation of cross-sections of nanofibers during evaporation. The nanofilm with different geometric shapes is also considered.

2.2 Liquid Evaporation-driven Crumpling of a Single 1-D Material

2.2.1 Theoretical framework

When a single hydrophilic 1-D nanofiber is fully suspended in the liquid (**Figure 2.1a**), once the liquid evaporation occurs at elevated temperatures, the system equilibrium will break due to the dynamic change of the solid-liquid interaction and deformation of solid. Generally, the evaporation of liquid will decrease the volume of liquid and thus reduces the surface energy of liquid droplets. As a consequence, the capillary force starts to compress both ends of the nanofiber [71], leading to its deformation (**Figure 2.1b**). The deformation is dominated by the competition of surface energy of the liquid, solid-solid interactive energy in the overlap parts if appear, and deformation energy of solids, toward the arrival of minimal total energy in the ultimate stable self-folded patterns. Given the free-standing of 1-D nanomaterials in liquid and the high aspect ratio of 1-D nanomaterials that can coordinate well with the capillary force in multiple directions, and the various self-folded patterns could be obtained at different evaporation conditions. Once the deformation of nanofiber occurs by evaporation, the total energy E_{tot} that will dominate deformation, instability, and self-folding of the nanofiber is

$$E_{tot} = E_{def} + E_{surf} + E_{int} + E_{vdW} \tag{2.1}$$

where E_{def} is the deformation energy of the nanofiber. E_{surf} is the surface energy of liquid, E_{int} is the nanofiber-liquid interfacial energy, and E_{vdW} is the binding energy of overlap parts in the nanofiber [72, 73]. Note that the present nanofiber is fully hydrophilic without any decorations of hydrophobic functional groups/surfaces, and the hydrophobic interaction can be neglected at the overlap parts[74-76]. In addition, when the liquid evaporation occurs in a noble gas environment such as nitrogen which is usually utilized in experiments[47, 77, 78], Eq. (2.1) will still hold by taking proper surface tension of liquids[79]. For nanofibers with homogenous mechanical properties and surface wettability, assume the deformation is uniform with the same bending curvature, elongation strain and torsional angle within the unit length, Eq. (2.1) can be rewritten as

$$E_{tot} = \frac{Bl_b}{2r_b^2} + \frac{EA_0}{2l}\Delta l^2 + \frac{GJ}{2l}\emptyset^2 + \gamma_l A_l + \gamma_i A_{s-l} + \gamma_b l_o \tag{2.2}$$

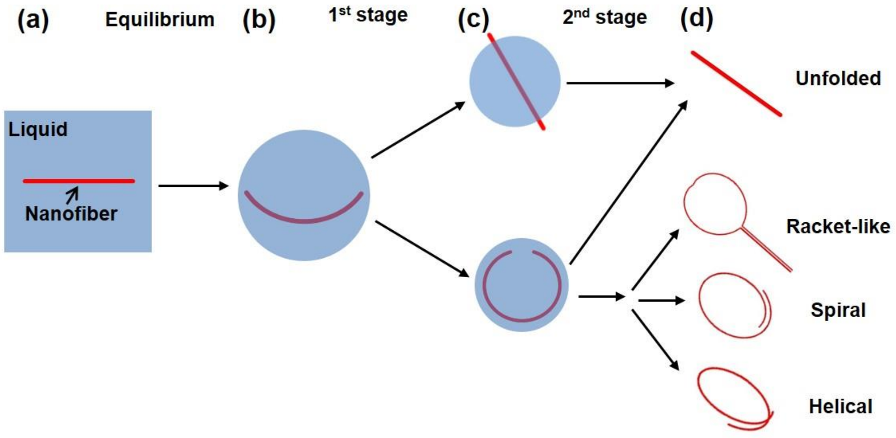

Figure 2.1. Overall map of the liquid evaporation-driven self-folding of a single nanofiber. (a) Suspension of a nanofiber inside a liquid environment at the equilibrium, where there is no deformation in the nanofiber due to a sufficient amount of liquid. **(b)** Deformed nanofiber confined inside the liquid droplet, where the nanofiber is compressed and bent by evaporation-induced capillary force during the evaporation of liquid. **(c)** Deformation status of nanofiber in the liquid droplet with the further evaporation of liquid, where the nanofiber penetrates the surface of the liquid droplet and recovers to its original straight configuration, or it is further bent and forms a whole circle to accommodate the spherical geometry of liquid droplet with a decreased volume. The deformation results from the competition between the surface energy of liquid and deformation energy of nanofiber and is driven by liquid evaporation, referred to as the 1st stage of evaporation. **(d)** Ultimate folded patterns of the nanofiber after complete evaporation of liquid, where racket-like, spiral, and helical patterns are focused. The formation of ultimately folded patterns is led by the competition of deformation energy and van der Waal force interactive energy of overlap parts in a pattern and is driven by nanofiber itself overlap, referred to as the 2nd stage of evaporation.

where $E_{def} = \frac{Bl_b}{2r_b^2} + \frac{EA_0}{2l}\Delta l^2 + \frac{GJ}{2l}\emptyset^2$, and $\frac{Bl_b}{2r_b^2}$, $\frac{EA_0}{2l}\Delta l^2$, and $\frac{GJ}{2l}\emptyset^2$ are the bending, stretching, and torsional energy, respectively[80, 81]. E, G and B are the Young's modulus, shear modulus, and bending stiffness of nanofibers, respectively, A_0 and l are the sectional area and total length of nanofibers, respectively, J is the polar moment of inertia, r_b and Δl are the bending radius and elongation of nanofibers, respectively, l_b is the length of bended part of 1-D nanofibers, and $\emptyset$ is the torsional angle. $E_{surf} = \gamma_l A_l$, γ_l is the surface tension of liquid[82], and A_l is the surface area of liquid droplet[83]. $E_{int} = \gamma_i A_{s-l}$, γ_i is the interfacial energy density between nanofibers and liquid[84], and A_{s-l} is the contact area between nanofibers and liquid. $E_{vdW} = \gamma_b l_o$, γ_b is binding energy density of nanofibers, and l_o is the length of overlap parts in the folded nanofiber patterns[73, 85].

With the evaporation of liquid, the size (or volume) of liquid droplet decreases, leading to a change of the configuration of the folded nanofibers. At the early stage of evaporation, there

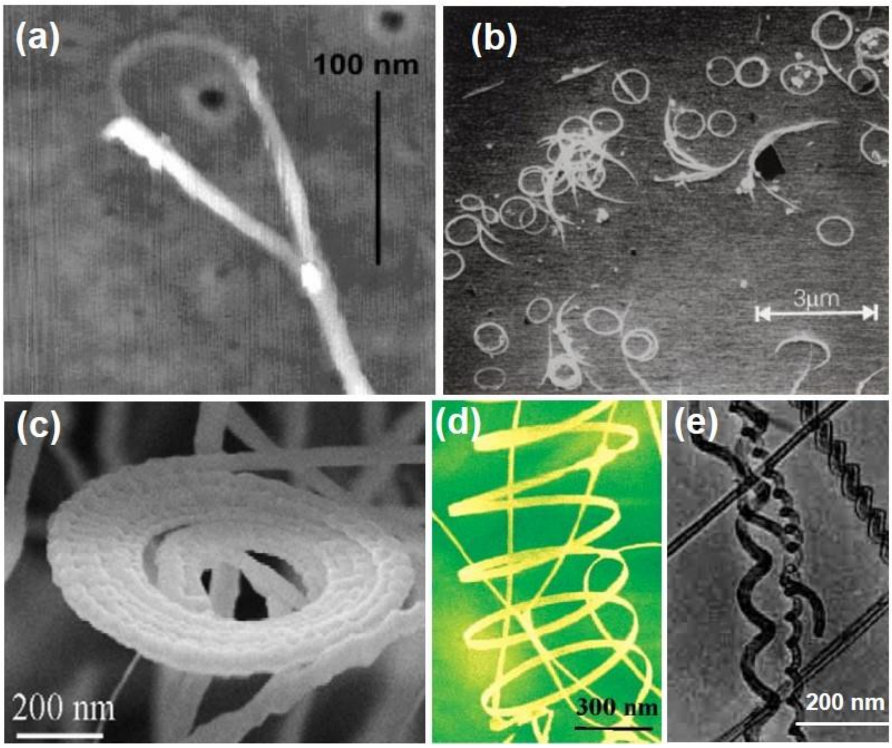

Figure 2.2. Self-folded patterns of 1-D nanomaterials in experiments. (a) The racket-like pattern of a single-walled carbon nanotube (CNT) folded by sonication in dichloroethane [86]. **(b)** Ring and spiral patterns of CNTs after sonication in concentrated sulphuric acid and hydrogen peroxide [87]. **(c)** The spiral pattern of ZnO nanowires folded as-fabricated [88]. **(d)** The helical structure of as-synthesized ZnO nanobelts [89]. **(e)** Helical graphite tubules grown by the cobalt catalyzed decomposition of acetylene [90].

is enough liquid to ensure full contact between nanofiber and liquid. As a consequence, A_{s-l}will not change and E_{int} will remain constant without change. The binding energy will also be zero because of the absence of overlapped part in the nanofiber. The self-folding of nanofiber will be dominated by the competition between E_{def} and E_{surf} (**Figure 2.1c**). With the further evaporation of liquid, the volume of the liquid becomes small enough, both E_{int} and E_{surf} are very weak and can be neglected. The self-folding will be driven by E_{vdW}, which is similar to the self-folding in a long carbon nanotube [73] or self-peeling of graphene [91-93]. Once the liquid is completely evaporated, E_{int} and E_{surf} will be zero, and the final stable folded pattern will be determined by E_{def} and E_{vdW}, where the racket-like, spiral and helical patterns commonly reported in experiments in **Figure 2.2** will be focused in this study, as illustrated in **Figure 2.1d**. Therefore, we will develop our theoretical model by considering these two stages of liquid evaporations—self-folding driven by liquid evaporation (1st stage) and self-folding driven by itself overlap (2nd stage), as elaborated below.

2.2.1.1 Crumpling driven by liquid evaporation (1st stage)

At the equilibrium before the liquid evaporation begins (**Figure 2.1b**), our theoretical analyses show that only the bending deformation of nanofibers is energetically favorable, and the out-of-plane torsion will not happen due to the free ends of nanofibers[94, 95]. Besides, when the aspect ratio of nanofibers ($\eta = l/2r$, r is the radius of nanofiber) is more than 10, the elongation deformation can be neglected. Because there is no binding energy in this stage, Eq. (2.2) becomes

$$E_{tot} = E_{def} + E_{surf} + E_{int} = \frac{Bl_b}{2r_b^2} + \gamma_l A_l + \gamma_i A_{s-l} \tag{2.3}$$

As the liquid evaporation begins, the radius of the liquid droplet r_l and the associated surface area $A_l (= 4\pi r_l^2)$ will decrease. When $l_b = l > 2r_l$, the confinement force induced by the surface tension of liquid along with the decrease of liquid volume will compress both ends of the nanofiber [77], leading to bending deformation, and thus promoting E_{def}. Given the requirement of minimization to the bending energy of the nanofiber suspended inside the liquid droplet, the radius of bending curvature in the nanofiber r_b can be obtained **(Figure 2.3)**

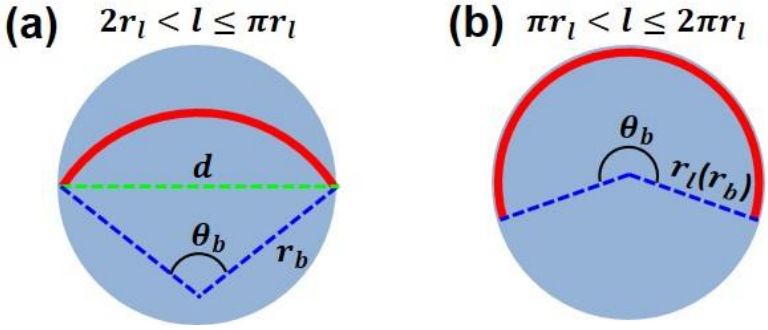

Figure 2.3. Determination of the curvature radius of bent nanofiber inside a liquid droplet during evaporation at (a) $2r_l < l \leq \pi r_l$ and **(b)** $\pi r_l < l \leq 2\pi r_l$. l is the length of nanofiber, r_l is the radius of liquid droplet, r_b is the bending radius of nanofiber and θ_b is the bending angle of nanofiber.

$$r_b = \begin{cases} r_l / \sin\left(\frac{\theta_b}{2}\right), 2r_l < l \leq \pi r_l \\ r_l, \qquad \pi r_l < l \leq 2\pi r_l \end{cases} \tag{2.4}$$

where θ_b is the bending angle of nanofiber. In this process, the deformation energy will increase ($\Delta E_{def} > 0$) meanwhile the surface energy will decrease ($\Delta E_{surf} < 0$), and the interfacial energy will not change due to the full contact of nanofiber with liquid ($\Delta E_{int} = 0$).

To characterize the energy competition, we define an evaporation-driven-folding energy ratio (EER) as

$$EER = \left|\frac{\Delta E_{def}}{\Delta E_{surf}}\right| \tag{2.5}$$

where ΔE_{def} and ΔE_{surf} represent the increase of deformation energy (i.e. bending energy) of the nanofiber and the decrease of the surface energy of liquid droplet, respectively. If $EER > 1$, E_{tot} in Eq. (2.3) will increase, and the evaporation cannot drive the deformation of the nanofiber, and if $EER < 1$, E_{tot} in Eq. (2.3) will decrease, favorable to deforming the nanofiber. Consider a decrease of a liquid droplet in radius Δr_l, and the resultant decrease of bending radius in nanofiber Δr_b, we can calculate $\Delta E_{def} = Bl(1/(r_b - \Delta r_b)^2 - 1/r_b^2)/2$ and $\Delta E_{surf} = 4\pi\gamma_l((r_l - \Delta r_l)^2 - r_l^2)$, and Eq. (2.5) becomes

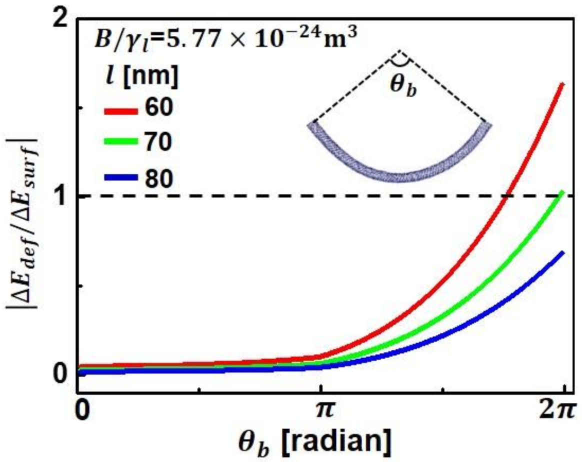

Figure 2.4. Evaporation-driven-folding energy ratio (EER) in the variation of deformation energy of nanofiber and surface energy of liquid, $EER = |\Delta E_{def}/\Delta E_{surf}|$, versus the bending angle of nanofiber, θ_b, during liquid evaporation. B is the bending stiffness of nanofiber, γ_l is the surface tension of liquid and l is the length of nanofiber.

$$EER = \frac{Bl}{8\pi\gamma_l}\left|\frac{1/(r_b-\Delta r_b)^2 - 1/r_b^2}{(r_l-\Delta r_l)^2 - r_l^2}\right| \tag{2.6}$$

To derive the critical length of nanofiber driven by the first stage of liquid evaporation, assume the nanofiber has been folded as much as close to a whole circle ($\pi r_l < l \leq 2\pi r_l$) and under this circumstance, $r_b = r_l$, $l = l_b$, and $r_b = l/\theta_b$, Eq. (2.6) becomes

$$EER = \frac{B}{\gamma_l} \cdot \frac{\theta_b^2(\theta_b + \Delta\theta_b)^2}{8\pi} \cdot \frac{1}{l^3} \tag{2.7}$$

note that when $\theta_b > 2\pi$, an overlap part in the folded nanofiber will appear (i.e. $l_o > 0$), and

E_{vdW} needs to be included in Eq. (2.3). Therefore, at $\theta_b = 2\pi$, $EER = 1$ and $\Delta\theta_b = 0$, a circle pattern of a folded nanofiber driven by the first stage of liquid evaporation can be obtained, and accordingly, the critical elastocapillary length of the nanofiber can be obtained via

$$l_{ec} = \pi \left(\frac{2B}{\gamma_l}\right)^{1/3} \tag{2.8}$$

Eq. (2.8) shows that if the length of nanofiber (l) is larger than l_{ec}, the nanofiber will be folded into a whole circle ($\theta_b = 2\pi$), and the further evaporation will continue to drive its folding, otherwise, the folded pattern will recover to the original straight configuration, as shown in **Figure 2.1c**. As an example, consider a single-walled (10,10) CNT whose bending stiffness is $B = 3.54 \times 10^{-25} N \cdot m^2$ [81, 96] and water whose surface tension is $\gamma_l = 0.0613 J/m^2$ [97, 98], which leads to $B/\gamma_l = 5.77 \times 10^{-24}\, m^3$. And thus from Eq. (2.8), the critical length of the CNT can be calculated and is $l_{ec} = 71\, nm$. **Figure 2.4** presents the variation of *EER* with θ_b. When the length of the CNT is l=80 *nm* ($> l_{ec} = 71\, nm$), the *EER* is always less than 1 at $0 \le \theta_b \le 2\pi$, suggesting the formation of a folded circular pattern by liquid evaporation. In contrast, for the CNT with the length of $l = 60\, nm$ or $70\, nm$ ($<l_{ec} = 71\, nm$), the *EER* is always larger than 1 at $\theta_b = 2\pi$, and the CNT will not be fold into a whole circular pattern by liquid evaporation.

2.2.1.2 Crumpling by nanofiber itself overlap (2nd stage)

Once the 1-D nanofiber is folded into an entire circle, the continuous evaporation of the liquid droplet will induce an overlap in the deformed nanofiber. As a consequence, the binding energy E_{vdW} at the overlapped part will be important. On the other hand, the liquid will gradually become discontinuous “water islands” rather than “continuous film”, and the effect of surface energy of the liquid E_{surf} can be neglected. Similarly, the interfacial energy E_{int} could also be neglected, and in particular, it will be zero after the complete evaporation of water due to A_{s-l}=0. Therefore, the driving energy for folding the nanofiber becomes the binding energy, and the total energy in this stage is

$$E_{tot} = E_{def} + E_{vdW} = \frac{B l_b}{2 r_b^2} + \gamma_b l_o \tag{2.9}$$

and *EER* in Eq. (2.5) now becomes

$$EER = \left|\frac{\Delta E_{def}}{\Delta E_{vdW}}\right| \tag{2.10}$$

where ΔE_{def} represents the increase of deformation energy, and ΔE_{vdW} represent the

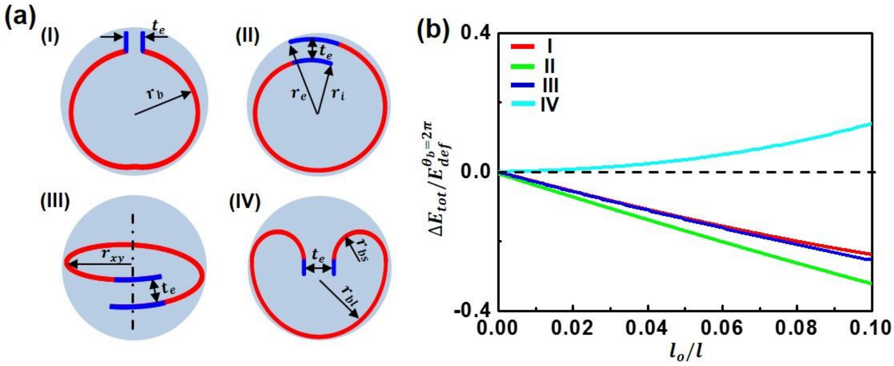

Figure 2.5. Comparison of energy variation at the onset of a whole circular pattern formation by liquid evaporation. (a) Schematics of typical four relative positions of two ends in nanofiber, (I) up-up. r_b is the radius of curvature of the deformed part, (II) up-down. r_i and r_e are the inner and outer radius of curvature, respectively, (III) left-right. r_{xy} is the in-plane radius of curvature, and (IV) down-down. r_{bl} and r_{bs} are the bending radius of large and small arc, respectively. t_e is the equilibrium distance in the overlap part. **(b)** Total energy variation normalized by deformation energy at the bending angle of nanofiber $\theta_b = 2\pi$, $\Delta E_{tot}/E_{def}^{\theta_b=2\pi}$, versus the overlap length (highlighted in blue in Figure 2.5a) in folded pattern l_o for four different patterns. l is the length of nanofiber.

decrease in binding energy. When *EER*>1 at the beginning of the 2nd stage (i.e. l_o=0), the energy requirement on the continuous deformation is larger than the decreased binding energy, and the self-folding will not happen. As a consequence, the pre-folded structure in the 1st stage will recover to its original straight form. In contrast, when *EER*<1 at the beginning of the 2nd stage (i.e. l_o=0), the decreased binding energy could satisfy the energy requirement of the continuous deformation and the folding will continue with an increased $l_o(> 0)$ until *EER*=1 which represents the arrival of the minimum total energy. Further analysis demonstrates that only the racket-like, spiral and helical patterns are energetically favorable for achieving a stable folded pattern (**Figure 2.5**), and these patterns are also in good agreement with the experimental observations in **Figure 2.2**. Given these stable patterns, their corresponding total energies and energy ratios can be calculated.

For the racket-like pattern (**Figure 2.5a (I)**), assume the deformed part has the same radius of curvature[99], the bending radius r_b and overlap length l_o satisfy $r_b = l/2\pi - kl_o$, assume an infinitesimal increase of overlap length Δl_o, the *EER* in Eq. (2.10) can be written as

$$EER^{racket} = 2\pi^2 B \left| \frac{(l-2(l_o+\Delta l_o))/\left(l-2\pi k(l_o+\Delta l_o)\right)^2 - (l-2l_o)/(l-2\pi k l_o)^2}{\gamma_b \Delta l_o} \right| \tag{2.11}$$

Similarly, for the spiral pattern (**Figure 2.5a (II)**), given the equilibrium distance at the overlap part t_e, the *EER* in Eq (2.10) can be written as

$$EER^{spiral} = \frac{B\pi}{t_e} \left| \frac{log\left[\left(((l-(l_o+\Delta l_o))^2+\pi t_e l)/((l-(l_o+\Delta l_o))^2-\pi t_e l)\right)/(((l-l_o)^2+\pi t_e l)/((l-l_o)^2-\pi t_e l))\right]}{\gamma_b \Delta l_o} \right| \tag{2.12}$$

and for the helical pattern (**Figure 2.5a (III)**), with $r_b = (l - l_o)/2\pi$, the *EER* in Eq. (2.10) can be written as

$$EER^{helices} = 2\pi^2 Bl \left| \frac{1/(l-(l_o+\Delta l_o))^2 - 1/(l-l_o)^2}{\gamma_b \Delta l_o} \right| \tag{2.13}$$

Therefore, the critical length for 1-D nanofibers that will be eventually folded to the racket-like, spiral and the helical patterns can be obtained through $EER^{racket} = 1$, $EER^{spiral} = 1$, and $EER^{helices} = 1$ at l_o=0, respectively. Further, the determinations of these critical lengths can be generalized into the following unified equation

$$l_{cr} = 2\pi\sqrt{2\pi k - 1}\sqrt{\left|\frac{B}{\gamma_b}\right| + \delta t_e^2} \tag{2.14}$$

where (k, δ) is the shape factor of the ultimately folded patterns, for example, $(k, \delta) = \left(\frac{2l_{cr}-t_e(2\pi-2)}{2\pi l_{cr}-t_e\pi^2}, 0\right)$ for the racket-like pattern, $(k, \delta) = \left(\frac{1}{\pi}, \frac{1}{4}\right)$ for the spiral pattern, and $(k, \delta) = \left(\frac{1}{\pi}, 0\right)$ for the helical pattern. When $t_e \ll l_{cr}$, $k = \frac{2l-t_e(2\pi-2)}{2\pi l-t_e\pi^2} \cong \frac{1}{\pi}$ for racket-like pattern, and k will be the same for all three patterns. In particular, (k, δ) will reduce to the same for both racket-like and helical pattern. In addition, for the spiral pattern, $t_e \ll l_{cr}$ will lead to $t_e^2 \ll |B/\gamma_b|$, and δt_e^2 can be neglected. As a consequence, the critical length of self-folding l_{cr} in Eq. (2.14) can be simplified to

$$l_{cr} = 2\pi\sqrt{\left|\frac{B}{\gamma_b}\right|} \tag{2.15}$$

When the folded patterns do not require to be differentiated, Eq. (2.15) will be in particular useful in the determination of the critical length of nanofibers that can be eventually folded by liquid evaporation. For example, for a single (8,8) CNT with a diameter of 1.4 *nm* and

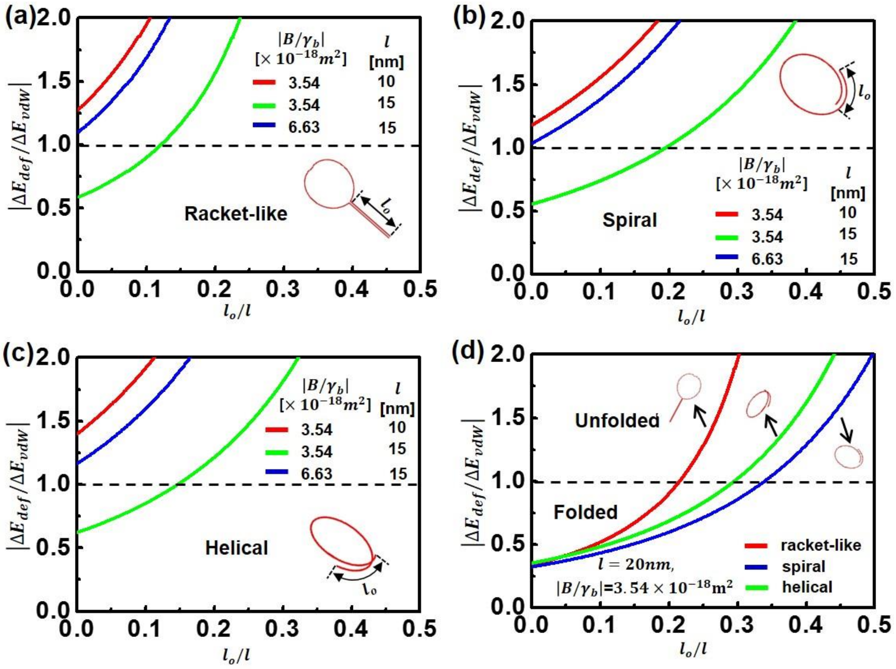

Figure 2.6. Evaporation-driven-folding energy ratio (*EER*) in the variation of deformation energy of nanofiber and binding energy in overlap parts of nanofiber, $EER = |\Delta E_{def}/\Delta E_{vdW}|$, versus the overlap length normalized by the length of nanofiber, l_o/l, during liquid evaporation for (a) racket-like pattern, **(b)** spiral pattern, and **(c)** helical pattern. **(d)** Comparison among racket-like, spiral and helical patterns. B is the bending stiffness of nanofiber, γ_b is the binding energy density of of nanofiber, l is the length of nanofiber and l_o is the overlap length of nanofiber.

equilibrium distance (the distance between the central axis of paralleled CNTs) t_e=1.4 *nm*, $B = 1.87 \times 10^{-25}\ N \cdot m^2$ [81, 96], and $\gamma_b = -2.08 \times 10^{-10} J/m$ [100] can be obtained. With Eq. (2.15), the critical self-folding length can be calculated and is l_{cr}=188.4 *nm*, which is close to the experimental measurement of 188.5 *nm* for the spiral pattern [87]. When the spiral pattern is known prior, Eq. (2.14) will be used and the calculations show l_{cr}=188.5 *nm*, which is in remarkable consistency with experimental measurement.

As a theoretical demonstration, for the racket-like pattern, **Figure 2.6a** gives the variation of energy ratio (EER^{racket}) with the overlap length normalized by the overall length of nanofiber l_o/l at $|B/\gamma_b|$ and l. It shows that EER^{racket} (calculated via Eq. (2.11)) is always larger than 1 at $|B/\gamma_b| = 3.54 \times 10^{-18}\ m^2$ and $l = 10\ nm$, indicating that the self-folded racket-like pattern cannot be obtained after the complete evaporation of liquid, in good consistency with the theoretical prediction of a large $l_{cr} = 11.82\ nm$ (calculated via Eq. (2.15)) over $l = 10\ nm$. Similarly, for the fiber with $|B/\gamma_b| = 6.63 \times 10^{-18}\ m^2$ and $l = 15\ nm$, the racket-like pattern cannot be formed due to $l = 15\ nm\ <\ l_{cr} = 16.18\ nm$, which corresponds to $EER^{racket} > 1$ as shown in **Figure 2.6a**. In contrast, given $|B/\gamma_b| = 3.54 \times 10^{-18}\, m^2$, at $l = 15\, nm > l_{cr} = 11.82\, nm$, a positive overlap length can be obtained at $EER^{racket} = 1$, indicating the successful formation of the racket-like pattern. Basically, the smaller $|B/\gamma_b|$, the longer nanofiber (i.e. the larger l), the easier self-folding with a stable folded pattern after evaporation of liquid. Similar conclusions can be drawn for spiral and helical patterns, as shown in **Figures 2.6b** and **c**, respectively. Given the same l and $|B/\gamma_b|$, **Figure 2.6d** shows the comparison of $|\Delta E_{def}/\Delta E_{vdW}|$ for these three folded patterns. Besides, once a stable folding stage arrives, the racket-like pattern has the smallest overlap length, and the spiral pattern has the largest one.

With the determination of the critical length l_{ec} and l_{cr} from Eqs. (2.8), and (2.14) or (2.15) at a given nanofiber and liquid system (i.e. B/γ_l and $|B/\gamma_b|$), we can determine whether the nanofibers can be eventually folded to a stable pattern after complete evaporation of liquid. For instance, if the length of nanofiber l is $l > l_{ec} > l_{cr}$ or $l > l_{cr} > l_{ec}$, the self-folding will be triggered by initial liquid evaporation, and the liquid evaporation (i.e. 1st stage) will continue to dominate the formation of ultimate stable folded pattern for $l > l_{ec} > l_{cr}$, while if $l > l_{cr} > l_{ec}$, the 2nd stage of evaporation will become crucial and dominates the continuous folding process. In contrast, when l is less than either l_{cr} or l_{ec}, the folded pattern will not be obtained after the complete evaporation of liquid. In particular, if $l_{cr} > l >$

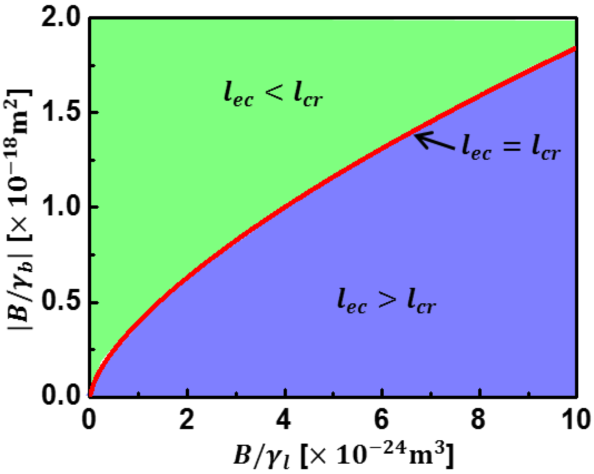

Figure 2.7. Self-folding competing mechanism of nanofibers characterized by the critical lengths l_{ec} $(= \pi(2B/\gamma_l)^{1/3})$ and l_{cr} $(= 2\pi\sqrt{|B/\gamma_b|})$ in variation of nanofiber and liquid systems B/γ_l and $|B/\gamma_b|$.

l_{ec}, the nanofiber will be bent by the 1st stage of liquid evaporation but will recover to its original straight configuration after complete evaporation of liquid. The competing domination of l_{ec} and l_{cr} in the formation of stable folded patterns will vary with B/γ_l and $|B/\gamma_b|$ and is summarized in **Figure 2.7**.

2.2.2 Computational modeling and method

When a nanofiber is fully immersed in a liquid environment, large numbers of solid atoms and liquid molecules will be involved. To validate the theoretical mechanics model and predictions in a cost-efficient manner, we here will conduct the coarse-grained molecular dynamics (CGMD) simulations. In the CGMD simulations, the popular bead-spring model will be employed to mimic the full atomic model of nanofibers, and the liquid will be water with the full atomistic model. **Figure 2.8a** illustrates the CG model of a nanofiber. A certain length of the nanofiber in the full atomic model is modeled by a bead, and the adjacent beads are

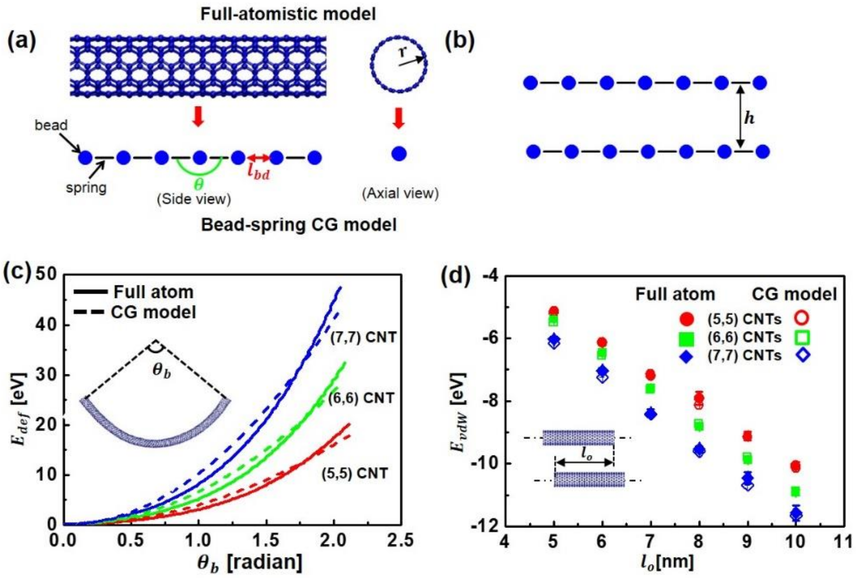

Figure 2.8. Bead-spring model of nanofiber in coarse-grained molecular dynamics (CGMD) simulations and validations. (a) Schematics of the full-atomic model of nanofiber and its bead-spring CG model, where a certain length of nanofiber with a radius of r in the full atomic model is modeled by a bead with a mass and is connected through a spring between the adjacent beads. l_{bd} is the bond length between adjacent beads, and θ is the bond angle of adjacent beads. **(b)** Schematic of two bead-spring CG models in parallel with a separation distance h. Comparison of **(c)** deformation energy as bending deformation, and **(d)** binding energy of two parallel CNTs with the same radius between full-atomistic and CGMD simulations.

connected through a spring[101], where m_b is the mass per CG bead, and l_{bd} is the bond length of the spring between adjacent beads. The total energy U_{b-s} in CG model is the sum of bond stretching energy U_b, angular potential energy U_θ , and torsional energy U_τ which are related with the bond length, bond angle and torsional angle, and can be written as

$$U_{b-s} = U_b + U_\theta + U_\tau \tag{2.16}$$

because the stretching and torsional deformation is not energetically favorable in the evaporation-induced deformation of nanofiber, as shown in theoretical analysis in Section 2.2.1, the stretching energy U_b and torsional energy U_τ will be not considered in this CG model. The total energy U_{b-s} only depends on U_θ [102], and Eq. (2.16) becomes

$$U_{b-s} = U_\theta = \sum_i k_\theta (\theta_i - \theta_0)^2 \tag{2.17}$$

where k_θ is the angular stiffness, and θ_i and θ_0 are the angle of adjacent bonds after and before the deformation, respectively. $\theta_0 = \pi$ represents a straight nanofiber.

Given the total length l of nanofiber in the full atomic model, and the bond length l_{bd} in the CG model, the number of bond and angle in the CG model can be determined, and they are $n_b = l/l_{bd},\ n_a = l/l_{bd} - 1$, respectively. Assume that the deformation is uniform along the bead-spring model and the bending angle θ_b, we can have $\theta_i = \pi - \theta_b/n_b$. Similar to that in the full atomic model, the total deformation energy is

$$E_{def}^{b-s} = \sum_{i=1}^{n_a} U_\theta^i = \frac{n_a k_\theta \theta_b^2}{n_b^2} \tag{2.18}$$

On the other hand, from the continuum mechanics point of view, for a 1-D nanofiber with bending stiffness B, length l and bending angle θ_b, the deformation energy is

$$E_{def}^{c-m} = \frac{B\theta_b^2}{2l} \tag{2.19}$$

given $E_{def}^{c-m} = E_{def}^{b-s}$, we will have

$$B = \frac{2n_a k_\theta l}{n_b^2},\ \text{ or }\ k_\theta = \frac{B n_b^2}{2n_a l} \tag{2.20}$$

Eq. (2.20) indicates that we can correlate the force field parameters into the CG model with the bending stiffness B in the continuum model, and this correlation has proved to well reproduce deformation of 1-D nanomaterials [100, 101].

Further, the non-bonded energy interaction in the CG model can be well described via the 12-6 L-J potential $(s) = 4\varepsilon(\sigma^{12}/s^{12} - \sigma^6/s^6)$ [100, 103], where ε and σ are the potential well depth and equilibrium distance, respectively, and s is the distance between beads. The non-bonded interaction energy in the folded part can be obtained via $E_{vdW}^{b-s} = \rho_l^2 \int_{-\infty}^{+\infty} V(s)\, dx$, where $\rho_l = 1/l_{bd}$ is the line density in bead-spring CG model. The integration yields [100, 104]

$$E_{vdW}^{b-s} = 4\varepsilon\rho_l^2\sigma^6\left(\frac{63\pi}{256}\sigma^6\frac{1}{h^{11}} - \frac{3\pi}{8}\frac{1}{h^5}\right) \tag{2.21}$$

where h is the distance of two parallel bead-spring models, as illustrated in **Figure 2.8b**. The energy minimization $\partial E_{vdW}^{b-s}/\partial h = 0$ will lead to $h = 1.0631\sigma$, and thus, the binding energy density in the bead-spring CG model can be obtained by substituting $h = 1.0631\sigma$ into Eq. (2.21) and it is

$$\gamma_b = -1.8927\rho_l^2\varepsilon\sigma \tag{2.22}$$

Once the CG model is validated by full-atomistic simulations, Eqs (2.20) and (2.22) will allow to bridge the CG model and continuum model and validate the proposed theoretical framework in Section 2.2.1.

By taking CNTs as a typical nanofiber, we will first validate the bead-spring model by performing CGMD and full atomistic simulations. The length of CNTs was $l = 20\ nm$ in both full atomic and bead-spring model, and the bond length in the bead-spring model was taken $l_{bd} = 0.1\ nm$. **Figure 2.8c** shows the comparison of its deformation energy E_{def} between full-atomistic and CGMD simulations. In both simulations, each CNT was fixed in one end, and the other end was subjected to an external force perpendicular to its axial direction to achieve a pure bending deformation. In the CGMD model, the angular stiffness k_θ was adjusted to mimic the different radius of CNTs (k_θ=$1.29 \times 10^{-16}\,J$ for (5,5) CNT, k_θ=$2.15 \times 10^{-16}\,J$ for (6,6) CNT, k_θ=$3.31 \times 10^{-16} J$ for (7,7) CNT). The good agreement between them indicates that the CGMD model can well reproduce the bending deformation of CNTs. We further performed the full-atomistic and CGMD simulations by employing two parallel CNTs and extracted the variation of their binding energy E_{vdW} with their overlap distance l_o , as shown in **Figure 2.8d**. In these CGMD simulations, the equilibrium distance between the beads in the 12-6 L-J potential was set as $\sigma = (2r_{CNT} + \sigma_{C-C})/1.0631$, where r_{CNT} is the radius of CNTs and σ_{C-C}(=3.4 nm) is the equilibrium distance of carbon-carbon atoms in the full-atomistic model. Similar to the regulation to k_θ in the plots of **Figure 2.8c**, the potential well depth ε was taken $8.33 \times 10^{-22} J$ for (5,5) CNT, $8.04 \times 10^{-22} J$ for (6,6) CNT, and $7.62 \times 10^{-22} J$ for (7,7) CNT in CGMD simulations so as to well reproduce the binding energy density in full atomistic simulations. The good agreement in **Figure 2.8d** shows that the CGMD simulations can also be used to model non-bonded van der Waal interactions of nanofibers.

Once the CG model of nanofibers is validated, we will employ the bead-spring model to study deformation in the CGMD simulations and to conduct the comparison with theoretical predictions. In the simulation of self-folding of nanofibers by evaporation, the bond length of bead-spring model was fixed to l_{bd} =0.1 *nm* and the equilibrium distance was taken as σ=0.2 *nm*. The SPC/E model for liquid water was used[105], and its surface tension is taken $\gamma_l = 0.0613\ \mathrm{N/m}$ [97, 98]. The length of bead-spring model was set no more than 20 *nm* to improve the computational efficiency, and the number of water was 4500 to guarantee a full immersion of nanofibers at the equilibrium. All the MD simulations were performed in LAMMPS [106]. The system was first equilibrated at 300 *K* and 1 *atm* for 1.0 *ns* with the NVT ensemble, and then the evaporation was performed with the NVE ensemble. The evaporation rate is defined as the number of water molecules that are removed in the system per time and was set to 4.5/ps after verifications to ensure stability of simulations and independence of folded patterns during evaporation of water molecules. After complete evaporation of water molecules, another 1.0 *ns* were kept to allow the arrival of ultimate folded stable patterns. The deformation energy and binding energy were documented every 0.01 *ns* so as to ensure sufficient data recorded during simulations.

2.2.3 Energy and morphology evolution during liquid evaporation

By taking $k_\theta = 75$ *kcal/mole* , $\varepsilon = 0.5625$ *kcal/mole* and $l = 7.9$ *nm* in CGMD simulations, **Figure 2.9a** shows the variation of the surface energy of liquid E_{surf}, binding energy of the overlapped part in the nanofiber E_{vdW}, and deformation energy of nanofiber E_{def} with simulation time. During the equilibrium process, E_{surf} shows an obvious decrease due to the minimization of liquid surface energy until reaching an equilibrium status of the system. As a consequence, the suspension liquid evolves to a spherical droplet at the end of equilibrium, as shown in insets. In contrast, both E_{vdW} and E_{def} do not change due to a sufficiently large volume of water, indicating that the nanofiber remains to be straight in geometry. Once the evaporation starts, in the 1st stage of self-folding, E_{surf} will continue to decrease due to the evaporation of liquid molecules. Due to the confinement force-induced bending deformation of nanofiber by evaporation (insets in **Figure 2.9a**), E_{def} increases steadily. E_{vdW} remains to be an approximate zero in this stage, indicating that there is no formation of a closed pattern in the bent nanofiber. As the evaporation continues, an overlap in the deformed pattern appears in the 2nd stage of self-folding (insets in **Figure 2.9a**). As a consequence, E_{vdW} shows a decrease and reaches a constant where a stable folded pattern is formed. Accordingly, the deformation of nanofiber stops and a constant E_{def} eventually arrives. During this stage, due to the evaporation of water molecules, E_{surf} quickly decreases to zero and its effect can be neglected, which validates the theoretical assumptions in Section 2.2.1.

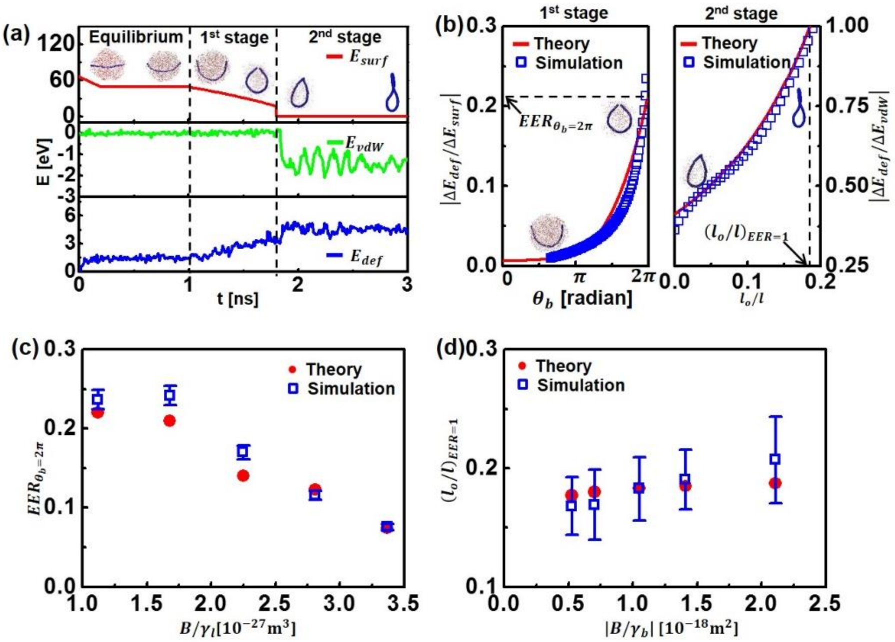

Figure 2.9. Variation of the system energy during liquid evaporation. **(a)** Variation of liquid surface energy E_{surf}, deformation energy of nanofiber E_{def} and binding energy in overlap parts of nanofiber E_{vdW} with simulation time. Insets show the CGMD snapshots of nanofiber deformation in liquid. **(b)** Comparison of $EER = |\Delta E_{def}/\Delta E_{surf}|$ and $EER = |\Delta E_{def}/\Delta E_{vdW}|$ in the 1st and 2nd stage of self-folding by evaporation respectively between CGMD simulations and theoretical predictions. **(c)** Variation of EER at $\theta_b = 2\pi$ in the 1st stage of evaporation with B/γ_l. **(d)** Variation of l_o/l at $EER = 1$ in the 2nd stage of evaporation with $|B/\gamma_b|$.

During the evaporation, EER is extracted and plotted in **Figure 2.9b**, where $EER = \left|\frac{\Delta E_{def}}{\Delta E_{surf}}\right|$ and $EER = \left|\frac{\Delta E_{def}}{\Delta E_{vdW}}\right|$ at the 1st and 2nd stage of liquid evaporation, respectively. Both of them increase with the deformation of the nanofiber. A closed pattern is formed at the end of 1st stage from an initial straight nanofiber (insets in **Figure 2.9b**), and eventually a racket-like folded pattern (insets in **Figure 2.9b**) is obtained at the end of the 2nd stage of evaporation. In parallel, given the CGMD modeling parameters $k_\theta = 75\, kcal/mole$, $\varepsilon = 0.5625\, kcal/mole$ and $l = 7.9\, nm$, we can calculate $B/\gamma_l = 1.67 \times 10^{-27} m^3$, and $|B/\gamma_b| = 7.03 \times 10^{-19} m^2$ via Eqs. (2.20) and (2.22) and obtain the *EER* in theory by solving Eqs. (2.6), (2.11-2.13). The theoretical plots of *EER* at both the 1st and 2nd stages are also given in **Figure 2.9b**, and good agreement between CGMD simulations and theoretical analyses in both stages is observed. Besides, the theoretical calculation via Eq. (2.15) indicates $l_{cr} = 5.27\, nm < l = 7.9\, nm$, suggesting the formation of a stable folded pattern after complete evaporation of water, which is also in good consistency with the observation in the CGMD simulations (inset in **Figure 2.9b**).

As a further comparison between CGMD simulations and theoretical analyses, more CGMD simulations were performed by employing a series of B/γ_l and $|B/\gamma_b|$. At the 1st stage of evaporation, $EER = \left|\frac{\Delta E_{def}}{\Delta E_{surf}}\right|$ at $\theta_b = 2\pi$, where the nanofiber is bent to a whole circular configuration, is extracted and its variation with B/γ_l is plotted in **Figure 2.9c**. At the 2nd stage of evaporation, l_o/l at $EER = \left|\frac{\Delta E_{def}}{\Delta E_{vdW}}\right| = 1$, where the folded pattern reaches a stable stage, is extracted and its variation with $|B/\gamma_b|$ is plotted in **Figure 2.9d**. Good agreement between CGMD and theoretical results in both **Figures 2.9c** and d is obtained, which further validates the theoretical model.

2.2.4 Crumpled patterns of 1-D materials

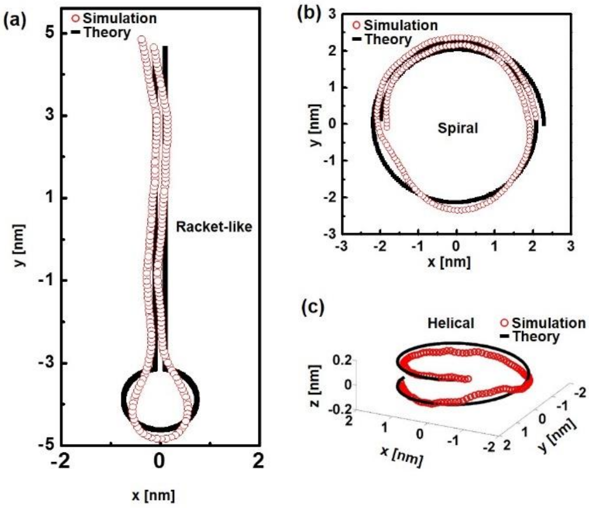

Figure 2.10. Comparison of self-folded patterns of nanofibers after complete evaporation of liquid between CGMD simulations and theoretical predictions. (a) Racket-like pattern. l=20 *nm*, k_θ=200 *kcal/mole*, ε=1 *kcal/mole* in CGMD model, and accordingly $B = 2.79 \times 10^{-28}\, J \cdot m$, $\gamma_b = 2.63 \times 10^{-10}$ *J/m*. **(b)** Spiral pattern. l=20 *nm*, k_θ=100 *kcal/mole*, ε=0.3 *kcal/mole* in CGMD model, and accordingly $B = 1.39 \times 10^{-28}\, J\cdot m$, $\gamma_b = 7.88 \times 10^{-11}$ *J/m*. **(c)** Helical pattern. l=13.7 *nm*, k_θ=150 *kcal/mole*, ε=0.375 *kcal/mole* in CGMD model, and accordingly $B = 2.09 \times 10^{-28} J\cdot m$, $\gamma_b = 9.85 \times 10^{-11}$*J/m*.

Figure 2.10 gives the configuration of three folded patterns after the complete evaporation of water molecules. For example, at l=20 *nm*, k_θ=200 *kcal/mole*, ε=1 *kcal/mole*, a racket-like pattern is obtained in CGMD simulations. In comparison, with these parameters, $l = 20nm$, and $|B/\gamma_b| = 1.0514 \times 10^{-18}\, m^2$, the calculation via Eq (2.11) also shows a formation of a racket-like pattern by evaporation, which agrees well with CGMD simulations. When l, k_θ, and ε change, the spiral and helical patterns can be obtained and also show good agreement with theoretical predictions from Eqs (2.12) and (2.13), respectively. More importantly, all of them show remarkable consistency with theoretical models in both geometric shapes and sizes. In addition, for the racket-like pattern, the approximately circular bent part is obtained in simulations and also agrees with the theoretical assumption in Section 2.2.1.

2.2.5 Influence of aspect ratio on the crumpling of 1-D materials

Our theoretical analyses and numerical simulations prove that the bending stiffness, liquid surface tension, and binding energy density play the critical roles in the determination of the elastocapillary length (l_{ec}) by liquid evaporation and the critical length for ultimate self-folding (l_{cr}). These parameters are obtained on the basis of the pure bending deformation. However, the bending deformation may induce variations of geometric parameters (e.g. cross-section, length), and in turn, affects the folding process during liquid evaporation, discussed as follows.

For nanofibers with a small aspect ratio (i.e. η<10), the nanofiber may be elongated during the folding process, and the stretching energy will become important. Under this circumstance, the stretching will lead to an increase of both length and bending radius of nanofiber and decreases the cross-section area, as illustrated in **Figure 2.11a**, and the deformation energy will include bending and stretching energies, and Eq. (2.3) will become

$$E_{def}^{b\&s} = \frac{B\theta_b^2}{2l} \cdot \frac{2+5\varepsilon_{sc}}{2(1+\varepsilon_{sc})^4} \tag{2.23}$$

where ε_{sc} is the deformation strain by stretching, and $\varepsilon_{sc}(1+\varepsilon_{sc})^4 = 3\theta_b^2/32\eta^2$. Define $\alpha = \frac{2+5\varepsilon_{sc}}{2(1+\varepsilon_{sc})^4}$ and it reflects the stretching deformation of nanofiber. In comparison with deformation energy with a pure bending event, E_{def}^{b}, because of $\alpha \leq 1$, $E_{def}^{b\&s}$ is always lower when the stretching deformation cannot be neglected, which favorites the self-folding process.

It should be noted that the radius of nanofibers cannot be larger than the bending radius so as to ensure to fold an entire circle at the end of the 1st evaporation stage, and the smallest η $(=\pi)$ can be determined. Take $B/\gamma_l = 5.77 \times 10^{-24}\, m^3$, and $\eta = 5$ as an example, **Figure 2.11b** shows a significant decrease in energy ratio $\left|\frac{\Delta E_{def}}{\Delta E_{surf}}\right|$ with the increase of bending deformation due to the stretching deformation in comparison with that without elongation during evaporation. Besides, the longer nanofiber, the more significance of decrease.

This stretching deformation also leads to a decrease of the critical length l_{ec}. For instance, for the nanofiber with $l = 70\, nm$, the calculation via Eq. (2.7) shows that it cannot be folded by evaporation-induced pure bending deformation, and with the consideration of stretching deformation, it can be folded because of $\left|\frac{\Delta E_{def}^{b\&s}}{\Delta E_{surf}}\right| < 1$ at bending angle equal to 2π. The elastocapillary critical length can be modified by replacing the deformation energy in Eq. (2.5) by Eq. (2.23), and it is

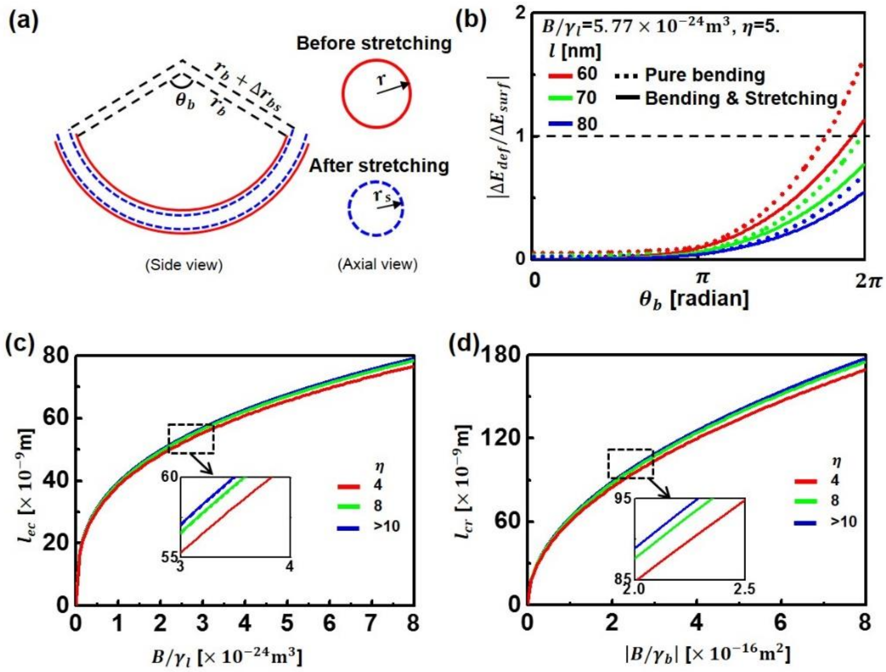

Figure 2.11. Effect of stretching deformation on liquid evaporation-induced self-folding of nanofibers. **(a)** Schematics of nanofiber with and without stretching deformation. r is the intrinsic radius of nanofiber, r_s the radius of nanofiber due to elongation-induced shrinkage of the cross-section. r_b is the bending radius without stretching and Δr_{bs} is the incremence of bending radius by stretching. The bending angle θ_b remains the same before and after stretching. **(b)** Comparison of $\left|\Delta E_{def}/\Delta E_{surf}\right|$ with bending angle of deformation θ_b between with and without stretching deformation. Variation of **(c)** the critical length of nanofiber l_{ec} versus B/γ_l and **(d)** the critical length l_{cr} versus $|B/\gamma_b|$ at different aspect ratios of nanofibers η.

$$l_{ec} = \pi\left(\frac{2\alpha B}{\gamma_l}\right)^{1/3} \tag{2.24}$$

when there is no elongation deformation, ε_{sc}=0 and α=1, Eq. (2.24) will reduce to Eq. (2.8). Similarly, when the stretching deformation cannot be neglected, the critical length l_{cr} will become

$$l_{cr} = 2\pi\sqrt{\left|\frac{\alpha B}{\gamma_b}\right|} \tag{2.25}$$

When the stretching deformation is neglected, α=1, and Eq. (2.25) will reduce to Eq. (2.15). **Figure 2.11c** and **d** give the variation of the critical length l_{ec} with B/γ_l and l_{cr} with $|B/\gamma_b|$ at different aspect ratios η. When $\eta < 10$, l_{ec} and l_{cr} will vary with η. When $\eta >$ 10, the effect of stretching on the self-folding process by liquid evaporation can be neglected.

2.2.6 Influence of cross-section shapes on the crumpling of 1-D materials

When the nanofiber is a hollow, core/shell or inhomogeneous structure such as CNTs, when the bending deformation is beyond a critical buckling strain, the local wrinkling or buckling deformation in nanofibers may happen and affect the self-folding of nanofibers [107, 108]. Assume the bending angle θ_b, the resultant maximum compressive strain in the fiber is [80]

$$\varepsilon_m = -\frac{r}{l}\theta_b \tag{2.26}$$

when ε_m or the associated stress is beyond the critical buckling strain/stress, the local wrinkling or buckling will occur, leading to kinks/wrinklings on the compressive side of nanofiber. This bending-induced local buckling or wrinkling is particularly important in hollow nanofibers or nanofibers with inhomogeneous properties such as core/shell structures [109-112]. Generally, the occurrence of local wrinkling or buckling will lead to a change of the cross-section of nanofibers and decreases the bending stiffness [109, 113]. Assume that the kinks/wrinklings after buckling of nanofibers can be described by a sinusoidal curve [114, 115] with the change of the cross-section from a circular to an elliptical shape, as illustrated in **Figure 2.12a**. The bending stiffness of nanofiber will become $B = EI_{buckle}$, where I_{buckle} is the moment of inertia for the buckled nanofiber with an elliptical cross-section. As a consequence, l_{ec} in Eq. (2.8) can be estimated via

$$l_{ec} = \pi\left(\frac{2\beta B}{\gamma_l}\right)^{1/3} \tag{2.27}$$

where $\beta = \frac{I_{buckle}}{I} \leq 1$ is the shape factor of the cross-section in nanofibers. When there is no buckling deformation, $I_{buckle} = I$ and $\beta = 1$, and Eq (2.27) will reduce to Eq. (2.8).

Take a hallow nanofiber with radius $r = 0.5\ nm$, thickness of shell $t = 0.1\ nm$, $B/\gamma_l = 5.77 \times 10^{-24}\ m^3$ and Poisson's ratio $v = 0.3$ as a representative, the critical buckling strain can be estimated by $\varepsilon_{c-b} = -\frac{1}{\sqrt{3}}\frac{t}{r\sqrt{1-v^2}}$ [111, 116], and the corresponding critical buckling bending angle will be $\theta_{bc} = \frac{l}{r}\varepsilon_{c-b}$ via Eq. (2.26). **Figure 2.12b** shows comparison of energy ratio $\left|\frac{\Delta E_{def}}{\Delta E_{surf}}\right|$ with and without consideration of buckling deformation. When the bending deformation is large enough, there is a sudden drop in $\left|\frac{\Delta E_{def}}{\Delta E_{surf}}\right|$ because of buckling deformation.The longer nanofiber, the larger bending deformation (i.e. a higher bending angle) is required to induce buckling deformation, which is in agreement with the theoretical predictions in Eq. (2.26). This energy drop will delay the bending deformation of nanofiber and also decreases the critical length of self-folding by evaporation, promoting self-folding. For example, assume the radius of the elliptical cross-section in the major and minor axis satisfies $r_1 = 2r_2$ after buckling deformation, we can calculate β =0.3529, and $l_{ec} = 50.17\ nm$ through Eq. (2.27). Apparently, because of $l = 60\ nm,$ and $70\ nm > 50.17\ nm,$ the nanofibers can be folded by evaporation. In contrast, with the sole bending deformation by evaporation, Eq. (2.8) shows that $l_{ec} = 71\ nm > l = 60\ nm,$ or $70\ nm$ and they cannot be folded.

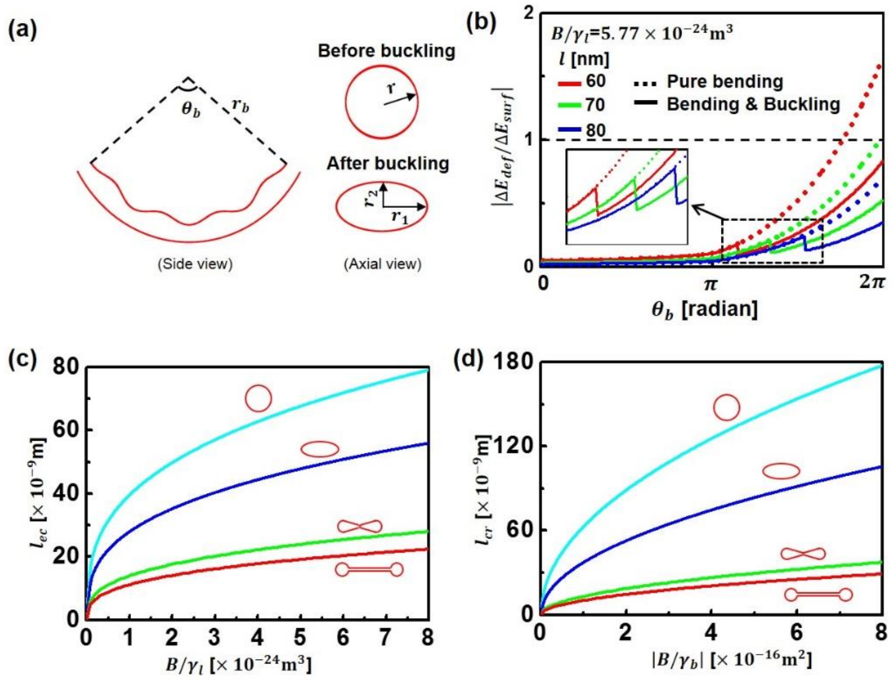

Figure 2.12. Self-folding of nanofibers with different geometric shapes of the cross-section by liquid evaporation. (a) Schematics of the nanofiber with bending-induced buckling deformation (left) and its associated change of cross-section from circular to elliptical shape before and after buckling deformation (right). r is the intrinsic radius of nanofiber without buckling deformation (upper right), and r_1 and r_2 are radius of elliptical cross-section of nanofiber along the major and minor axis respectively after buckling deformation (bottom right). **(b)** $|\Delta E_{def}/\Delta E_{surf}|$ verses bending angle of deformation θ_b with and without buckling deformation. Variation of **(c)** the critical length l_{ec} versus B/γ_l and **(d)** the critical length l_{cr} versus $|B/\gamma_b|$ for fibers with different cross-section shapes (insets).

Similarly, when we consider the bending-induced buckling deformation in the 2nd stage of evaporation, the critical length for self-folding will also be affected. Eq. (2.15) can be modified via the factor β to

$$l_{cr} = 2\pi\sqrt{\left|\frac{\beta B}{\gamma_b}\right|} \tag{2.28}$$

Similar to Eq. (2.27), when $\beta = 1$, the cross-section of nanofiber is circular, there is no buckling deformation and Eq. (2.28) will reduce to Eq. (2.15). **Figures 2.12c** and **d** give the variation of l_{ec} and l_{cr} with B/γ_l and $|B/\gamma_b|$, respectively, and both of them show a clear decrease when the bending-induced buckling deformation is considered with the change of a circular cross-section to an elliptical one. Besides, the larger B/γ_l or $|B/\gamma_b|$, the more decrease.

In addition, for hollow nanofibers, the capillary flow of liquid may happen during evaporation due to a pressure difference between inside and outside of the tubes, which will deform the cross-section of nanofiber to an elliptical one, and even to a contact mode [117]. Usually, three deformed shapes of the cross-section in hollow tubes are observed: elliptical, point contact, and wall contact. Similar to the change of cross-section by bending-induced buckling deformation, the variation of these cross-sections will also significantly affect the bending stiffness and self-folding, and the critical length l_{ec} and l_{cr} can also be obtained by Eqs. (2.27) and (2.28) with the modifications to bending stiffness at different cross-sections of nanofibers. For example, for the point- contact and wall-contact cross-section of nanofibers after deformation, $\beta = 0.0441$ and $\beta = 0.0266$, respectively. Their effects on l_{ec} and l_{cr} are also plotted in **Figures 2.12c** and **d**. A lower l_{ec} and l_{cr} are observed in comparison with that of nanofibers with circular cross-sections. These comparisons also indicate that the nanofibers with non-circular cross-sections will be favorable to be folded by liquid evaporation.

2.2.7 summary

We have proposed an energy-based theoretical framework to understand the self-folding of a single free-standing 1-D nanofiber by liquid evaporation. When the nanofiber is immersed inside a liquid droplet, on the basis of energy competition among liquid surface energy, solid-liquid interaction, deformation energy, and solid-solid interaction at overlap parts during evaporation, the self-folding of a 1-D nanofiber can be divided into two stages. The first stage of self-folding is driven by liquid evaporation and is dominated by the deformation energy of nanofiber and surface energy of the liquid. In this stage, a critical elastocapillary length of nanofiber beyond which self-folding will continue by evaporation is obtained, and it depends on the bending stiffness of nanofiber and surface tension of the liquid. Afterward, with the further evaporation of liquid, which is referred to as the second stage of evaporation, the self-folding will occur till to the arrival of a final stable folded pattern, and it is driven by the van der Waals force interaction at the overlap part in the folded pattern. The critical self-folding length beyond which a stable folded pattern can be formed after complete evaporation of the liquid is obtained. It depends on the bending stiffness and binding energy density of nanofiber, and also varies with the folded patterns. Three typical energy favorable folded patterns, racket-like, spiral and helical patterns observed in experiments are identified. Further, the size and folded patterns are evaluated and well determined after the complete evaporation of liquid.

In parallel, comprehensive coarse-grained molecular dynamics (CGMD) simulations are performed with the help of a bead-spring model of nanofibers to validate the theoretical models. Quantitative comparisons of deformation, self-folding energy, critical elastocapillary and self-folding length in both evaporation stages during evaporation, and folded pattern configurations and sizes after complete evaporation of liquid show remarkable agreement between theoretical estimations and CGMD simulations. In addition, the effect of bending-induced stretching deformation of nanofiber during evaporation on self-folding is investigated and both critical lengths of self-folding are updated by revisiting the bending stiffness of nanofibers. For hollow nanofibers, the bending-induced local buckling deformation and capillary flow-induced variation of cross-sections during evaporation are also discussed on the effect of self-folding and elucidated by introducing a cross-section factor of nanofibers. The present theoretical framework will provide fundamental guidance on the understanding of self-folding of nanofibers by liquid evaporation, and can also be easily extended to other 1-D nanomaterials with a broad range of geometric features. It is also envisioned that this study will facilitate the quantitative control of geometric shapes of 1-D nanomaterials by liquid evaporation, which is of great interest to achieve unique properties of 1-D nanomaterials with on-demand shapes for broad applications.

2.3 Liquid Evaporation-driven Crumpling of a Single 2-D Material

2.3.1 Theoretical framework

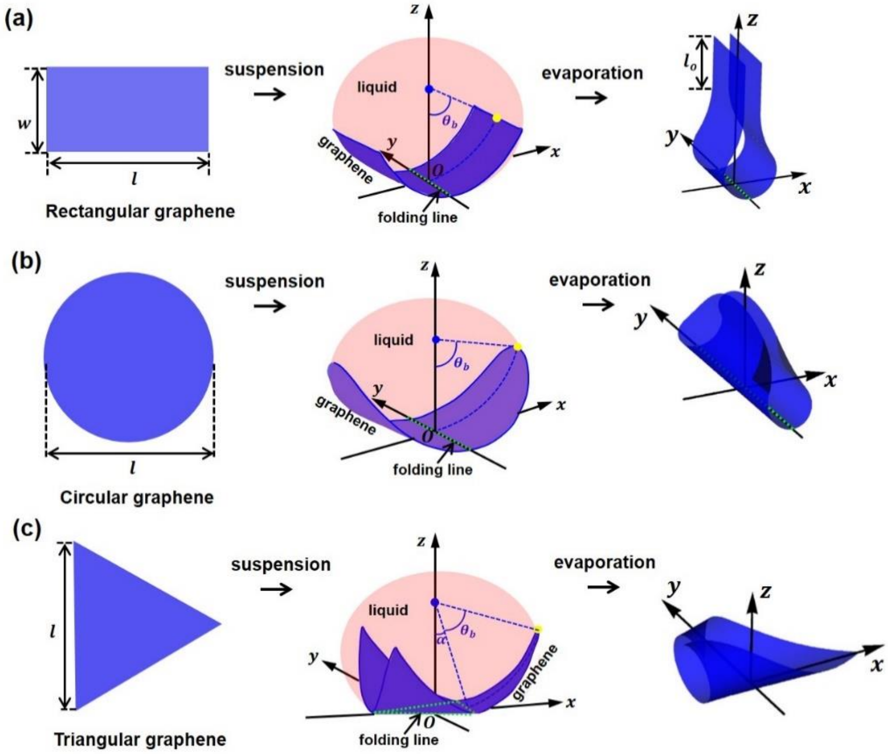

Figure 2.13. Evaporation-driven self-folding of a single suspended graphene sheet in a liquid environment. Schematics of planar **(a)** rectangular, **(b)** circular, and **(c)** triangular graphene, their suspended in liquid and self-folded pattern after complete evaporation of liquid. l and/or w are size of planar graphene. θ_b is the bending angle of graphene in liquid. l_o is the length of overlap part.

Consider a single free-standing graphene suspended in a liquid droplet, the total energy of the system is

$$E_{tot} = E_{def} + E_{surf}^{l} + E_{surf}^{g} + E_{inter} + E_{vdW} \tag{2.29}$$

where $E_{def} = \int_{A_d} \frac{B}{2r_b^2} dA$ is the deformation energy of graphene[118-122], $E_{surf}^{l} = \int_{A_l} \gamma_l dA$ is the surface energy of liquid, $E_{surf}^{g} = \int_{A_g} \gamma_s dA$ is the surface energy of graphene, $E_{inter} = \int_{A_i} \gamma_i dA$ is the interfacial energy between graphene and liquid, and $E_{vdW} = \int_{A_o} \gamma_b dA$ is the binding energy of graphene. A_d is the area of deformed graphene, B is the bending stiffness of graphene, r_b is the radius of curvature, A_l is the surface area of liquid exposed to vacuum/air, γ_l is the surface tension of liquid, A_g is the surface area of graphene exposed to vacuum/air, γ_s is the surface energy density of graphene, A_i is the contact area between solid and liquid, γ_i is the interfacial energy density, A_o is the overlap area in the deformed graphene and γ_b is the vdW binding energy density of overlap area. Once the liquid evaporation begins, the surface energy of liquid will decrease, i.e. $\Delta E_{surf}^{l} < 0$, and the capillary force will deform the graphene sheet to achieve a conformal contact between them. As a consequence, the deformation energy of graphene will increase, i.e. $\Delta E_{def} > 0$, leading to a competition between surface energy of liquid and deformation energy of graphene. Depending on the contact status between liquid and graphene, both interfacial energy and binding energy of graphene may also change, and when the total energy of the system keeps decreasing, i.e. $\Delta E_{tot} < 0$, and $\Delta E_{def} > 0$, the liquid evaporation-induced deformation of graphene will continue, and otherwise, $\Delta E_{tot} > 0$ or $\Delta E_{tot} < 0$ and $\Delta E_{def} < 0$, the folding will stop and no further folding will occur.

2.3.1.1 Elastocapillary by liquid evaporation

At the beginning of evaporation, there is no overlap in graphene and A_o=0, and thus $E_{vdW} = 0$. The graphene will stay in contact with the outmost surface of a water droplet with one surface side exposed to the vacuum/air due to the requirement of the minimum system energy, and $A_d = A_g = A_i$. Take the rectangular graphene with length l and width w $(l \geq w)$ as an example, as illustrated in **Figure 2.13a**, and assume the deformation is unidirectional along its long symmetric axis, r_b is a constant across the entire deformed graphene with the bending angle θ_b, and $\theta_b = l/2r_b$, Eq. (2.29) is simplified to

$$E_{tot} = \frac{2B\theta_b^2}{\eta} + A_l\gamma_l + lw\gamma_s + lw\gamma_i \tag{2.30}$$

where $\gamma_i = \gamma_s - \gamma_l cos\theta_c$ [123], θ_c is the contact angle and $\eta = l/w$. The surface area of liquid A_l will vary with θ_b. To derive this relation, **Figure 2.14a** shows a planar rectangular graphene with length l and width w. Keep the same assumption of bending direction and give a bending angle θ_b after deformation (**Figure 2.14b**), the bending radius is

$$r_b = \frac{l}{2\theta_b} \tag{2.31}$$

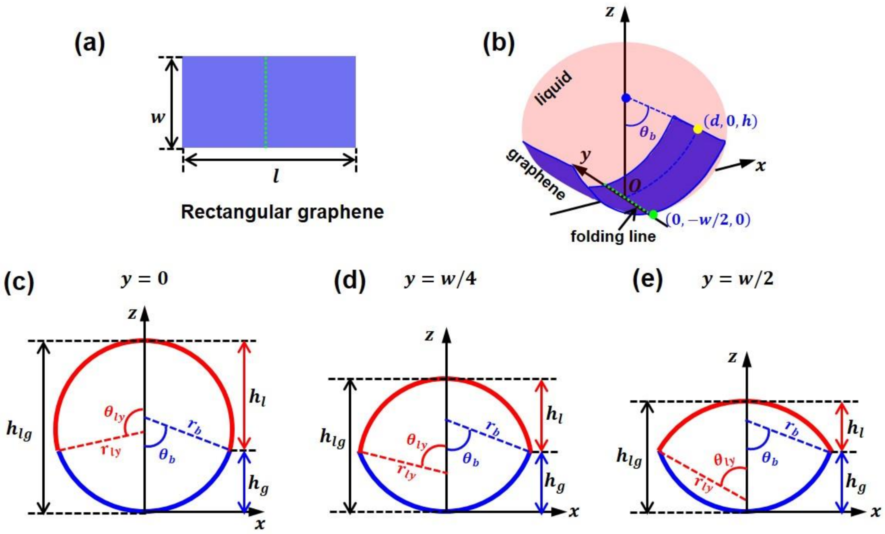

Figure 2.14. Evaporation-driven self-folding of a single suspended rectangular graphene sheet. Schematics of **(a)** planar rectangular graphene, and **(b)** suspended in liquid and the variation of the profile of graphene and liquid along the y direction at **(c)** $y=0$, **(d)** $y=w/4$ and **(e)** $y=w/2$.

The coordinate of the point marked by green is $(0,-w/2,0)$ and the coordinate of the point marked by yellow is $(d,0,h)$, where $d=r_b\sin\theta_b$ and $h=r_b(1-cos\theta_b)$. Based on the full contact assumption between solid and liquid, these two points should be also on the surface of the liquid. Then the profile of liquid can be estimated via

$$x^2+y^2+(z-c)^2=r_c^2 \tag{2.32}$$

With $(0,-w/2,0)$ and $(d,0,h)$, we can have

$$c=(d^2+h^2-w^2/4)/2h \tag{2.33}$$

and

$$r_c=\sqrt{w^2/4+c^2} \tag{2.34}$$

Due to the minimization of the system energy and the surface energy of liquid, the overall configuration of the liquid surface may not be a sphere. Only the molecules in the $x-z$ and $y-z$ planes satisfy Eq. (2.32). In order to get the overall profile of liquid surface, the total height of graphene and liquid along the y axis needs to be determined and it is

$$h_{lg}=\sqrt{r_c^2-y^2}+c, y\in[-w/2,w/2] \tag{2.35}$$

Take the height of graphene $h_g=h$, independent of y, the height of liquid is $h_l=h_{lg}-h_g$ (**Figures 2.14c-e**). Assume the profile of liquid is an arc, it can be determined by the points

$(0, y, h_{lg})$, (d, y, h) and $(-d, y, h)$, and could be represented by the radius of curvature, r_{ly} and half central angle of the profile of liquid, θ_{ly} (**Figures 2.141c-e**). With these analyses, the profile of liquid can be determined in each plane parallel to the $x - z$ plane in the range of $-w/2 \leq y \leq w/2$. So the surface area of liquid exposed to the vacuum is

$$A_l = 2\left(\int_0^{w/2} 2r_{ly}\theta_{ly}dy + A_{cap}\right) \tag{2.36}$$

where $A_{cap} = \varepsilon(r_c - w/2)2\pi r_{cap}(r_c - w/2)$ is the surface area of the spherical cap of liquid at $|y| > w/2$. $\varepsilon(r_c - w/2)$ is the Heaviside step function and $r_{cap} = (r_b^2 + (r_c - w/2)^2)/2(r_c - w/2)$ is the bottom radius of the spherical cap. Similarly, the volume of liquid can be obtained via

$$V_l = 2\left(\int_0^{w/2}[r_{ly}^2(\theta_{ly} - sin\theta_{ly}cos\theta_{ly}) + r_b^2(\theta_b - sin\theta_b cos\theta_b)]dy + V_{cap}\right) \tag{2.37}$$

where $V_{cap} = \varepsilon(r_c - w/2)\pi(r - w/2)^2\left(r_{cap} - (r - w/2)/3\right)$ is the volume of the spherical cap of the liquid.

It needs to be mentioned that the expression of A_l and V_l are derived based on the condition $h_{lg}^{|y|=w/2} > h$, and when $h_{lg}^{|y|=w/2} \leq h$, the point $(0, -w/2, 0)$ and $(d, 0, h)$ are no longer on the surface of the same sphere, a new point $(d, -w/2, h)$ will replace $(d, 0, h)$ to generate a new r_c and c, respectively. The spherical cap will also diminish and $A_{cap} = \pi r_b^2$, $V_{cap} = 0$. The surface area and volume of liquid can still be calculated based on Eqs. (2.36) and (2.37).

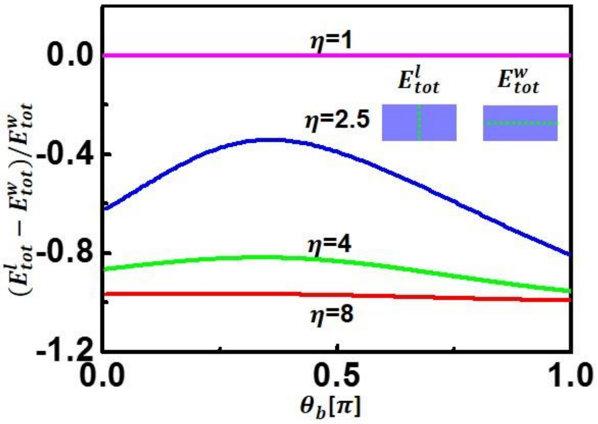

Figure 2.15. Normalized energy difference when the rectangular graphene is folded along its symmetric axis (green dotted line in insets) parallel to the length and width of the rectangle, respectively, where $\eta = l/w$ ($\geq$ 1) is the aspect ratio of graphene.

Once A_l is obtained, the total energy can be calculated via Eq. (2.30). With these geometric relationships, for a rectangular shape, the energy analysis shows that the self-folding deformation along the long symmetric axis is preferable in energy in comparison with along the short axis, consistent with that of graphene nanoribbons [124], as shown in **Figure 2.15**.

After the folding direction is determined, with liquid evaporation, the bending angle of graphene θ_b will increase. As discussed above, both surface energy of graphene $lw\gamma_s$ and interfacial energy $lw\gamma_i$ remain constant, the total energy E_{tot} in Eq. (2.30) is a function of θ_b via the first and second terms and can be solved through numerical iterations. Therefore, a successful self-folding by liquid evaporation requires $E_{tot}(\theta_b + \Delta\theta_b) < E_{tot}(\theta_b), (\Delta\theta_b > 0, \theta_b \in [0, \pi])$. Define $\Delta E_{tot}(\theta_b) = E_{tot}(\theta_b + \Delta\theta_b) - E_{tot}(\theta_b)$, if $\Delta E_{tot}(\theta_b) < 0$, the evaporation-induced folding can be achieved and a fully wrapped state of graphene with liquid droplet will be obtained. As a consequence, from Eq. (2.30), we will have

$$\Delta E_{tot} = \Delta E_{def} + \Delta E_{surf}^{l} \tag{2.38}$$

where $\Delta E_{def} = \frac{2B}{\eta}[(\theta_b + \Delta\theta_b)^2 - \theta_b^2]$ represents the increase of deformation energy of graphene and $\Delta E_{surf}^{l} = A_l(\theta_b + \Delta\theta_b)\gamma_l - A_l(\theta_b)\gamma_l$ represents the decrease of the surface energy of liquid. Therefore, the criterion for a successful folding process by liquid evaporation can be defined as

$$\left|\frac{\Delta E_{def}}{\Delta E_{surf}^{l}}\right| < 1, (\theta_b \in [0, \pi]) \tag{2.39}$$

The critical self-folding length of graphene can be calculated via $\left|\Delta E_{def}/\Delta E_{surf}^{l}\right|_{\theta_b=\pi} = 1$ and it is $l_{ec} = \sqrt{4\pi^3/(\eta + \pi)}\sqrt{B/\gamma_l}$.

Following a similar analysis, we also determine the profile and energy for the liquid evaporation-driven folding of circular and triangular graphene. For circular graphene, the folding line could be an arbitrary diameter (**Figure 2.13b**), and the analysis leads to $l_{ec} = 6.32\sqrt{B/\gamma_l}$. For triangular graphene, unlike the axisymmetric folding of rectangular and circular graphene, its self-folding will be conducted along the centrosymmetric direction (**Figure 2.13c**), and we can have $l_{ec} = 3.45\sqrt{B/\gamma_l}$. By introducing a geometric factor, s, the critical length of these three graphene geometries can be unified into

$$l_{ec} = s\sqrt{\frac{B}{\gamma_l}} \tag{2.40}$$

where $\sqrt{B/\gamma_l}$ represents the material constants of solid and liquid, and $s = \sqrt{4\pi^3/(\eta + \pi)}$ (Rectangle), 6.32 (Circle) and 3.45 (Triangle). In particular, for rectangular graphene with a small aspect ratio, i.e. $\eta \ll 1$, $s = 2\pi$, and the critical length l_{ec} in Eq. (2.40) will be the same as that of graphene nanoribbons [99].

2.3.1.2 Effect of surface wettability

In the determination of l_{ec} in Eq. (2.40), a full-contact between graphene and liquid droplet is assumed, associated with constant interfacial energy during evaporation. Essentially, l_{ec} in Eq. (2.40) reflects the energy competition between liquid surface and deformation of graphene. However, the detaching between graphene and liquid may happen during the folding of graphene with liquid evaporation, as illustrated in **Figure 2.16**. In particular, when the effect of surface wettability of graphene is considered[125, 126], the interfacial energy may change with evaporation. Besides, once the graphene does not remain in contact with the liquid surface, the detached section will recover to be planar [127, 128]. Consider the surface area of detached graphene A_s (>0), the total energy of the system in Eq. (2.30) will become

$$E_{tot} = \frac{B(lw - A_s)}{2r_b^2} + (A_l + A_s)\gamma_l + (lw + A_s)\gamma_s + (lw - A_s)\gamma_i \tag{2.41}$$

The energy difference between the scenarios with full (Eq. (2.30), E_{tot}^{fold}) and partial contact (Eq. (2.41), E_{tot}^{detach}) between graphene and water is $\Delta E_{tot}^{d-f} = E_{tot}^{detach} - E_{tot}^{fold}$, and define the surface wettability of graphene θ_c, we can have

$$\Delta E_{tot}^{d-f} = A_s\left[-\frac{B\theta_b^2}{2l^2} + \gamma_l(1 + cos\theta_c)\right] \tag{2.42}$$

at $\Delta E_{tot}^{d-f} > 0$, no detaching occurs, and the folding will continue with a full-contact between liquid and graphene, and otherwise, detachment will happen and self-folding will stop. Apparently, a hydrophobic surface (larger θ_c) will promote the detachment and suppresses the self-folding process. With the consideration of this effect of surface wettability, the critical length of graphene that can be folded by evaporation, here referred to as wet-capillary critical

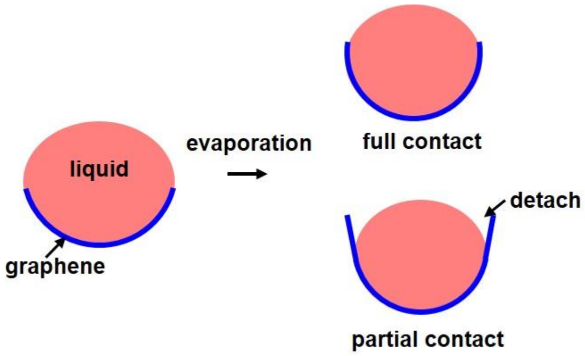

Figure 2.16. Schematic illustrations (side view) of full and partial contact of graphene with a liquid droplet.

length l_{wc}, can be derived via $\Delta E_{tot}^{d-f} = 0$ and it is

$$l_{wc} = g\sqrt{\frac{B}{2\gamma_l(1+cos\theta_c)}} \tag{2.43}$$

where g is the geometry factor and $g = \pi$ for rectangular and circular graphene, and $g = 2.9\pi/\sqrt{3}$ for triangular graphene.

The comparison between Eqs. (2.40) and (2.43) shows that the critical length of graphene to be folded by liquid evaporation will be determined by both the size dimension and surface wettability of graphene, rather than by the sole size dimension via l_{ec}. For example, given the aspect ratio η, bending stiffness B of a rectangular graphene and surface tension γ_l of liquid, a critical contact angle θ_c^c can be derived by $l_{ec} = l_{wc}$, which yields $\theta_c^c = acos(\eta/8\pi - 7/8)$. When $\theta_c < \theta_c^c$, $l_{ec} > l_{wc}$ and a successful folding process requires $l > l_{ec}$, and when $\theta_c \geq \theta_c^c$, a successful folding process requires $l > l_{wc}$.

2.3.1.3 Van der Waals (vdW) energy-driven self-folding

With the continuous evaporation of liquid and self-folding of graphene, the deformed graphene starts to contact with each other ($A_o > 0$), where the vdW binding energy E_{vdW} needs to be considered [99]. Take the rectangular graphene as an example, the total energy of the system now becomes

$$E_{tot} = \frac{B(l-2l_o)w}{2r_b^2} + A_l\gamma_l + lw\gamma_s + (lw - 2l_ow)\gamma_i + l_ow\gamma_b \tag{2.44}$$

where l_o is the overlap length ($A_o = l_ow$, as illustrated in **Figure 2.13a**) and γ_b is the binding energy density of graphene (=$-0.232J/m^2$ [129]). In this stage, because most water has been evaporated, the surface energy of liquid can be neglected and the interfacial energy between solid and liquid could be replaced by the surface energy of solid in theoretical analysis. After the complete evaporation of liquid, the folded solid will be independent of liquid and the variation of total energy is

$$\Delta E_{tot} = \Delta E_{def} + \Delta E_{surf}^{g} + \Delta E_{vdW} \tag{2.45}$$

With the liquid evaporation, a continuous folding of graphene will lead to $\Delta E_{tot} < 0$, $\Delta E_{def} > 0$, $\Delta E_{surf}^{g} < 0$ and $\Delta E_{vdW} < 0$, and therefore the successful self-folding process of graphene will require

$$\left|\frac{\Delta E_{def}}{\Delta E_{surf}^{g} + \Delta E_{vdW}}\right| < 1 \tag{2.46}$$

During the self-folding process, $\left|\Delta E_{def}/(\Delta E_{surf}^{g} + \Delta E_{vdW})\right|$ will increase until to 1 where a stable self-folded arrives, and the overlap length in the folded graphene l_o can be obtained via $\left|\Delta E_{def}/(\Delta E_{surf}^{g} + \Delta E_{vdW})\right|$=1. Accordingly, the critical self-folding length l_{cr} due to vdW energy can be determined by $\left|\Delta E_{def}/(\Delta E_{surf}^{g} + \Delta E_{vdW})\right|_{l_o=0} = 1$ and it is

$$l_{cr} = k\sqrt{\frac{B}{|\gamma_b - 2\gamma_s|}} \tag{2.47}$$

where $k = 2\pi$ for rectangle, k=11.72 for circle, and k=13.57 for triangle.

2.3.2 Computational modeling and simulations

To validate the theoretical analysis, full-scale molecular dynamics (MD) simulations were conducted using LAMMPS[130]. SPC/E model was used to model water molecules[105], and the AIREBO force field was employed to model graphene[131, 132]. The dangling carbon bonds at the edge of graphene sheet are decorated with hydrogen atoms to avoid the effect of edge and bonding effects. The 12-6 Lennard-Jones (L-J) non-bonded pairwise potential $V_{L-J}(r) = 4\varepsilon_{c-o}(\sigma^{12}/r^{12} - \sigma^{6}/r^{6})$ was used to model the carbon-water vdW interactions, where ε_{c-o} is the potential well depth, σ is the equilibrium distance and r is the distance between two atoms. The coulomb interaction $V_q(r) = q_i q_j/4\pi\varepsilon_0 r$ was used to model the electrostatic interaction between water molecules i and j. The cut-off radius of 1.0 nm was chosen, and the particle-particle-particle-mesh (PPPM) with a root mean of 0.0001 was employed to calculate the long-range Coulomb interactions between oxygen and hydrogen atoms in water molecules. Periodic boundary conditions were applied in the x, y and z directions of the simulation cubic box that was far larger than the graphene-water system to avoid the effect of periodic image[120, 133].

The simulations of liquid evaporation included three major steps. First, the equilibrium of the system consisting of 21296 water molecules and a graphene sheet was reached under the NVT ensemble with Nose/Hoover thermostat at 300K at 1.0 atmosphere. The simulations were run for 1.0 ns with a time step of 1.0 fs. Second, water molecules were removed randomly to mimic evaporation of liquid and the evaporation rate was 10000 water molecules per nanosecond under the NVE ensemble. Afterward, the system would be re-equilibrated under the NVE ensemble to ensure slow liquid evaporation without affecting the deformation of graphene. The evaporation and equilibrium procedures were repeated until all the water molecules were removed completely. During this process, the coordinates of atoms in both water and graphene were monitored every 10000 time steps to ensure to document enough data. Third, the NVE ensemble was run for another 1.0 ns after the complete evaporation of water molecules to make sure the arrival of a folded stable graphene.

2.3.3 Energy and morphology evolution during liquid evaporation

Figure 2.17a illustrates the comparison of the volume of water (V_l) and deformation of graphene (θ_b) between the theoretical and simulation results for rectangular planar graphene. With the decrease of volume of water (evaporation), the bending angle of graphene increase (folding), and good agreement between simulations and theoretical analysis is observed. Moreover, **Figure 2.17b** shows that both profiles of water and graphene during simulation are well consistent with theoretical predictions. **Figure 2.17c** shows the history of the surface energy of liquid E_{surf}^{l}, deformation energy of graphene E_{def} and binding energy of the overlap part in the graphene E_{vdW} with evaporation. During the equilibrium process, E_{surf}^{l} shows an obvious decrease due to the minimization of liquid surface energy, and E_{def} and E_{vdW} do not change due to the large volume of water. Upon liquid evaporation begins, at the

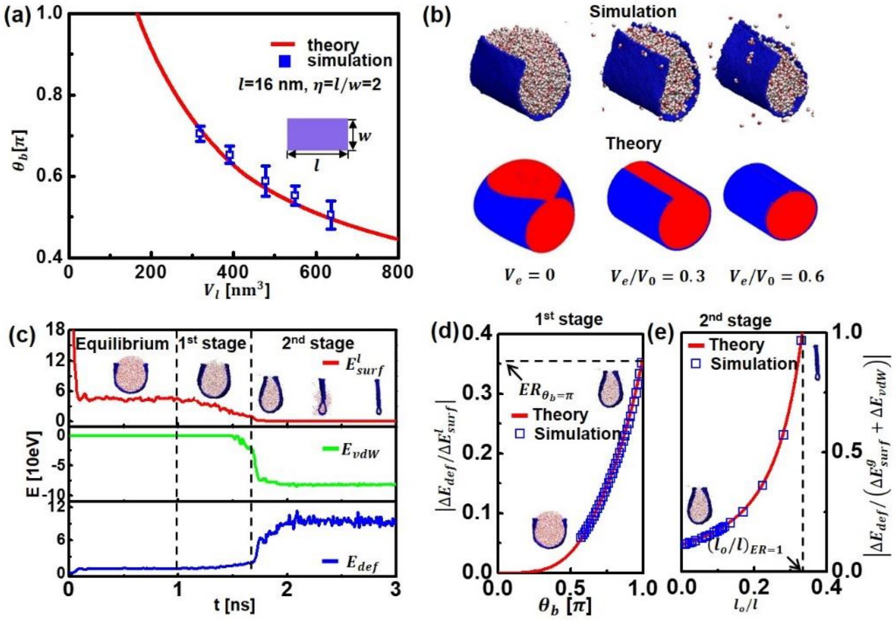

Figure 2.17. Self-folding deformation and energy variation of graphene with initial planar rectangular geometry with liquid evaporation. (a) Variation of bending deformation-bending angle θ_b of graphene with volume of water V_l. **(b)** Comparison of deformation configuration of graphene and water droplet with evaporation between simulations and theoretical analysis (V_0 is the initial volume of water and V_e is the evaporated volume of water). **(c)** Variation of liquid surface energy E^l_{surf}, binding energy in overlap parts of graphene E_{vdW} and deformation energy of graphene E_{def} with simulation time. Insets show the MD snapshots of graphene deformation in liquid. **(d)** Comparison of the energy ratio $|\Delta E_{def}/\Delta E^l_{surf}|$ and $|\Delta E_{def}/(\Delta E_{vdW}+\Delta E^g_{surf})|$ in the elastocapillary mechanism driven by liquid evaporation (1st stage) and self-folding mechanism driven by vdW energy (2nd stage) between simulations and theoretical analysis. The size dimension of rectangular graphene: l=16 nm and η=2, and surface wettability: $\theta_c = 60^\circ$.

elastocapillary folding stage, E^l_{surf} continues to decrease, E_{def} increases steadily and E_{vdW} remains to be an approximate zero, indicting the deformation of graphene yet without any overlap, which validates the assumption made in the derivations of Eqs. (2.38) and (2.40) in Section 2.3.1. As the evaporation continues, an overlap appears in the closest region of folded graphene, and E_{vdW} starts to dominate the folding, as discussed in Section 2.3.1, showing a decrease till to a constant that corresponds to the formation of a folded stable pattern. At the same time, E_{def} increases rapidly and reaches a constant along with E_{vdW}, and E^l_{surf} quickly decreases to zero due to the evaporation of water molecules. **Figures 2.17d** and **e** show the energy ratio of these two stages, $|\Delta E_{def}/\Delta E^l_{surf}|$ and $|\Delta E_{def}/(\Delta E^g_{surf}+\Delta E_{vdW})|$, respectively, and the representative snapshots of graphene deformation and water droplet

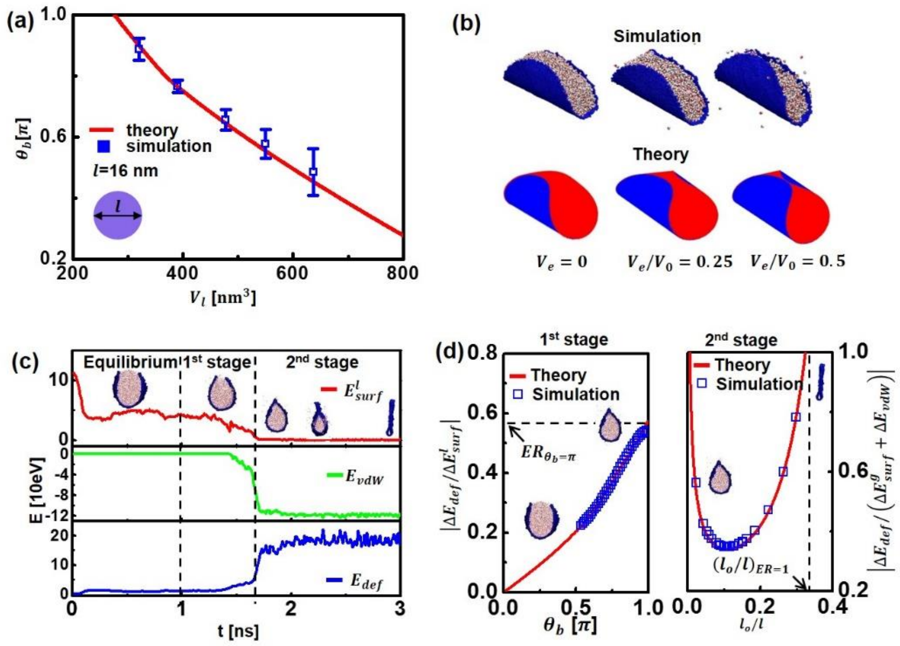

Figure 2.18. Self-folding deformation and energy variation of graphene with initial planar circular geometry with liquid evaporation. (a) Variation of bending deformation-bending angle θ_b of graphene with volume of water V_l. **(b)** Comparison of deformation configuration of graphene and water droplet with evaporation between simulations and theoretical analysis (V_0 is the initial volume of water and V_e is the evaporated volume of water). **(c)** Variation of liquid surface energy E^l_{surf}, binding energy in overlap parts of graphene E_{vdW} and deformation energy of graphene E_{def} with simulation time. Insets show the MD snapshots of graphene deformation in liquid. **(d)** Comparison of the energy ratio $|\Delta E_{def}/\Delta E^l_{surf}|$ and $|\Delta E_{def}/(\Delta E_{vdW} + \Delta E^g_{surf})|$ in the elastocapillary mechanism driven by liquid evaporation (1st stage) and self-folding mechanism driven by vdW energy (2nd stage) between simulations and theoretical analysis. The size dimension of circular graphene: l=16 nm, and surface wettability: $\theta_c = 60^\circ$.

profile (insets in **Figure 2.17d**). A closed pattern is obtained at the end of the elastocapillary folding by liquid evaporation, and an ultimately stably racket-like pattern is formed at the end of the self-folding by vdW energy. Given the bending stiffness of graphene B for a specific length l and width w, and surface tension of water γ_l, the theoretical energy ratios can be calculated based on Eqs. (2.39) and (2.46) and are also plotted in **Figures 2.17d** and **e**. Good agreement in both stages is observed between simulations and theoretical analysis.

Figures 2.18 and **2.19** give the comparison between theoretical analysis and simulations for graphene with circular and triangular shapes, respectively, including deformation of graphene, profile of water droplet and variations of energy. Similarly, good agreement is also obtained. we should mention that for the triangular graphene, due to its centrosymmetric folding type, the maximum bending angle is different from that of axisymmetric folding cases (rectangle and circle) and this maximum bending angle can be determined based on the geometric characteristic of triangle (θ_b^{max}=0.72π).

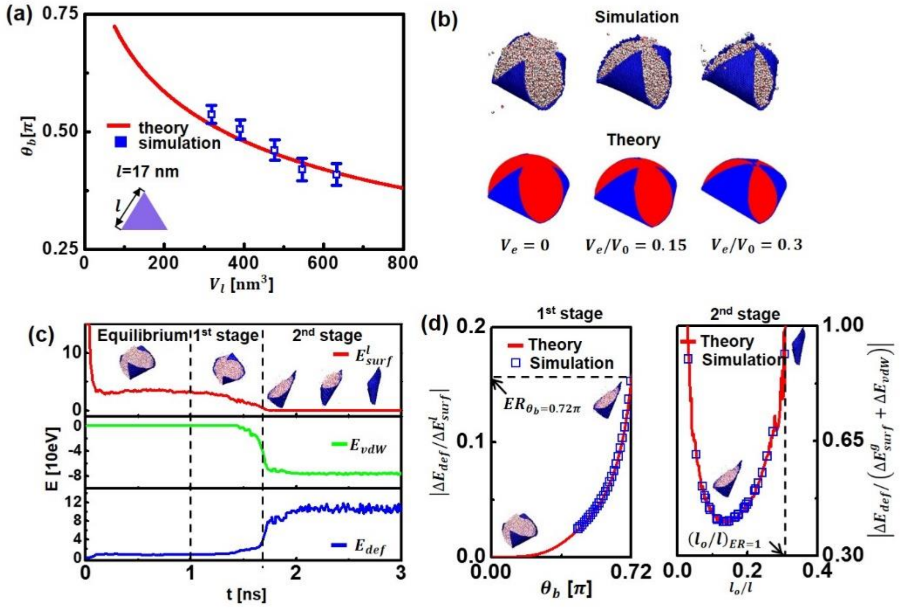

Figure 2.19. Self-folding deformation and energy variation of graphene with initial planar triangular geometry with liquid evaporation. (a) Variation of bending deformation-bending angle θ_b of graphene with volume of water V_l. **(b)** Comparison of deformation configuration of graphene and water droplet with evaporation between simulations and theoretical analysis (V_0 is the initial volume of water and V_e is the evaporated volume of water). **(c)** Variation of liquid surface energy E_{surf}^l, binding energy in overlap parts of graphene E_{vdW} and deformation energy of graphene E_{def} with simulation time. Insets show the MD snapshots of graphene deformation in liquid. **(d)** Comparison of the energy ratio $\left|\Delta E_{def}/\Delta E_{surf}^l\right|$ and $\left|\Delta E_{def}/(\Delta E_{vdW} + \Delta E_{surf}^g)\right|$ in the elastocapillary mechanism driven by liquid evaporation (1st stage) and self-folding mechanism driven by vdW energy (2nd stage) between simulations and theoretical analysis. The size dimension of triangular graphene: l=17 nm, and surface wettability: $\theta_c = 60^{\circ}$.

2.3.4 Crumpled patterns of 2-D materials

With the continuous evaporation of liquid, once there is an overlap in the folded graphene, the theoretical analysis shows that the binding energy starts to dominate the subsequent folding process. In the MD simulations, the rectangular and circular graphene will be folded into a 2-D “racket-like” pattern. In contrast, for the triangular graphene, it will be folded into a 3-D “cone-like” structure. **Figure 2.20** gives the comparison of the overall configuration of the final patterns folded from planar rectangular, circular and triangular graphene, and all agree with theoretical analyses. Further, **Figures 2.21a** and **b** plot the overlap length normalized by original size, l_o/l for the folded 2-D racket-like pattern, and good agreement between

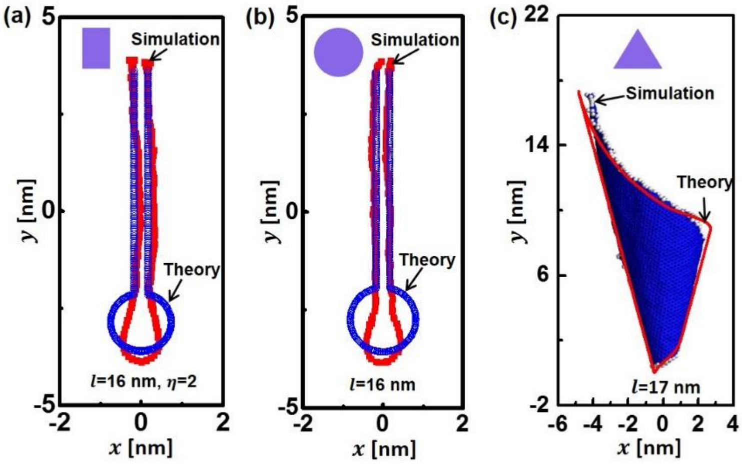

Figure 2.20. Comparison of overall configurations of self-folded graphene after complete evaporation of liquid between simulations and theoretical analysis. "Racket-like" pattern folded from planar **(a)** rectangular graphene with a length of l=16 nm, and **(b)** circular graphene with a length of l=16 nm. **(c)** "Cone-like" pattern folded from planar triangular graphene with a length of l=17 nm. Surface wettability of graphene in water $\theta_c = 60^\circ$.

theoretical analysis and simulations for both folded patterns is obtained. To characterize the 3-D folded cone-like pattern, two parameters, the ending radius r_e at the "mouth" and the initial radius r_i at the "bottom" are extracted to describe this structure and are given in **Figure 2.21c**. Remarkable agreement between simulations and theoretical analysis is also observed.

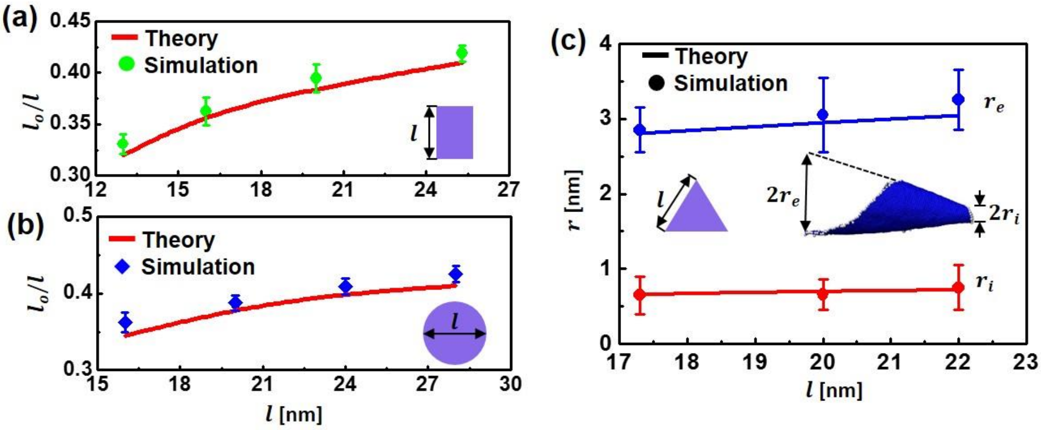

Figure 2.21. Parametric characterizations of the self-folded profile of graphene after complete evaporation of water. 2-D "Racket-like" pattern folded from **(a)** rectangular and **(b)** circular graphene. **(c)** 3-D "Cone-like" pattern folded from triangular graphene. Surface wettability of graphene in water $\theta_c = 60^\circ$.

2.3.5 summary

We propose a theoretical framework to describe the self-folding process of graphene by liquid evaporation. The unified theoretical model is built by considering the energy competition of solid deformation, liquid surface, and solid-liquid interface, and the effect of surface wettability is also incorporated. Three representative geometries of graphene sheet, rectangular, circular and triangular shapes, are studied. The theoretical analysis shows that the ultimate success of the self-folding of graphene is determined by both liquid evaporation-induced and vdW energy-induced self-folding processes, where the former will trigger the self-folding, and the latter will determine the stability of self-folded pattern. In particular, in the determination of the critical self-folding length of graphene by liquid evaporation, our theory indicates that a sole elastocapillary length of graphene is not sufficient and the effect of surface wettability needs to be taken into account. A new critical length, referred to as wet-capillary length, is given by considering the variation of interfacial energy during liquid evaporation, and the liquid-evaporation-triggered self-folding of graphene relies on the competition with elastocapillary length and wet-capillary length. Further, the critical length of graphene induced by vdW energy is determined by analyzing competition between deformation energy and binding energy. For different shapes of graphene (axial or central symmetry), the modes of deformation change, and eventually leads to various folded configurations, including 2-D “racket-like” for graphene with axial symmetry in geometry, and 3-D “cone-like” for graphene with central symmetry in geometry. The parallel full-atom molecular dynamics (MD) simulations are conducted to verify theoretical models from energy evolution and liquid droplet profile with liquid evaporation to the final folded patterns and sizes, and show good agreement with the theoretical analysis. The proposed framework could be easily extended to study the self-folding of other 2-D materials by updating the geometric parameters in the models and provides quantitative guidance on the conversion of 2-D materials into other non-planar structures by liquid evaporation required by broad applications of 2-D materials.

Chapter 3 Liquid Evaporation-driven Crumpling and Assembling of Multiple 2-D Materials

3.1 Overview of the Chapter

In this chapter, we ascertain and establish a theoretical mechanics framework for the liquid evaporation-driven crumpling and assembling of 2-D deformable materials suspended in a free-standing liquid droplet, as illustrated in **Figure 3.1a** for the experiment setup, and further develop a coarse-grained modeling to conduct large-scale molecular dynamics simulations and validate the proposed mechanics theory, in parallel with the comparison of theoretical and computational results with experimental results. The details of the theoretical framework are given in Section 3.2. An equivalent pressure model is first developed to unify the driving forces of crumpling and assembling 2-D materials including capillary force, carrier gas pressure, vapor pressure, vapor recoil pressure, and capillary flow-induced shear force. Then, a rotational spring-mechanical slider model is proposed to describe mechanical deformation and self-folding of individual 2-D sheets and their self-assembly during evaporation. The resultant energies are derived to quantitatively elucidate the energy competition between crumpling and self-assembly of 2-D materials. By minimizing the ultimate energy state after complete evaporation of liquid, the morphology and size of assembled 3-D particles are also predicted in theory. A high-efficiency coarse-grained modeling is developed to conduct large-scale molecular dynamics simulations and validate the proposed theoretical model in Section 3.3. Graphene is taken as a representative of 2-D deformable materials and is modeled by a coarse-grained model. A controllable virtual spherical force field that exerts on graphene is developed to mimic the liquid evaporation-induced pressure, thereby significantly reducing computational cost yet with high accuracy. The quantitative comparison between simulations and theoretical predictions is presented in Sections 3.4-3.5, including deformation, crumpling, and assembling energies of graphene with liquid evaporation and morphology evolution of assembled graphene. The size and accessible area of assembled particles from both theoretical and simulation results are obtained with excellent agreement with each other and also agree well with experiments in the literature. The extension of the proposed theory that takes into account the numbers, size distribution, and geometric shapes of graphene sheets in the droplet is further discussed in Section 3.6 and the results show good consistency with simulations and experiments. The concluding remarks are given in Section 3.7.

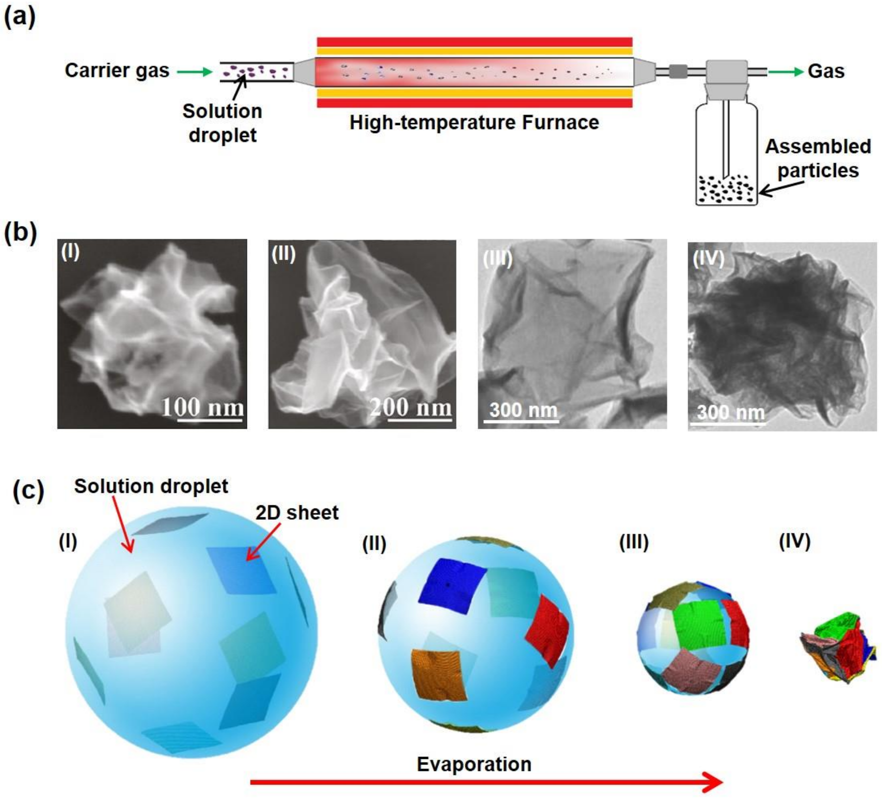

Figure 3.1. Liquid evaporation-driven crumpling and assembling of two-dimensional (2-D) deformable nanomaterials. (a) Schematics of the popular experimental setup for the liquid evaporation-induced crumpling and assembling of 2-D nanomaterials to bulk forms [44-48]. The liquid droplets consisting of 2-D materials and solvent liquid solution are generated by atomization and sent into the high-temperature furnace with the help of carrier gas for liquid evaporation. The assembled solid particles are collected at the outlet of the furnace. **(b)** Electron microscopy images of four assembled graphene oxide particles at different concentration of graphene oxide (C_m) and furnace temperature (T_f). (I) C_m=0.2 mg/ml, T_f=100$°C$ [47]and (II) C_m=1 mg/ml , T_f=100$°C$ [47], (III) C_m=2 mg/ml, T_f=350$°C$ and (IV) C_m=2 mg/ml, T_f=750$°C$ [48]. **(c)** Schematic illustrations of the crumpling and assembling process of 2-D material sheets by liquid evaporation. (I) uniform distribution of multiple 2-D sheets suspended in the liquid droplet after atomization. (II) 2-D sheets immigrate to the surface of liquid droplet with the initial evaporation of liquid due to the capillary flow and/or amphiphilicity. (III) 2-D sheets crumple and assemble with the continuous evaporation of liquid. (IV) 2-D sheets further assemble and self-fold until the complete evaporation of liquid, and a solid particle is generated.

3.2 Theoretical Framework

3.2.1 Equivalent evaporation pressure model of liquid evaporation-induced forces

As illustrated in **Figure 3.1c**, the liquid droplet of solution suspension is first generated by atomization (**Figure 3.1c (I)**) and once the liquid evaporation occurs at an elevated temperature in the furnace, the 2-D sheets will be gradually in contact with the vapor air and immigrate to the surface of droplet due to intrinsic amphiphilicity of 2-D sheets (**Figure 3.1c (II)**) [36, 134]. Besides, these 2-D sheets at the solid-vapor-liquid interface will lead to certain constraints to other 2-D sheets inside the droplet, similar to the pinning effect of a substrate to nanoparticles in coffee-ring phenomena [135], which generates a capillary flow with evaporation, and in turn, promotes immigration of 2-D sheets to the surface of the droplet. As a consequence, the evaporation of liquid molecules will result in a recoil force at the liquid-vapor interface and it is perpendicular to the interface squeezing the interface toward the liquid side [136]. This recoil force will bend the 2-D sheets around the center of liquid droplet and influences the deformation and assembly of the 2-D sheets. At the same time, similar to a pressure increase led by the heated carrier gas in the relatively sealed tube furnace, the liquid vapor will lead to an increase of the pressure, and in turn, promotes the deformation and self-assembly of 2-D sheets. Besides, the dynamics flow of liquid around 2-D sheets, often referred to as capillary flow, will lead to a shear force exerting on the contact surface of 2-D sheets with liquid droplet [137]. In addition, the capillary force along the tangential direction of liquid at the contact line between solid and liquid will further promote the deformation of 2-D sheets [138-140]. **Figure 3.2a (I)** illustrates the directions and locations of these forces which are all led by liquid evaporation. Under these forces, the 2-D sheets will be crumpled till to the complete evaporation of liquid. In our analysis, these driving pressures and forces will be unified to a generalized equivalent pressure to describe the crumpling and self-assembly of 2-D sheets.

Specifically, once the liquid droplet is sent to the high-temperature furnace by a carrier gas, the carrier gas will be heated, leading to an increase of pressure (P_g) in the furnace. Based on the ideal gas law, the gas pressure is [141]

$$P_g = \frac{P_0 T_f}{T_0} \tag{3.1}$$

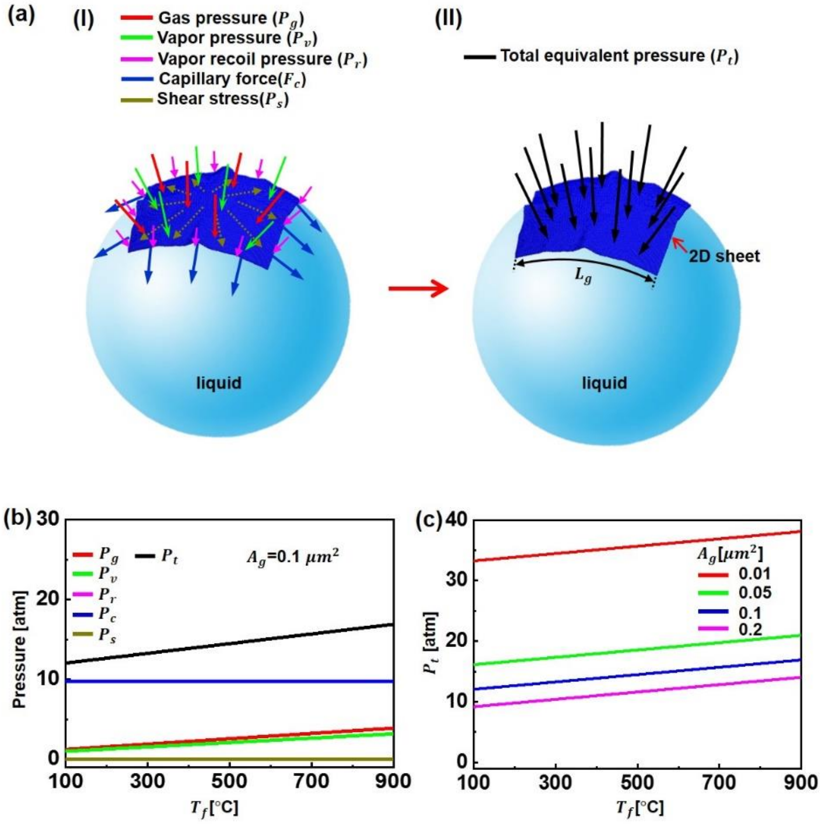

Figure 3.2. Equivalent model of evaporation pressure for assembling and crumpling of 2-D nanomaterials by liquid evaporation. (a) Schematic illustrations of the various resultant forces (including both direction and location) exerted on a 2-D sheet by liquid evaporation (I) and their total equivalent pressure (II). The gas pressure of thermally expanded carrier gas (P_g) and vapor pressure (P_v) act on the surface of 2-D sheet, and their direction both are perpendicular to the surface of 2-D sheet; The capillary force (F_c) acts on the boundary of 2-D sheet pointing to the tangential direction of the liquid surface; The vapor recoil pressure (P_r) acts on the boundary of solid, and it is perpendicular to the tangential direction of the liquid surface; The shear stress (P_s) acts on the inner side of 2-D sheet, and it is parallel to the surface of the 2-D sheet. In the total equivalent pressure (P_t) model, it acts on the surface of solid in perpendicular to the surface of the 2-D sheet. **(b)** Variation of various resultant forces exerted on a square 2-D sheet with an area $A_g = 0.1\ \mu m^2$ as a function of furnace temperature (T_f). Both P_r and P_s are at least three orders of magnitude lower than P_g, P_v and P_c and are not included in the following analysis of P_t. **(c)** Total equivalent evaporation pressure exerted on the squared 2-D sheet with different areas A_g versus furnace temperature (T_f).

where P_0 and T_0 are the pressure and temperature of the carrier gas at the inlet of furnace, respectively, and T_f is the furnace temperature. For the liquid droplet, when flying through the high-temperature furnace, the liquid phase will be changed into the vapor phase by direct vaporization to liquid on the surface of droplet and possibly by cavitation to liquid near the 2-D sheets inside the droplet at the very high temperature of evaporation (e.g. $T_f \gg T_b$), and leads to an increase of the vapor pressure in the furnace. Besides, the resultant instant pressure or dynamic impact to the suspended 2-D sheets due to breakage of cavitation can be neglected due to the good flexibility of 2-D sheets and their free motion inside the liquid. Assuming all the liquid in the droplet is vaporized, the resultant vapor pressure (P_v) can be calculated using the ideal gas law, similar to P_g in Eq. (3.1), and it is

$$P_v = \begin{cases} \frac{nRT_f}{V}, \left(T_f \geq T_b\right) \\ 0, \left(T_f < T_b\right) \end{cases} \tag{3.2}$$

where n is the amount of vapor, R is the ideal gas constant, V is the volumetric capacity of the furnace, and T_b is the boiling point of solution liquid. We should note that the droplet size generated by atomization is usually at the microscale and the enhancement of vapor pressure due to the curvature of liquid droplet surface, usually named as Kelvin effect [142], can be neglected because such effect becomes significant only when the radius of droplet (R_d) is less than 10 nm. In addition to P_v, the generation of liquid vapor will lead to a vapor recoil pressure (P_r) that exerts on the boundary of 2-D sheets. The vapor recoil pressure P_r depends on both droplet size and furnace temperature and can be determined by [136]

$$P_r = q^2 \left(\frac{1}{\rho_v} - \frac{1}{\rho_l}\right) \tag{3.3}$$

where $q = m_d/A_d t_e$ represents the mass evaporation rate of liquid, m_d is the mass of liquid droplet, A_d is the total surface area of liquid droplet, and t_e is the evaporation time. ρ_v and ρ_l are the density of vapor and liquid, respectively.

Unlike the constant loading direction of gas and vapor pressure that vertically exerts on the surface of 2-D materials, the capillary force (F_c) that appears at the solid-vapor-liquid interface changes its direction dynamically due to free suspension of 2-D sheets in the droplet and its contribution to deformation of 2-D sheets can be evaluated by an equivalent pressure (P_c). For a free-standing deformable sheet suspended in a liquid droplet, its centroid will not deform and can be taken as a constraint reference point. Consider an entire 2-D sheet composed of infinite numbers of cantilever beams with the fixed centroid, with the principle of deflection of beam, the capillary force applied at the free ends can be equivalent to a pressure exerted on the surface [143] (**Figure 3.3**). For example, for a cantilever beam of rectangular-shaped 2-D materials with a length l and width w, the capillary force ($F_c = \gamma_l w$) that acts at the free end of 2-D sheet due to the receding of liquid by evaporation will generate a deflection $\delta_F = F_c l^3/3EI$ [143, 144], where E is Young's modulus and I is the moment of inertia of the cross-section of 2-D sheets. For comparison, when a uniform pressure P_c is applied to the beam, the beam will have a deflection at the free end, $\delta_P = P_c w l^4/8EI$. $\delta_F = \delta_P$ will yield $P_c = 8F_c/3lw$, which leads to an equivalence between capillary force and uniform pressure for the mechanical deformation of the beam. Similarly, we can have $P_c = 16\gamma_l/3L_g$, $P = 32\gamma_l/3\sqrt[4]{3}L_g$, and $P = 16\gamma_l/3L_g$ for a square, and triangular, and circular shaped 2-D sheets, respectively, where γ_l is the surface tension of liquid and L_g is the size of 2-D material (i.e. length of square- and equilateral triangular-, and diameter of circular-shaped 2-D sheets). As a result, the equivalent pressure that could be used to replace the capillary force can be summarized as $P_c = 16S\gamma_l/3L_g$, where S is a dimensionless geometric factor of 2-D sheets (S=1 for square and circular shaped 2-D sheets, $S = 2/\sqrt[4]{3}$ for triangular-shaped 2-D sheets).

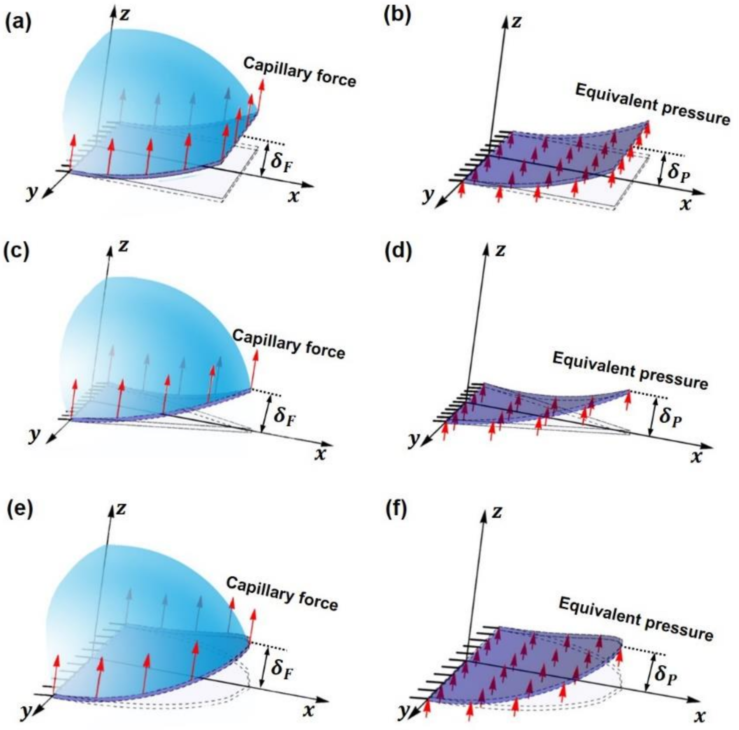

Figure 3.3. Schematics illustrations of the capillary force exerts on the free end of the 2-D sheet and the deflection δ_F and the equivalent pressure exert on the surface of the 2-D sheet and the deflection δ_P. **(a)** and **(b)**, rectangular sheet. **(c)** and **(d)**, triangular sheet. **(e)** and **(f)**, circular sheet.

Further, the surface tension of liquid solution in the droplet usually is a function of temperature [145, 146], and for example, the surface tension of water is $\gamma_w(T) = 94.74 + 1.87 \times 10^{-3}T - 2.63 \times 10^{-4}T^2$ (mN/m) between 273 and 373K [147]. Therefore, the equivalent pressure to the capillary force for driving deformation of 2-D sheet by liquid evaporation can be written as

$$P_c = \begin{cases} s\frac{16\gamma_l(T_f)}{3L_g}, T_f \leq T_b \\ s\frac{16\gamma_l(T_b)}{3L_g}, T_f > T_b \end{cases} \tag{3.4}$$

Besides the capillary force, the dynamic interaction between 2-D sheets and liquid during liquid evaporation will generate a capillary flow along the surface of 2-D sheets. The convection of liquid between the inside and on the surface of droplet will lead to a capillary flow and exert shear stress to the 2-D sheets in contact with the liquid droplet. The capillary flow-induced shear stress is [148]

$$P_s = \mu v_l \tag{3.5}$$

where μ is the friction coefficient between 2-D sheets and liquid, and v_l is the velocity of liquid flow on the surface of 2-D sheets. For a given liquid and 2-D sheets, μ can be determined from the solid-liquid interaction [149] and v_l can be estimated via the evaporation rate of liquid [135, 150].

With these analyses in Eqs. (3.1)-(3.5), the total equivalent evaporation pressure that could drive crumpling and assembly of 2-D sheets by liquid evaporation can be summarized to

$$P_t = P_g + P_v + P_r + P_c + P_s \tag{3.6}$$

Take a square 2-D graphene sheet with an area $A_g = 0.1\ \mu m^2$ and liquid water as an example, and set T_0=300 K and P_0=1 atm, n=0.01 $mole$, $V = 3 \times 10^{-4}\ m^3$ and $R_d = 1.45\ \mu m$, **Figure 3.2b** shows these forces as a function of the furnace temperature (T_f) and all of them are temperature dependent. Compared with P_g, P_v and P_c, both P_r and P_s are at least three orders of magnitude lower, and thus will not be included in the following discussion unless otherwise stated; that is, Eq. (3.6) reduces to

$$P_t = P_g + P_v + P_c \tag{3.7}$$

In addition, both P_g and P_v increase with the furnace temperature, and P_c remains constant because the temperature has exceeded the boiling point of liquid water (T_b=100 $°C$) and the temperature of liquid water will not change. **Figure 3.2b** further shows that the evaporation pressure (P_t) increases with the increase of furnace temperature, indicating that a high temperature will benefit the crumpling and assembling of 2-D materials [77]. When the size of 2-D materials changes, **Figure 3.2c** shows the variation of the evaporation pressure (P_t) with the furnace temperature, and crumpling a smaller 2-D material requires a higher evaporation pressure. It should be noted that when the 2-D sheets are highly hydrophilic or the liquid solution of 2-D sheets is highly diluted, all 2-D sheets might stay inside the droplet [151] during the early stage of evaporation, and the evaporation will condense the solution droplet, which could lead to the crumpling and self-assembly of 2-D sheets by self-constraint each other due to the incompressibility of liquid, similar to the forced crumpling of elastic sheets in an impenetrable rigid cylinder [152]. As the evaporation continues, once 2-D sheets are in partial contact with vapor air, the driving force will be dominated by pressures such as capillary force as shown in **Figure 3.2a**, which could lead to the formation of intensely crumpled solid-like balls or restacking of 2-D sheets after complete evaporation of liquid. In addition, at elevated temperatures, the evaporation rate will become high, but we assume that there still is enough time to allow 2-D materials to be crumpled and assembled during liquid evaporation.

3.2.2 Energy-based continuum mechanics model for crumpling a single 2-D sheet

When planar 2-D sheets are in contact with the surface of the liquid droplet, their curvature mismatch will lead to energy competition between mechanical deformation of 2-D sheets and solid-liquid interaction. As a consequence, the deformation of 2-D sheets such as local wrinkling will occur, as illustrated in **Figure 3.4a** [153, 154] and may eventually transform to folding with the continuous evaporation of liquid. Take a single square 2-D sheet with a length L_g in the liquid droplet with a radius R_d as an example, and consider the evaporation-induced pressure of P_t, the compressive hoop strain in the 2-D sheet is axisymmetric and can be estimated via

$$\varepsilon_{\theta\theta}(r) = \frac{R_d \sin(r/R_d) - r}{r}, r \in \left[0, L_g/2\right] \tag{3.8}$$

where r is the local radial coordinate on the 2-D sheet **(Figure 3.5c**). Note that there is no radial strain in the 2-D sheet because of the free boundary in the radial direction. With Eq. (3.8), for the 2-D sheet, the strain energy of a fully conformal thin torus with the width dr in the position r (**Figure 3.5c**) is

$$E_s^I = \pi E t \varepsilon_{\theta\theta}^2 r dr + \frac{B\pi}{R_d^2} r dr \tag{3.9}$$

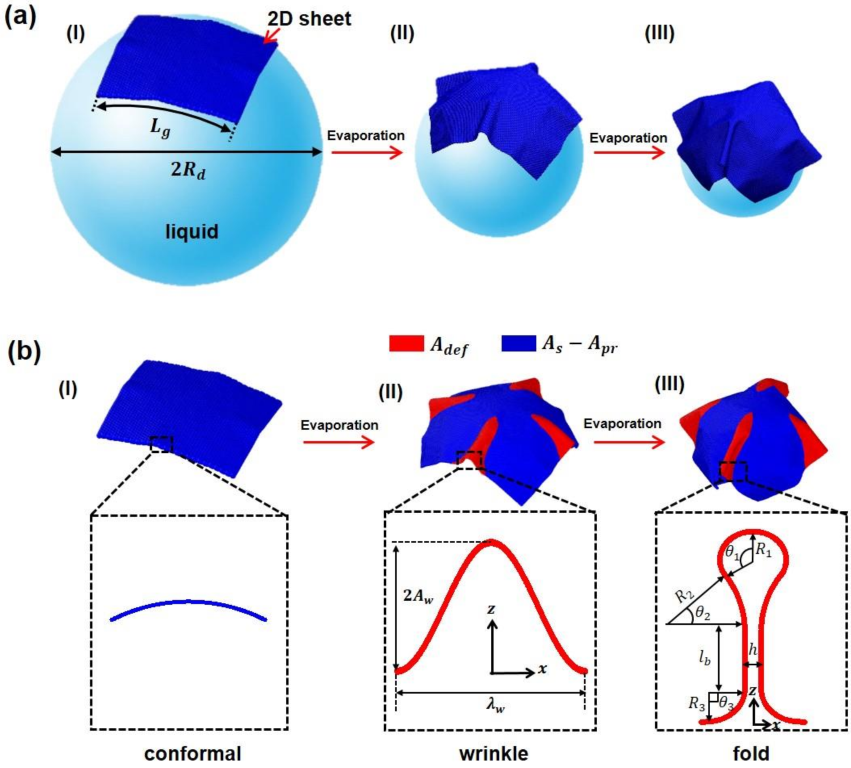

Figure 3.4. Evolution of deformation morphology of a single 2-D sheet by liquid evaporation. (a) Schematic illustrations of typical deformation of a single 2-D sheet on the surface of liquid droplet with the evaporation of liquid (represented by a decreased liquid droplet (R_d) with the evaporation time). The evaporation of liquid will drive the deformation of the 2-D sheet on the liquid droplet. **(b)** Deformation transition of the 2-D sheet from (I) the initial fully conformal state with only in-plane compression within the sheet (inset), to (II) the local out-of-plane wrinkling deformation (highlighted in red and can be described by a cosinusoidal wave function with a wavelength λ_w and amplitude A_w, inset) state in the sheet along the axisymmetric axis and to (III) the final local self-folding deformation highlighted in red. With the help of geometric analysis (inset), it can be well defined with geometric parameters via arc radius and angles R_1, R_2, R_3, θ_1, θ_2, θ_3, and the interlayer distance (h) and overlapping length (l_b) are used to describe the deformed profile state at wrinkled locations.

where the first term on the right hand is the in-plane compressive energy and the second term is the bending energy. t is the thickness, and B is the bending stiffness of 2-D sheet. Consider the center of liquid droplet as a reference point, the potential energy of the thin torus under P_t is

$$E_p^I = 2\pi P_t R_d r dr \tag{3.10}$$

with Eqs. (3.9) and (3.10), the total energy that is required to keep a fully conformal torus for

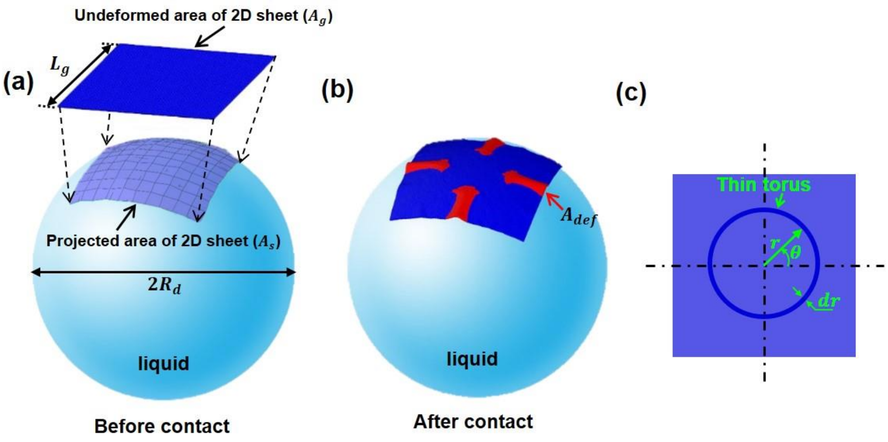

Figure 3.5. (a) Schematic illustrations of the undeformed planar area (A_g) of the 2-D sheet, and the projected area (A_s) in the surface of the droplet. R_d is the radius of liquid droplet. **(b)** The morphology illustration of a 2-D sheet in contact with the surface of the liquid droplet. **(c)** The polar coordinate on the undeformed planar 2-D sheet with the radial distance r and polar angle θ.

2-D sheet at the position r is $E_t^I = E_s^I + E_p^I$.

With the liquid evaporation (i.e. a smaller R_d), $|\varepsilon_{\theta\theta}|$ will increase and wrinkles in the 2-D sheet will occur, primarily along the symmetric axis in a square 2-D sheet, as highlighted in red in **Figure 3.4b**. Once the wrinkles appear, the compressive strain will be released by the out-of-plane wrinkling deformation [154], and the morphology of the wrinkled parts can be described by a cosinusoidal wave function with the wavelength λ_w and amplitude A_w [155-157], $f(x) = A_w \cos\left(\frac{2\pi}{\lambda_w}x\right) + A_w$, where x is the local coordinate on the surface of liquid droplet **(Figure 3.4b)** and the conservation of length of torus at the position r requires $4\int_{-\lambda_w/2}^{\lambda_w/2}\sqrt{1+(df/dx)^2}dx + 2\pi R_d \sin(r/R_d) - 4\lambda_w = 2\pi r$. Thus, we can calculate the strain energy within the torus via

$$E_s^{II} = 2B\left[\int_{-\lambda_w/2}^{-\lambda_w/2}\kappa^2(x)\sqrt{1+(df/dx)^2}\,dx + (2\pi R_d \sin(r/R_d) - 4\lambda_w)/4R_d^2\right]dr \tag{3.11}$$

where $\kappa(x) = |df^2/dx^2|/(1+(df/dx)^2)^{3/2}$ is the local curvature of wrinkles. Similar to Eq. (3.10), the potential energy due to wrinkle can be obtained via

$$E_p^{II} = P_t\left[4\int_{-\lambda_w/2}^{\lambda_w/2}(f(x)+R_d)\sqrt{1+(df/dx)^2}dx + (2\pi R_d \sin(r/R_d) - 4\lambda_w)R_d\right]dr \tag{3.12}$$

Therefore, the total energy for the wrinkling deformation is $E_t^{II} = E_s^{II} + E_p^{II}$ and is a function of λ_w. The minimization of E_t^{II} can be used to determine λ_w, A_w, E_s^{II} and E_p^{II}.

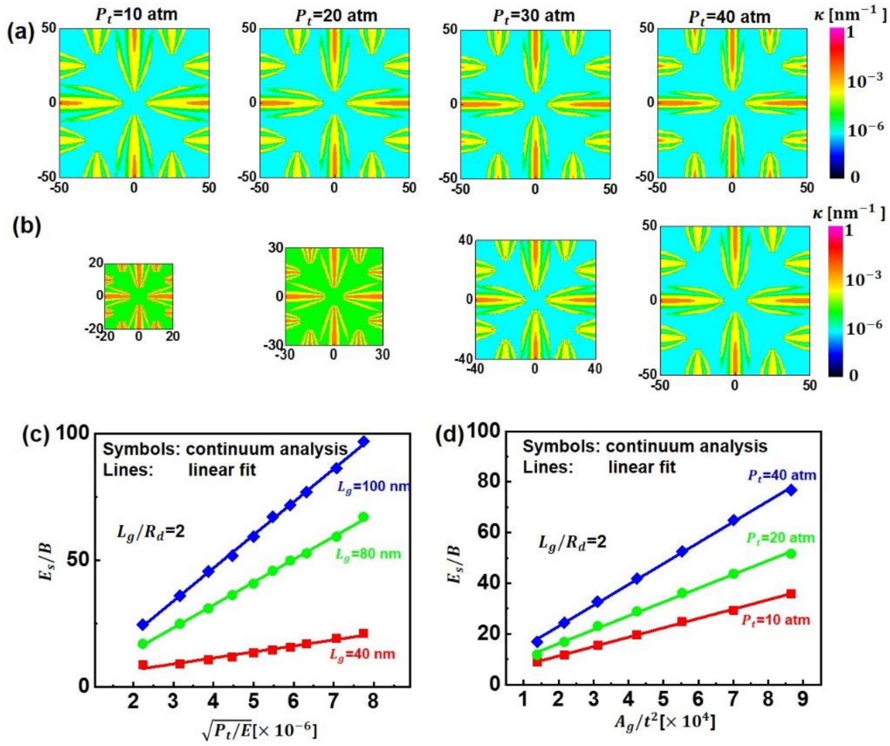

Figure 3.6. Continuum mechanics analysis on the evolution of local curvature and strain energy with the evaporation pressure for different total areas of a single 2-D sheet. (a) The local curvature distribution in a 2-D sheet with L_g=100 *nm* under different pressures at R_d=50 *nm*. (b) The local curvature distribution in 2-D sheets with different size under the same pressure P_t=20 *atm*. The ratio of 2-D sheet size to the radius of droplet is kept the same, L_g/R_d=2, to make sure the degree of deformation in each 2-D sheet is the same. (c) Normalized strain energy E_s/B by bending stiffness of 2-D sheet versus the normalized pressure $\sqrt{P_t/E}$ by Young's modulus of 2-D materials. The perfect linear relationship between them is obtained and remains for different sizes of the 2-D sheet. (d) Normalized strain energy E_s/B by bending stiffness of 2-D sheet versus normalized area A_g/t^2 with the thickness of 2-D sheet. The perfect linear relationship between them is also obtained and is independent of evaporation pressures.

With the further evaporation of liquid, $|\varepsilon_{\theta\theta}|$ and the amplitude of wrinkles A_w will continue to increase [158]. Beyond a critically high enough $|\varepsilon_{\theta\theta}|$, the wrinkles will transit to folds, and the deformed 2-D sheet becomes close enough till to being in contact with each other [157, 159, 160]. Such contact will lead to the binding energy and changes the local curvature within the fold (**Figure 3.4b**). Assume the overlap length l_b and equilibrium distance h, local radius of curvature R_1, R_2 and R_3 and arc angle θ_1, θ_2 and θ_3 in the folded configuration [161], the conservation of length of torus will yield $8[R_3\theta_3 + l_b + R_2\theta_2 +$

$R_1\theta_1] + 2\pi R_d \sin(r/R_d) - 4(2R_3 + h) = 2\pi r$, and the strain energy in the folds is

$$E_s^{III} = B[4(\theta_1/R_1 + \theta_2/R_2 + \theta_3/R_3) + [2\pi R_d \sin(r/R_d) - 4(2R_3 + h)]/2R_d^2]dr \quad (3.13)$$

Similar to Eq. (3.10) or (3.12), we can calculate the potential energy via

$$E_p^{III} = 8P_t \left[\int_{-\theta_3}^{0} (R_d + R_3 + R_3 sin\theta)R_3 d\theta + \int_{R_3}^{R_3+l_b} (y + R_d)dy + \int_0^{\theta_2} (R_d + R_3 + l_b + R_2 sin\theta)R_2 d\theta + \int_{\pi/2}^{\pi/2+\theta_1} (R_d + R_3 + l_b + R_2 sin\theta_2 + R_1\, sin(\theta_1 - \pi/2) + R_1 sin\theta)R_1\, d\theta\right] dr + P_t[2\pi R_d\, sin(r/R_d) - 4(2R_3 + h)]R_d dr \quad (3.14)$$

In this folding stage, in addition to the strain energy and potential energy, the binding energy in the overlaps of the folds needs to be taken into account and it is

$$E_b^{III} = 4\Gamma_b l_b dr \quad (3.15)$$

where Γ_b is the binding energy density of the 2-D sheet. Therefore, the total energy of the folding deformation state is $E_t^{III} = E_s^{III} + E_p^{III} + E_b^{III}$.

These three stages of conformal, wrinkling, and folding states of 2-D sheet in droplet would emerge in a sequence with the increase of $|\varepsilon_{\theta\theta}|$ and liquid evaporation [154, 158]. The transition point between them can be determined by minimizing their corresponding energy at the position r, i.e.

$$E_t^{min} = \min[E_t^I, E_t^{II}, E_t^{III}] \quad (3.16)$$

With Eq. (3.16), the local curvature κ can be determined by $\kappa = f\left(E_t^{min}\right)$. For example, when there is a conformal contact between 2-D sheet and liquid droplet, we will have $E_t^{min} = E_t^I$, and $\kappa(\theta) = 1/R_d$ $(0 \le \theta \le 2\pi)$ in the polar coordinate system (**Figure 3.5**); when the 2-D sheet wrinkles, we will have $E_t^{min} = E_t^{II}$, and $\kappa(\theta) = \begin{cases} \frac{|df^2/dx^2|}{(1+(df/dx)^2)^{\frac{3}{2}}}, |x| \le \lambda_w/2 \\ 1/R_d, |x| > \lambda_w/2 \end{cases}$, where $\theta = \left(\int_0^x \sqrt{1 + (df/dx)^2}\, dx\right)/r$; when 2-D sheet folds, we will have $E_t^{min} = E_t^{III}$ and $\kappa(\theta) = \begin{cases} 1/R_1, & |\theta| \le \theta_1 R_1/r \\ 1/R_2, & \theta_1 R_1/r < |\theta| \le (\theta_2 R_2 + \theta_1 R_1)/r \\ 0, & (\theta_2 R_2 + \theta_1 R_1)/r < |\theta| \le (\theta_2 R_2 + \theta_1 R_1 + l_b)/r \\ 1/R_3, & \theta_2 R_2 + \theta_1 R_1 + l_b)/r < |\theta| \le (\theta_2 R_2 + \theta_1 R_1 + l_b + \theta_3 R_3)/r \\ 1/R_d, & |\theta| > (\theta_2 R_2 + \theta_1 R_1 + l_b + \theta_3 R_3)/r \end{cases}$. Specifically, for graphene sheet, the geometric parameters are $R_0 = 0.68$ *nm*, R_1 =0.967 R_0, R_2 =3.401 R_0, $R_3 = \sqrt{2\pi/(2+\pi)}R_0$, θ_1=0.685π, θ_2=0.185π, θ_3=0.5π, and h=0.34 *nm* [161], and the material parameters are B=2.38e-19 J, E=1 *TPa*, t=0.34 *nm* and Γ_b=-0.232 J/m^2 [140].

Figures 3.6a and **b** plot the curvature distribution of $\kappa(\theta)$ in the 2-D sheet (graphene) at these three different stages of liquid evaporation. Once the local curvature is obtained, the strain energy, potential energy and binding energy in the deformed 2-D sheet can be determined. More importantly, define the deformed area in the 2-D sheet as "ridge", similar to that of crumpling thin elastic sheet in a confined hollow sphere [152, 162, 163], the strain energy stored in the ridges can be written as [164]

$$E_s = B\xi\varphi(\theta_t - \pi)^2 \tag{3.17}$$

where ξ and φ are dimensionless geometry factors, and ξ is often referred to as the Föppl-von Kármán number. Our analysis on crumpling 2-D sheet by liquid evaporation shows that $\xi = A_g/t^2$ and $\varphi = \sqrt{P_t/E}$ (**See Figure 3.6**). A_g is the original surface area of 2-D sheet. θ_t is the angle between the two planes of the ridge and $\theta_t - \pi$ represents the degree of deformation relative to a flat 2-D sheet without deformation.

3.2.3 Rotational spring-mechanical slider model of crumpling a single 2-D sheet

As analyzed in Section 3.2.2, both local wrinkles and folds reflect the out-of-plane mechanical deformation of 2-D sheets centered about a symmetric line (marked in red in **Figure 3.4b**) and contribute to the strain energy and potential energy due to their high local curvature compared to the other parts of the 2-D sheet with negligible deformation. More importantly, with the evaporation of liquid droplet, the out-of-plane deformation will increase and these negligible deformation parts are packed more closely. The packing of negligible deformation parts about symmetric lines in the 2-D sheets is analogous with the folding process of origami structures along a flexible axis or reference point[165]. With this analogy, the crumpling deformation of one single 2-D sheet can be modeled by a rotational spring connected with two planes that cannot be crumpled and are considered to be rigid, as illustrated in **Figure 3.7a (I)**. The associated out-of-plane deformation energy can be characterized by the energy storage of the deformed rotational spring. When the interactive binding energy between folded rigid parts needs to be taken into account, it can be described by introducing a mechanical slider between two rigid planar sheets, as illustrated in **Figure 3.7a (III)**. With this 2-D rotational spring-mechanical slider mechanics model, the crumpling of a single 2-D sheet now can be characterized through the energy analysis.

The energy stored in the rotational spring that corresponds to the total compressive,

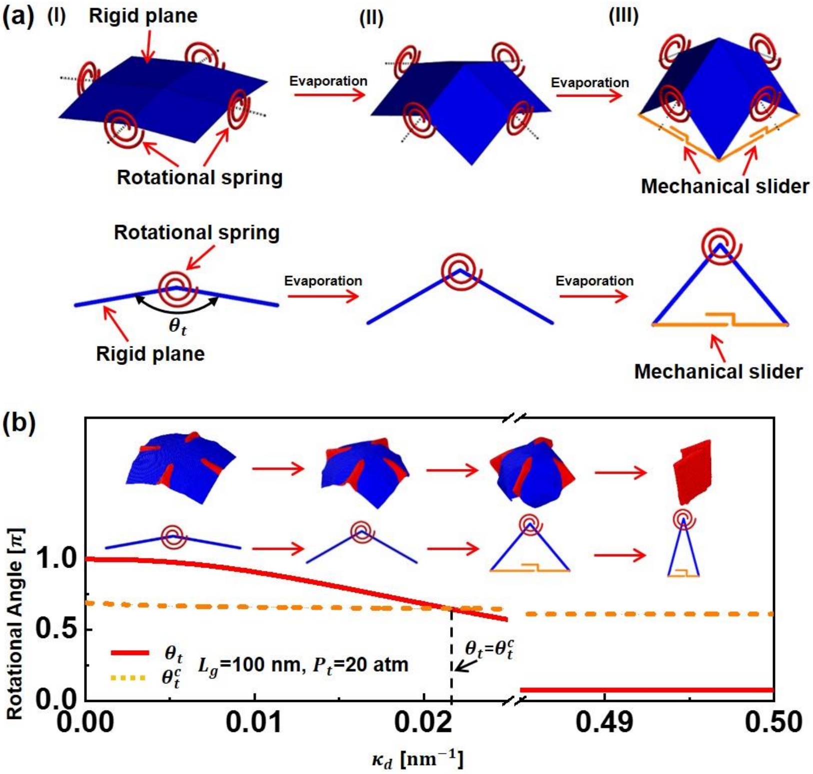

Figure 3.7. The rotational spring-mechanical slider model of crumpling a single 2-D sheet by liquid evaporation. (a) Out-of-plane deformation of 2-D sheet modeled by rotational spring located at the axisymmetric axis connecting two rigid planes with the rotational angle of θ_t and the binding interaction modeled by mechanical slider when the two rigid planes are close enough with the evaporation of liquid (top) and the simplification of this rotational spring-mechanical slider system into a 2-D model due to its symmetry (bottom). The critical moment for introducing the mechanical slider to the rotational spring model is referred to as the critical rotational angle θ_t^c and depends on liquid evaporation. **(b)** Variation of the rotational angle θ_t and critical rotational angle θ_t^c with the liquid evaporation (plotted by an increase of liquid droplet curvature κ_d (=1/R_d)). When $\theta_t > \theta_t^c$, the mechanical slider will not effective, and when $\theta_t \leq \theta_t^c$, the mechanical slider starts to take effect to represent the binding energy in the folded deformation. The inserts show the deformed states of 2-D sheet and their corresponding state of the spring-slider mechanics model.

wrinkling and self-folding deformation in the 2-D sheet can be defined as

$$E_s^{spring} = \frac{1}{2} k_s (\theta_t - \pi)^2 \tag{3.18}$$

where k_s is the constant of rotational spring and θ_t is the rotational angle (**Figure 3.7a (I)**). k_s can be determined from the continuum mechanics model of compression, wrinkling, and self-folding deformation of a single 2-D sheet in Section 3.2.2. That is, the energy from this rotational spring model should be equal to that from the continuum model analysis in Eq. (3.17), which is, $E_s^{spring} = E_s$ and it yields to $k_s = 2B\frac{A_g}{t^2}\sqrt{\frac{P_t}{E}}$.

With the continuous deformation of 2-D sheet, the gap between local wrinkled sheets will decrease, and the interactive binding energy will emerge. Different from the out-of-plane deformation, it reflects the van der Waals interactions, and will further promote the wrinkling toward the appearance of self-folding of 2-D sheets. The interactive binding energy depends on both gap distance and area of overlapped rigid parts and can be defined as

$$E_b^{slider} = k_b A_{def}[sin(\theta_t^c/2) - sin(\theta_t/2)]H(\theta_t^c - \theta_t) \tag{3.19}$$

where k_b is the constant of the mechanical slider, A_{def} is the area that contributed to the out-of-plane deformation. θ_t^c is the critical angle between the two connected rigid plates, and when $\theta_t < \theta_t^c$, the two rigid plates are considered to be close enough and the resultant binding energy needs to be considered [159]. $H(\theta_t^c - \theta_t)$=1 when $\theta_t < \theta_t^c$[166]. Since the binding energy only occurs between two overlaps in 2-D sheet, we have $k_b = \Gamma_b/2$.

Similar to the definition of the projected area ($A_s = 2\pi R_d^2[1 - \cos(L_g/2R_d)]$) on the surface of liquid droplet for a planar 2-D sheet (**Figure 3.5**), we define the projection of out-of-plane deformed area of 2-D sheet A_{def} on the surface of liquid droplet as A_{pr}, and $A_{def} = A_{pr} + \pi A_g/4 - A_s$. The overall nominal compressive strain in the 2-D sheet can be written as $\varepsilon_s = (A_{pr} - A_{def})/A_{def}$. Apparently, $\varepsilon_s < 0$, and we have $\theta_t = \pi(1 + \varepsilon_s)$. For example, consider the bending stiffness (B) and size (L_g) of a square 2-D sheet, under the radius of liquid droplet (R_d) and evaporation pressure (P_t), A_{pr} can be determined via [159] $A_{pr} = (BR_d/P_t)^{\frac{1}{4}}\pi L_g/2$ and $\theta_t^c = \pi/(1 + (E/P_t A_{pr}^2)^{1/9} t^{4/9})$. **Figure 3.7b** plots the variations of θ_t and θ_t^c with the increase of curvature of liquid droplet κ_d (=$1/R_d$, which reflects the liquid evaporation process). When the curvature is zero, the 2-D sheet is a flat surface and $\theta_t = \pi$. The 2-D sheet is in a fully conformal contact with the liquid surface and there is no out-of-plane deformation. With the increase of curvature (κ_d) during evaporation, the strain energy of 2-D sheet increases, and θ_t decreases accordingly but is larger than θ_t^c. By contrast, θ_t^c remains approximately the same. Beyond a critical curvature, θ_t is smaller than θ_t^c, indicating the distance between two rigid plates in the spring model is close enough and the binding energy will appear, where the slider will play a role in the spring-slider mechanics model and needs to be considered, as illustrated in the inset.

In addition to the strain energy E_s^{spring} and binding energy E_b^{slider}, the evaporation pressure will deform 2-D sheet. Take the center of liquid droplet as the reference point, its induced mechanical deformation of 2-D sheet can be described by a potential energy E_p to the reference point, which is

$$E_p = P_t\left[A_{def}\left(R_d + \sqrt{A_{def}}cos(\theta_t/2)/2\right) + A_s R_d\right] \tag{3.20}$$

where the first term reflects the contribution by the out-of-plane deformation of 2-D sheet. Eq. (3.20) shows that the potential energy of a single 2-D sheet during liquid evaporation is a function of the curvature of liquid droplet (κ_d, see Appendix A), similar to that in Eqs. (3.18) and (3.19). With Eqs. (3.18)-(3.20), the total energy of crumpling 2-D sheet can be written as

$$E_{tot} = E_s^{spring} + E_b^{slider} + E_p \tag{3.21}$$

$dE_{tot}/d\kappa_d < 0$ is favorable of folding process of 2-D sheets by evaporation and $dE_{tot}/d\kappa_d$ will increase as the evaporation continues, leading to a continuous folding of 2-D sheets till to $dE_{tot}/d\kappa_d = 0$. Besides, when the folding stops ($dE_{tot}/d\kappa_d = 0$), if $\theta_t < \theta_t^c$, the 2-D sheet could be folded into a stable pattern due to the attractive van der Waals interaction between rigid parts by the liquid evaporation. Otherwise, the deformed 2-D sheet will bounce back into its planar form. As an example, **Figure 3.8a** plots the variation of E_{tot}, E_s^{spring}, E_b^{slider}, E_p, and rotational angle (θ_t) in the spring-slider model with the increase of liquid droplet curvature κ_d for a square graphene sheet, where for the 2-D sheet (graphene), B=2.38e-19 J, E=1 TPa, t=0.34 nm and Γ_b=-0.232 J/m^2 [140], L_g=40 nm and P_t=10 atm. With the evaporation of liquid, θ_t decreases, and E_s^{spring} increases. When κ_d is large enough, $\theta_t \leq \theta_t^c$ and E_b^{slider} starts to emerge and increase (magnitude). At the same time, E_p will decrease due to the decrease of the radius of liquid droplet and deformation of the 2-D sheet. When $dE_{tot}/d\kappa_d = 0$ appears earlier than $\theta_t = \theta_t^c$ (i.e. κ_d^E<κ_d^G, and $\theta_t > \theta_t^c$, see Appendix A for the definition of κ_d^E and κ_d^G), the folding will stop without van der Waals attractive energy and the deformed 2-D sheet will recover. At a higher evaporation pressure of P_t=40 atm,

Figure 3.8b shows that E_p decreases more rapidly and E_b^{slider} emerges earlier. This synergistic effect delays the emergence of $dE_{tot}/d\kappa_d = 0$, and when the folding stops, $\theta_t < \theta_t^c$ ($\kappa_d^E > \kappa_d^G$), which leads to a folded 2-D sheet stabilized by the van der Waals attractive energy.

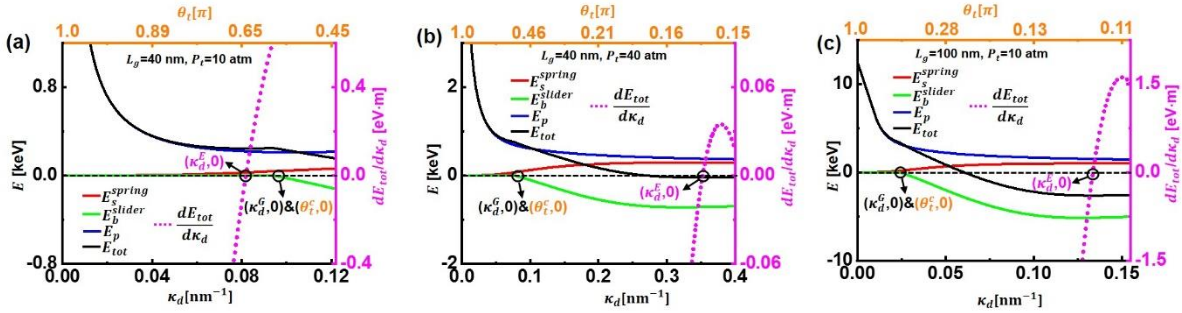

Figure 3.8. Energy variation of a single 2-D material graphene sheet with liquid evaporation from the spring-slider mechanics model. Various energy variation during liquid evaporation in the forms of both liquid droplet curvature κ_d and rotational spring angle θ_t for a square graphene sheet with **(a)** L_g=40 *nm* under P_t=10 *atm*, **(b)** L_g=40 *nm* under P_t=40 *atm* and **(c)** L_g=100 *nm* under P_t=10 *atm*. The point when E_b^{slider} starts to emerge and $dE_{tot}/d\kappa_d = 0$ correspond to $\theta_t = \theta_t^c$ and κ_d^G and κ_d^E, respectively.

Similarly, by increasing the size of 2-D sheet to L_g=100 *nm* (**Figure 3.8c**), a stabilized folded graphene by van der Waals attractive energy can also be obtained due to $\theta_t < \theta_t^c$ ($\kappa_d^E > \kappa_d^G$) at $dE_{tot}/d\kappa_d = 0$. This demonstration indicates that the size and evaporation pressure play the crucial roles in the folding of 2-D sheet and their relationship can be obtained by analyzing Eq. (3.21) as follows.

Before the emergence of binding energy, the total energy for a liquid evaporation-driven folding of a single 2-D sheet is

$$E_{tot} = E_s^{spring} + E_p \tag{3.22}$$

The self-folding deformation of 2-D sheets stops at $dE_{tot}/d\kappa_d$=0 , i.e. $dE_s^{spring}/d\kappa_d$+$dE_p/d\kappa_d$=0. From Eq. (3.18), $E_s^{spring} = 1/2k_s(\theta_t - \pi)^2$ and $\theta_t = \pi A_{pr}/(A_{pr} + \pi A_g/4 - A_s)$ where $A_{pr} = (BR_d/P_t)^{\frac{1}{4}}\pi L_g/2$, $A_s = 2\pi R_d^2[1 - cos(L_g/2R_d)]$ and $\kappa_d = 1/R_d$. We can further write E_s^{spring} as a function of κ_d,

$$E_s^{spring} = B\pi^2 \frac{A_g}{t^2}\sqrt{\frac{P_t}{E}}\left(\frac{D}{C}\right)^2 \tag{3.23}$$

where $C = 2(B/P_t)^{\frac{1}{4}} L_g \kappa_d^{\frac{7}{4}} + A_g\kappa_d^2 - 8 + 8\cos\left(L_g\kappa_d/2\right)$, and $D = 8 - 8\cos\left(L_g\kappa_d/2\right) - A_g\kappa_d^2$.

Similarly, the potential energy E_p can also be expressed as a function of κ_d, which is

$$E_p = P_t[F + MH + J] \tag{3.24}$$

where $F = (B/P_t)^{\frac{1}{4}}\pi L_g\kappa_d^{-\frac{5}{4}}/2 + A_g/\kappa_d - 2\pi/\kappa_d^3 + 2\pi\cos\left(L_g\kappa_d/2\right)/\kappa_d^3$, $M = \left[\pi(B/P_t)^{\frac{1}{4}}L_g\kappa_d^{-\frac{1}{4}}/2 + A_g - 2\pi/\kappa_d^2 + 2\pi\cos\left(L_g\kappa_d/2\right)/\kappa_d^2\right]^{\frac{3}{2}}/2$, $H = \cos\left(\pi L_g(B/P_t)^{\frac{1}{4}}\kappa_d^{\frac{7}{4}}/C\right)$

and $J = 2\pi/\kappa_d^3 - 2\pi\cos\left(L_g\kappa_d/2\right)/\kappa_d^3$.

$dE_s^{spring}/d\kappa_d + dE_p/d\kappa_d = 0$ yields

$$2B\pi^2\frac{A_g}{t^2}\sqrt{\frac{P_t}{E}}\left[\frac{DD'C - D^2C'}{C^3}\right] + P_t[F' + M'H + MH' + J'] = 0 \tag{3.25}$$

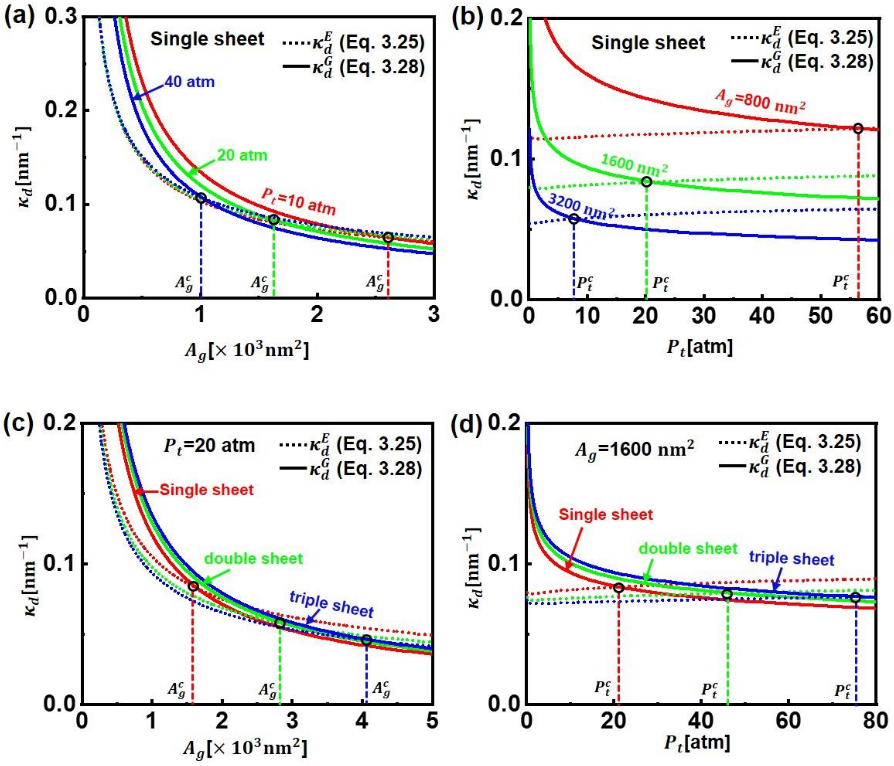

Figure 3.9. Variation of κ_d^G and κ_d^E with the area of graphene A_g (a) under different evaporation pressure P_t and (c) with different numbers of layers of graphene sheet (bending stiffness). Variation of κ_d^G and κ_d^E with the evaporation pressure P_t for (b) different areas of graphene and (d) different numbers of layers of graphene sheet (bending stiffness). Both critical area A_g^c and critical pressure P_t^c are defined at $\kappa_d^G = \kappa_d^E$.

When A_g, B and P_t are given, the solution to Eq. (3.25) can be solved numerically, referred to as κ_d^E, and it will depend on the energy competition between self-folding deformation of 2-D sheets and evaporation pressure.

In parallel, when we write θ_t as a function of κ_d, we will have

$$\theta_t = \frac{2\pi A_g^{\frac{1}{2}}\left(\frac{B}{P_t}\right)^{\frac{1}{4}}\kappa_d^{\frac{7}{4}}}{C} \tag{3.26}$$

When the binding energy needs to be considered, the critical angle θ_t^c can also be expressed as

$$\theta_t^c = \frac{\pi}{1+\left(\frac{4E\kappa_d^{\frac{1}{2}}}{\pi^2 A_g P_t^{\frac{1}{2}} B^{\frac{1}{2}}}\right)^{1/9} t^{4/9}} \tag{3.27}$$

$\theta_t = \theta_t^c$ yields

$$\frac{2\pi A_g^{\frac{1}{2}}\left(\frac{B}{P_t}\right)^{\frac{1}{4}}\kappa_d^{\frac{7}{4}}}{2A_g^{\frac{1}{2}}\left(\frac{B}{P_t}\right)^{\frac{1}{4}}\kappa_d^{\frac{7}{4}}+A_g\kappa_d^2-8\left(1-cos\left(\frac{L_g}{2}\kappa_d\right)\right)} - \frac{\pi}{1+\left(\frac{4E\kappa_d^{\frac{1}{2}}}{\pi^2 A_g P_t^{\frac{1}{2}}(B)^{\frac{1}{2}}}\right)^{\frac{1}{9}} t^{\frac{4}{9}}} = 0 \tag{3.28}$$

Similar to Eq. (3.25), we can numerically solve Eq. (3.28) and its solution, referred to as κ_d^G, depends on the geometrical analysis.

Given A_g, B and P_t, if $\kappa_d^E > \kappa_d^G$, the folding will stop without adhesive van der Waals energy and the deformed 2-D sheet will recover; $\kappa_d^E < \kappa_d^G$ will suggest that the folding stops after the emergence of van der Waals energy, and the deformed 2-D sheet will be obtained with a stable folded pattern; $\kappa_d^E = \kappa_d^G$ corresponds to the critical condition. Take the 2-D material graphene as an example, **Figure 3.9a** plots the variation of κ_d^E and κ_d^G with the area of 2-D sheets under different pressures. At P_t=10 *atm*, small graphene sheets cannot be folded, in good consistence with $\kappa_d^E<\kappa_d^G$. With the increase of graphene sheet area, both κ_d^E and κ_d^G decrease, and after a critical large area of graphene sheet, $\kappa_d^E > \kappa_d^G$, indicating a successful self-folding of graphene by liquid evaporation. Define the graphene area as the critical area A_g^c at $\kappa_d^E = \kappa_d^G$. It decreases with the increase of evaporation pressure, suggesting that higher evaporation pressure promotes the self-folding of graphene. **Figure 3.9b** further gives the plots of κ_d^E and κ_d^G as a function of the evaporation pressure. At A_g=800 nm^2 and a low evaporation pressure, we always have $\kappa_d^E < \kappa_d^G$. With the increase of evaporation pressure, κ_d^G decreases, and κ_d^E increases, eventually leading to $\kappa_d^E > \kappa_d^G$ beyond this, the self-folding of graphene will happen. Similar to the definition of A_g^c, we define the critical evaporation pressure as P_t^c at $\kappa_d^E = \kappa_d^G$. Smaller P_t^c is obtained for large areas of graphene sheet, indicating larger graphene is easier to be folded than smaller one by liquid evaporation. Further, **Figure 3.9c** illustrates A_g^c increases with the increase of layer numbers of graphene sheet (i.e. the bending stiffness, B) under the same evaporation pressure, indicating the 2-D sheet with a lower bending stiffness is much easier to be folded. When the evaporation pressure changes, similar results are also obtained in **Figure 3.9d**,

Based on these analyses and with the help of the dimensional analysis, we can summarize

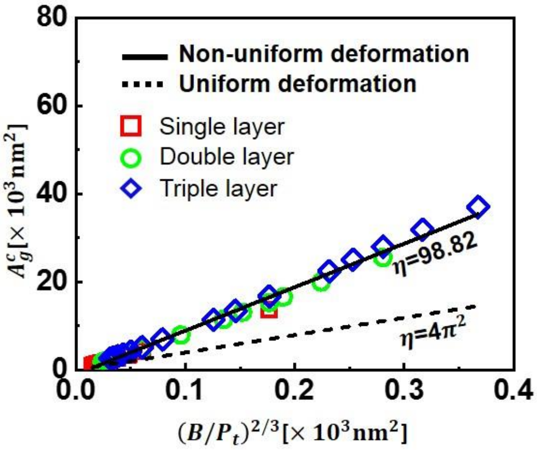

Figure 3.10. Relationship between the critical area A_g^c and $(B/P_t)^{2/3}$. The points are extracted from the parameters of the numerical solutions of Eqs. (3.25) and (A3.8) at κ_d^E=κ_d^G. All the points can be well linearly fitted with a slope of η=98.82. The relationship when the deformation is uniform (η=4π^2) can be derived in theory and is also included.

the relationship among the critical area A_g^c of 2-D sheets, the bending stiffness B, and the evaporation pressure P_t and it can be written as

$$A_g^c = \eta\left(\frac{B}{P_t}\right)^{\frac{2}{3}} \tag{3.29}$$

Eq. (3.29) is confirmed by substituting it into Eqs. (3.25) and (3.28) with the same solutions between them. **Figure 3.10** shows the linear relationship between A_g^c and $(B/P_t)^{2/3}$, which further validates the expression of Eq. (3.29). Note that the η =98.82 can be obtained by the best linear fit of the numerical solutions to **Figure 3.10**, independent of bending stiffness of graphene and areas. η reflects the deformation homogeneity and intensity of 2-D sheet. In particular, when the 2-D sheet experiences uniform deformation, the 2-D sheet remains a conformal contact with the liquid droplet and pertains a constant radius of curvature, where the rotational angle $\theta_t = \pi - \theta_b/2$, and the bending angle of the 2-D sheet $\theta_b = L_g/R_d$ [99, 140]. Eq. (3.21) will become $E_{tot} = E_s^{spring} + E_p$, where $E_s^{spring} = 2B/(\theta_t - \pi)^2$, and $E_p = P_t A_g L_g/(2\pi - 2\theta_t)$. $dE_{tot}/d\kappa_d$=0 at $\kappa_d = 2\pi/L_g$ will yield $A_g^c = 4\pi^2 (B/P_t)^{\frac{2}{3}}$, where $\eta = 4\pi^2$, which agrees well with self-folding of one single graphene sheet by liquid evaporation [140].

3.2.4 Spring-slider network mechanics model of crumpling and assembly of multiple 2-D sheets

When there are multiple 2-D sheets in the droplet, in addition to the mechanical deformation of individual 2-D sheets, because the surface area of droplet will decrease with the liquid evaporation, and 2-D sheets will be packed and assembled closely. This assembly of individual 2-D sheet will lead to an emergence of interactive energy between 2-D sheets, which is similar to the binding energy of the folded parts in a single 2-D sheet and can also be described by a mechanical slider with the same as that in folded parts, referred to as inter-layer slider. **Figure 3.11** shows the illustration of a network distribution of rotational spring-slider mechanics models for the crumpling and assembly of multiple 2-D sheets in solution droplet by liquid evaporation.

Consider n_l ($n_l \geq 2$) 2-D sheets in a liquid droplet, each 2-D sheet has the area $A_g^{(i)} (i = 1,2,3 \dots\dots n_l)$, and the total area is $A_g^t = \sum_{i=1}^{n_l} A_g^{(i)}$. Given $A_g^t \leq A_d (= 4\pi R_d^2)$ at the beginning of evaporation, the surface of droplet is not fully covered by the 2-D sheets, and there is no overlap between 2-D sheets. As a consequence, the assembly energy between individual 2-D sheets can be neglected and the total deformation energy is

$$E_s^{spring} = \sum_{i=1}^{n_l} E_s^{spring(i)} = \frac{1}{2} \sum_{i=1}^{n_l} k_s^{(i)} \left(\theta_t^{(i)} - \pi\right)^2 \tag{3.30}$$

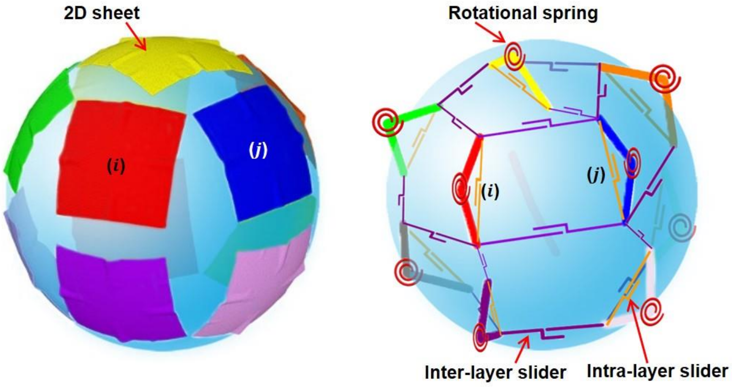

Figure 3.11. Crumpling and assembling multiple 2-D material sheets by liquid evaporation (left) and its rotational spring-mechanical slider network model (right). The intra-layer (orange) and inter-layer (purple) slider reflect the van der Waals interaction in the self-folding deformation of individual 2-D sheet and self-assembly of adjacent individual 2-D sheet, respectively.

where $E_s^{spring(i)}$ is the deformation energy of the i^{th} 2-D sheet, $k_s^{(i)} = 2B\frac{A_g^{(i)}}{t^2}\sqrt{\frac{P_t}{E}}$, $\theta_t^{(i)} = \pi\left(1+\varepsilon_s^{(i)}\right)$ and $\varepsilon_s^{(i)} = (A_{pr}^{(i)} - A_{def}^{(i)})/A_{def}^{(i)}$. Similarly, the total binding energy in 2-D sheets can be obtained by

$$E_b^{slider} = \sum_{i=1}^{n_l} E_b^{slider(i)} = \sum_{i=1}^{n_l} k_b^{(i)} A_{def}^{(i)}\left[sin\left(\theta_t^{c(i)}/2\right) - sin\left(\theta_t^{(i)}/2\right)\right] H\left(\theta_t^{c(i)} - \theta_t^{(i)}\right) \tag{3.31}$$

where $k_b^{(i)} = \Gamma_b/2$ and $\theta_t^{c(i)} = \pi/(1+\left(E/P_t A_{pr}^{(i)2}\right)^{1/9} t^{4/9})$. And the total potential energy contributed by evaporation pressure is

$$E_p = \sum_{i=1}^{n_l} E_p^{(i)} = \sum_{i=1}^{n_l} P_t\left[A_{def}^{(i)}\left(R_d + \sqrt{A_{def}^{(i)}}cos\left(\theta_t^{(i)}/2\right)/2\right) + A_s^{(i)} R_d\right] \tag{3.32}$$

Thus, the total energy without assembling among multiple 2-D sheets by liquid evaporation is

$$E_{tot} = E_s^{spring} + E_b^{slider} + E_p \tag{3.33}$$

With the evaporation of liquid, the surface area of liquid droplet will decrease, eventually leading to $A_g^t \geq A_d$. After that, the 2-D sheets start to assemble (**Figure 3.1c**) and the assembly energy emerges. Unlike the layer by layer stacking of planar 2-D sheet, the assembled 2-D sheet will stuck at the boundaries on the liquid droplet due to the out-of-plane deformation of wrinkling and self-folding [167, 168]. Besides, these boundary inter-lockings between 2-D sheets will lead to both hoop and radial compressive strain within a single 2-D sheet, similar to that of the deformation in granular particles [169], and the total deformation energy characterized by Eq. (3.30) at $A_g^t < A_d$ will becomes

$$E_s^{spring} = \sum_{i=1}^{n_l} E_s^{spring(i)} = \sum_{i=1}^{n} k_s^{(i)}\left(\theta_t^{(i)} - \pi\right)^2 \tag{3.34}$$

When the assembly between different 2-D sheet starts, the out-of-plane deformation will not be constrained in the intra-layer wrinkling and self-folding, and the inter-layer assembly will also partially occupy the deformed area. As a result, $A_{def}^{(i)} = A_{bind}^{(i)} + A_{asm}^{(i)}$, where $A_{bind}^{(i)}$ represents the deformed area of wrinkling and self-folding and $A_{asm}^{(i)}$ represents the assembled area in the *ith* 2-D sheet. Therefore, the binding energy becomes

$$E_b^{slider} = \sum\nolimits_{i=1}^{n_l} E_b^{slider(i)} = \sum_{i=1}^{n_l} k_b^{(i)} A_{bind}^{(i)} \left[sin\left(\theta_t^{c(i)}/2\right) - sin\left(\theta_t^{(i)}/2\right)\right] H\left(\theta_t^{c(i)} - \theta_t^{(i)}\right) \tag{3.35}$$

The assembly energy due to the van der Waals interaction between individual 2-D sheets can be calculated by

$$E_{asm} = \sum_{i=1}^{n_l} E_{asm}^{(i)} = \sum_{i=1}^{n_l} k_a^{(i)} A_{asm}^{(i)} \tag{3.36}$$

where $k_a^{(i)} = \Gamma_b/2$ is the assembly coefficient and is the same with $k_b^{(i)}$ in Eq.(3.35). The potential energy that will crumple and assemble multiple 2-D sheets by the evaporation pressure can be calculated via

$$E_p = \sum_{i=1}^{n_l} E_p^{(i)} = P_t \sum_{i=1}^{n_l} \begin{bmatrix} A_{bind}^{(i)}\left(R_d + \sqrt{A_{bind}^{(i)}}\cos\left(\theta_t^{(i)}/2\right)/2\right) \\ +A_{asm}^{(i)}(R_d + \sqrt{A_{asm}^{(i)}}/2) + A_s^{(i)} R_d \end{bmatrix} \tag{3.37}$$

With Eqs. (3.35)-(3.37), the total energy of crumpling and assembling multiple 2-D sheets by liquid evaporation is

$$E_{tot} = E_s^{spring} + E_b^{slider} + E_{asm} + E_p \tag{3.38}$$

Similar to Eq. (3.21), Eq. (3.38) can be solved numerically. For example, take $A_g^{(i)}$=10000 nm^2, n_l=5 (A_g^t=50000 nm^2) and P_t=10 atm, **Figure 3.12a** shows the deformation energy E_s^{spring}, binding energy E_b^{slider}, assembly energy E_{asm}, potential energy E_p

as well as the total energy E_{tot} as the liquid evaporates. During the liquid evaporation, $dE_{tot}/d\kappa_d$ will increase as the evaporation continues, leading to a continuous crumpling and assembly of 2-D sheets till to $dE_{tot}/d\kappa_d = 0$. When the crumpling and assembly stop ($dE_{tot}/d\kappa_d = 0$), the multiple 2-D sheets will be crumpled into a particle stabilized by the van der Waals energy of adhesive self-folding and assembly.

After the complete evaporation of liquid, **Figure 3.12b** plots the normalized crumpling energy E_s^{spring}+E_b^{slider} by the assembly energy E_{asm} with the increase of pressure P_t. It increases (magnitude) with the increase of P_t, indicating a higher pressure will promote the self-folding of 2-D sheets. Further, we define

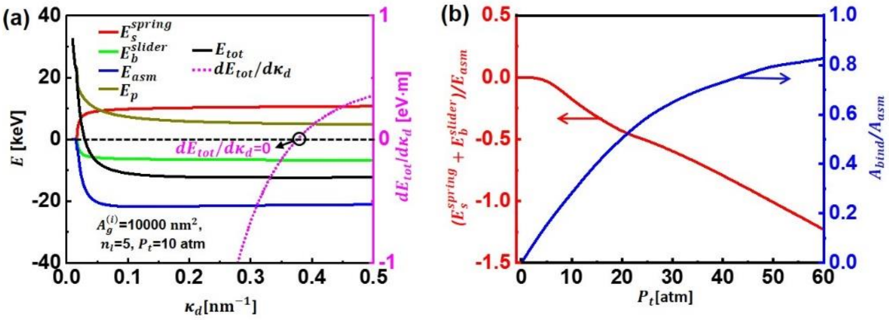

Figure 3.12. Energy variation of multiple 2-D material graphene sheets with liquid evaporation from the spring-slider network model. (a) Energy variation as a function of liquid droplet curvature κ_d. $A_g^{(i)}$=10000 nm^2, n_l=5 and P_t=10 atm. $dE_{tot}/d\kappa_d$=0 corresponds to the stopping of the crumpling and assembling. **(b)** Normalized crumpling energy $E_s^{spring} + E_b^{slider}$ by the assembling energy E_{asm} in the particles after complete evaporation of liquid (in red) and normalized self-folding area (A_{bind}) by the assembling area (A_{asm}) (in blue) with the increase of pressure.

$$\zeta = A_{bind}/A_{asm} \tag{3.39}$$

where A_{bind} and A_{asm} can be used to characterize the surface morphology and the overall structure of the particle. $\zeta = 0$ indicates there is no deformation of individual 2-D sheet and only self-assembly of 2-D sheets occurs by liquid evaporation. As a consequence, a bulk form of restacking of 2-D sheets will be obtained. These areas can be determined from energy analysis, where $A_{bind} = \sum_{i=1}^{n_l} A_{bind}^{(i)}$, $A_{bind}^{(i)} = E_b^{slider(i)}/(k_b^{(i)}\left[sin\left(\theta_t^{c(i)}/2\right) - sin\left(\theta_t^{(i)}/2\right)\right])$ and $A_{asm} = \sum_{i=1}^{n_l} A_{asm}^{(i)}$, and $A_{asm}^{(i)} = E_{asm}^{(i)}/k_a^{(i)}$. Apparently, a large ζ suggests a dominative role of the crumpling energy over the assembly energy, and promotes local deformation of individual 2-D sheets including ridges. These local ridges will prevent direct restacking of 2-D sheets and lead to “porous” structures of assembled particles. **Figure 3.12b** shows a monotonic variation of A_{bind}/A_{asm} with the pressure, which agrees well with that of energy variations. In particular, when the surface area of each 2-D sheet is the same, we will have $E_s^{spring} = n_l E_s^{spring(i)}$, $E_b^{slider} = n_l E_b^{slider(i)}$, $E_{asm} = n_l E_{asm}^{(i)}$ and $E_p = n_l E_p^{(i)}$, and as a result, $A_{bind} = n_l A_{bind}^{(i)}$, $A_{asm} = n_l A_{asm}^{(i)}$, and $A_g^t = n_l A_g^{(i)}$. $\zeta = 0$ will lead to A_{bind}=0 and $E_b^{slider} = E_b^{slider(i)} = 0$, and there will be no permanent deformation in each 2-D sheet due to the lack of van der Waals energy, which is the same as that of unfolded 2-D sheet in the crumpling of a single 2-D sheet in Section 3.2.3. Therefore, the critical area of each 2-D sheet will be $A_g^{c(i)} = \eta (B/P_t)^{\frac{2}{3}}$, and consider $A_g^t = n_l A_g^{(i)}$, the critical total area of multiple 2-D sheets will be

$$A_g^{tc} = n_l \eta \left(\frac{B}{P_t}\right)^{2/3} \tag{3.40}$$

If $A_g^t \leq A_g^{tc}$, there will be no deformation within each 2-D sheet and only assembly of 2-D sheets among each other, which is the same as the assembly process of colloidal particles [170]. When $A_g^t > A_g^{tc}$, both self-folding and assembly will appear and ζ will be larger than zero.

More importantly, once the total energy of assembled particle after the complete evaporation of liquid is determined, and if we assume the local curvature and central angle in the fold are constant [161], the density of fold (ridge) can be calculated and it is

$$D_r = \frac{E_s^{spring}}{B A_g^t} \left[\frac{R_1}{\theta_1} + \frac{R_2}{\theta_2} + \frac{R_3}{\theta_3}\right] \tag{3.41}$$

Similarly, the radius of gyration (r_g) can be employed to approximately estimate the size of assembled particles after the complete evaporation of liquid, and R_g is

$$R_g = \frac{E_p}{P_t A_g^t} \tag{3.42}$$

We should note that when there is no deformation in 2-D sheets, E_p will be the same with the potential energy of assembled particles in colloidal science and Eq. (3.42) will reduce to the radius of assembled hollow spheres by rigid particles [171]. In addition, the accessible area of the assembled particle [47] (i.e. the surface area of particle that is accessible to air) can be obtained by excluding the stacked areas within a particle from the total surface area of 2-D materials and it is

$$A_{acc} = 2\left[A_g^t - (\zeta + 1)A_{asm}\right] \tag{3.43}$$

3.3 Computational Modeling and Methods

3.3.1 Coarse-grained modeling of graphene

Large numbers of atoms will be involved so as to model the crumpling and assembly of 2-D sheets by liquid evaporation and validate the theoretical mechanical model in Section 3.2. For example, take 2-D material graphene suspended in a water droplet as an example, consider the typical size of the solution liquid droplet of $R_d = 1.45\,\mu m$ in experiments, and the concertation of graphene C_m=1 *mg/mL* [48], one liquid droplet will contain 4.27×10^{11} water molecules and 6.39×10^{8} carbon atoms, largely beyond the capacity of current computational cost. In this section, we will present a high-efficiency simulation procedure by coarse-graining graphene sheets and mimicking solid-liquid interaction using a virtual spherical interactive force field.

Graphene will be modeled by a coarse-grained (CG) model, as illustrated in **Figure 3.13a**. Similar to the intrinsic lattice structure of the full-atomic graphene model, this graphene CG model is a hexagonal lattice, and each CG bead represents a certain number of carbon atoms in the full-atom model. The total energy of this CG model E_{CG} includes bond stretching energyE_{bond}, angular bending energy E_{angle}, dihedral torsional energy E_{dih} and non-bonded van der Waals energy E_{vdW}, and is

$$E_{CG} = E_{bond} + E_{angle} + E_{dih} + E_{vdW} \tag{3.44}$$

For graphene-like 2-D nanomaterials that will experience a large deformation, these energies of bonded interaction between CG beads can be expressed as $E_{bond} = \sum_{i=1}^{n_{bond}} D_0 \left[1 - e^{-\alpha\left(d - d_0^{cg}\right)}\right]^2$, $E_{angle} = \sum_{i=1}^{n_{angle}} k_\theta (\theta - \theta_0)^2$, and $E_{dih} = \sum_{i=1}^{n_{dih}} k_\emptyset [1 - cos(2\emptyset)]$ [172], where D_0 and α are parameters of the potential well depth of bonds and d_0^{cg} is the equilibrium distance of the CG bond, k_θ, θ_0, and $k_\emptyset$ are the constant of bead angle, equilibrium angle and constant of dihedral in the CG model, respectively. n_{bond}, n_{angle}, and

n_{dih} are the number of bond, angle and dihedral in the CG model, respectively. d_0^{cg} and θ_0

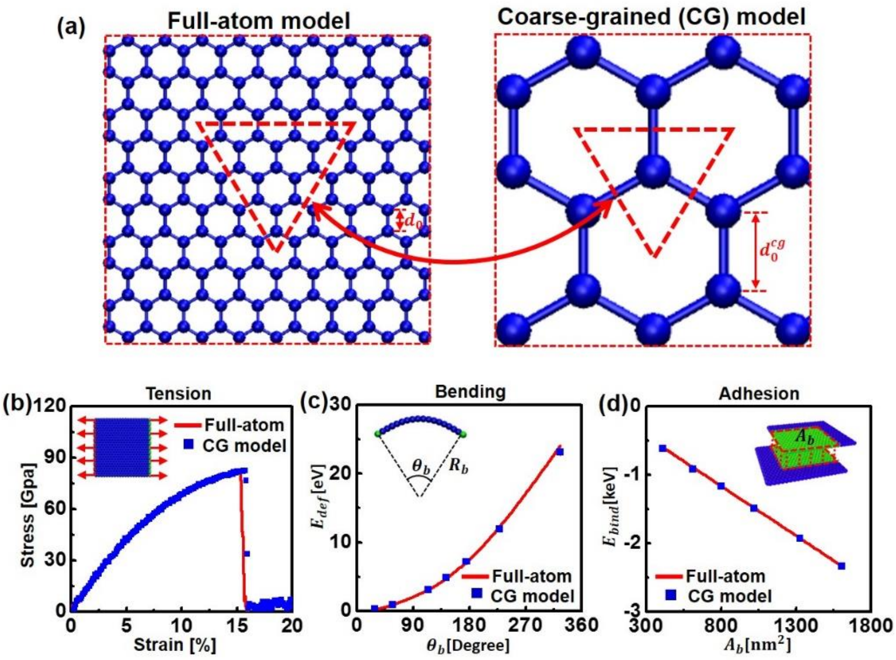

Figure 3.13. Coarse-grained (CG) model of 2-D material graphene. (a) Full-atom lattice (left) and coarse-grained (CG) lattice (right) models of graphene. The highlighted triangle area indicates coarse-grained scaling of 16:1; i.e., one bead in the CG model represents 16 atoms in the full-atom model. As a consequence, with the bond length of d_0 in the full-atom model, and the bond length in CG model is $d_0^{cg}=4d_0$. Comparison of **(b)** the stress-strain curve of graphene sheet under a tensile test, **(c)** the deformation energy of graphene sheet under a bending load and **(d)** the binding energy of two parallel graphene sheets between full-atom and coarse-grained model. The insets illustrate the loading conditions.

determine the geometrical and scaling features of the CG model. For example, for the CG model with hexagonal lattice structure and 16:1 coarse-graining mapping, $d_0^{cg} = 0.56\ nm$ and $\theta_0 = 120^{\circ}$. On the other hand, the continuum mechanics analysis to graphene-like 2-D nanomaterials will lead to $\alpha = log2/(\varepsilon_f d_0^{cg})$, where ε_f is the maximum failure strain of the 2-D material; $D_0 = \sqrt{3}hEG/\alpha^2(4G - E)$ and $k_\theta = \sqrt{3}\left(d_0^{cg}\right)^2 hEG/6(3E - 4G)$ [173], where G is the in-plane shear modulus of graphene and h is the interlayer distance and is 0.34 *nm* for graphene. Similarly, the parameters of CG model in the torsional energy E_{dih} can be obtained by considering a pure bending deformation of 2-D materials in continuum mechanics. For a rectangular shaped 2-D sheet in length L_g and width W_g with a radius of curvature R_b (insets in **Figure 3.13c**), based on the continuum mechanics analysis, the bending energy

$E_{bend} = BL_gW_g/2R_b^2$ [140]. $E_{bend} = E_{dih}$ will lead to a linear correlation between $k_{\emptyset}$ and B, $k_{\emptyset} = \beta B$, where β depends on the coarse-graining scale in the CG model. For example, it is $\beta = 0.0758$ for 16:1 coarse-grained mapping and $\beta = 0.1125$ for 4:1 coarse-grained mapping [172].

For non-bonded van der Waals energy E_{vdW} in the CG model, similar to the full atomic model, it can be described by 12-6 Lennard-Jones (L-J) potential, and $E_{vdW} = \sum_{i=1}^{n_{bead}-1}\sum_{j=i+1}^{n_{bead}} 4\epsilon\left[\left(\frac{\sigma}{d}\right)^{12} - \left(\frac{\sigma}{d}\right)^{6}\right]$, where ϵ is the potential well depth of CG beads and $\sigma = 0.346$ *nm* is the parameter associated with the equilibrium distance between two non-bonded CG beads. n_{bead} is the number of beads in the CG model and d is the distance between two beads. For two layers of materials with an overlap area A_b (inset in **Figure 3.13d**), the binding energy is $E_{bind} = \Gamma_b A_b$, and $E_{bind} = E_{vdW}$, i.e. $\Gamma_b A_b = \sum_{i=1}^{n_{bead}-1}\sum_{j=i+1}^{n_{bead}} 4\epsilon\left[\left(\frac{\sigma}{d}\right)^{12} - \left(\frac{\sigma}{d}\right)^{6}\right]$ leads to a linear correlation between ϵ and Γ_b via $\epsilon = \vartheta\Gamma_b$. Similar to β, ϑ also depends on the coarse-graining scale in the CG model, and it is ϑ=$2.1892 \times 10^{-20}\, m^2$ and $\vartheta = 1.84 \times 10^{-19}\, m^2$ for 4:1 and 16:1 coarse-grained mapping, respectively [172].

For a well-defined coarse-graining scale of 16:1 in 2-D material graphene, the potential parameters D_0, α, k_θ, $k_{\emptyset}$ and ϵ in its CG model can be determined. For graphene, take $E = 1\,TPa$, $G = 450\,GPa$, $\varepsilon_f = 0.16$ [172], B=2.38× $10^{-19}J$ and Γ_b=-0.232 J/m^2, we can obtain D_0=797.4283 *kcal/mole*, α=0.7736 $Å^{-1}$, k_θ=1662.9 *kcal/mole*, $k_{\emptyset}$=2.6 *kcal/mole* and ϵ=6.15 *kcal/mole* by following above analysis. With these parameters in the CG mode, we performed both coarse-grained molecular dynamics (CGMD) and full-atom molecular dynamics (MD) simulations to validate our CG model. All the simulations were performed in LAMMPS [174]. **Figure 3.13b** and **c** show the comparison of the proposed CG model and full-scale atom model in tension and bending deformation, respectively. Both Young's modulus and maximum tensile strength of graphene are well reproduced by the proposed CG model. Further, under a relatively broad range of bending angle θ_b, good agreement of the bending deformation is obtained between the CG model and full-atom model, which validates the CG model for the study of crumpling 2-D graphene. **Figure 3.13d** shows that the non-bonded interaction between graphene sheet from CGMD simulations agrees well with that in full-atom

MD simulations, indicating that the CG model can also be used to study the interactive binding energy of self-folding and assembly of graphene sheets.

3.3.2 Virtual spherical van der Waals force field simulation method

Once the CG model of graphene is validated, we will introduce a computational method to mimic the interactions of liquid molecules to graphene by employing a virtual spherical L-J force field. The simulation procedure consists of three steps: In the first step, the liquid droplet was replaced by a virtual sphere with radius $R_d = R_i$. The initial positions of graphene were uniformly distributed on the outside surface of the sphere to mimic a uniform distribution of graphene in the liquid droplet. The initial radius of sphere (R_i) was determined based on the number of graphene sheets and area of each sheet to ensure no overlap between individuals and no self-folding within a single sheet. The interaction between graphene and surface of the virtual sphere was modeled by a 12-6 L-J potential to mimic the interaction between liquid droplet and graphene. By setting up the cut-off radius of the L-J potential $2^{1/6}\sigma$ between graphene sheets and the sphere surface, there would be only repulsive for the sphere surface to the graphene and this setting would also not allow penetration of graphene sheet into the sphere. A constant force pointing to the center of the virtual sphere was added on each CG bead to provide a driving force for crumpling and assembling graphene, and the magnitude of force was determined by $F_b = \frac{P_t A_g^t}{n_{bead}}$. Such the force depends on the evaporation pressure and reflects the influence of temperature on the liquid evaporation. After that, the system was equilibrated at 300 *K* for 2.0 *ns* with NVT ensemble under Nose/Hoover thermostat. In the second step, all the settings in the first step would remain the same except that the radius of the virtual sphere decreased with time by following a well-defined function to mimic the evaporation process of liquid droplet [175, 176], which is $R_d = R_i + (R_e - R_i)(t_s - t_i)/t_e, (t_i < t_s \le t_i + t_e)$, where t_s is the instantaneous time step during simulation, t_i is the time period required for equilibrium of the system in the first step, and t_e is the time period for the radius of sphere that changes from R_i (initial radius of sphere) to R_e (final radius of sphere). The evaporation rate is taken into account by the decreasing rate of radius of the virtual sphere $|R_e - R_i|/t_e$ and was taken $\sim 50\ \mathrm{nm/ns}$ to ensure both stability of simulations and independence of assembled and self-folded morphology with the shrinking rate of the virtual sphere. Afterward, the NVT ensemble under Nose/Hoover thermostat that mimics a constant temperature of high-temperature furnace during evaporation in experiments was employed to monitor the crumpling and assembly of graphene sheets. In the third step, the applied force pointing to the center of sphere was removed at $R_d = R_e$. Another 2 ns was performed under NVT ensemble to monitor the final morphology of assembled graphene sheets. The strain energy, binding energy, assembling energy and radius of gyration of assembled particle were documented every 0.01 *ns* during simulations to ensure sufficient data recorded.

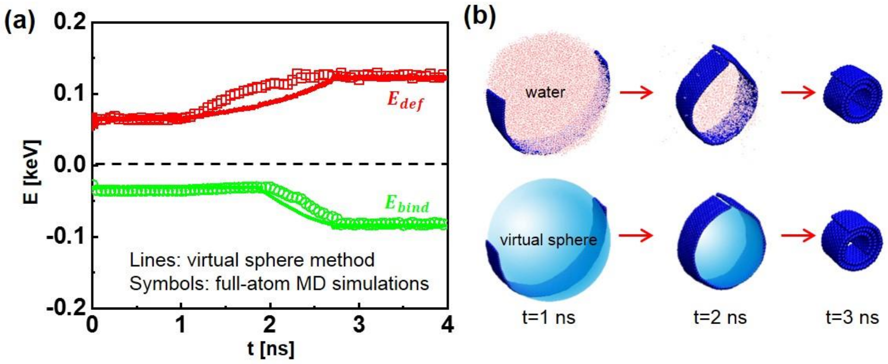

Figure 3.14. Validation of the virtual sphere force field method. (a) Comparison of deformation energy (E_{def}) and binding energy (E_{bind}) of a single graphene nanoribbon obtained by the full-atom water/graphene simulations and virtual spherical force field/full-atom graphene. **(b)** Snapshots of crumpled morphology of graphene during simulations.

To validate this simulation method, the full-atomic molecular dynamics simulation is conducted. The simulation system consisted of 4200 SPC/E water molecules [105] (corresponding the volume of water droplet V=125.55 nm^3) and a graphene ribbon with the dimension of 20 *nm* ×2 *nm*. The AIREBO force field was employed to model the flexible neutral graphene sheet [131, 132]. The 12-6 pairwise Lennard-Jones potential $V(d) = 4\epsilon(\sigma^{12}/d^{12} - \sigma^6/d^6)$ was used to model the water-water and carbon-water non-bonded interactions [125], where ϵ is the potential well depth, ρ was the parameters associated with the equilibrium distance and d was the distance between two atoms. σ_{O-O}=0.3166 *nm*, ϵ_{C-O}=0.0937 *kcal/mole*, and σ_{C-O}=0.319 *nm* were chosen to model the interaction between water molecules and graphene sheet. The simulation procedure includes three steps: First, after energy minimization of the water and graphene sheet, NVT ensemble with Nose/Hoover thermostat was employed for 1.0 ns with a time step of 1.0 *fs* to equilibrate the system at 300 K and 1.0 atm. Secondly, 11 water molecules were removed from the system for every 1000 time steps until all the water molecules were completely removed. During these processes, the energy and position of water molecules and graphene sheet were monitored every 1000 time steps to ensure the sufficient data recorded. Thirdly, after all the water molecules were evaporated, another 1.0 ns under the NVE ensemble was run to make sure the deformed graphene sheet reached the stable folded pattern.

When a virtual spherical force field was used in the simulations, all water molecules were replaced by a virtual sphere with an initial radius of R_i=3.106 nm that is the same as the water droplet size of 4200 water molecules and the graphene ribbon was kept the same. At the same time, Eq. (3.7) was used to calculate the overall pressure exerted on the graphene by liquid evaporation and P_t=188.2 *atm*. This pressure was applied as a force to on each carbon atoms, i.e. F_b=0.0067 *kcal/mole*-Å. In the simulations, first, after energy minimization of the graphene sheet, NVT ensemble with Nose/Hoover thermostat was employed for 1.0 ns with a time step of 1.0 fs to equilibrate the system at 300 K and 1.0 atm. Afterward, the radius of sphere was decreased by following the law of $R_d = R_i - \frac{R_i}{0.381ns}(t - 1ns)$ to ensure that the volume of sphere equals the volume of water in the full-atom simulations at the same timesteps of liquid evaporation. During this process, the variation of energy, position of water molecules and graphene sheet were monitored every 1000 time steps to ensure the data recorded sufficiently. In the last step, R_d=0 was set to run another 1.0 ns under the NVE ensemble to make sure that the folded graphene sheet reached a stable stage.

Figure 3.14a plots the comparison of deformation energy (E_{def}) and binding energy (E_{bind}) of graphene ribbon between simulations by the full-atom water and graphene and the virtual sphere and full-atom graphene systems. Excellent agreement between them is obtained. Note that the bit early emergence and consequent quick decrease of binding energy in the full-atom simulations than that in the virtual spherical simulations is expected to result from the early partial contact of water liquid with the edge tips of graphene, and the consequent squeezing out of water liquid by the folded section of graphene, as shown in **Figure 3.14b**. However, both final energies and morphologies of folded graphene after complete liquid evaporation or removal of virtual spheres agree with each other, which validates the employment of a virtual spherical force model in the simulations.

Further, To validate the proposed equivalent evaporation pressure model in Section 3.2.1, two parallel CGMD simulations on crumpling a single graphene sheet via a virtual sphere were performed. The modeling and simulation procedure follows Section 3.3. Only the driving forces were different between the two simulations. For the full driving force model, a constant force pointing to the center of the sphere was added on each CG bead to represent the contribution of gas pressure (P_g) and vapor pressure (P_v). At the same time, another force with constant magnitude was added on each CG bead at the boundary of graphene to represent the capillary force (F_c). The direction of force is always perpendicular to the initial orientation of the boundary after it was added and is also always tangential to the surface of the sphere. For the equivalent evaporation driving force model, a constant force pointing to the center of the sphere was added on each CG bead of the graphene to represent the total equivalent pressure (P_t). The length of graphene was L_g=100 *nm*, and the initial radius of the sphere was R_i=100 *nm* and the final radius of the sphere was R_e=1 *nm*. The time of equilibrium was t_i=1 *ns*, and the time of evaporation was t_e=2 *ns*. After the evaporation, another 1*ns* was following to make sure the final folded pattern was stable. **Figure 3.15a** plots the variation of deformation energy E_{def} and binding energy E_{bind} during the folding. E_{def} increases slowly at the beginning

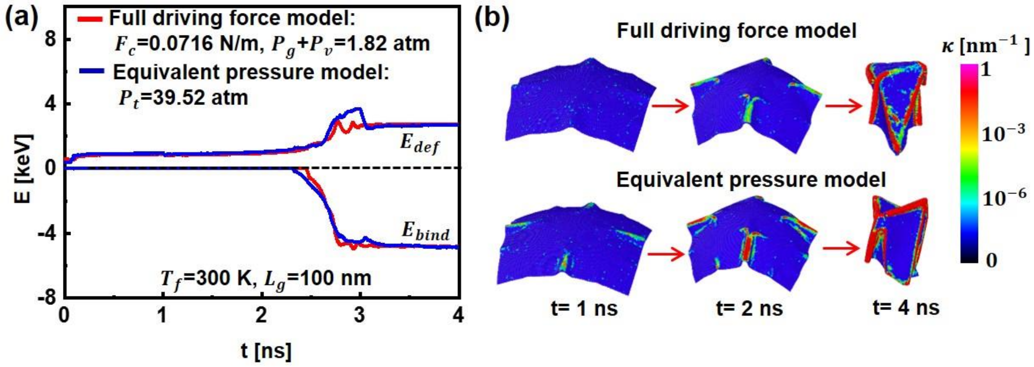

Figure 3.15. Energy and morphology variation of a single layer graphene during the liquid evaporation. **(a)** Comparison of the deformation energy E_{def} and binding energy E_{bind} at T_f=300 *K* between the full driving force model and equivalent pressure model for a square graphene with L_g=100 *nm* during liquid evaporation. **(b)** Snapshots of the crumpled graphene under different driving force models.

of evaporation, followed by a quick increase after a critical evaporation time. After that, it arrives at an approximate stable stage. By contrast, E_{bind} remains zero at the beginning, followed by a quick decrease at the moment when there is a significant increase of E_{def} and then reaches a stable stage. More importantly, both E_{def} and E_{bind} have been well predicted by the equivalent evaporation pressure model (Eq. 3.7), with good agreement with those from full-force model. The non-zero of E_{bind} indicates the occurrence of self-folding in the graphene, which is also consistent with a quick increase of E_{def}. The final non-zero stable E_{def} and E_{bind} suggest that the deformed graphene by evaporation of liquid possesses a stable morphology. **Figure 3.15b** shows the snapshots of simulations, and the deformation evolution of graphene with evaporation time, ranging from the initial bending deformation, to self-folding and to a final stable crumpled pattern, is observed, which corresponds well with variation of E_{def} and E_{bind}. Besides, good agreement of these deformation patterns with approximately the same curvature from the equivalent pressure model (Eq. 3.8) and full force model is obtained.

3.4 Energy and Morphology when Crumpling a Single 2-D Sheet

Figure 3.16a shows comparison of energy variation of a single graphene sheet with a size of L_g=40 *nm* between theoretical and simulation results during the liquid evaporation. The radius of liquid droplet R_d decreases from R_i=100 *nm* to R_e=1 *nm*, and the evaporation-induced pressure is taken P_t=10 *atm* and P_t=40 *atm*, respectively. With the increase of curvature of liquid droplet (κ_d=1/R_d), both the deformation energy E_{def} (i.e. E_s^{spring} in the mechanics model, Eq. (3.18)) and binding energy E_{bind} (i.e. E_b^{slider} in the mechanics model, Eq. (3.19)) under P_t=10 *atm* remain zero, indicating there is no self-folding in the graphene, in good agreement with snapshots in **Figure 3.16b**. This unfolding is caused by the absence of binding energy E_{bind} which will prevent the "bouncing back" of initial bending deformation, and is well predicted by Eq. (3.29), where a small graphene sheet cannot be folded by a weak driving force for graphene L_g=40 *nm* ($<$ critical $L_g^c = \sqrt{A_g^c}$=61.34 *nm* when P_t=10 *atm* from Eq. (3.29)) or pressure of P_t=10 *atm* ($<$ critical P_t^c=36.05 *atm* when A_g=1600 nm^2 from Eq.

(3.29)). At higher pressure, P_t=40 *atm*, both E_{def} and E_{bind} increase after a critical

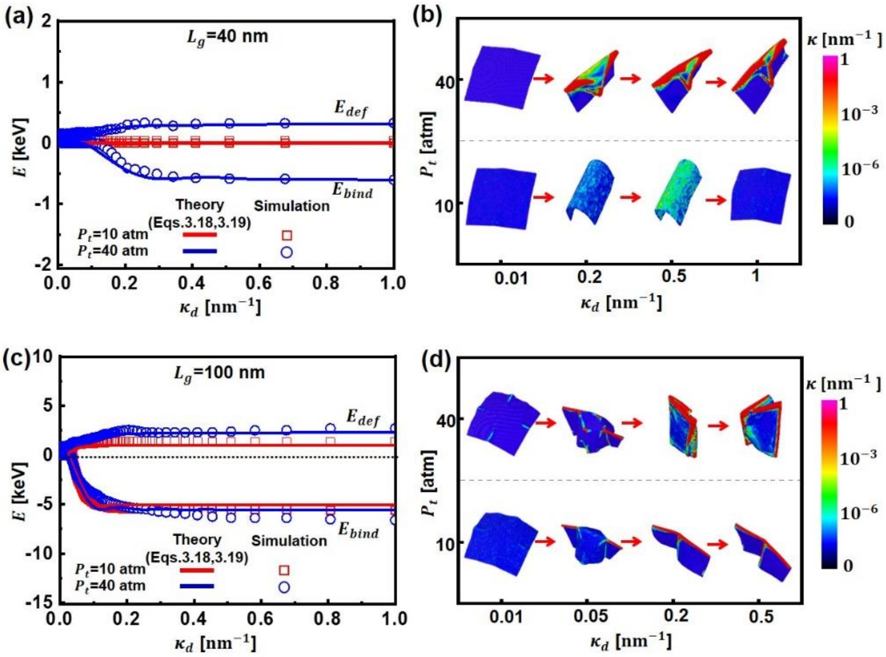

Figure 3.16. Comparison of energy and morphology evolution of a single graphene sheet during the liquid evaporation between the theoretical predictions and simulations. Comparison of energy variation of a single graphene sheet with a size of **(a)** L_g=40 *nm* and **(c)** L_g=100 *nm* between theoretical and simulation results with liquid droplet curvature κ_d. Morphology evolution of a square graphene sheet with **(b)** L_g=40 *nm* and **(d)** L_g=100 *nm* with liquid droplet curvature κ_d under evaporation pressure P_t=10 *atm* and 40 *atm*. κ is the local curvature in the deformed sheet.

evaporation time and a folded graphene is obtained, as shown in snapshots in **Figure 3.16b**. Besides, the good agreement of these energies between simulation and theoretical predictions indicates that deformation and self-folding can be well captured by our rotational spring-mechanical slider model. For a larger graphene sheet (L_g=100 *nm*), both E_{def} and E_{bind} (**Figure 3.16c**) show non-zero magnitudes with the evaporation of liquid, and a higher pressure leads to higher magnitudes. As a consequence, successful folded patterns of graphene are obtained with a higher crumpling density at a higher pressure, as indicated in **Figure 3.16d**. More importantly, the good agreement between theoretical predictions and simulations remains. Both the pressure and graphene sheet size can affect the final folded morphology as well as the deformation energy and binding energy after the complete evaporation of liquid. The equilibrated energy of graphene sheet during simulation is extracted and compared with the theoretical predictions. **Figure 3.17a** plots the comparison of equilibrated energy of graphene after complete evaporation of liquid between the theoretical predictions and simulations. Both the deformation energy and binding energy increase (magnitude) linearly with the increase of graphene area A_g, suggesting a favorable crumpling process for large graphene. More importantly, the energies show good agreement between simulations and theoretical predictions. In particular, zero deformation and binding energies in the extremely small graphene that correspond to an unsuccessful folding under the evaporation pressure P_t=10 *atm* are well captured by our theoretical model (Eq. (3.29)). For a higher pressure P_t=40 *atm*, the good agreement between theoretical prediction and simulations still remains (**Figure 3.17b**). The minimum size of graphene sheet for a successful folding decrease and the magnitude of deformation energy E_{def} increases, while the binding energy E_{bind} remains approximately the same. These different responses to pressure are dependent on intrinsic deformation nature that E_{def} is sensitive to the local curvature of bending deformation and E_{bind} is determined by overlap area in graphene [161], and also agree with the spring constant and slider constant in Eqs. (3.18) and (3.19). These different crumpling energies in these graphene sizes and evaporation pressures reflect different crumpling morphologies. In particular, if the graphene is large enough, the size of first folded graphene may be larger than the critical length to be folded and multiple foldings are expected.

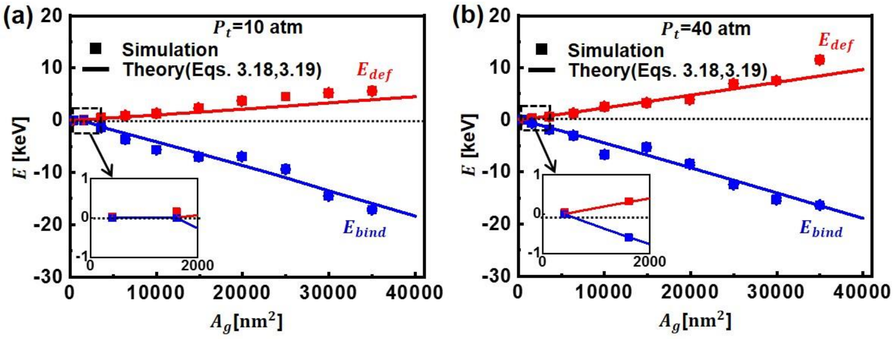

Figure 3.17. Comparison of the deformation energy E_{def} and binding energy E_{bind} of the single layer graphene after the complete evaporation of liquid between the theoretical predictions and simulations under evaporation pressure (a) P_t=10 *atm* and (b) P_t=40 *atm*. The inset highlights at the small area where if both of the energies are zero, graphene cannot be folded by the liquid evaporation.

To illustrate the multiple folding of graphene by liquid evaporation, simulations on series of a single graphene sheet with different sizes were performed. **Figure 3.18** shows the map of folded graphene as the variation of pressure after complete evaporation of liquid water, where the local curvature distribution on the folded graphene is given to highlight the folding density and locations. When the graphene size is small and the evaporation pressure is low, the graphene sheet cannot be folded and is referred to the "unfold" region. When either the pressure or graphene size increases, a successful folding such as a "racket-like" pattern is observed, referred to as a "racket-like" region in the map, similar to the folding pattern of graphene nanoribbon [99, 140, 177]. In particular, when the graphene size or pressure continues to increase, folding becomes intense and multiple foldings are observed. Besides, higher pressure or larger graphene size is, the stronger folding with larger folding curvature will be, which echoes well with higher deformation and binding energies in **Figure 3.17**. The folded pattern with intense folding, in particular with multiple foldings, is similar to a shape of spatial particle, referred to as a "particle" region and its size decreases with the increase of folding pressure. With the definition of these three deformation regions, their transition can be further predicted through the theoretical analysis by Eq. (3.29). The good agreement between theoretical predictions and simulations in **Figure 3.18** further validates the energy analysis through the proposed rotational spring-mechanical slider model.

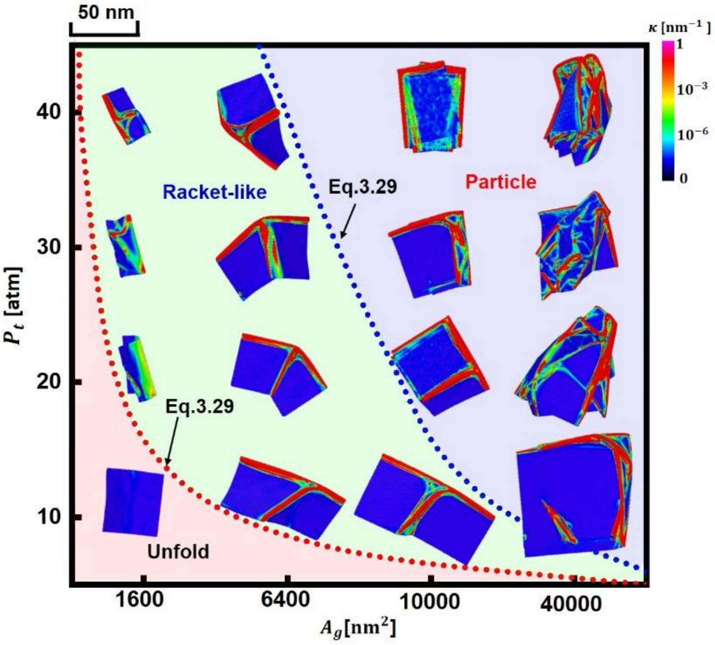

Figure 3.18. Morphology and size map of folded graphene with highlights of local curvature after complete evaporation of liquid. Three patterning regions are identified, referred to as "unfold", "racket-like pattern" and "particle" with the increase of evaporation pressure or/and total area of 2-D graphene sheet.

3.5 Energy and Morphology when Crumpling Multiple 2-D Sheets

When there are multiple graphene sheets in the liquid droplet, similar simulations were performed, and 5 pieces of square graphene sheets with the size of L_g=100 *nm* were taken as an example. In the simulations, the initial radius of liquid droplet was R_i=100 *nm* to ensure no overlap between each graphene sheets at the equilibrium, and the final radius of liquid droplet after complete evaporation of liquid was set to be R_e=1 *nm* to make sure the droplet is small enough for a sufficient crumpling and assembly of graphene sheets. **Figures 3.19a** and **b** show the comparison of energy variation between theoretical predictions via Eqs. (3.30)-(3.38) and simulations for their assembling and self-folding with liquid evaporation under the evaporation pressure of 10 *atm* and 40 *atm*, respectively. The deformation energy E_{def} (i.e. E_s^{spring} in Eqs. (3.30) and (3.34)), binding energy E_{bind} (i.e. E_b^{slider} in Eqs. (3.31) and (3.35)) and assembling energy E_{asm} (i.e. E_{asm} in Eq. (3.36)) all increase (magnitude) rapidly at the onset of liquid evaporation and then reach a plateau when the size of droplet is small enough

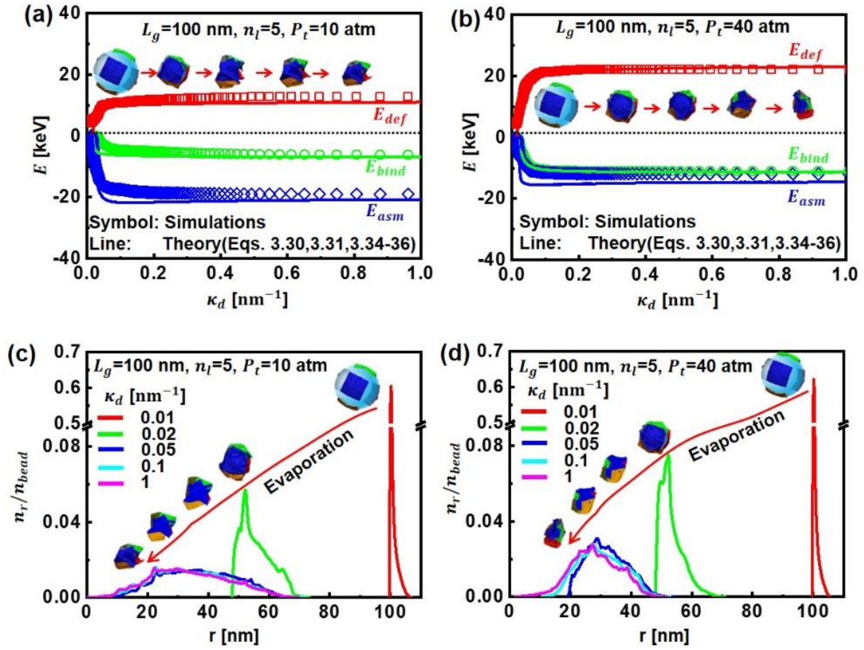

Figure 3.19. Energy and mass variation of crumpling and assembling multiple 2-D material graphene sheets by the liquid evaporation. Comparison of the deformation energy E_{def}, binding energy E_{bind} and assembling energy E_{asm} of 5 square graphene sheets with each size of L_g=100 *nm* between the theoretical predictions and simulations under **(a)** P_t=10 *atm* and **(b)** P_t=40 *atm*. Mass distribution of the graphene in the droplet during liquid evaporation under **(c)** P_t=10 *atm* and **(d)** P_t=40 *atm*. The inserts show the evolution of assembled morphologies of the crumpled graphene sheets with liquid evaporation.

(κ_d>0.1 nm^{-1}). Similar to that in a single graphene sheet in **Figure 3.16**, the increase of E_{def} and E_{bind} (magnitude) with evaporation reflects the crumpling or self-folding of graphene associated with generation and propagation of folded ridges, and higher pressure leads to larger E_{def} and E_{bind}. The appearance and increase of E_{asm} with evaporation represents the assembly of multiple graphene sheets and higher pressure leads to lower E_{asm} (magnitude). The final stable stage of these energies suggests the arrival of crumpled and assembled graphene with a stable pattern. Besides, higher pressures lead to higher E_{def}, E_{bind}, and lower E_{asm}, promoting both crumpling and self-assembly of graphene sheets. In parallel, the variation of energies with evaporation (i.e. the radius of liquid droplet) can be predicted by Eq. (3.38) and the results show excellent agreement with the simulation results for both evaporation pressures, as shown in **Figure 3.19a** and **b**, which validates the proposed network mechanics model of rotational spring-mechanical slider for multiple graphene sheets.

In order to monitor the evolution of morphology and size of the folded particles during the liquid evaporation, **Figure 3.19c** and **d** give the mass distribution of coarse-grained carbon beads n_r/n_{bead} along the radial direction, where n_r and n_{bead} is the number of beads at the position of r and total number of beads in the graphene particle, respectively. We should mention that the centroid of assembled graphene particle may not the same as the center of the liquid sphere and the starting point of each distribution could be smaller than the instantaneous R_d of liquid droplet radius. At the beginning of evaporation (κ_d=0.01 nm^{-1}), most of the beads are distributed on the surface of sphere, which corresponds to the uniform distribution of graphene sheets (see inset), resulting in the distribution limited to a narrow region with an extremely high peak. With the liquid evaporation, the peak becomes lower and the distribution region of beads becomes wider, which is led by the out-of-plane deformation in crumpling and assembly of graphene. After complete liquid evaporation (κ_d=1 nm^{-1}), the mass shows a normal distribution spanning across the entire particle, leading to a “ball-like” particle of assembled graphene. The insets further illustrate the evolution of morphology of graphene sheets. When the evaporation pressure increases from 10 *atm* to 40 *atm*, similar mass evolution with liquid evaporation is also observed, but is more concentrated with a higher peak after complete liquid evaporation, in good agreement with a denser assembly of graphene in a higher evaporation pressure.

Figures 3.20a and **b** give the simulation snapshots of graphene sheets with liquid evaporation and the ridge distribution in one of the representative graphene sheets (marked in blue and numbered as (I)) under these two different pressures. At the beginning of evaporation (κ_d=0.01 nm^{-1}), graphene sheets were distributed uniformly without any overlap between each other on the surface of liquid sphere and the small curvature in the graphene results from the deformation due to the conformal contact between graphene and liquid droplet. This conformal contact with small deformation in each individual graphene but without assembly

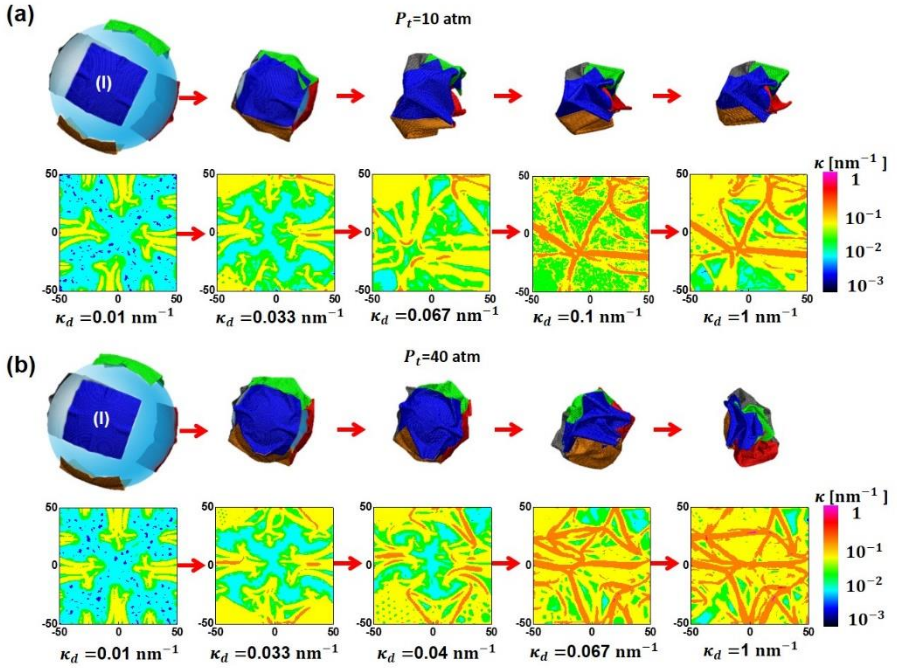

Figure 3.20. CGMD simulated morphology evolution of 5 square graphene sheets with each L_g=100 *nm* with liquid evaporation (liquid droplet curvature κ_d) under (a) P_t=10 *atm* and (b) P_t=40 *atm* (top) and distribution of folded ridges in one of the representative graphene sheet marked as (I) in blue (bottom).

continues with the evaporation till the κ_d~0.033 nm^{-1}. Afterward, graphene sheets start to contact with each other, in consistence with the appearance of self-assembly energy E_{asm} in **Figure 3.19a**. Once self-assembly begins, graphene will be subjected to a biaxial compression strain due to interaction with adjacent ones. As a consequence, folding ridges increase and propagate and more importantly, they bifurcate beyond the main folding axis of symmetry, which in turn accelerates a rapid increase of E_{asm} as obtained in **Figure 3.19a**. With further evaporation, κ_d>0.1 nm^{-1}, the crumpled and assembled pattern becomes stable and the ridges will not increase with approximately stable local curvatures in the graphene sheets, also in good agreement with the arrival of the stable energies in **Figure 3.19a**. When the evaporation pressure increases from 10 *atm* to 40 *atm*, similar evolutions of crumpling and assembly but intense local ridges in both size and curvature in the representative graphene sheet are observed. Besides, more numbers and larger sizes of ridges are obtained and an assembled particle with more intense crumpling is obtained, which also agrees with higher energies in **Figure 3.19b**. To compare the crumpling morphology of each graphene sheet in the assembled graphene particle after complete evaporation of liquid, **Figure 3.21** gives morphology of the particles and the density of ridges with local deformation curvatures in these five graphene sheets under these two different evaporation pressures. The higher density of ridges under higher pressure is further confirmed. We further calculate the ridge density (D_r) by the image processing algorithm [178] (**Figure 3.22**), as given in **Figures 3.21c** and **d**. Under the same evaporation pressure, although the distribution of ridges is different among each individual sheet, their total ridge density is approximately the same, suggesting the equality of crumpling and assembly in each graphene sheet by evaporation pressure.

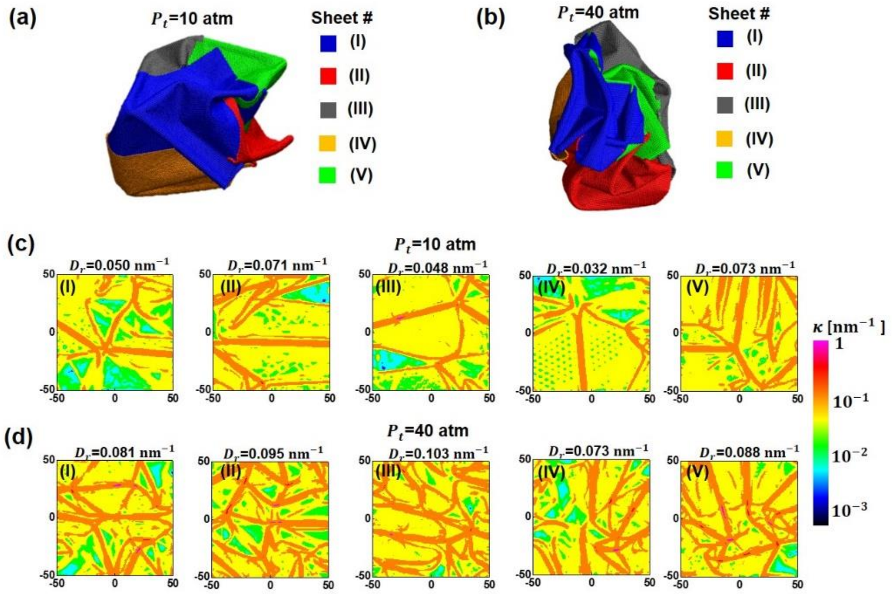

Figure 3.21. Overall morphology of the assembled graphene particle after complete evaporation of liquid and comparison of crumpled morphology among their individual graphene sheet under (a) and (c) P_t=10 *atm* and (b) and (d) P_t=40 *atm*. Graphene is a square shape with the size of L_g=100 *nm*

Figures 3.23a and **b** show the comparison of crumping and assembly energy in the final folded particle with the total area of graphene between the theoretical predictions and simulations under these two evaporation pressures. Similar to that in a single graphene sheet in

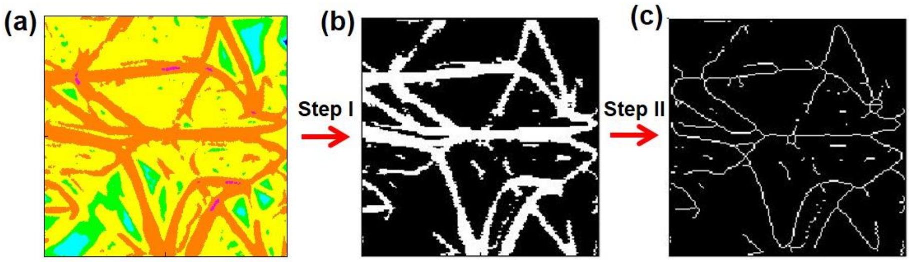

Figure 3.22. Determination of ridge density using the image processing procedure. (a) Local curvature distribution of the raw image from CGMD simulations. **(b)** Image after converting the colored image to grayscale. **(c)** Image after the skeletonization to calculate the ridge density.

Figure 3.17, the deformation energy E_{def}, binding energy E_{bind} and assembling energy E_{asm} increase (magnitude) with the increase of total area of graphene, and higher pressures lead to larger energies. The larger E_{bind} indicates an intense deformation, in good consistence with a larger E_{def}; a larger E_{asm} indicates a closer packing of each deformed graphene. Good agreement between simulations and theoretical results is obtained. More importantly, given the total area of graphene sheets, this agreement is independent of numbers of graphene sheets.

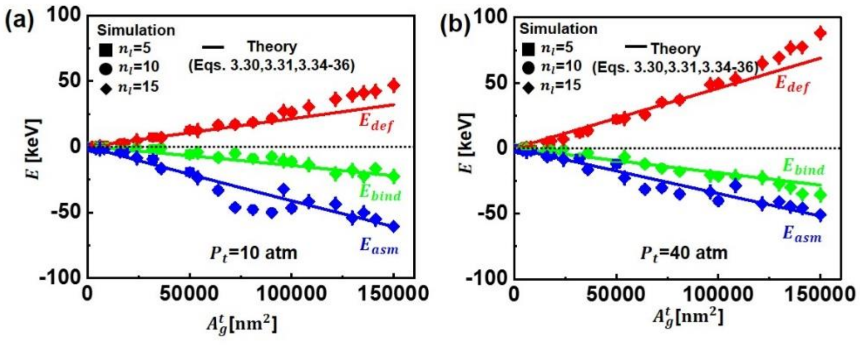

Figure 3.23. Comparison of energy of the assembled particles after complete evaporation of liquid between the theoretical predictions and simulations under (a)P_t=10 *atm* and (b)P_t=40 *atm*.

Figure 3.24a shows the effect of evaporation pressure on the mass distribution in assembled particles after the complete evaporation of liquid. Higher pressure will lead to a higher peak with narrower distribution, indicating that the increase of the pressure will promote the crumpling of graphene and will also enhance the geometric regularity of assembled particles toward a “ball-like” shape. However, the location of peaks is nearly the same, implying the averaged size of assembled particles is insensitive to evaporation pressure. When the total area of graphene A_g^t increases, **Figure 3.24b** shows that the location of peaks shifts to a high position and larger particles will be assembled, which agrees well with experimental measurements [47, 179] (**Figure 3.1b**). In addition to the size of particles, the surface roughness of particles is directly related to the out-of-plane deformation of 2-D sheets, which is controlled by the total area and evaporation pressure. **Figure 3.24c** gives the comparison of the ridge density (D_r) between theoretical predictions (Eq. (3.41)) and simulations in all the graphene layers within a single particle. As the liquid evaporates, the density of ridges shows a rapid increase at the beginning and then arrives at a stable stage. Besides, higher pressures lead to large densities. Note that in the image processing algorithm to simulation results, the wrinkles with small curvatures at the initial stage of liquid evaporation are not considered as folds, leading to a small overestimate of the ridge density over theoretical predictions. **Figure 3.24d**

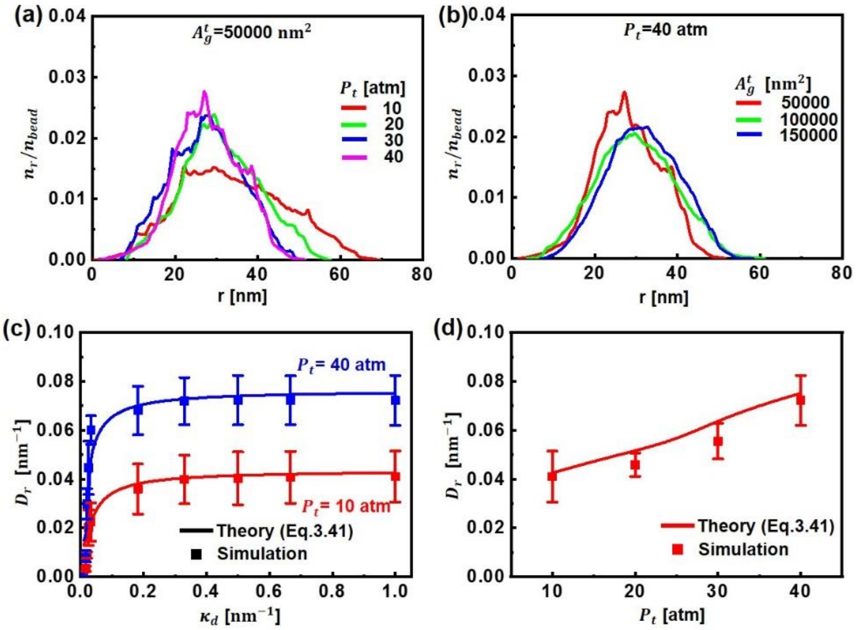

Figure 3.24. Mass distribution and the ridge density evolution of assembled graphene during the liquid evaporation. The effect of **(a)** evaporation pressure and **(b)** total area of graphene sheets on the mass distribution of the assembled particles after complete evaporation of liquid. **(c)** Comparison of the ridge density with the liquid evaporation (liquid droplet curvature κ_d) between theoretical predictions and simulations. **(d)** Comparison of the ridge density in the assembled particles between theoretical predictions and simulations after complete evaporation of liquid.

further shows comparison of ridge density in the final folded particle between the theoretical predictions and simulations with the evaporation pressure. The ridge density increases with the increase of pressure. Both the evolutions of crumpling and assembly of graphene with liquid evaporation and the effect of pressure are well consistent with variations of energies in **Figure 3.19**. More importantly, they are captured by the theoretical prediction with good agreement with simulations.

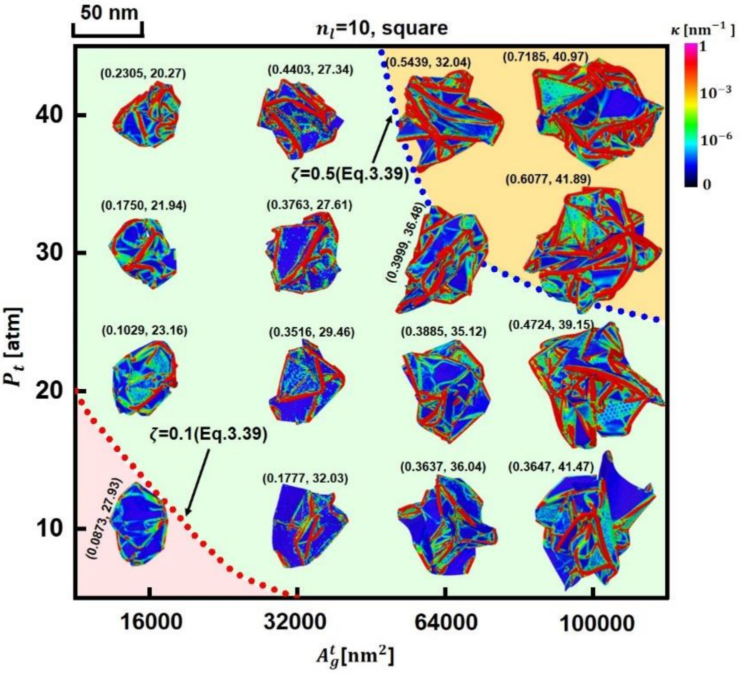

Figure 3.25. Morphology and size map of crumpled and assembled graphene with highlights of local curvature in each individual sheet after complete evaporation of liquid. The ratio of the crumpled area to assembled area, $\zeta = A_{bind}/A_{asm}$ and the radius R_g(in nanometer) in each particle are given, denoted as (ζ, R_g). At a low evaporation pressure and small total area of graphene sheet, self-folding in individual sheet is very small and can be neglected, leading to $\zeta < 0.1$; At a high evaporation pressure and a large total area of graphene sheet, each graphene will be self-folded intensively and assembled after complete evaporation of liquid ($\zeta > 0.5$).

Figure 3.25 summarizes the assembled particles by square graphene sheets (n_l=10) with the same size as a function of the total area and evaporation pressure. The curvature is given to illustrate the local deformation and morphologies of particles. The ratio between the crumpled area and assembled area $\zeta = A_{bind}/A_{asm}$ and the radius R_g(in nanometer) of each particle is also given, denoted as (ζ, R_g). At a small evaporation pressure and total area of graphene (e.g. A_g^t<20000 nm^2 and P_t<20 atm), these multiple graphene sheets will experience assembly with very limited deformation on individual graphene during evaporation, similar to that unfolded region I for a single graphene sheet in **Figure 3.19**, where this region is “assembly dominant” ($\zeta < 0.1$). Increasing evaporation pressure or the total area of graphene, crumpling deformation in individual graphene occurs, and local ridges with large curvatures will appear on the surface of particles, where this region reflects the competition between assembly and crumpling. The transition of regions between the “assembly dominant” and “assembly & crumpling” ($0.5 \leq \zeta \leq 0.1$) can be predicted well through our theoretical model via Eq. (3.39). At both high pressure and large total area of graphene sheets, crumpling in individual sheets will become intense associated with increased local ridges and high local curvatures, where it is referred to as the crumpling dominant region ($\zeta > 0.5$). Similarly, the transition between “assembly & crumpling” and “crumpling dominant” region can also be predicted in theory via Eq. (3.39) with good agreement each other. This deformation map further confirms that the overall size of the assembled particles is independent of evaporation pressure, but their overall profile in geometries are close to being spherical at high pressure. To demonstrate the role of graphene assembly in the formation of particles by liquid evaporation, **Figure 3.26** highlights

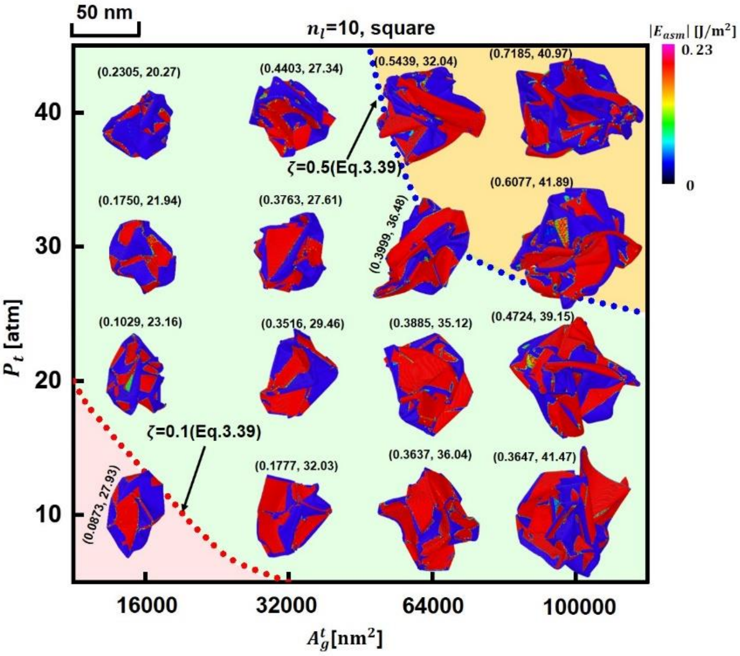

Figure 3.26. Morphology and size map of crumpled and assembled graphene with highlights of local assembled regions in each individual sheet after complete evaporation of liquid. The assembled regions and fraction of the assembled area among the whole particle are reflected by assembling energy distribution. (ζ, R_g) is the same as that in Figure 3.25.

the regions where individual crumpled graphene sheet is closer enough in the assembled particles and the assembly energy needs to take into account. The assembled areas over the total area will decrease with the increase of evaporation pressure, in line with the intense ridge densities that will reduce the deformed area of graphene in assembly. In contrast, it remains approximately the same with the increase total area of graphene, although the total assembly area increases.

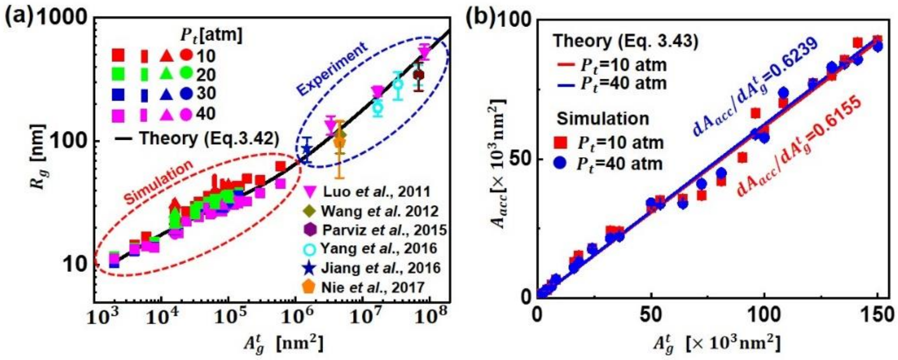

Figure 3.27. Comparison of (a) dimension size and **(b)** accessible area of assembled particles after complete evaporation of liquid under different evaporation pressures, shapes, and total areas of graphene sheets among theoretical predictions, CGMD simulations and available experiments.

In addition to the theoretical prediction to the morphology evolution and energy variations of crumpling and assembling graphene sheets by liquid evaporation, the energy of assembled particles after complete evaporation of liquid can be employed to estimate the overall size and accessible area of assembled ball-like particles as demonstrated in Eq. (3.42). **Figure 3.27a** gives the comparison of the overall radius of particles R_g between simulations and theoretical analyses. The experimental results available from the works of literatures are also included. Our theoretical predictions show remarkable agreement with both simulations and experimental results. The independent of evaporation pressure is also consistent with mass distribution in **Figure 3.24a**. With Eq. (3.43), the accessible area of the assembled particle can also be predicted and show good agreement with simulations, as shown in **Figure 3.27b**. More importantly, the slope in their linear relationship is 0.6239 for P_t=10 *atm* and 0.6155 for P_t=40 *atm*, insensitive to evaporation pressure, which are also close to 0.586 reported in the simulations [180] and experiments [47],

3.6 Influence of Graphene Shapes, Sizes, and Numbers on the Sizes and Morphologies of Assembled Particles

In experiments, given the same concentration of graphene in liquid solutions, graphene sheets may have variations of shapes, sizes, and numbers [51, 181, 182]. These parameters may influence the crumpling and assembly process during evaporation and the eventual morphology and size of assembled particles. Take the squared graphene as an example, given a series of total area of graphene in solvent solution, **Figure 3.28** plots the map of sizes and morphologies of the assembled particles by different numbers of graphene sheets after complete liquid evaporation under evaporation pressure of 20 *atm*. Similar to that in **Figure 3.25**, the local curvature distribution κ, and the ratio between the crumpled area and assembled area $\zeta = A_{bind}/A_{asm}$ and the radius R_g(in nanometer) of each particle, (ζ, R_g) are highlighted. When the total area of graphene sheets is kept the same, the overall size (R_g) of assembled particles show no significantly difference while ζ decreases with the increase of n_l. This different response is because the area of individual sheet will decrease with the increase of n_l, leading to the $A_g^{(i)}$ close to A_g^c (Eq. (3.29)) and suppressing the self-folding of graphene sheets. Larger n_l will require larger total areas of 2-D sheets to self-folding deformation in the 2-D sheet, as shown in Eq. (3.40). At the same time, both the overall size and density of ridges will increase with the increase of total area of graphene sheets, similar to the results in **Figure 3.25**.

Further, we consider the size distribution of graphene sheets in liquid solutions in experiments. As observed in the synthesis of graphene [182], the normal distribution is employed to take into account the area variation of graphene sheets via $n(A_g) = \frac{1}{\sqrt{2\pi}} exp\left(-\frac{(A_g - A_\mu)^2}{2A_\sigma^2}\right)$, where A_g is the area of graphene sheet and $n(A_g)$is the number of sheets at this area. A_μ is the median area and A_σ is the standard deviation. Consider the total area A_g^t and number of graphene sheets n_l in the liquid solution, we define the standard median as $A_\mu = A_g^t/n_l$, and the standard deviation can be determined by $A_\sigma = A_\mu/m$ (m is integer and $m \geq 3$ to ensure $A_g > 0$). In our simulations, five cases at n_l=10 with $A_\mu -$

$2A_\sigma$, $A_\mu - A_\sigma$, A_μ, $A_\mu + A_\sigma$ and $A_\mu + 2A_\sigma$ under evaporation pressure of 20 atm are studied and graphene remains a squared shape. **Figure 3.29** gives the map of sizes and morphologies of particles as a function of standard deviation of the area. The difference of size among individual graphene sheet only slightly causes a small change in both size and morphology of assembled particles. In addition, by taking four different shapes of graphene sheets, square, rectangle with an aspect ratio of 2, circle and equilateral triangle, we performed the simulations on the effect of graphene geometry on assembled particles after complete evaporation of liquid. **Figure 3.30** gives the map of assembled particles. Significant change of the overall particle size and morphology is not observed, similar to that effect of graphene number and shape size in **Figures 3.28** and **3.29**. The strong dependence of the total area of graphene sheets, but very insensitive to individual graphene number, shape geometry and size suggests the importance of graphene concentration in the crumpling and assembly process of graphene sheets into particles, which also agrees well with experiments.

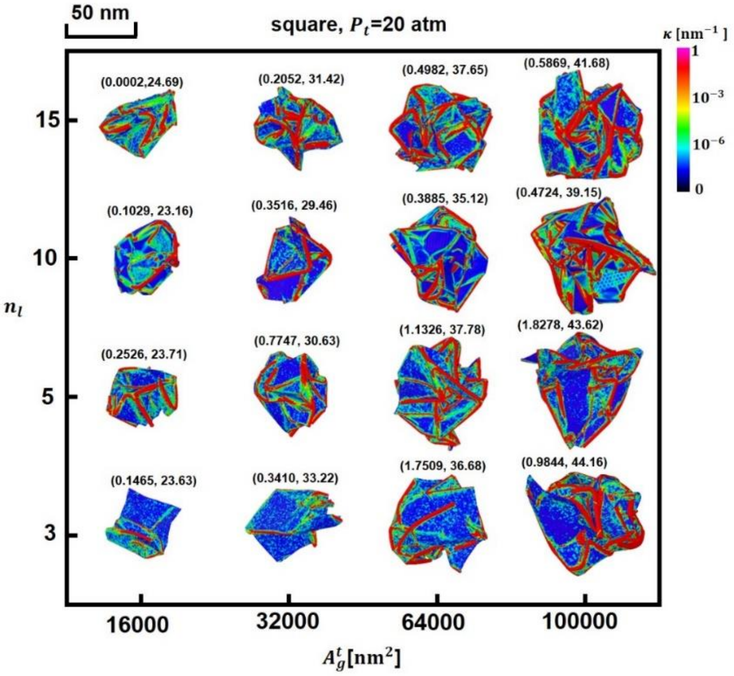

Figure 3.28. Effect of graphene sheet numbers on the size and morphologies of the assembled particles after complete evaporation of liquid under P_t=20 atm. (ζ, R_g) is the same as that in Figure 3.25.

As a quantitative characterization of these effects, **Figure 3.31** plots the effect of number, size distribution and shape of graphene sheets on the mass distribution in assembled particles after complete evaporation of liquid. Moreover, the overall size and accessible area in these assembled particles are also collected and are plotted in **Figure 3.27**. These data show good agreement with theoretical predictions, which further indicates their insensitivities to these size and geometric factors of individual graphene sheets and also confirms the robustness of our proposed rotational spring-mechanical slider mechanics model.

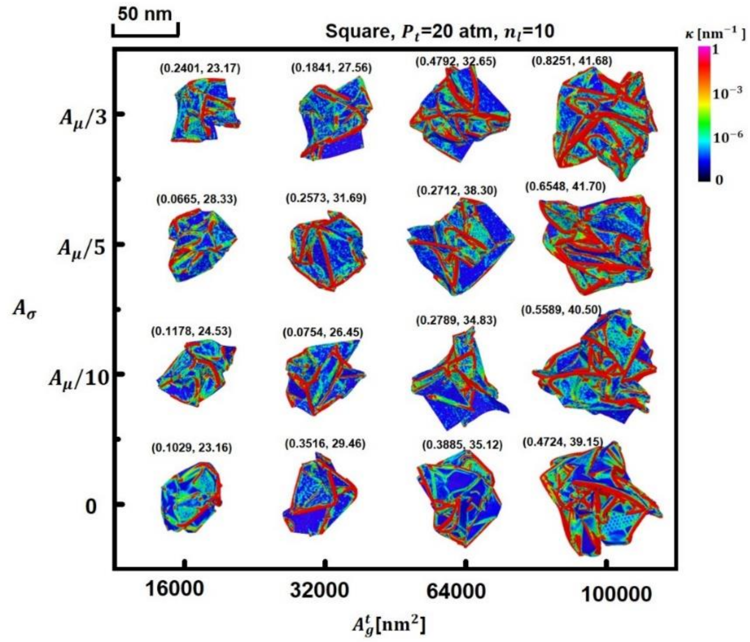

Figure 3.29. Effect of size distribution of square graphene sheet on the size and morphologies of the assembled particles after complete evaporation of liquid under P_t=20 *atm*. (ζ, R_g) is the same as that in Figure 3.25.

We should mention that these 2-D graphene sheets before deformation by liquid in above analyses are conducted on the basis of pristine graphene that can be considered a homogeneous thin film in continuum mechanics, and the effect of defects, edge configurations and chirality, and the resultant initial deformation morphologies that may influence the crumpling and assembling process during evaporation are not considered. For example, the edge stress may exist due to different bonding configurations of atoms at the edge of free standing 2-D materials such as graphene [119, 183]. Such stress will lead to local wrinkling of edge and even curling deformation in graphene sheets, in particular, in graphene nanoribbons with a large aspect ratio [183, 184], and the 2-D sheet will not remain a planar form. When these edge stressed 2-D sheets are in contact with the surface of liquid droplet, the edge stress is expected to increase the compressive hoop strain (Eq. 3.8) near the edges and leads to a higher energy for the fully conformal contact, which will benefit the subsequent wrinkling or buckling of 2-D sheet near the edge.

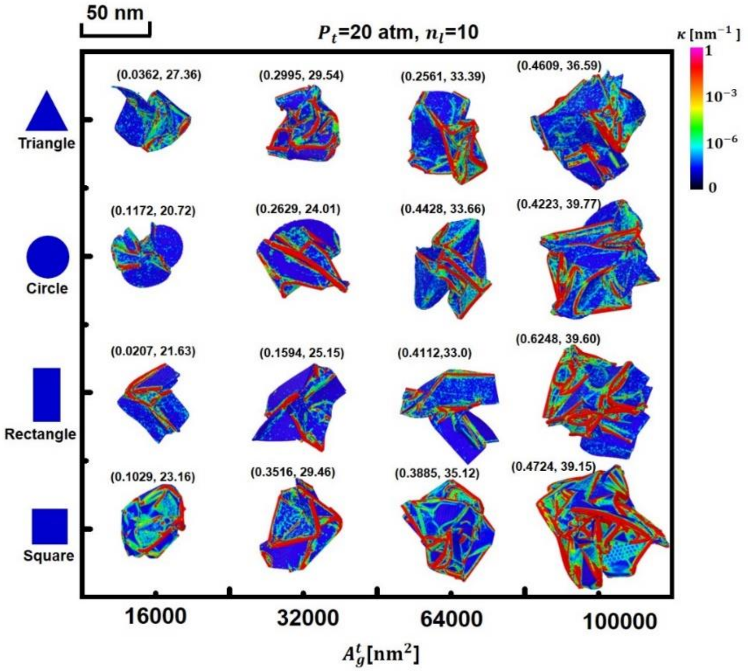

Figure 3.30. Effect of graphene sheet shapes on the size and morphologies of the assembled particles after complete evaporation of liquid under P_t=20 *atm*. (ζ, R_g) is the same as that in Figure 3.25.

In addition, once 2-D materials are immersed in the liquid solution, we assume a homogenous distribution of 2-D sheets is achieved in the liquid solution with full exfoliation of 2-D materials prior and no overlapped multiple layers exist. By contrast, when the proposed theoretical models are extended to study the crumpling and assembling process of 2-D layered materials such as 2-D heterostructures, where the mechanical properties including Young's modulus, bending stiffness and binding energy density that are needed in the models needs to be calibrated for the 2-D layered materials as a whole rather than their individual layer components, it is expected that the shear stress led by evaporation is usually very small and cannot lead to delamination of the layered materials. For example, delaminating a multiple

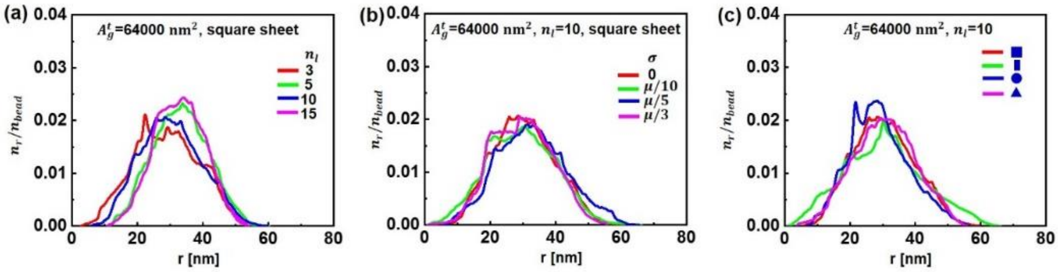

Figure 3.31. The effect of (a) graphene sheet number and **(b)** size distribution of graphene sheet and **(c)** graphene sheet shape on the mass distribution of the assembled particles after complete evaporation of liquid.

layered graphene structure with sole weak van der Waal interactions will require the shear stress as high as 0.4 GPa [185], while our calculation in Eq. (3.5) show that the shear stress (P_S) by the capillary flow exerted on the surface of 2-D sheet is only 5.69 Pa at the evaporation temperature of 900°C, eight orders of magnitude lower than that of the required delamination stress (0.4 GPa). In addition, the wrinkling and folding in 2-D layered materials may be different from that of a 2-D material planar sheet because of a small local deformation gradient may exist along the thickness direction [186], but local delamination is also not expected under such small deformation. As a result, the 2-D layered materials as a whole will experience mechanical deformation such as wrinkling and folding and the local deformation gradient can be taken into account by introducing a local strain or stress into the continuum mechanics model via Eq. (3.8).

3.7 Summary

We have proposed a theoretical mechanics framework of the rotational spring-mechanical slider model to quantitatively describe the crumpling and self-assembling of 2-D material sheets suspended in liquid droplets prior by liquid evaporation. An equivalent evaporation pressure model that takes account of capillary force, vapor pressure, gas pressure, vapor recoil pressure and capillary flow-induced force is developed to unify the driving force of crumpling and assembling 2-D materials by liquid evaporation. In the theoretical model of rotational spring-mechanical slider, rotational spring model is introduced to describe the out-of-plane large deformation of 2-D material sheets and the mechanical slider is developed to take account of van der Waal binding energy in overlaps of both self-folding deformation of individual sheets and self-assembly among multiple sheets. Both of them are correlated with the continuum mechanics model of self-folding deformation of 2-D sheets and the associated parameters are determined with the help of energy analysis. Further, the extended network mechanics model composed multiple pairs of rotational spring-mechanical slider and inter-layer mechanical slider is developed to understand the energy competition between crumpling and self-assembling deformation and is used to determine the critical evaporation conditions and geometric features of 2-D sheets toward successful assembly of stable particles after complete evaporation of liquid. Besides, the energy of final assembled particles after the complete evaporation of liquid is formulated to predict the surface morphology and size.

To validate the proposed theoretical model, we have developed a coarse-grained molecular dynamics (CGMD) model for 2-D material sheets and also proposed a computational procedure to simulate solid-liquid interactions through a virtual spherical force field. The CG model of 2-D materials is well calibrated by comparing with the full-scale atomistic model including stretching, bending and adhesive deformation with a focus on their corresponding energy. The virtual spherical force field is applied to the CG model of 2-D materials through the well-defined decreasing rate of spherical radius to mimic an evaporation process of liquid at an elevated temperature and is confirmed with good agreement with full-scale simulations on solid-liquid interactions. Comprehensive CGMD simulations were performed to reveal the effect of geometric shape, number, size and area of 2-D material sheets on their evolution of energy and morphology during crumpling and assembling by liquid evaporation and show remarkable agreement with theoretical predictions. In particular, the transition between crumpling and assembling deformation when evaporation conditions and geometric features of 2-D materials change are well captured by the theoretical analysis of the proposed rotational spring-mechanical slider model. More importantly, good agreement between simulations and theoretical predictions on both overall size and accessible area of assembled stable particle after complete evaporation of liquid is obtained, and both of them are also in a good consistency with independent experimental results in literatures.

It is envisioned that the developed mechanics scheme of rotational spring-mechanical slider model will advance our understanding of large deformation, instabilities and self-assembly of 2-D nanomaterials under dynamic solid-liquid interaction environments, and could also be extended to study liquid evaporation-induced deformation of a broad variety of nanomaterial such as lipid members, nanowires, and nanofibers and beyond 2-D nanomaterials. In addition, the theoretical model and computational procedure at the large scale are expected to shed immediate light on controlling the overall size and morphology of 2-D nanomaterials-based crumpled particles made by aerosol processing. It should also be useful for guiding the printing process of 2-D materials for applications in high-performance electrodes, supercapacitors, and sensors, where large deformation, instabilities, and self-assembly of 2-D nanomaterials are expected by liquid evaporation of droplet on substrates.

Chapter 4 Liquid Evaporation-driven Crumpling and Assembling of 1-D/2-D Hybrid Materials

4.1 Overview of the Chapter

In this chapter, guided by both theoretical predictions and large-scale molecular dynamics simulations together with the independent experimental validations, we report the synthesis of crumpled composite particles comprised of graphene and carbon nanotubes (CNTs) by solution evaporation. We propose comprehensive kinetic diffusion models of graphene and CNTs in the liquid solution at both the equilibrium and liquid evaporation stage. The theoretical analysis shows that the graphene will prefer to accumulate at the liquid/air interface while the CNTs will stay inside the liquid droplet during the liquid evaporation. Further, we develop a virtual spherical van der Waal force field to mimic interactions of liquid to both graphene and CNTs and establish a coarse-grained molecular dynamics model to simulate the crumpling and assembling of CNTs and graphene by liquid evaporation and to reproduce the generation of the CNTs-encapsulated crumpled graphene assembled nanoparticles. The underlying mechanism is fully elucidated by monitoring the structural evolution of the assembled nanoparticles with liquid solution evaporation. The accessible area, 3-D interconnected network, crumpling ridge density in assembled particles and particle size are also extracted. In particular, these structural morphologies are correlated with electrical conductance and mechanical strength and show good agreement with both theoretical predictions and independent experiments.

4.2 Theoretical Framework

4.2.1. Diffusion model of graphene and CNT in the liquid droplet

Figure 4.1 illustrates a suspension of mixed graphene and CNTs inside a liquid droplet with a radius R_d. Assume the graphene and CNTs are dispersed uniformly in the region $[r, R_d]$, where r is the local radial coordinate originating from the geometric center of the droplet, and $[0, r]$ represents the pure liquid region, the total energy of the system at equilibrium is $E_t = E_{ele} +$

$E_{vdW} + E_{def} + E_{surf}$. E_{ele} is the electrostatic energy of the system and can be estimated by the Derjaguin-Landau-Verwey-Overbeek (DLVO) theory [187, 188], E_{vdW}, E_{def} and E_{surf} are van der Waals energy, mechanical deformation energy and surface energy of graphene and CNTs, respectively[189, 190], and they all can be theoretically determined. The DLVO theory includes both the van der Waals energy and electrostatic energy of graphene (E_{vdW}^{g} and E_{ele}^{g}) and CNTs (E_{vdW}^{c} and E_{ele}^{c}). At the same time, unlike the rigid particles in colloidal science, both graphene and CNTs will subject to large deformation during the evaporation and thus the deformation energy of graphene (E_{def}^{g}) and CNT (E_{def}^{c}) will need to be considered. As a result, the total system energy is

$$E_t = E_{def} + E_{vdW} + E_{ele} + E_{surf} \tag{4.1}$$

where $E_{def} = E_{def}^{g} + E_{def}^{c}$, $E_{vdW} = E_{vdW}^{g} + E_{vdW}^{c}$, $E_{ele} = E_{ele}^{g} + E_{ele}^{c}$ and $E_{surf} = E_{surf}^{g} + E_{surf}^{c} + E_{surf}^{l}$. E_{surf}^{g}, E_{surf}^{c} and E_{surf}^{l} are the surface energy of graphene, CNT and liquid, respectively.

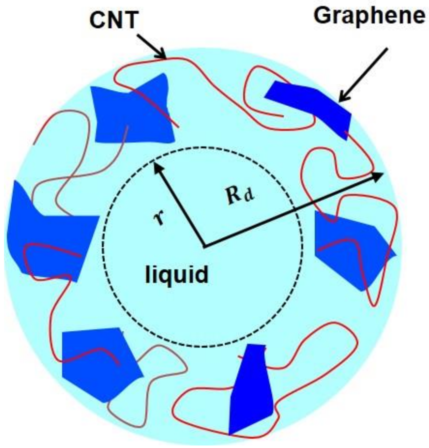

Figure 4.1. Schematics of graphene/CNTs suspended inside a liquid droplet. R_d is the radius of droplet and r is the local coordinate originating from the center of the droplet.

4.2.1.1 Diffusion of graphene in a liquid droplet

Assume there is a uniform distribution of graphene sheets in the region of $[r, R_d]$, and each graphene sheet is equal-sized and in square shape, the inter-layer distance can be calculated based on two principles. One is the volume-averaged distance via

$$d_g^v = \left(\frac{V_d}{n_g}\right)^{\frac{1}{3}} \tag{4.2}$$

where $V_d = 4\pi(R_d^3 - r^3)/3$ and n_g is the number of graphene sheets. The other is the area-averaged distance via

$$d_g^a = \left(\frac{A_d}{n_g}\right)^{\frac{1}{2}} \tag{4.3}$$

where $A_d = 4\pi((R_d + r)/2)^2$. The interlayer distance between graphene (**Figure 4.2a**) can be determined by

$$d_g = max[d_g^v, d_g^a] \tag{4.4}$$

To calculate the deformation energy of graphene, we assume that graphene sheets immersed in the liquid have no deformation and only when graphene sheets have immigrated to the surface of the liquid, significant deformation will be considered. The area of graphene sheets on the liquid surface can be calculated by

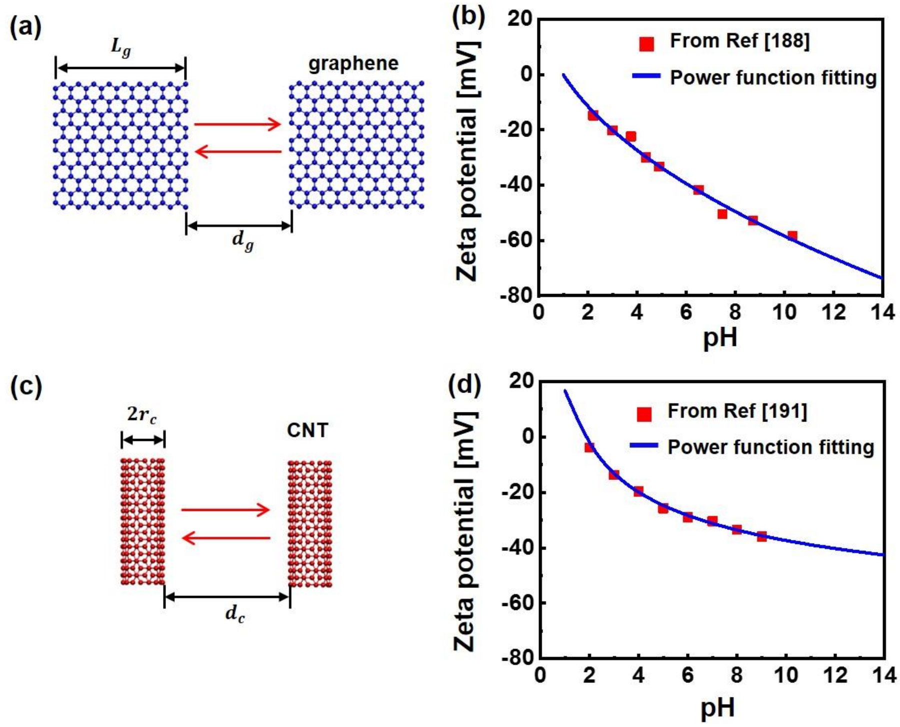

Figure 4.2. (a) Schematics of the interaction and inter-layer distance between graphene sheets. **(b)** pH-dependent zeta potential (ξ) of graphene from experiments[188] and its power function fitting. **(c)** Schematics of the interaction and inter-strip distance between CNT strips. **(d)** pH-dependent zeta potential (ξ) of CNT from experiments[191] and its power function fitting.

$$A_{def} = \begin{cases} 0, l_g < R_d - r \\ A_g^t \left(1 - \frac{R_d - r}{L_g}\right), L_g \geq R_d - r \end{cases} \tag{4.5}$$

where $L_g = \sqrt{A_g}$ is the size of graphene sheet and $A_g = A_g^t / n_g$ is the area of a single graphene sheet. A_g^t is the total area of graphene sheets and can be calculated based on the size of the droplet (R_d) and concentration of the solution (C_t) via

$$A_g^t = \frac{4\pi C_t R_d^3}{3\rho_g} \tag{4.6}$$

where ρ_g is the area mass density of graphene (e.g. ρ_g=7.621× 10^{-7}kg/m^2 for single-layer graphene).

The deformation energy of graphene is

$$E_{def}^g = A_{def} E_{def}^\rho \tag{4.7}$$

where E_{def}^ρ is the deformation energy density when graphene sheets are on the liquid surface and can be determined by our spring-slider mechanics model (See **Chapter 3** or Ref[192]). The van der Waals energy of graphene is

$$E_{vdW}^g = \gamma_b^g \frac{A_g^t}{2} \tag{4.8}$$

where γ_b^g is the binding energy density and is[193]

$$\gamma_g^b = 2\pi \rho_c^2 \varepsilon_{c-c} \sigma_{c-c}^2 \left(\frac{2\sigma_{c-c}^{10}}{5d_g^{10}} - \frac{\sigma_{c-c}^4}{d_g^4}\right) \tag{4.9}$$

where $\rho_c = 4/3\sqrt{3} l_c^2$ is the area density of carbon atoms in hexagonal lattice and l_c is the length of C-C bond without deformation. ε_{c-c}=0.00239 eV and σ_{c-c}=0.3415 nm are the potential well depth and parameter related to the equilibrium distance between different beads in the 12-6 L-J potential.

The electrostatic energy of graphene is

$$E_{ele}^g = \gamma_g^e \frac{A_g^t}{2} \tag{4.10}$$

where γ_g^e is the electrostatic energy per unit area and is a function of distance d_g, which is

$$\gamma_g^e = \frac{2\sigma^2}{\varepsilon\varepsilon_0} \kappa^{-1} exp(-\kappa d_g) \tag{4.11}$$

where ε_0 is the permittivity of vacuum, ε is the dielectric constant of the solvent, κ is the inverse of Debye length, and

$$\kappa^{-1} = \sqrt{\frac{\varepsilon\varepsilon_0 k_B T}{2N_A e^2 I}} \tag{4.12}$$

k_B is the Boltzmann constant, T is the absolute temperature, N_A is the Avogadro number, e is the elementary charge, and I is the ionic strength of the solution and will be kept at $I = 1 \times 10^{-2}$ mol/L through the analysis. σ is the surface charge density and can be calculated based on the zeta potential[188]

$$\sigma = \frac{4k_B T}{e} arctanh\left[exp(\kappa d_{Stern})\, tanh\left(\frac{e\xi}{4k_B T}\right)\right] \tag{4.13}$$

where d_{Stern}=0.7 nm is the Stern layer thickness and ξ is the zeta potential. Zeta potential (in the unit of mV) is pH-dependent and can be obtained in experiments. Based on the experimental data[188], the zeta potential of graphene can be expressed in the form of

$$\xi = a(pH)^b + c \tag{4.14}$$

where a=-28.66, b=-0.4822 and c=28.55 (**Figure 4.2b**).

The surface energy of the system is

$$E_{surf}^{g} = 2\left(A_g^t - A_{def}\right)\gamma_g^{ls} + \left(A_l^{surf} - A_{def}\right)\gamma_l + A_{def}\gamma_g^s \tag{4.15}$$

where γ_g^s is the surface energy density of graphene, γ_l is the surface tension of liquid, γ_g^{ls} = γ_g^s - $\gamma_l\, cos(\theta_c)$ and θ_c is the contact angle of the liquid on graphene surface. A_l^{surf}=$4\pi R_d^2$ is the surface area of liquid droplet.

4.2.1.2 Diffusion of CNTs in a liquid droplet

The deformation of CNTs during packing is bending dominant, and the resultant deformation energy is

$$E_{def}^{c} = \frac{B_c}{2}\int R^{-2}(s)ds \tag{4.16}$$

where B_c is the bending stiffness of CNTs and R is the local radius of curvature of CNTs. Assume CNTs are packed into s shape of helix[190], and the geometry is a stacking of hoops with radius R. With this assumption, the deformation energy can be written as[194]

$$E_{def}^{c} = \pi B_c \sum_i \frac{N(R_i)}{R_i} \tag{4.17}$$

where $N(R_i)$ is the number of loops that are packed at the radius R_i. It can be further converted into

$$E_{def}^{c} = \frac{\pi B_c}{\sqrt{3}d_c/2}\int_{r}^{R_d}\frac{N(R\prime)}{R\prime}dR' \tag{4.18}$$

where d_c is the spacings between packed CNTs. Especially, when CNTs are packed in a sphere, we have

$$N(R') = \frac{\pi R\prime}{d_c} \tag{4.19}$$

And the deformation energy becomes

$$E_{def}^{c} = \frac{2\pi^2 B_c}{\sqrt{3}d_c^2}(R_d - r) \tag{4.20}$$

The inter-strip distance between CNTs is (**Figure 4.2c**)

$$d_c = 2\pi\sqrt{\frac{R_d^3 - r^3}{3\sqrt{3}L_c^t}} \tag{4.21}$$

L_c^t is the total length of CNTs in the liquid droplet and can be calculated based on the size of the droplet (R_d) and concentration of the solution (C_t), which is

$$L_c^t = \frac{4\pi C_t R_d^3}{3\rho_c} \tag{4.22}$$

where ρ_c is the line mass density of CNT (e.g. ρ_g=3.2499× 10^{-15}kg/m for (10,10) CNT). Substituting d_c into Eq. (4.20), the deformation energy can also be written as

$$E_{def}^{c} = \frac{3B_c L_c^t}{R_d + R_d r + r^2} \tag{4.23}$$

Based on d_c, the van der Waals energy among packed CNT strips is

$$E_{vdW}^{c} = 3\gamma_c^b L_c^t \tag{4.24}$$

where γ_c^b is the van der Waals energy per unit length[193] and is a function of distance d_c,

$$\gamma_c^b = 2\pi\rho_c^2\varepsilon_{c-c}\sigma_{c-c}^2\left(\frac{2\sigma_{c-c}^{10}}{5h_c^{10}} - \frac{\sigma_{c-c}^4}{h_c^4}\right)\pi d_c \tag{4.25}$$

The electrostatic energy of CNTs is[194]

$$E_{ele}^{c} = 3\gamma_c^e L_c^t \tag{4.26}$$

where γ_c^e is the electrostatic energy per unit length and is a function of distance d_c

$$\gamma_c^e = \frac{2\sigma^2\pi r_c}{\varepsilon\varepsilon_0}\kappa^{-1}\,exp(-\kappa d_c) \tag{4.27}$$

Similar to graphene, Zeta potential (in the unit of mV) is pH-dependent and can be obtained in experiments. Based on the experimental data[191], the zeta potential of CNTs can be expressed in the form of

$$\xi = a(pH)^b + c \tag{4.28}$$

where a=108.2, b=-0.3005 and c=-91.55 (**Figure 4.2d**).

The surface energy of the system is

$$E_{surf}^{c}=2\pi r_c(L_c^t-L_c^s/2)\gamma_c^{ls}+\left(A_l^{surf}-2r_cL_c^s\right)\gamma_l+\pi r_cL_c^s\gamma_g^s \tag{4.29}$$

where γ_c^s is the surface energy density of CNTs, γ_l is the surface tension of liquid, γ_c^{ls}=γ_c^s-$\gamma_l\,cos(\theta_c)$ and θ_c is the contact angle of the liquid on CNT surface. $L_c^s=\frac{4\pi^2}{3\sqrt{3}d_c^2}\left[R_d^3-\left(R_d-\sqrt{3}d_c/2\right)^3\right]$ is the packing length of CNTs on the outmost layer.

Take R_d=150 nm, the total mass concentration of graphene and CNTs in the liquid droplet, C_t=4 mg/mL, the mass fraction of graphene over the total mass, m_g/m_t=50%, and liquid solution pH=7 as an example, **Figure 4.3a** shows the normalized total system energy $(E_t^r-E_t^{r=0})/E_t^{r=0}$ versus r/R_d, where $E_t^{r=0}$ represents the energy of the system with uniformly suspended graphene or/and CNTs. Especially, when only CNTs are suspended in the droplet, $(E_t^r-E_t^{r=0})/E_t^{r=0}$ shows a monotonic increase with r/R_d, indicating an energy barrier that prevents CNTs from diffusing toward the outmost surface of the droplet. Besides, the larger radius of CNTs is, the higher the energy barrier will be because of an increased bending stiffness. As a result, the CNTs are expected to stay inside the droplet at equilibrium. By contrast, when graphene sheets are suspended in the droplet, $(E_t^r-E_t^{r=0})/E_t^{r=0}$ increases

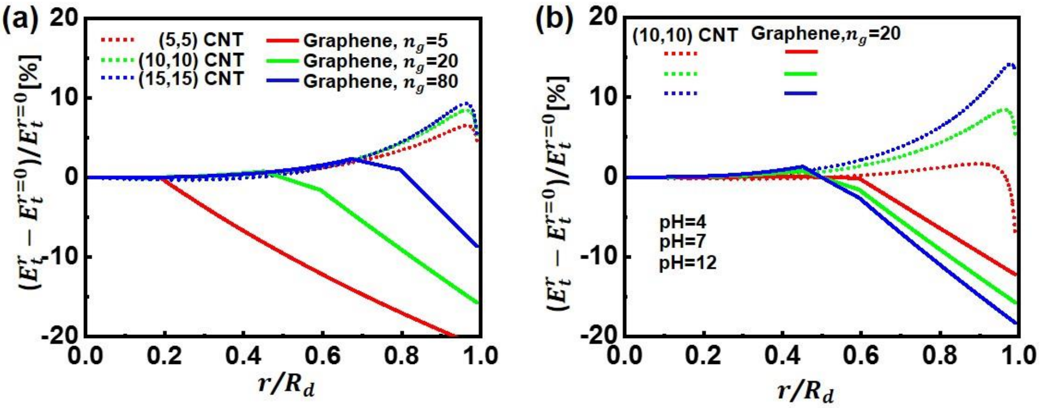

Figure 4.3. Kinetic diffusion model of CNTs/graphene in a liquid droplet. (a) The normalized total system energy $(E_t^r-E_t^{r=0})/E_t^{r=0}$ for different sizes of CNTs and graphene sheets at pH=7. $E_t^{r=0}$ represents the energy of system uniformly filled by graphene or CNTs without pure liquid region ($r=0$). The geometric shape of graphene is square with a total area of 37100 nm^2 and n_g is the number of graphene sheets. The total number of CNTs is 8 and the length of each CNTs, is 2172.5 nm for (5,5) CNTs, 1087.5nm for (10,10) CNTs, and 725 nm for (15,15) CNTs. **(b)** Effect of pH on the normalized total system energy $(E_t^r-E_t^{r=0})/E_t^{r=0}$.

with the increase of r/R_d for graphene sheets with small areas, similar to that of CNTs. For large-area graphene, $(E_t^r - E_t^{r=0})/E_t^{r=0}$ shows a decrease with the increase of r/R_d, indicating that large graphene sheets prefer to stay on the surface of droplet while small ones will stay inside the liquid droplet, which agrees well with experimental observations [151, 195]. This size-dependent diffusion behavior of graphene sheets can be explained by the energy competition between electrostatic energy and surface energy and can also be well captured by the energy-based analytical model. In addition, the pH of liquid solution could affect the diffusion behavior of graphene and CNTs (**Figure 4.3b**). For example, at pH=12, there is a large energy barrier preventing graphene sheets from migrating to the droplet surface. When pH decreases to as low as 4, the energy barrier diminishes, which energetically leads to the diffusion of graphene sheets to the outmost surface of the droplet. This pH-dependent behavior provides an option to tune the position of graphene in the dispersion and is also confirmed in the experiments[195]. For CNTs, regardless of size, there is always preferable in energy to support their stay inside of droplet. In practice, size of graphene sheets in experiments is always beyond hundreds of nanometers[182], therefore, the graphene sheets usually stay at the surface of droplet while CNTs stay inside the droplet with a uniform distribution, as observed in experiments[196]. More importantly, depending on the total mass concentration of graphene

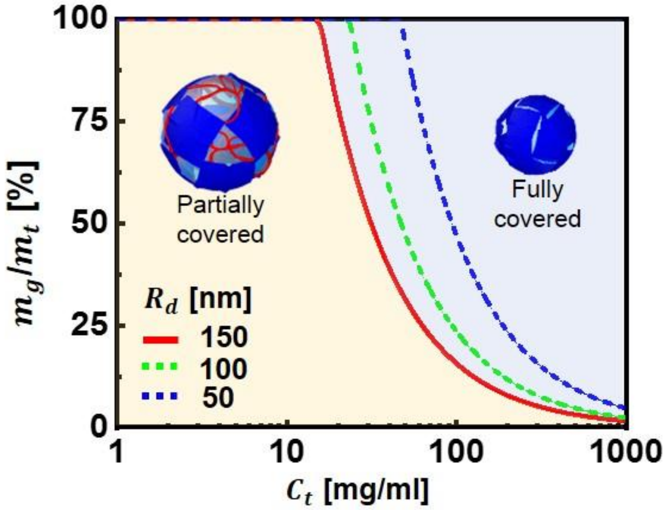

Figure 4.4. Phase diagram of surface status of liquid droplet under the mass fraction of graphene over the total mass of CNTs and graphene m_g/m_t and concentration of graphene/CNTs mixture (C_t) at different size of droplet.

and CNTs, ($C_t = m_t/V_d$, $m_t = m_g + m_c$ and V_d=$4\pi R_d^3/3$), mass fraction of graphene ($\emptyset = m_g/m_t$), and radius of the droplet (R_d), the immigration of graphene sheets to the outmost surface of droplet would lead to a transition of the liquid surface from "partially-covered" to "fully-covered" status by graphene at equilibrium or subsequent evaporation of liquid. The critical transition condition can be determined by $\emptyset C_t V_d/\rho_g$=A_d, where ρ_g is the mass density of graphene per area (e.g. ρ_g=7.621× 10^{-7}kg/m^2 for single-layer graphene), and A_d=$4\pi R_d^2$ is the surface area of liquid droplet. **Figure 4.4** plots the variation of this critical transition with m_g/m_t and C_t for different droplet sizes. A low C_t will benefit the initial formation of "partially-covered" status and a large droplet size will promote the transition from "partially-covered" to "fully-covered" status. This transition variation will also hold during the liquid evaporation. For example, when the liquid evaporation occurs, m_g/m_t will keep a constant while R_d will decrease, and thus the total mass concentration C_t will increase, which results in a transition of the liquid surface from "partially-covered" to "fully-covered" status.

4.2.2 Theoretical model of CNTs packing by liquid evaporation

In this section, we will propose the mechanics model to predict the radius of particles by packing pure CNTs. It is expected that the total energy during CNTs packing $E_{tot}^c \propto 1/R_d$, where R_d is the radius of droplet (**Figure 4.5a**). To predict the size of the particle after complete evaporation of liquid, we neglect the influence of liquid so that the electrostatic energy and surface energy will not be considered here and there are only three energies need to be considered, the deformation energy E_{def}^c due to the packing of CNTs, the vdW energy between packed CNTs E_{vdW}^c and the potential energy of packed CNTs with respect to the center of liquid droplet due to the existence of driving forces E_{pt}^c. As a result, the total energy of the system will become

$$E_{tot}^c = E_{def}^c + E_{vdW}^c + E_{pt}^c \tag{4.30}$$

The packing spacings between CNTs strips will be the equilibrium distance d_c^e by minimizing Eq. (4.25) and the binding energy density will be the corresponding Γ_c^{min}. Given the total length of CNTs L_c^t, and the equilibrium packing spacings d_c^e, the inner packing radius of CNTs is

$$R_{in} = \left(\frac{R_d^3 - 3\sqrt{3} d_c^{e2} L_c^t}{4\pi^2}\right)^{1/3} \tag{4.31}$$

The number of packing layer is

$$N_l = \frac{R_d - R_{in}}{\sqrt{3} d_c^e / 2} \tag{4.32}$$

and the maximum possible number of packing layer is

$$N_{max} = \frac{R_d}{\sqrt{3} d_c^e / 2} \tag{4.33}$$

Substituting R_{in} with r in Eq. (4.23), the deformation energy becomes

$$E_{def}^c = \frac{3 B_c L_c^t}{R_d^2 + R_d R_{in} + R_{in}^2} \tag{4.34}$$

The van der Waals energy is

$$E_{vdW}^c = 3 (N_l / N_{max})^\eta \, L_c^t \Gamma_c^{min} \tag{4.35}$$

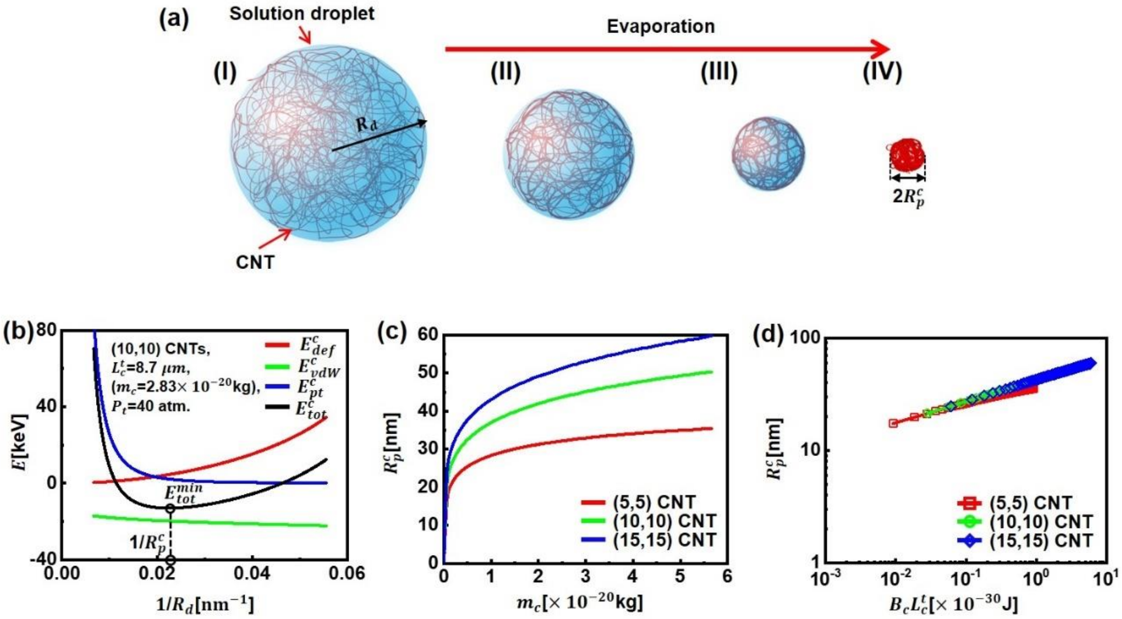

Figure 4.5. (a) Schematics show the packing of CNTs inside the liquid droplet during liquid evaporation. R_d is the radius of the liquid droplet. R_p^c is the radius of CNT particle after complete evaporation. **(b)** Energy variation of CNTs packing during liquid evaporation. The total length of CNT L_c^t=8.7 μm, w/ (10,10) CNT and P_t=40 atm. E_{tot}^{min} is the minimum total system energy and packing will stop at this point. **(c)** Variation of R_p^c with the mass and radius of CNTs. **(d)** The unified linear relationship between R_p^c and $B_c L_c^t$.

where the coefficient of 3 accounts for six (divide 2 to avoid double counting) nearest neighbor

CNT strands for perfectly surrounded strands, and $(N_l/N_{max})^{\eta}$ accounts for the ratio of CNT strands perfectly surrounded by other strands and η=1/25. The potential energy is

$$E_{pt}^{c} = \eta P_t \pi r_c L_c^s R_d \tag{4.36}$$

where $L_c^s = \frac{4\pi^2}{3\sqrt{3}d_c^{e2}}\left[R_d^3 - \left(R_d - \sqrt{3}d_c^e/2\right)^3\right]$ is the packing length of CNTs on the outmost layer. **Figure 4.5a** illustrates the schematics of CNT packing during liquid evaporation and **Figure 4.5b** plots the variation of energies for (10,10) CNT at a total length of L_c^t=8.7 μm (total mass m_c=2.83× 10^{-20}kg) under P_t=40 atm with the surface curvature of the droplet $1/R_d$. The minimum point of E_{tot}^c can be identified and the corresponded size of packed CNT particle R_p^c can be obtained. **Figure 4.5c** further plots the variation of R_p^c with the mass and radius of CNT. To unify the relationship between R_p^c and length and radius of CNTs, **Figure 4.5d** plots the variation of R_p^c with $B_c L_c^t$, and a linear relationship can be observed regardless of the length and radius of CNTs.

4.2.3 Theoretical predictions of the hybrid particles' size

With the size of pure CNT particles R_p^c and pure graphene particles R_p^g (can be predicted based on the analysis in Section 3.2.4), Here, we define the size of graphene/CNTs hybrid particles as

$$R_p^h = \left(R_p^c\right)^{1-\emptyset_g}\left(R_p^g\right)^{\emptyset_g} \tag{4.37}$$

where $\emptyset_g$=m_g/m_t and $m_t = m_c + m_g$.

4.2.4 Theoretical predictions of the particles' surface pore ratio

The surface pore ratio is defined by dividing the surface area not covered by graphene sheets (pore, A_p^p) over the total surface area of the crumpled particle (A_p^h) and it is

$$P_r = \frac{A_p^p}{A_p^h} \tag{4.38}$$

From the definition and considering $A_p^h = A_p^p + A_p^g$, surface pore ratio P_r can be characterized by A_p^g/A_p^h, where A_p^g=$4\pi\left(R_p^g\right)^2$ and A_p^h=$4\pi\left(R_p^h\right)^2$ are the surface area of particles assembled by pure CNTs and hybrid CNTs and graphene, respectively. Note that, at

R_p^g/R_p^h=0, there is no graphene on the surface, and P_r=100 %; at $R_p^g/R_p^h \geq$1, the CNTs are fully encapsulated by graphene, and P_r=0. When $0 < R_p^g/R_p^h$ <1, the particle surface will be partially covered by graphene, as a result, we will have P_r =1- $\left(R_p^g/R_p^h\right)^2$ and R_p^g/R_p^h represents the crumpling intensity. In theory, the surface pore ratio can be obtained via

$$P_r = \begin{cases} 1-\left(\frac{R_p^g}{R_p^h}\right)^2, R_p^g < R_p^h \\ 1, R_p^g \geq R_p^h \end{cases} \tag{4.39}$$

4.2.5 Theoretical predictions of the particles' spatial contacts and specific accessible surface areas

After the size of hybrid CNTs and graphene particles R_p^h is obtained via Eq. (4.37), R_p^h will be used as an "anchor point" on the energy curves in **Figures 3.12a** and **4.5b**. The procedure to get the accessible area of the hybrid particles are as follows,

(1) E_{vdW}^{c-c}: The location of $1/R_p^h$ on the horizontal coordinate of the energy curves for CNTs packing (e.g. **Figure 4.5b**) will be determined, then the corresponded E_{vdW}^c will be obtained at $1/R_p^h$, which is E_{vdW}^{c-c} in theory.

(2) E_{vdW}^{c-g}: The packing length on the outmost layer of packed CNT can be obtained by $L_c^s = \frac{4\pi^2}{3\sqrt{3}d_c^{e2}}\left[\left(R_p^h\right)^3 - \left(R_p^h - \sqrt{3}d_c^e/2\right)^3\right]$, then $E_{vdW}^{c-g} = \pi r_c L_c^s \gamma_{c-g}$.

(3) E_{vdW}^{g-g}: Firstly, calculate the corresponded potential energy E_{pt}^g at $R_p^g = R_p^h$ via $E_{pt}^{g-h} = R_p^h A_g^t P_t$. Then the horizontal coordinate $1/R_d$ when $E_{pt}^g = E_{pt}^{g-h}$ can be determined and denoted as $1/R_p^h$. Finally the value of E_{vdW}^g can be obtained at $1/R_p^h$, which is E_{vdW}^{g-g} in theory.

After these energies are obtained, the contact area can be calculated via[18]

$$A_{contact}^{c-c} = \pi r_c E_{vdW}^{c-c}/3\gamma_b^C \tag{4.40}$$

where r_c is the radius of CNT and γ_b^{CNT} is the binding energy density between parallel CNTs.

Similarly,

$$A_{contact}^{c-g} = \pi r_c E_{vdW}^{c-g} / \gamma_b^{C-G} \tag{4.41}$$

where γ_b^{C-G} is the binding energy density when CNT is in contact with graphene. And

$$A_{contact}^{g-g} = E_{vdW}^{g-g} / \gamma_b^{G} \tag{4.42}$$

where γ_b^{G} is the binding energy density of overlapped graphene sheets. After the contact area is obtained, the specific contact area can be obtained by $A_{con}^{c-c} = A_{contact}^{c-c}/m_t$, $A_{con}^{c-g} = A_{contact}^{c-g}/m_t$ and $A_{con}^{g-g} = A_{contact}^{g-g}/m_t$, where m_t is the total mass of the particle. The total specific contact area can be obtained by

$$A_{con} = A_{con}^{c-c} + A_{con}^{c-g} + A_{con}^{g-g} \tag{4.43}$$

The accessible area can be obtained by

$$A_{ss} = \begin{cases} A_c + A_g - 2A_{con}^{c-c} - 2A_{con}^{c-g} - 2A_{con}^{g-g}, R_p^g < R_p^h \\ A_g - 2A_{con}^{g-g}, R_p^g \geq R_p^h \end{cases} \tag{4.44}$$

where A_c (=1315 m^2/g for single-walled CNT) is the intrinsic surface area of CNT and A_g (=2630 m^2/g for single-layer graphene) is the intrinsic surface area of graphene.

4.3 Computational Modeling and Methods

4.3.1 Coarse-grained modeling of CNT/graphene interactions

The carbon nanotube (CNT) is modeled by a coarse-grained bead-spring model following the procedures in Section 2.2.2 (**Figure 2.8**). The parameters associated with the bonded interactions are k_θ^{CNT}=3804.1 *kcal/mole* for (5,5) CNT, k_θ^{CNT}=23543 *kcal/mole* for (10,10) CNT, and k_θ^{CNT}=75153 *kcal/mole* for (15,15) CNT when the inter-bead distance d_0^{CNT}=0.5 *nm*. The parameters associated with nonbonded interactions are ϵ_{CNT} =2.0364 *kcal/mole*, σ_{CNT}=0.962 *nm* for (5,5) CNT, ϵ_{CNT}=1.7875 *kcal/mole*, σ_{CNT}=1.5425 *nm* for (10,10), and ϵ_{CNT} =1.7195 *kcal/mole*, σ_{CNT} =2.1229 *nm* for (15,15) CNT. All of these parameters are validated by parallel full-atomic molecular dynamics simulations.

Once the CG model of graphene and CNT are established and validated, the non-bonded van der Waals interaction between graphene beads and CNT beads (**Figure 4.6a**) is modeled by the 12-6 L-J potential via $V(r) = 4\epsilon_{C-G}((\sigma_{C-G}/d)^{12} - (\sigma_{C-G}/d)^{6})$, where ϵ_{C-G} is the potential well depth and σ_{C-G}=r_c+z is the parameter associated with the equilibrium distance between CNT and graphene beads. The non-bonded van der Waals energy can be obtained by $E_{vdW}^{C-G} = \rho_c^2 \int_0^{L_b} V(r)dx$, where $\rho_c = 1/d_0^{CNT}$ is the line density of bead-spring model of CNT

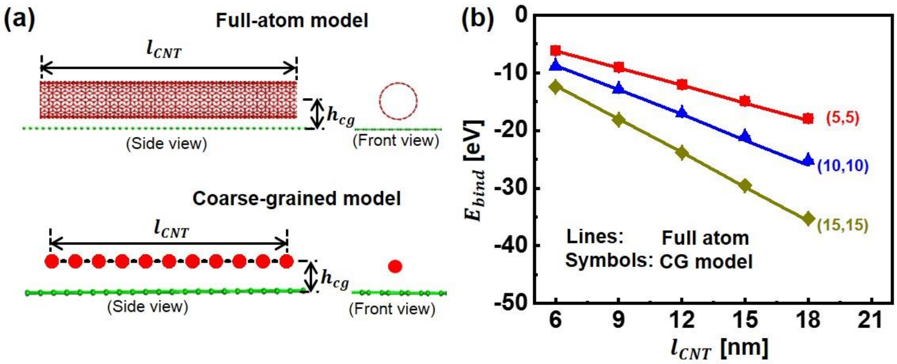

Figure 4.6. (a) Schematics to show full-atom CNT on full-atom graphene and coarse-grained CNT on coarse-grained graphene with a separation distance h_{cg}. **(b)** Comparison of binding energy of CNTs on graphene between full-atom and CGMD simulations.

and L_b is the length of CNT in parallel with graphene. $E_{vdW}^{C-G} = \gamma_b^{C-G} L_b$ leads to the correlation between γ_b^{C-G} and ϵ_{C-G}, where γ_b^{C-G} is the binding energy density of CNT on graphene surface. Such binding energy density can be obtained from the full-atom simulation of CNT on graphene and is γ_b^{C-G}=-0.1616× 10^{-9} *J/m* ((5,5) CNT on graphene), γ_b^{C-G}=-0.2314× 10^{-9}*J/m* ((10,10) CNT on graphene) and γ_b^{CNT}=-0.3133× 10^{-9}*J/m* ((15,15) CNT on graphene). Based on the above analysis, we get ϵ_{C-G}=3.20 *kcal/mole*, σ_{C-G}=0.672 *nm* for (5,5) CNT on graphene, ϵ_{C-G}=1.77 *kcal/mole*, σ_{C-G}=0.961 *nm* for (10,10) CNT on graphene, and ϵ_{C-G}=1.50 *kcal/mole*, σ_{C-G}=1.252 *nm* for (15,15) CNT on graphene. With these parameters, we performed both CGMD and full-atom simulations to validate our CG model. Good agreement is obtained (**Figures 4.6b**).

4.3.2 Virtual spherical van der Waals force field simulation method

The total number of sheets/strips of graphene/CNT is fixed at n_g+n_c=16 in a single droplet and the mass of each sheet/strip is kept the same. The mass fraction ratio m_g/m_t is tuned by changing the number of graphene sheets (n_g) and CNT stripes (n_c) in the droplet (e.g. m_g/m_t=25%, n_g=4, n_c=12; m_g/m_t=50%, n_g=8, n_c=8; m_g/m_t=75%, n_g=12, n_c=4;). Based on these settings, the length of individual CNT strip is L_c=2172.5 *nm* for (5,5) CNT, L_c=1087.5 *nm* for (10,10) CNT and L_c=725 *nm* for (15,15) CNT. At the same time, the graphene sheet is in square shape with a size of L_g=68.1 *nm*. Initially, the CNT strips are generated by the random walk method (RWM)[101] inside a sphere with R_d=150 *nm*, and the graphene sheet is distributed uniformly on the surface of sphere. Further, we introduce a computational method to mimic the interaction of liquid molecules to graphene and CNT by employing a virtual spherical L-J force field (**Figure 4.7a**). The interaction between graphene sheets and the surface of the sphere was modeled by a 12-6 L-J potential to mimic the interaction between liquid droplet and graphene. The cut-off radius of the L-J potential is set as $2^{1/6}\sigma$, so there would be only repulsive forces between graphene sheets and sphere surface and this would not allow penetration of graphene into the sphere. A constant force P_t^g pointing to the center of sphere was added on each bead in graphene to provide a driving force for crumpling and assembling of graphene (enlarged view in **Figure 4.7**a). After the initial generation of CNT strips and graphene sheets, the distribution of CNT beads is non-uniform while the graphene sheets stay on the surface of sphere (see the insets and density distribution of CNT and graphene in **Figure 4.7b**). After that, the system was equilibrated at 300K for t_i=2.0 ns with the NVT ensemble under Nose/Hoover thermostat. During the equilibrium process, the potential well depth in the L-J potential between CNT beads was set equal to the 1/10 of the normal values, so that the attractive force between CNT beads was very weak to mimic the repulsive electrostatic force in the aqueous environment and the CNT strips would start to untangle inside the sphere. This process mimics the dispersion behavior of CNTs strips in the solution. During that, some of the CNT beads might penetrate the surface of sphere, and if this happens, a constant pressure P_t^c pointing to the center of sphere was added on the exposed beads to provide a driving force for the packing of CNT (enlarged view in **Figure 4.7a**). It needs to be clarified that P_t^g and P_t^c may have different values due to different effective area of each bead in the CG model of graphene and CNTs. The equivalent pressure exerted on graphene and CNT should be the same, which is $P_t = P_t^g/A_{bead}^g$=P_t^c/A_{bead}^c, where

A_{bead}^{g}=$3\sqrt{3}(d_0^G)^2/4$ andA_{bead}^{c}=$2d_0^{CNT}r_c$. After the equilibrium, the CNT strips will disperse uniformly inside the sphere while the graphene sheets accumulated on the surface of sphere

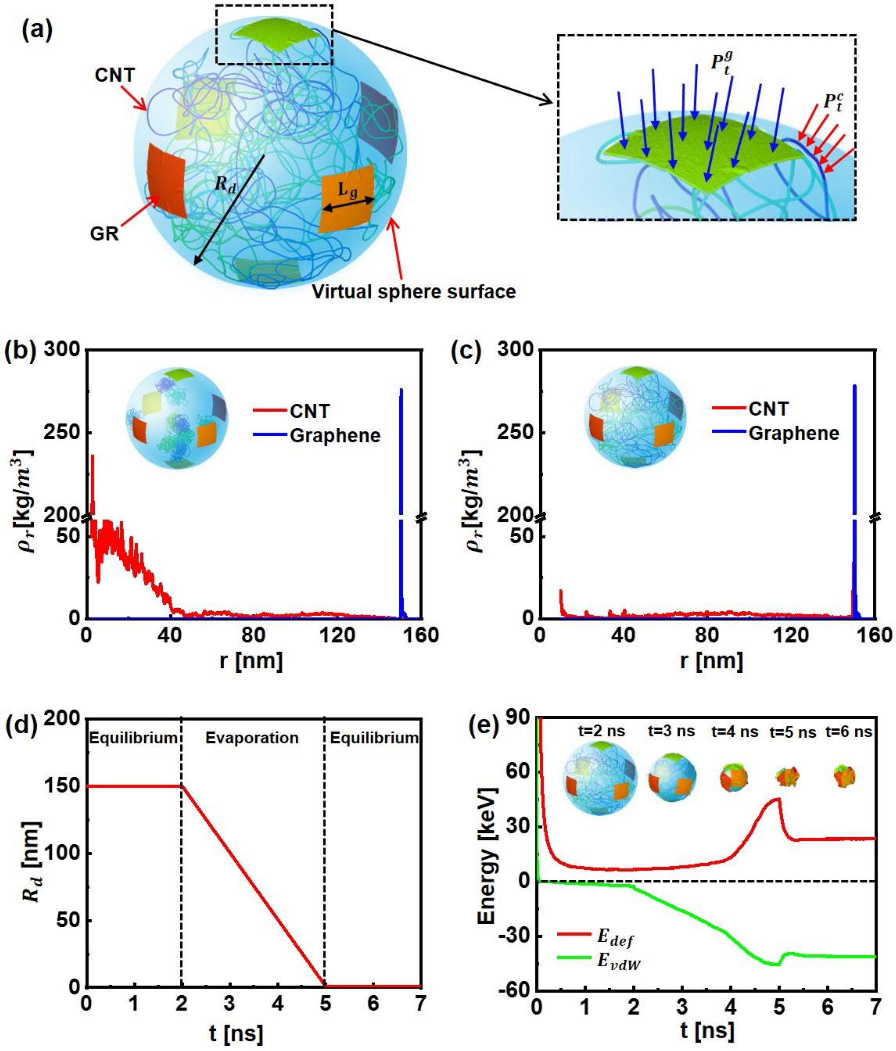

Figure 4.7. Simulation method of the liquid evaporation process. (a) The liquid droplet containing hybrid graphene and CNTs dispersion before liquid evaporation. The CNT strips stay inside the droplet while the graphene sheets stay on the surface of droplet. The liquid droplet is modeled by a virtual force field with a radius R_d. The enlarged figure indicates when graphene/CNTs beads are out of the liquid surface, a constant force P_t^g on the graphene beads and P_t^c on CNT beads will be applied towards the center of liquid. **(b)** The density distribution of CNT and graphene in the droplet after the generation of CNT strips and graphene sheets. **(c)** The density distribution of CNT and graphene in the droplet after equilibrium and before liquid evaporation. **(d)** Variation of the liquid radius with the simulation time. **(e)** Variation of the deformation energy (E_{def}) and van der Waals energy (E_{vdW}) of CNT and graphene during the liquid evaporation. The insets show the snapshots from the CGMD simulations.

(see the insets and density distribution of CNT and graphene in **Figure 4.7c**), which is in good agreement with the analytical analysis. Secondly, all the settings in the first step would remain the same except that the potential well depth in the L-J potential between CNT beads was set back to the normal value, and the radius of virtual sphere started to decrease with time by following a well-defined function to mimic the liquid evaporation process, which is $R_d = R_i + (R_e - R_i)/(t - t_i)/t_e$, $(t_i \leq t \leq t_i + t_e)$, where t is the instantaneous time step during simulation and t_e=3 ns is the time period for the radius of sphere that changes from R_i(initial radius) to R_e(final radius) (**Figure 4.7d**). In the third step, the applied forces were removed from the graphene sheets and CNT strips. Another 2 ns was performed under the NVT ensemble to get the final morphology of hybrid graphene/CNT nanoparticles. During the whole evaporation processes, the coordinates of graphene and CNT beads and energies of CNT strips and graphene sheets were documented to monitor the folding and assembling of CNT strips and graphene sheets (**Figure 4.7e**).

4.3.3 Calculation of particle size, surface pore ratio, spatial contacts, accessible areas, contact probability, surface ridge density and mechanical properties from CGMD simulations

4.3.3.1 Particle size

Once the particle is obtained, a Cartesian coordinate system is established originating at the center of mass of the particle (**Figure 4.8a**). After that, the beads in the particle is projected in the $x - y$ plane (**Figure 4.8b**). Such projection is then be divided into n_s sectors, who share the same apex at the position of the center of mass. The central angle of each sector can be obtained by θ_s=$2\pi/n_s$ (**Figure 4.8b**). The distance of each bead to the center of mass of the particle in a single sector is calculated and the maximum value is selected, which corresponds to the outmost bead in the sector and the distance is denoted as $R_s^{(x-y)i}$ (**Figure 4.8b**). Then the averaged size of particle in the $x - y$ plane can be obtained via

$$R_p^{h(x-y)} = \frac{\sum_{i=1}^{n_s} R_s^{(x-y)i}}{n_s} \tag{4.46}$$

Same procedures are applied in $x - z$ and $y - z$ planes, and the size of the particle is obtained by

$$R_p^h = \frac{R_p^{h(x-y)} + R_p^{h(x-z)} + R_p^{h(y-z)}}{3} \tag{4.47}$$

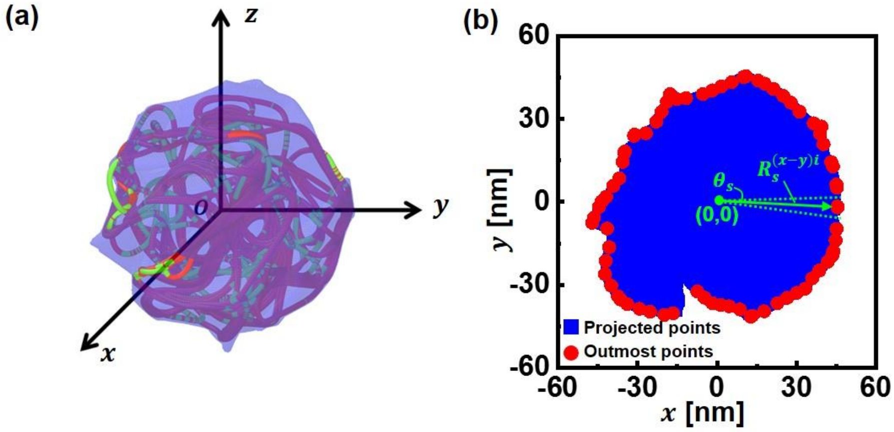

Figure 4.8. Procedure to calculate the radius of fabricated particles. (a) The origin of the coordinate system is moved to the center of the mass of the particle. After that, the projection of the particle is documented and the distance of the outmost beads in the projection on the **(b)**$x-y$ **(c)** $x-z$ and **(d)** $y-z$ plane to the origin of the coordinate system is calculated.

4.3.3.2 Particle surface pore ratio

Once the particle is obtained, a Cartesian coordinate system is established originating at the center of mass of the particle (**Figure 4.9a**). Then an equivalent sphere is plotted with a radius

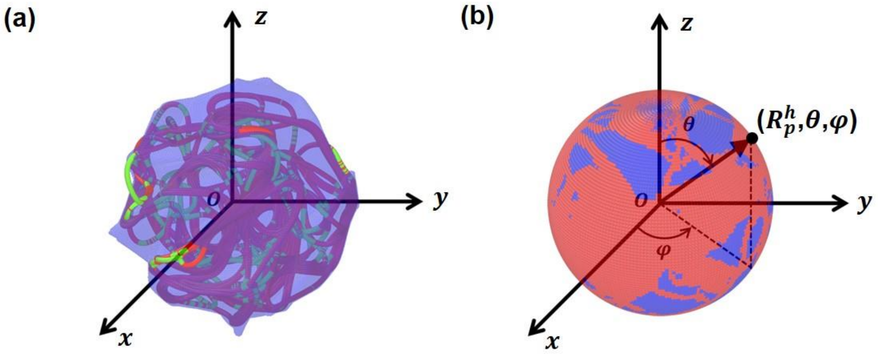

Figure 4.9. Procedure to project the pore/contacts/ridges on the surface of equivalent sphere. (a) The center of mass (COM) of the particle is moved to the origin of the Cartesian coordinate system. **(b)** The distance of beads to the COM of the particle is fixed at R_p^h and its position on the surface of the equivalent sphere is denoted by (R_p,θ,φ) in the spherical coordinate. The pore/contact/ridge is searched within the area $\theta - d\theta/2 < \theta \le \theta + d\theta/2$ and $\varphi - d\varphi/2 < \varphi \le \varphi + d\varphi/2$, in which $d\theta$ and $d\varphi$ are the increment angle on the surface of sphere (e.g. $d\theta = d\varphi = \pi/60$), and if the pore/contact/ridge exists in the area, the bead will be rendered in the specific color (e.g. red), otherwise it will be rendered in another kind of color (e.g. blue).

R_p^h (**Figure 4.9b**). The coordinate of graphene beads in **Figure 4.9a** is converted into the coordinate in **Figure 4.9b**, in which the distance of beads to the center of mass is kept at R_p^h. After that, the Cartesian coordinate (x, y, z) (satisfying $\sqrt{x^2 + y^2 + z^2} = R_p^h$) is transformed into a spherical coordinate (R_p^h, θ, φ), where θ ($\in [0, \pi]$) is the azimuthal angle and $\theta = arccos\frac{z}{\sqrt{x^2+y^2+z^2}}$, φ is the polar angle ($\in [0,2\pi)$) and $\varphi = arctan\frac{y}{x}$. In order to get the pore ratio, a step angle $d\theta$ is introduced. If a graphene bead exists in the range of $\theta - d\theta/2 < \theta < \theta + d\theta/2$ and $\varphi - d\theta/2 < \varphi < \varphi + d\theta/2$, then the sphere surface will be regarded as a graphene surface, otherwise, it will be regarded as a pore. By setting $d\theta = \pi/60$, the sphere surface will consist of 7200 blocks. The pore ratio can be obtained by

$$P_r = \frac{n_h}{7200} \tag{4.48}$$

where n_h is the number of blocks not occupied by graphene beads.

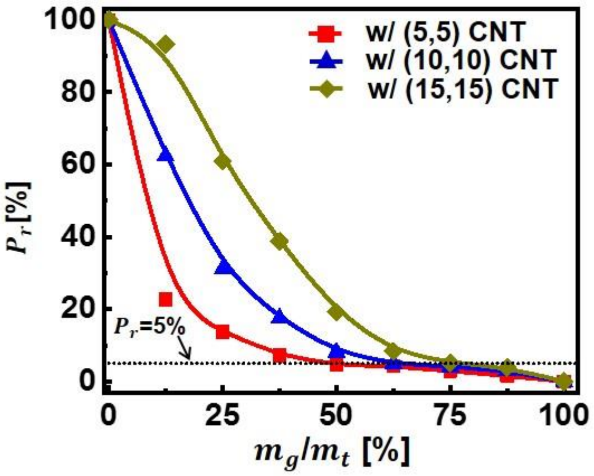

Figure 4.10. Variation of surface pore ratio (P_r) with m_g/m_t and radius of CNTs in the CGMD simulations. P_r=5% is the critical value to determine the particle is closed (<5%) or opened (≥5%).

Figure 4.10 further plots the variation of P_r with m_g/m_t and radius of CNTs. When m_g/m_t is low and CNTs are large, a high pore ratio can be obtained, which represents a particle with open-celled structure. Keep the size of CNT and increase m_g/m_t, the pore ratio will decrease. Finally, when $P_r \leq 5\%$, the surface pore size is small enough and the surface of particles will be sealed by graphene sheets. The particles will exhibit closed core-shell structures. Similarly, keep m_g/m_t and decrease the size of CNTs, the surface pore ratio will also decrease.

4.3.3.3 Spatial contacts and specific accessible surface areas

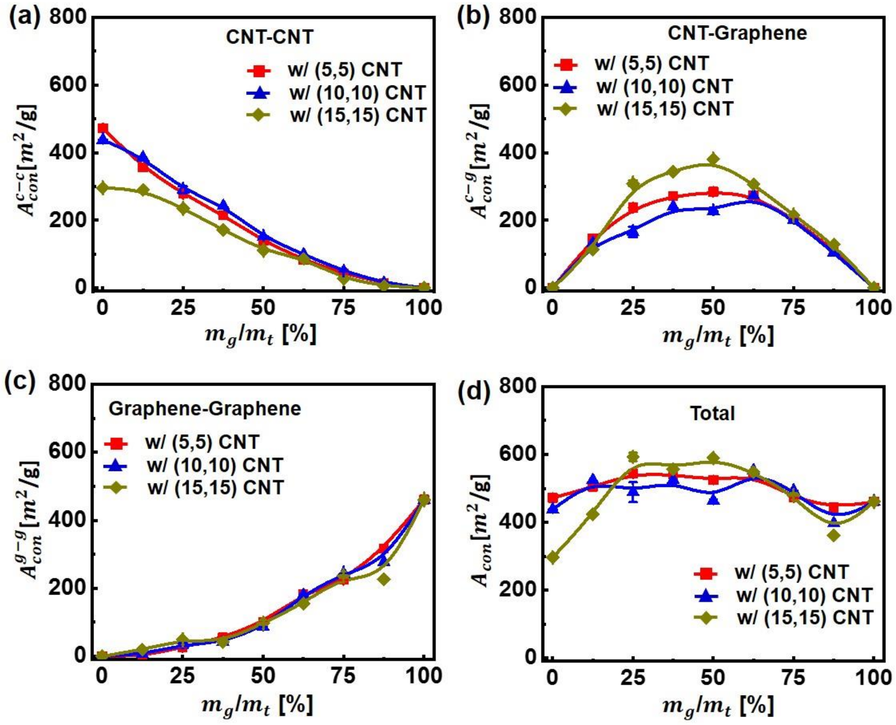

Figure 4.11. Variation of the specific contact area with m_g/m_t and radius of CNTs. The specific contact area between **(a)** CNT and CNT, **(b)** CNT and Graphene, and **(c)** Graphene and Graphene. **(d)** The total specific contact area by summing all of the three types of contacts.

The total van der Waals energy between CNT-CNT (E_{vdW}^{c-c}), CNT-graphene (E_{vdW}^{c-g}), and graphene-graphene (E_{vdW}^{g}) in the fabricated particles is monitored and is converted to contact area following Eqs. (4.40)-(4.42). The specific accessible surface area is obtained following Eq. (4.43). **Figure 4.11** plots the variation of specific contact area with m_g/m_t and types of CNT in the simulations.

4.3.3.4 Contact probability

The van der Waals energy of each CNT bead by surrounding CNT beads is calculated, then the position of CNT beads is transformed on the equivalent sphere as shown in **Figure 4.9b**. Following the same procedure to determine the sphere surface covered/not covered by graphene beads, each block on the sphere surface is distinguished by “contact” or “no contact” based on whether the magnitude of van der Waals energy of the CNT bead is non-zero or not. Then the contact probability between CNT and CNT can be determined by

$$C_p^{C-C} = \frac{n_c^{C-C}}{7200} \tag{4.49}$$

where n_c^{C-C} is the number of blocks with non-zero van der Waals energy. The same procedure can be applied to determine the contact probability between graphene and CNT and between graphene and graphene.

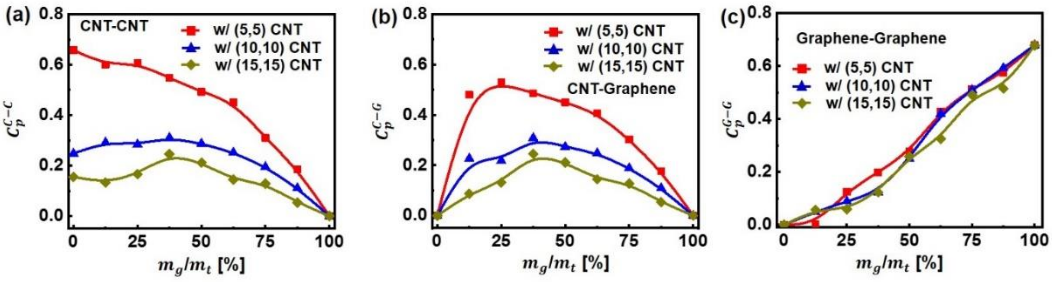

Figure 4.12. Variation of the contact probability with m_g/m_t and radius of CNTs. The contact probability between **(a)** CNT and CNT, **(b)** CNT and Graphene, and **(c)** Graphene and Graphene.

Figure 4.12a plots the variation of contact probability between CNTs and CNTs with m_g/m_t and radius of CNT. It shows a monotonic decrease with the increase of m_g/m_t until reaches zero. At the same time, small CNTs (e.g. (5,5) CNTs) have a higher contact probability with each other than the large CNTs (e.g. (15,15) CNTs). Keep m_g/m_t and increase the size of CNTs, the contact probability also shows a monotonic decrease. **Figure 4.12b** shows the variation of contact probability between CNTs and graphene with m_g/m_t and radius of CNTs. For fixed CNTs size (e.g. (5,5) CNTs), the contact probability shows an increase with m_g/m_t from zero until reaches its maximum, after that, the contact probability starts to decrease until reaches zero when m_g/m_t=100%. Similar trends can also be observed for (10,10) and (15,15) CNTs. Moreover, the larger the sizes of CNTs, the lower of the contact probability between CNTs and graphene. **Figure 4.12c** plots the variation of contact probability between graphene and graphene with m_g/m_t and radius of CNTs. A monotonic increase of contact probability can be observed with m_g/m_t regardless of the size of CNTs.

4.3.3.5 Surface ridge density

The deformation energy on each graphene bead E_{def}^{bead} is calculated, then assuming the deformation energy is generated by the bending of graphene sheets, which is

$$E_{def}^{bead}=\frac{B_g A_{bead}^{g}}{2r_{bead}^{2}} \tag{4.50}$$

where $A_{bead}^{g}=3\sqrt{3}(d_0^{GR})^2/4$ is the area occupied by a single bead, and r_{bead} is the equivalent radius of curvature at the position of the bead. Further, the local curvature can be calculated by

$$\kappa_d=1/\sqrt{\frac{B_g A_{bead}}{2E_{def}^{bead}}} \tag{4.51}$$

If $\kappa_d>0.5nm^{-1}$, the bead will be regarded as a part of ridges. The position of graphene beads is transformed on the equivalent sphere as shown in **Figure 4.9b**. After that, an image processing procedure is implemented to determine the ridge density (**Figure 3.22**). **Figure 4.13** plots the variation of D_r with m_g/m_t and radius of CNTs.

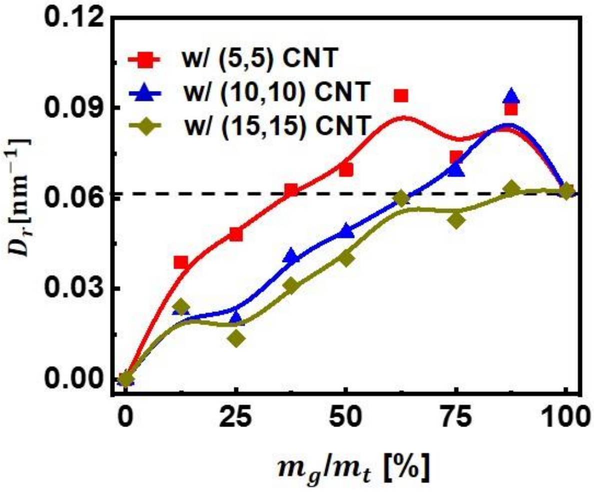

Figure 4.13. Variation of particle surface ridge density (D_r) with m_g/m_t and radius of CNTs in the CGMD simulations.

4.3.3.6 Mechanical properties of particles

Molecular dynamics simulations of uniaxial compression on individual particles were conducted to extract the effective Young's modulus of particles. During the simulation, the particle was sandwiched by two rigid virtual plates (**Figure 4.14a**), where the bottom plate was fixed and the top one was movable to apply the loads. The simulation was conducted under the NVT ensemble at 300K and 1 atm under the Nose-Hoover thermostat. The reactive force along the compressed direction was documented every 10 fs.

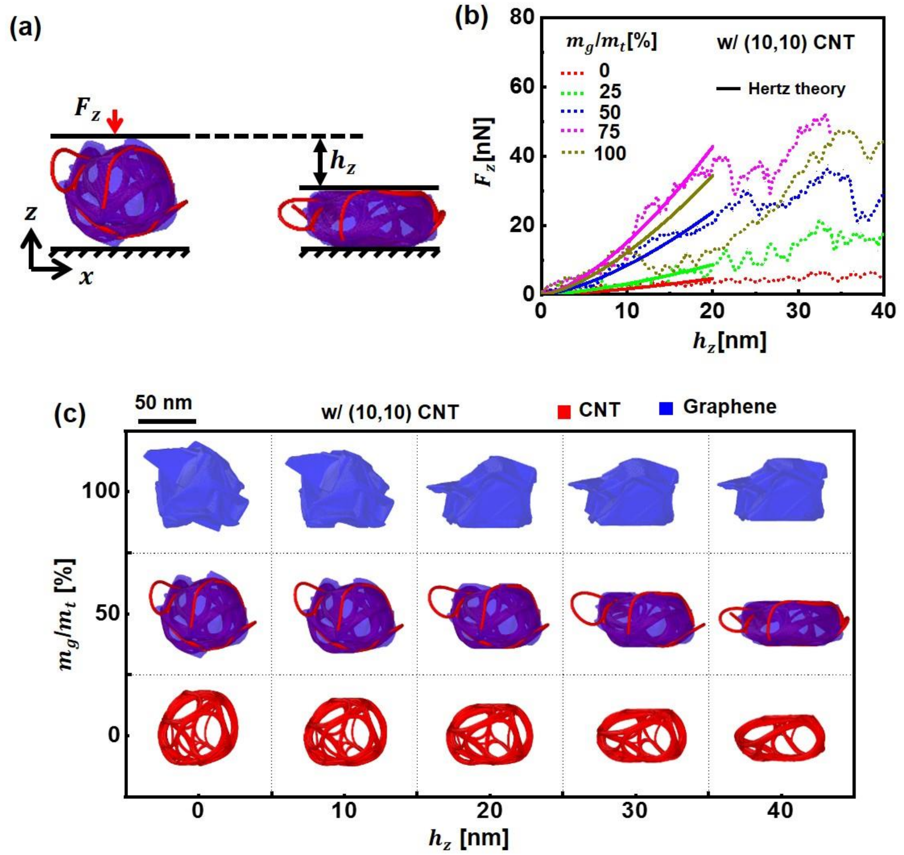

Figure 4.14. **(a)** Molecular dynamics simulation model of the uniaxial compression on a particle. **(b)** Force-displacement curves of the crumpled graphene/(10,10)CNTs particles with different m_g/m_t along the uniaxial compression *z*-direction. **(c)** Simulation snapshots of particles during compression.

Figures 4.14b gives the force-displacement curves of the particles under uniaxial compression on crumpled graphene/(5,5) CNT particles with different m_g/m_t along x, y and z direction, respectively. After the force-displacement curve is obtained, the Young's modulus E_{eff} can be obtained with Hertz contact theory via

$$F = \frac{4E_{eff}\left(R_p^h\right)^{1/2}}{3(1-v^2)}\left(\frac{h}{2}\right)^{\frac{3}{2}} \tag{4.52}$$

where v is the Poisson's ratio and is taken 0.3 [197].

Figure 4.14c shows the simulation snapshots of pure CNTs, hybrid, and pure graphene particles during compression. Local crumpling on graphene surface and buckling in CNTs can be observed during compression.

Figure 4.15a plots the variation of effective Young's modulus of hybrid particles with (10,10) CNTs obtained from the compression test in different directions. The overall effective

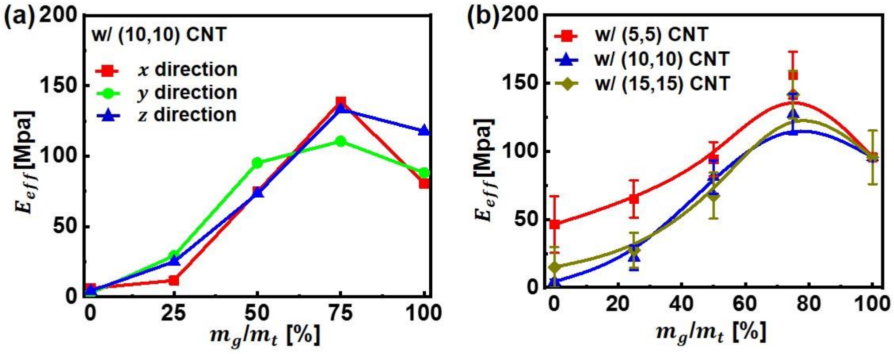

Figure 4.15. (a) Effective elastic modulus of hybrid particles with (10,10) CNTs obtained from the uniaxial compression test in x, y, and z direction.. **(b)** Variation of effective elastic modulus averaged by that obtained from x, y, z-compression direction with m_g/m_t and radius of CNTs.

Young's modulus of particles is obtained by averaging the data obtained from the compression test in the x, y and z direction and **Figure 4.15b** plots the variation of averaged elastic modulus with m_g/m_t and radius of CNTs.

4.4 Encapsulation Mechanism of Crumpled Graphene/CNTs Composite Particles

With the diffusion behavior of CNTs and graphene at both equilibrium and evaporation stages, **Figure 4.16a** shows the schematic illustration of crumpling and assembling graphene and CNTs suspended in a droplet with liquid evaporation that can be achieved through the aerosol-like process (See **Figure 3.1a** for a typical experimental setup). Assume the droplet is sufficiently large enough, with the liquid evaporation, graphene sheets will migrate to the surface of droplet, and CNTs remain inside. Further evaporation will crumple the graphene on the droplet surface and pack the CNTs inside the droplet, and a CNTs-encapsulated, crumpled graphene hybrid composite nanoparticle will be eventually formed after the complete evaporation of liquid. The overall size and morphologies of the hybrid nanoparticles rely on the competition between the packing of CNTs inside and the crumpling of graphene on the

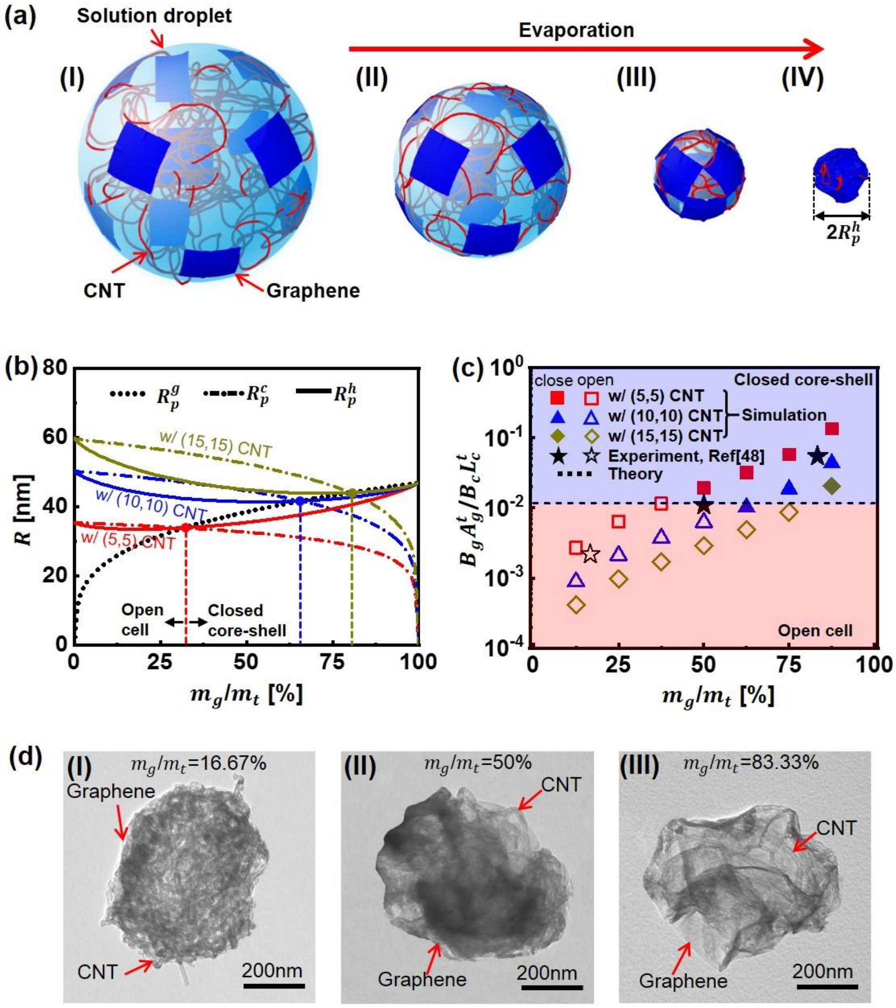

Figure 4.16. Size and pore structures of crumpled graphene/CNT hybrid particles. (a) Schematics of crumpling graphene/CNTs mixture with the evaporation of liquid solution. At the early stage of evaporation (stage I and II), the graphene sheets begin to diffuse and accumulate at the liquid/air interface; the CNTs stay inside the droplet and only a small portion pierces the droplet surface and exposes to air. With the continuous evaporation of liquid (stage III), the graphene sheets on the liquid surface will be crumpled and assembled, and the CNTs inside the droplet will be deformed and packed, which eventually lead to the formation of the CNT-encapsulated crumpled graphene assembled nanoparticles after complete evaporation of liquid (stage IV). **(b)** Theoretical prediction on the size of crumpled hybrid particles (R_p^h) at different m_g/m_t. R_p^g and R_p^c show the size of crumpled particle with only graphene and CNTs in an initial droplet liquid, respectively. The radius of the initial droplet R_d is 150 nm and the concentration of graphene/CNTs in droplet solution C_t is 4 mg/mL. **(c)** Comparison of pore structures between theoretical predictions and simulation results. B_g and A_g^t are the bending stiffness and total area of graphene, respectively; B_c and L_c^t are the bending stiffness and total length of CNTs, respectively. The critical $B_gA_g^t/B_cL_c^t$=0.012 can be obtained in theory regardless of CNTs size and C_t. At $B_gA_g^t/B_cL_c^t$>0.012, the crumpled hybrid particles are “closed core-shell” pore structure and at $B_gA_g^t/B_cL_c^t$<0.012, the crumpled hybrid particles are “open-cell” pore structure. **(d)** SEM images of the crumpled hybrid graphene/CNT particles synthesized by evaporation of microdroplet at different mass fraction of graphene (m_g/m_t) [48].

surface and can be theoretically determined through energy analysis. Assume the radius of crumpled particles by pure graphene and CNTs is R_p^g and R_p^c, respectively, the radius of their hybrid particles can be defined by $R_p^h = \left(R_p^c\right)^{1-\emptyset_g}\left(R_p^g\right)^{\emptyset_g}$, where $\emptyset_g = m_g/m_t$. If $R_p^g < R_p^h$, the hybrid particles will have an "open-celled" structure, and otherwise, the hybrid particles will have a "closed core-shell" structure. Take R_d=150 nm and C_t=4 mg/mL as an example, **Figure 4.16b** plots the variation of R_p^g, R_p^c and R_p^h with m_g/m_t. At $R_p^g = R_p^c = R_p^h$, the critical m_g/m_t that leads to an "open-celled" or "closed core-shell" structure of hybrid particles can be obtained, and it increases with the increase of CNTs radius. To further reflect the competition between the packing of CNTs and crumpling of graphene, an intrinsic parameter, $B_g A_g^t / B_c L_c^t$ (**Figure 4.16c**) can be obtained from our analysis to describe the transition of particles morphologies from "open-celled" to "closed core-shell" status, where B_g and A_g^t are the bending stiffness and total area of graphene, respectively, and B_c and L_c^t are the bending stiffness and total length of CNTs, respectively. The analysis shows the critical $B_g A_g^t / B_c L_c^t$=0.012 for the transition, regardless of the types of CNTs or m_g/m_t, which agrees well with our simulation results. In addition, **Figures 4.16d** illustrates the TEM images of the hybrid graphene/CNTs composite nanoparticles obtained by the evaporation of microdroplet at different m_g/m_t [48]. When the graphene mass fraction is very low (i.e. m_g/m_t=16.67%, **Figure 4.16d (I)**), the fibrillar structures of CNTs are clearly observed in the crumpled particle, and only partial CNTs are encapsulated by graphene, suggesting that the crumpled particle is an "open-celled" structure. By increasing the graphene mass fraction, (i.e. m_g/m_t=50%, **Figure 4.16d (II)**), both the "out-of-surface" CNTs and pores disappear, and the surface is fully covered by graphene sheets, indicating the crumpled particle becomes a "closed core-shell" structure. When the graphene mass fraction is very high (i.e. m_g/m_t=83.33%, **Figure 4.16d (III)**), the crumpled particle remains to be closed and crumpled ridges on the surface could be observed. These experimental data are also given in **Figure 4.16c** and agree well with both theoretical analysis and simulation results.

4.5 Interconnected 3-D Networking Structures and Electrical Properties of Crumpled Graphene/CNTs Composite Particles

Figure 4.17a shows the morphology of the crumpled composite particles from simulations at different m_g/m_t and diameters of CNTs. The CNTs and the graphene are highlighted in red and blue, respectively, to reflect their crumpled and interconnected spatial 3-D structures. To characterize the surface morphology of each crumpled particle, the radius R_p^h is calculated by averaging the distance of outmost atoms to the center of mass of the particles in the projection on each coordinate plane and their corresponding equivalent sphere is constructed (**Figure 4.9**). This equivalent sphere also allows extracting the surface pore ratio (P_r) of the crumpled particle. P_r is defined by dividing the surface area not covered by graphene sheets (pore) over the total surface area of the crumpled particle (**Figure 4.10**), and $P_r =$ 1-A_p^g/A_p^h, where A_p^g=4$\pi\left(R_p^g\right)^2$ and A_p^h=4$\pi\left(R_p^h\right)^2$ are the surface area of particles assembled by pure graphene and hybrid CNTs and graphene, respectively. That is, we will have P_r=1-$\left(R_p^g/R_p^h\right)^2$, and R_p^g/R_p^h reflects the crumpling intensity. P_r decreases with the increase of m_g/m_t and small CNTs lead to small P_r (**Figure 4.10**). **Figure 4.17b** plots P_r versus R_p^g/R_p^h. Good agreement is obtained between the theoretical predictions and simulations. Especially, at R_p^g/R_p^h=0, there is no graphene, and P_r=100 %; at $R_p^g/R_p^h \geq$1, the CNTs are fully encapsulated by graphene, and P_r=0; and at $0 < R_p^g/R_p^h <$1, the particle surface will be partially covered by graphene. Further, define a critical pore ratio $P_r^c = 5\%$ to describe the transition from “open-celled” to “closed core-shell” structure of hybrid particles, the critical m_g/m_t can be obtained and is plotted in **Figure 4.17a**, which agrees well with theoretical predictions. Besides, the theoretical analysis shows $P_r \propto -\left({R_p^g}^{1-\emptyset_g}/{R_p^c}^{1-\emptyset_g}\right)^2$ and $R_p^c \propto B_c L_c^t$, $R_p^g \propto B_g A_g^t$ (See **Figures 3.27a and 4.5d**), and therefore the characterization of crumpling status can be unified by$B_g A_g^t/B_c L_c^t$. **Figure 4.17c** plots P_r versus $B_g A_g^t/B_c L_c^t$, and a linear relationship is obtained, independent of CNT sizes, which agrees well with the theoretical predictions.

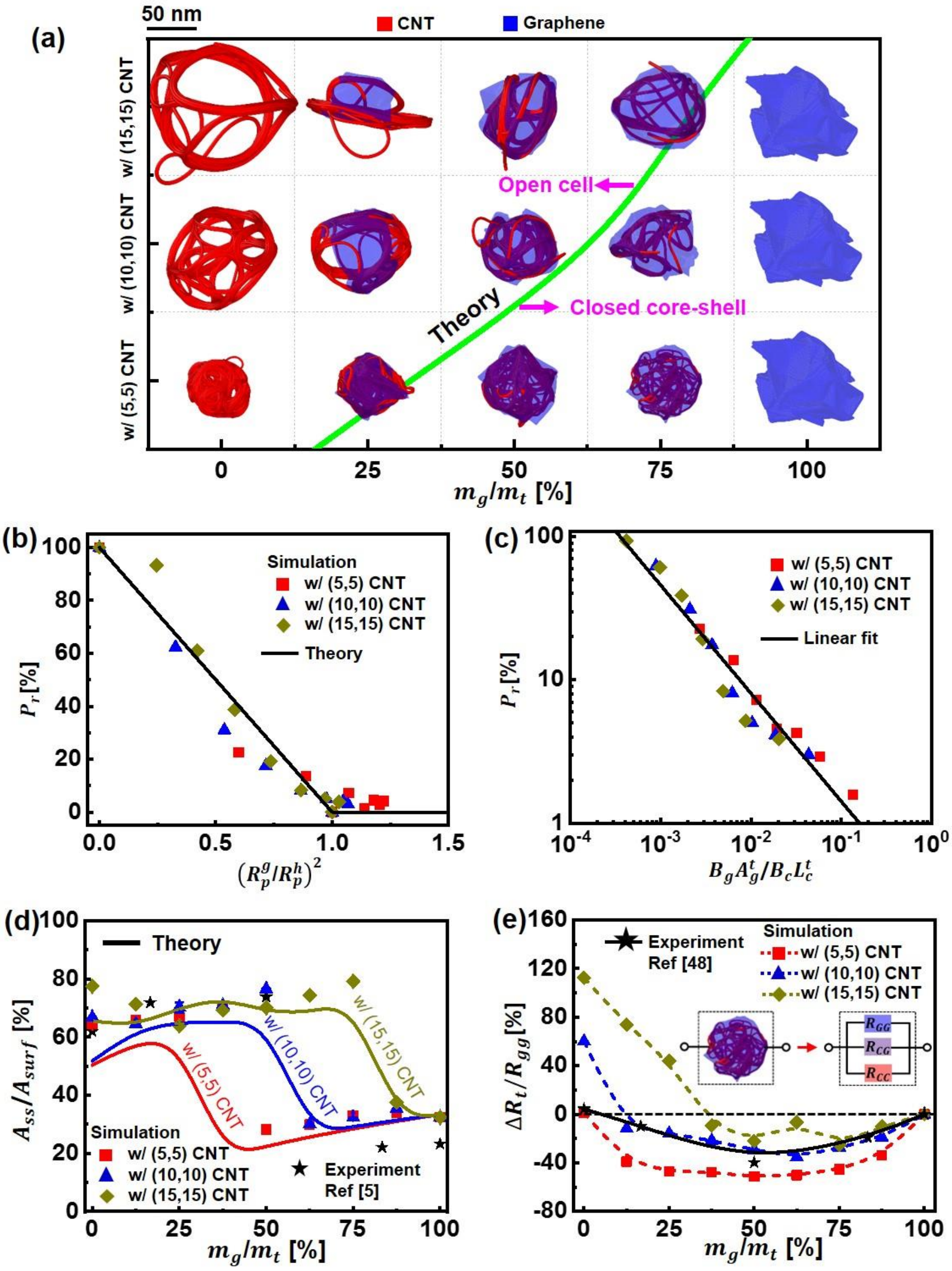

Figure 4.17. Characterization of interconnected spatial networking structures in the crumpled graphene/CNTs hybrid particles and the electrical properties of an individual particle. (a) Simulation snapshots on spatial networking structures, size, and morphology of the crumpled particles obtained at different m_g/m_t and sizes of CNTs. **(b)** Comparison of theoretical predictions and simulations on the surface pore ratio (P_r) of the crumpled particles with the crumpling intensity R_p^g/R_p^h. **(c)** Variation of P_r with the unified intrinsic material parameter $B_g A_g^t / B_c L_c^t$. **(d)** Specific surface area of particles (A_{ss}) normalized by the intrinsic specific area of CNTs and graphene (A_{surf}) versus m_g/m_t with different sizes of CNTs. **(e)** Estimation of electrical resistance of individual crumpled particles. Insets are schematics of a crumpled particle and its equivalent circuit model. R_{GG}, R_{CG}, are R_{CC} represent the electrical resistance of electron passing through the contacts between graphene and graphene, CNTs and graphene, and CNTs and CNTs, respectively.

Figure 4.17d shows the variation of the accessible area in crumpled particles A_{ss} normalized by A_{surf} with m_g/m_t, where $A_{surf}=A_c(1-\emptyset_g)+A_g\emptyset_g$, A_c is the intrinsic surface area of CNT (e.g. A_c=1315 m^2/g for single-walled CNT) and A_g is the intrinsic surface area of graphene (e.g. A_g=2630 m^2/g for single-layer graphene)[18]. We should note that both the surface area of graphene/CNT inside and on the surface of the particles can be accessed in "open-celled" crumpled particles, but only the surface area is accessible in "closed core-shell" crumpled particles. At a low m_g/m_t, the crumpled particle is open and shows a high A_{ss}/A_{surf}. With the increase of m_g/m_t, the crumpled particle becomes a closed core-shell structure and shows a rapid decrease of A_{ss}/A_{surf}. Besides, A_{ss}/A_{surf} shows a strong dependence of the size of CNTs due to the close relevance to wrapping status by graphene. The accessible surface area predicted in theory (See Section 4.2.5) and independent experimental results from the nitrogen adsorption-desorption isotherms measurements are also potted in **Figure 4.17d**, where A_g=262.16 m^2/g, and A_c=263.21m^2/g in experiments [48]. Both of them show good agreement with simulations.

When the crumpled composite particles with hybrid graphene and CNTs are used in electrical devices, the interconnected contacts between graphene and CNTs in comparison with that by pure graphene or CNTs will benefit the transport of electrons, where CNTs are analogous to a bridge connecting individual crumpled graphene sheets. Their spatial contacts among CNTs and graphene in the crumpled particles can also be extracted (See Section 4.3.3.4 and **Figure 4.12**). As a demonstration, the insets in **Figure 4.17e** illustrates the schematics of electric transport through a single crumpled particle and its equivalent circuit. The overall electrical resistance of the crumpled composite particle (R_t) is $1/R_t=1/R_{cc}+1/R_{cg}+1/R_{gg}$, where $R_{cc}=2\rho_{cc}R_p^h/(A_p^hC_p^{C-C})$, $R_{cg}=2\rho_{cg}R_p^h/(A_p^hC_p^{C-G})$, and $R_{gg}=2\rho_{gg}R_p^h/(A_p^hC_p^{G-G})$ represent the electrical resistance for the transport of electrons along with contacts between CNTs-CNTs, graphene-CNTs and graphene–graphene, respectively, ρ_{cc}, ρ_{cg}, ρ_{gg} and C_p^{C-C}, C_p^{C-G} , C_p^{G-G} are their corresponding electrical contact resistance density [198, 199], and contact probability (**Figure. 4.13**), respectively. We should note that for the particles assembled by pure CNTs, $R_{cg}=R_{gg}=\infty$ and R_t=R_{cc}, and for the particles assembled by pure graphene, $R_t = R_{gg}$. **Figure 4.17e** shows the variation of normalized resistance difference $(R_t - R_{gg})/R_{gg}$ with m_g/m_t. As m_g/m_t increases, $(R_t - R_{gg})/R_{gg}$ shows an initial decrease to a minimum value and after that it increases. In general, the resistance of the crumpled particles with hybrid graphene and CNTs is lower than that of crumpled particles by pure CNTs or graphene due to enhanced spatial 3-D contacts. The smaller CNTs are, the lower electrical resistance will be, indicating the flexible CNTs will benefit the formation of contacts during evaporation due to smaller bending stiffness. Similarly, the experimental results [48] are also given, and good agreement between them is obtained.

4.6 Surface Morphology, Ridge Density and Mechanical Strength of Crumpled Graphene/CNTs Composite Particles.

Figure 4.18a shows the surface morphology of the crumpled particles with highlights on the local deformation curvature, where the local curvature is calculated from the deformation energy (See Section 4.3.3.5). Further, if the local curvature is larger than 0.5 nm^{-1}, we will define such the sharp local deformation as a ridge[192]. The equivalent sphere is also given to reflect the distribution of ridges on the surface of crumpled particles, and where the total length of ridges in graphene over the entire surface area of the crumpled particle is defined as the ridge density (D_r, in nm^{-1}), and is calculated using the image processing technique (**Figure 3.22**)[192]. For the crumpling with a (5,5) CNT at m_g/m_t=25%, the ridges only exist in the localized area due to partial encapsulation of CNTs by crumpled graphene. When m_g/m_t increases to 75%, the crumpling of graphene becomes sever with CNTs fully encapsulated inside, and more ridges appear. Similar results are also observed for the crumpled particles with large (10,10) and (15,15) CNTs. The equivalent radius of particles and ridge density $\left(R_p^h, D_r\right)$ are also denoted in **Figure 4.18a**. In theory, the ridge density can be obtained from the analysis on deformation energy of graphene in the hybrid particles and is characterized as a function of R_p^g/R_p^h [192], similar to **Figure 4.17b**. **Figure 4.18b** shows the comparison of D_r between the theoretical predictions and simulation results and good agreement is obtained. More importantly, at R_p^g/R_p^h=0, there is no graphene in the particle, and D_r=0; at R_p^g/R_p^h>1, a large

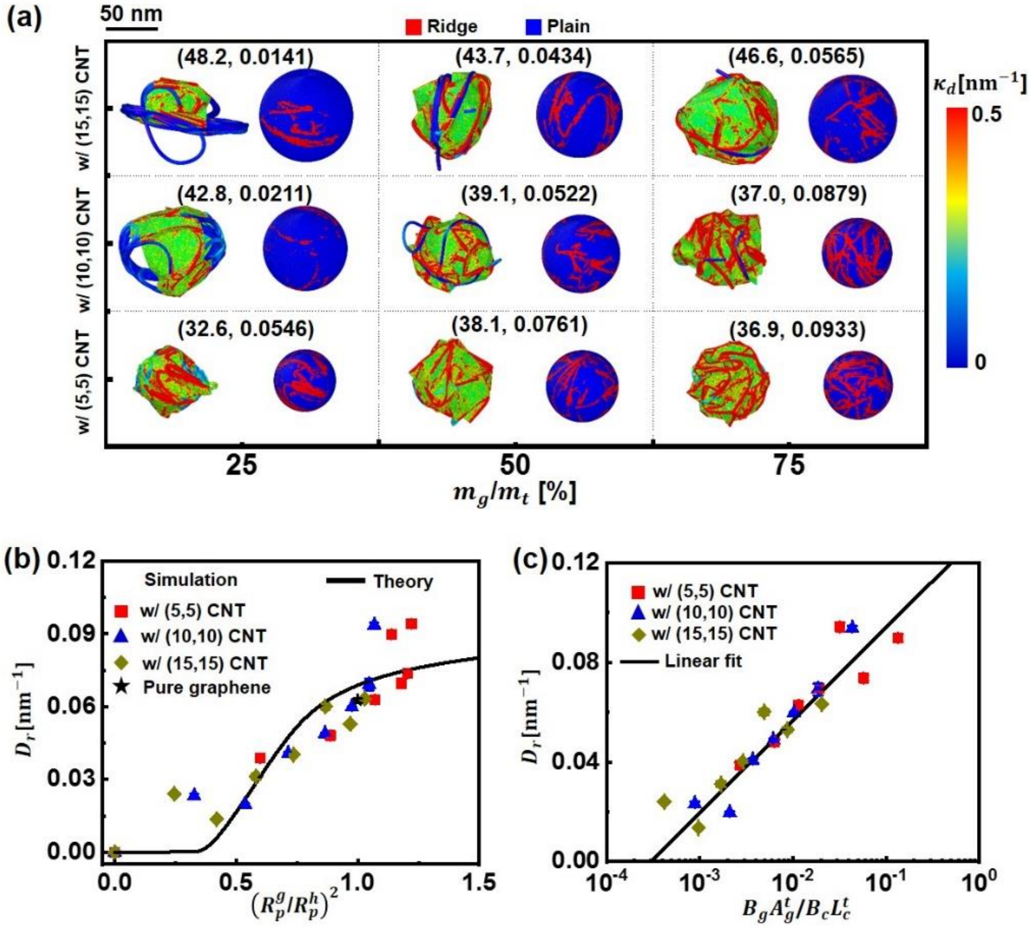

Figure 4.18. Surface crumpling morphology and local ridge distribution in the crumpled graphene/CNTs hybrid particles. (a) Simulation snapshots showing the local surface curvature distribution in the particles (left) and their equivalent spheres highlighting the size and ridge distribution (right). The inset bracket "()" in each block represents the radius (R_p^h, in nm), and ridge density (D_r, in nm^{-1}) of the crumpled particle. **(b)** Comparison of D_r between the theoretical predictions and simulation results with the crumpling intensity ($\left(R_p^g/R_p^h\right)^2$). **(c)** D_r as a function of unified intrinsic material parameter $B_gA_g^t/B_cL_c^t$.

D_r is obtained, indicating the inside packed CNTs enhance crumpling of graphene. **Figure 4.18c** further plots the variation of D_r with the unified material parameter $B_gA_g^t/B_cL_c^t$, and it shows a linear relationship, similar to **Figure 4.17c**.

To investigate the mechanical performance of the crumpled particles, the compression test on a single particle is conducted (See simulation model and method in Section 4.3.3.6 and simulation snapshots in **Figures 4.14**). To further understand the effect of surface ridge density on E_{eff}, **Figure 4.19** shows the variation of E_{eff} with D_r. E_{eff} increases linearly with D_r, suggesting that the local curvature could be utilized to enhance the mechanical properties of crumpled graphene particles and can be adjusted by mixing CNTs in the liquid solution. The

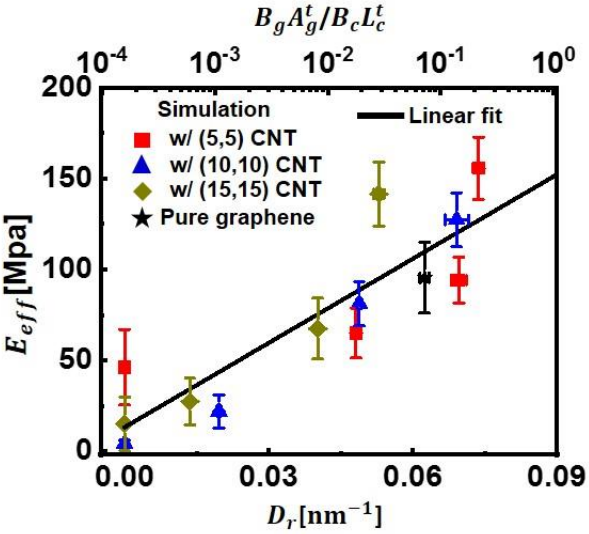

Figure 4.19. Correlation of elastic modulus (E_{eff}) with the ridge density (D_r) of the crumpled particles and the unified material parameter $B_gA_g^t/B_cL_c^t$. E_{eff} is the averaged Young's modulus by performing compression experiments on *x*, *y*, and *z*- three compression directions.

variation of E_{eff} with the unified material parameter $B_gA_g^t/B_cL_c^t$ is also illustrated, and it shows a linear relationship, similar to **Figure 4.17c**.

4.7 Summary

In summary, in this chapter, we have developed an energy-based analytical diffusion model, and demonstrate that the graphene will prefer to immigrate and accumulate at the liquid/air interface while the CNTs stay inside the liquid droplet for their suspended liquid solution. This diffusion model also confirms the formation of CNTs-encapsulated, crumpled graphene assembled composite nanoparticles by solution evaporation. Further, guided by the coarse-grained molecular dynamics simulations, we have systemically investigated the crumpling and assembling of graphene and CNTs by liquid evaporation and monitored the evolution of crumpled graphene/CNTs composite particles. The effect of CNTs types and mass fraction of graphene on the crumpled composite particles including surface crumpling morphology, overall size, pore status and density is elucidated. In particular, the spatial 3-D interconnected contacts between CNTs and graphene are extracted and are further correlated with the electrical properties of crumpled composite particles to demonstrate practical applications. Besides, the crumpled surface roughness, referred to as ridge density, is quantitatively characterized and its relationship with the mechanical strength of crumpled composite particles is established by performing compression tests. These results show the presence of CNTs in the crumpled graphene particles promotes both electrical transports and mechanical strength and agrees well with independent experimental results. The crumpled composite particles will help seek electrically conductive and mechanically strong nanoparticles for potential applications in electrical and devices and could also serve the unit building blocks for assembling large-scale quantities of graphene and CNTs. The proposed fundamental mechanism will provide immediate guidance to control the formation of crumpled CNTs/graphene composite particles from the overall size to pore density and could also be extended to study of crumpling and assembling other materials encapsulated composite nanoparticles in a broad of low-dimensional nanomaterials such as nanowires, nanoparticles and nanofibers through the aerosol-like processing technique.

Chapter 5 Liquid Evaporation-driven Crumpling and Assembling of Multiple 2-D Materials on a Substrate

5.1 Overview of the Chapter

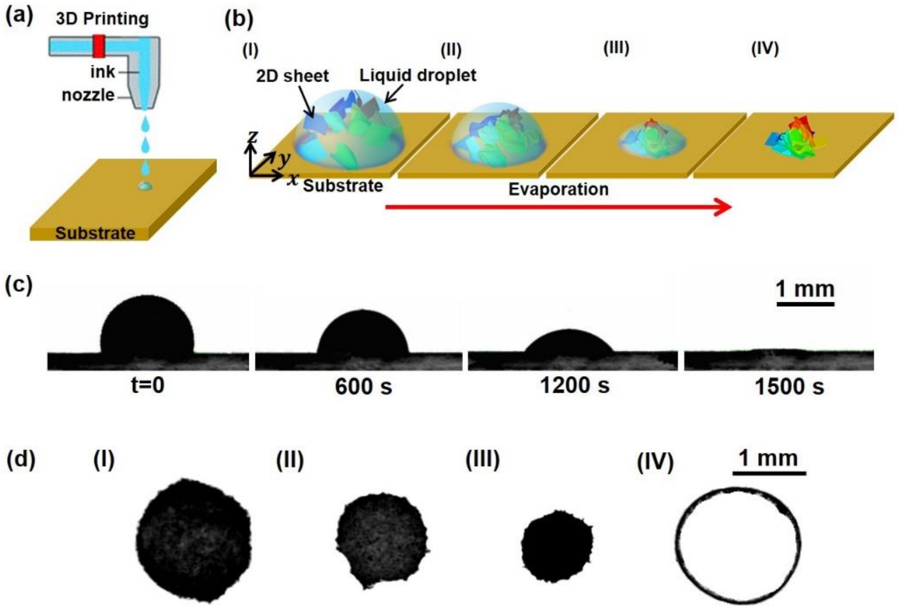

Figure 5.1. Liquid evaporation-driven crumpling and assembling of two-dimensional (2-D) deformable nanomaterials on a substrate. (a) Schematics of the popular experimental setup for the liquid evaporation-induced crumpling and assembling of 2-D nanomaterials on a substrate in 3D printing. The liquid droplets consisting of 2-D materials and solvent liquid solution are deposited onto the substrate for liquid evaporation. **(b)** Schematic illustrations of the crumpling and assembling process of 2-D deformable nanomaterials by liquid evaporation on a substrate. (I) uniform distribution of multiple 2-D sheets in the liquid droplet on the substrate. (II) The droplet starts to shrink after evaporation occurs and to deform and assemble the 2-D sheets inside the droplet. (III) 2-D sheets start to crumple and assemble with the continuous evaporation of liquid. (IV) 2-D sheets further assemble and self-fold until complete evaporation of liquid, and a stable deposited pattern on the substrate is generated. **(c)** Snapshots from the evaporation experiment when 1μL, 0.5mg/mL graphene oxide solution in DI water evaporates on 10:1 PDMS film. **(d)** Optical microscopy images of assembled patterns on the substrate after complete evaporation of 1μL droplet contains graphene oxide suspension with a concentration of 0.5mg/mL with different solvents and substrates: (I) in DI water and on a Sylgard 184 10:1 PDMS film; (II) in water-ethanol mixture with 50% water and 50% ethanol and on a Sylgard 184 10:1 PDMS film; (III) in water-ethanol mixture with 70% water and 30% ethanol and on a Sylgard 184 10:1 PDMS film; (IV) in pure ethanol and on VHB tape.

In this chapter, we establish a theoretical mechanics framework for the liquid evaporation-driven crumpling and assembling of multiple 2-D deformable materials in a sessile liquid droplet on a substrate, as illustrated in **Figure 5.1a** for the experiment setup in the 3D printing[200, 201]. An evaporation route model is first developed to unify the evaporation process of a sessile droplet on the substrate. Then, a spring-mechanical slider model is proposed to describe mechanical deformation, self-folding, assembly, and adhesion of 2-D sheets on the substrate during evaporation. The resultant energies are derived to quantitatively elucidate the competition between the crumpling and adhesion. The morphologies of assembled 3-D particles are predicted in theory. High-efficiency coarse-grained modeling is developed to conduct large-scale molecular dynamics simulations and validate the proposed theoretical model. Graphene is taken as a representative 2-D deformable material and is modeled by a coarse-grained model. A controllable virtual van der Waals force field that exerts on graphene is developed to mimic the liquid evaporation-induced pressure. The setup in the CGMD simulation is validated by experiments. The quantitative comparison between simulations and theoretical predictions are presented, including the projected area and height of assembled graphene. The extension of the proposed theory that takes into account the initial surface wettability is further discussed and the results show good consistency with simulations and experiments.

5.2 Theoretical Framework

5.2.1 Evaporation route of a sessile droplet on a substrate

As illustrated in **Figure 5.1a**, the liquid droplet is generated through a nozzle in the 3D printing. During the flying of the liquid droplet and after it is deposited on the substrate, liquid evaporation will occur and form crumpled and assembled particles on the substrate after complete evaporation of liquid (**Figures 5.1b** and **c**). Unlike the free-standing liquid droplet, the evaporation of sessile droplet on the substrate is more complex[202, 203]. The profile of droplets during liquid evaporation will be highly influenced by the properties of the substrate[204-206]. So the crumpling and assembling of 2-D materials during liquid evaporation will be dominated by the profile of liquid and properties of the substrate, simultaneously (**Figure 5.1d**), leading to different morphologies and properties of the deposited patterns[207-209].

When the liquid droplet is in contact with the substrate, due to the interaction between the liquid and substrate and neglecting the gravity effect, a contact angle θ_c will be formed based on the famous Young's equation[204],

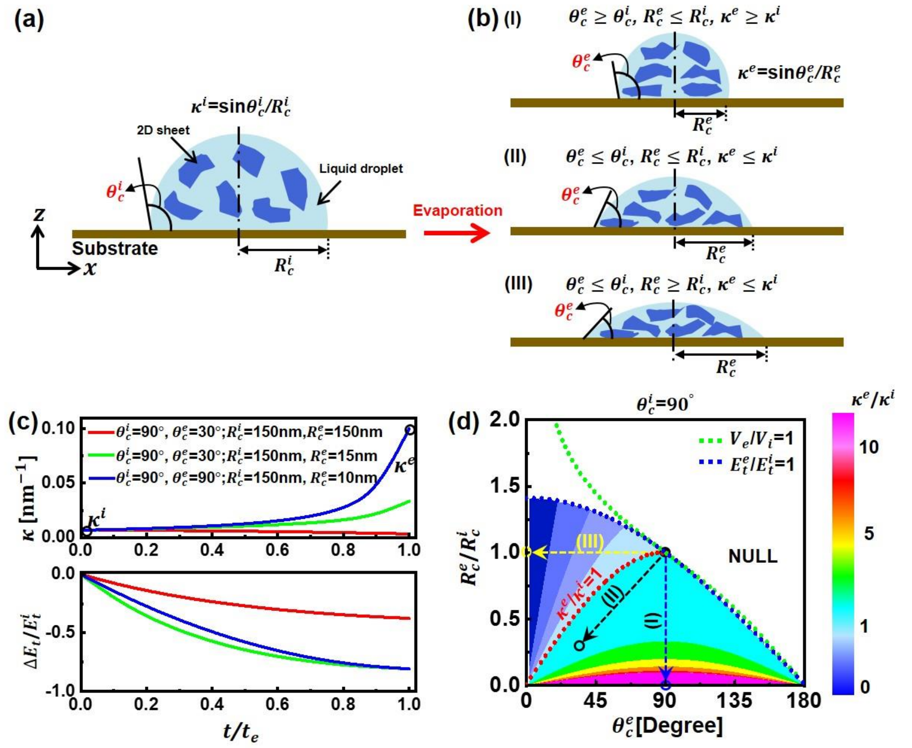

Figure 5.2. Schematic to show the crumpling and assembling process of multiple 2-D material sheets on a substrate by liquid evaporation. (a) Uniform distribution of multiple 2-D sheets suspended in the sessile droplet before evaporation. Before the evaporation occurs, the droplet will form a contact angle θ_c^i and contact radius R_c^i on the substrate. The surface curvature of the droplet is $\kappa^i = sin\theta_c^i/R_c^i$. **(b)** Profile of the droplet after liquid evaporation occurs. (I) Only the contact radius will decrease. (II) Both the contact radius and contact angle will decrease. (III) Only the contact angle will decrease. **(c)** Variations of surface curvature and energy during liquid evaporations at different modes. **(d)** Evaporation route of liquid droplets on the substrate when θ_c^i=90°. The color bar indicates the variation of surface curvature. Route (I): constant contact angle mode with $\theta_c^e = 90°$ and κ^e/κ^i =150. Route(II): mixed mode with $\theta_c^e = 30°$ and κ^e/κ^i=2.5. Route(III): constant contact radius mode with $\theta_c^e = 1°$ and κ^e/κ^i=0.0175.

$$cos\theta_c = \frac{\gamma_s-\gamma_{sl}}{\gamma_l} \tag{5.1}$$

where γ_s, γ_{sl}, and γ_l are the surface tension of solid surface, solid-liquid interface, and liquid surface, respectively. At the same time, a contact radius R_c will be formed, which reflects the size of the droplet. When the evaporation occurs at elevated temperature, both the properties of the liquid (e.g. solution concentration, surface tension, internal flow) and solid surface (e.g. surface roughness, charge density) will change, leading to the variation of R_c and θ_c in accompany with the removal of liquid. Denote the contact angle and contact radius before evaporation as θ_c^i and R_c^i (**Figure 5.2a**) and those after evaporation as θ_c^e and R_c^e (**Figure 5.2b**). Based on their evolutions, the evaporation process can be categorized into three modes:

(I) The constant contact angle mode (CCA, **Figure 5.2b(I), Figure 5.3a(I)**), in which only the contact radius will decrease and the contact angle will not[210, 211].

(II) The mixed mode (**Figure 5.2b (II), Figure 5.3a(II)**), in which both the contact angle and contact radius will decrease[212, 213].

(III) The constant contact radius mode (CCR, **Figure 5.2b(III), Figure 5.3a(III)**), in which only the contact angle will decrease and the contact radius will not[214, 215].

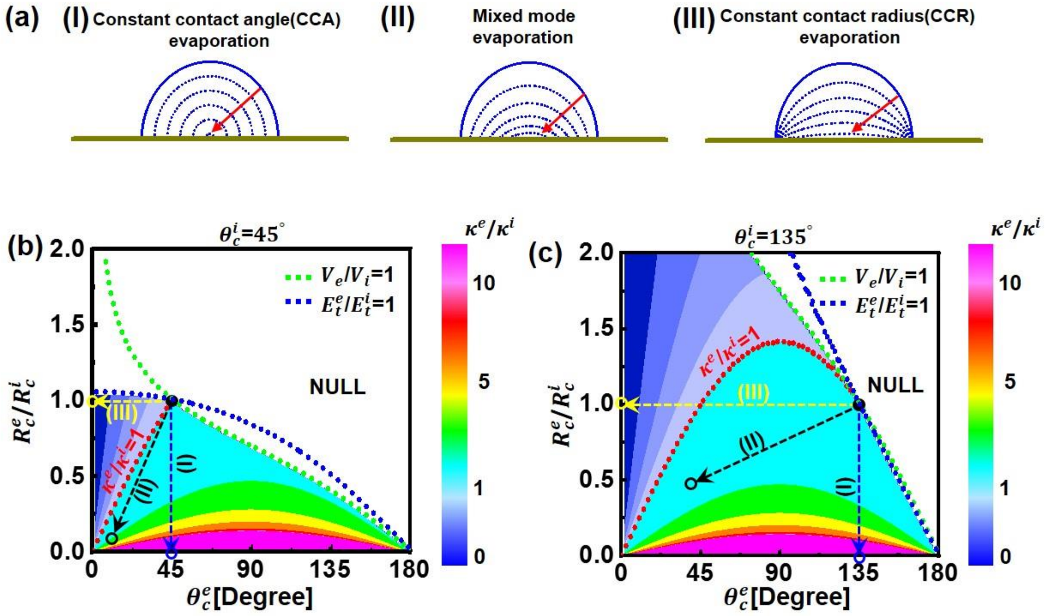

Figure 5.3. (a) Schematics of droplet profile during liquid evaporation in different modes. **(b)** Evaporation route of liquid droplets on the substrate when θ_c^i=45°. The color bar indicates the variation of surface curvature. **(c)** Evaporation route of liquid droplets on the substrate when θ_c^i=135°. The color bar indicates the variation of surface curvature.

Such modes will lead to different deposited patterns after the complete evaporation of liquid. For example, the CCA mode tends to aggregate the suspensions and pack them into particles with a high height-to-width ratio while the CCR mode tends to spread out the suspensions on the substrate and form film-like structures[216].

In geometry, the surface curvature of a liquid droplet on a substrate is

$$\kappa = \frac{sin\theta_c}{R_c} \tag{5.2}$$

The surface curvature of the liquid has been proved that it is a key parameter to control the crumpling and assembling of 2-D materials in a free-standing droplet[192] (**Chapter 3**). Here, we find that again the surface curvature plays a vital role in the crumpling and assembling of 2-D materials on a substrate driven by the liquid evaporation. At the same time, the differences between evaporation modes will lead to different evolution route of surface curvature. **Figure 5.2c** plots the variation of surface curvature as well as the surface energy of droplet with liquid evaporation. The CCA mode (i.e. θ_c^i=90°, θ_c^e=90°, R_c^i=150 nm, R_c^e=10 nm) shows the most dramatic increase of surface curvature and the most significant decrease in surface energy. The CCR mode (i.e. θ_c^i=90°, θ_c^e=30°, R_c^i=150 nm, R_c^e=150 nm) shows a decrease of surface curvature and the minimum increase in surface energy. The variations of surface curvature and surface energy of the mixed mode (i.e. θ_c^i=90°, θ_c^e=30°, R_c^i=150 nm, R_c^e=15 nm) are between the CCA and CCR modes. These indicate that $-\Delta E_t \propto \kappa^e/\kappa^i$, whereas an increase of surface curvature will lead to an decrease of surface energies. In the droplet, the higher the increase of surface curvature, the higher the confinement will be exerted on the suspended 2-D deformable materials, leading to intensive crumpling and assembling of the 2-D materials. At the same time, more work will be done by the liquid on the 2-D materials by liquid evaporation, which is in good consistency with the variations of surface energies. As a result, the surface curvature κ can be selected as a unified parameter to describe the evolution of liquid profile and be used to characterize the liquid-evaporation-driven crumpling and assembling of 2-D materials in the droplet. Taking $\theta_c^i = 90°$ as an example, **Figure 5.2d** illustrates the variation of surface curvature when a liquid droplet evaporates along different evaporation modes. There is a one-to-one relationship between the evaporation modes and the curvature evolution routes in **Figure 5.2d,** so we can define the evolution of surface curvature as the evaporation route. **Figures 5.3b and c** further illustrate the map and evaporation route when the initial contact angle is different, and similar results can be obtained.

5.2.2 Mechanical model of crumpling and assembling of multiple 2-D sheets on a substrate by liquid evaporation

In addition to the evaporation route, the interactions between the 2-D materials and substrate also influent the final morphologies of deposited patterns. A higher binding energy density between 2-D materials and substrate will benefit the adhesion of 2-D materials on the substrate and generate more flattened patterns, while a lower binding energy density will benefit the self-folding and assembling of 2-D materials and generate more crumpled patterns.

Such curvature-dominated, substrate-regulated crumpling and assembling process of 2-D materials during liquid evaporation (**Figure 5.4a**) can be described by a 2-D linear spring-mechanical slider mechanics model after considering the symmetry of droplet (**Figure 5.4b**). The three-phase contact line and apex of the droplet in **Figure 5.4a** are modeled by geometric confinement points in this 2-D model. The positions of these geometric confinement points are directly determined by the contact radius and height of droplet to account for the profile evolution of the droplet and geometric confinement of liquid on 2-D sheets during evaporation. After this, sliding hinge supports are attached with the geometric confinement points at the three-phase contact line to represent the evolution of contact radius and make sure these confinement points can only move in the horizontal direction. During the liquid evaporation, distances between the confinement points at the apex and three-phase contact line will change and when it is small enough, the liquid starts to deform the 2-D sheets. The deformation of 2-D sheets in the droplet is modeled by linear spring connecting the confinement point at the three-phase contact line and apex. When the deformation of 2-D sheets is large enough, self-folding will occur and the interactive binding energy of 2-D sheets in the folded part is modeled by mechanical sliders in parallel with linear springs (MSA in **Figure 5.4b**). As the evaporation continues, the distance between 2-D sheets and the substrate will be close enough and adhesion energy needs to be considered. The interactive adhesion energy between 2-D sheets and the substrate can be modeled by mechanical sliders connecting the three-phase contact line and a fixed wall (MSB in **Figure 5.4b**). The wall has a distance L_0 to the axis of symmetry of the droplet and $L_0=(A_t/\pi)^{1/2}$, where A_t is the total area of 2-D sheets in the droplet. A_t can be

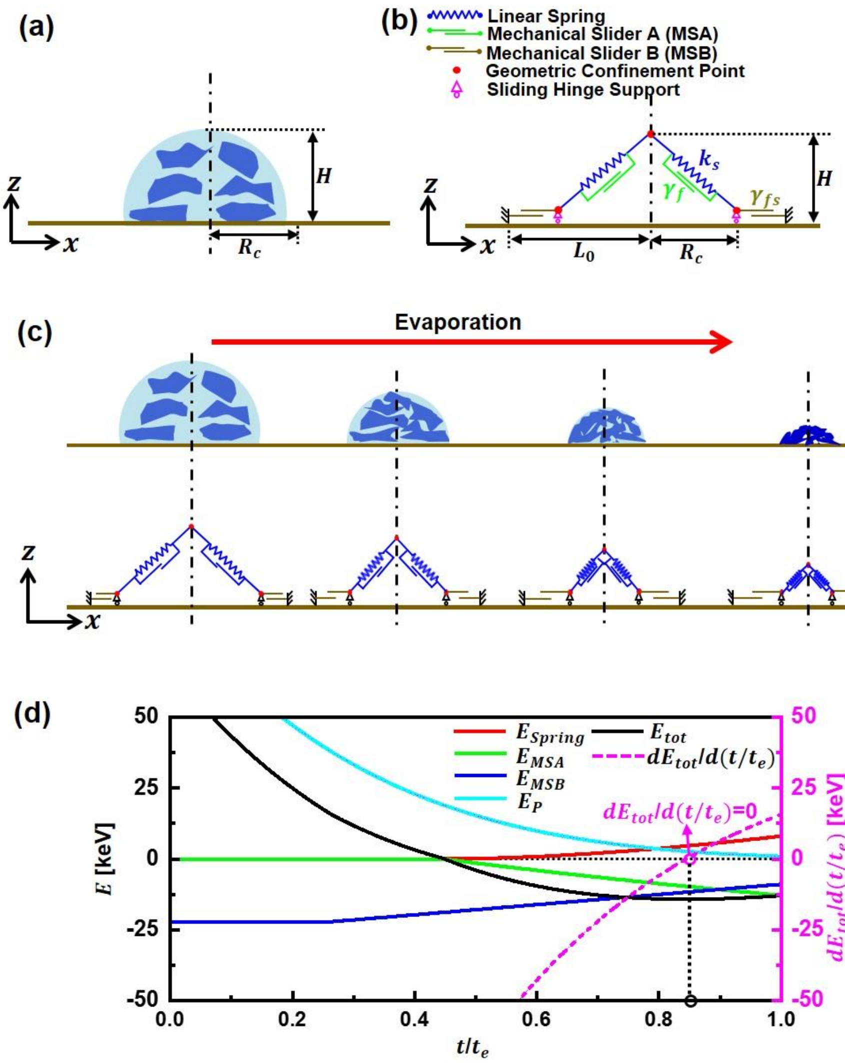

Figure 5.4. The linear spring-mechanical slider mechanics model of crumpling and assembling multiple 2-D sheets on a substrate by liquid evaporation. (a) Liquid droplet contains deformable 2-D nanomaterials on the substrate with contact radius R_c and height H during liquid evaporation. **(b)** 2-D mechanics model to describe the crumpling and assembling of multiple 2-D sheets by liquid evaporation on a substrate after considering the symmetry of liquid droplet. The three-phase contact line and apex of the droplet in (a) are modeled by geometric confinement points in this 2-D model to account for the profile evolution of the droplet and geometric confinement of liquid on 2-D sheets. Sliding hinge supports are attached with the geometric confinement points at the three-phase contact line to represent the evolution of contact radius and make sure these confinement points can only move in the horizontal direction. Deformation of 2-D sheets in the droplet is modeled by linear springs (with stiffness k_s) connecting the confinement points at three-phase contact line and apex. The interactive binding energy of 2-D sheets is modeled by mechanical sliders with a coefficient γ_f at the same locations. The interactive adhesion energy between 2-D sheets and substrate is modeled by mechanical sliders with a coefficient γ_{fs} connecting the three-phase contact line and a fixed wall, whose distance to the symmetric axis is L_0. **(c)** Schematics show the crumpling and assembling multiple 2-D sheets in the droplet and their corresponding state of the spring-slider mechanics model. **(d)** Energy variation of multiple graphene sheets during liquid evaporation from the spring-slider mechanics model. θ_c^i=*90°*, θ_c^e=*30°*, R_c^i=*150 nm*, R_c^e=*50 nm*, A_t=*48000* nm^2, and P_t=*40 atm*. $dE_{tot}/d(t/t_e)$=*0* corresponds to the stopping of the crumpling and assembling process.

obtained by $A_t = V_d C/\rho_g$, where V_d is the volume of the liquid droplet, C is the concentration of 2-D materials, and ρ_g is the area density of the 2-D sheet. **Figure 5.4c** illustrates the schematics of crumpling and assembling of 2-D sheets on the substrate during liquid evaporation and the corresponded state of this 2-D mechanics model. With this 2-D spring-slider mechanics model, the crumpling and assembling of multiple 2-D sheets on a substrate can be analyzed through the energy analysis.

The energy stored in the linear spring that corresponds to the deformation of 2-D sheets can be defined as

$$E_{spring} = \begin{cases} 0, L > L_0 \\ \frac{k_s}{2}(L - L_0)^2, L \leq L_0 \end{cases} \tag{5.3}$$

where L is the length of linear spring and can be obtained by geometry analysis via $L = (R_c^2 + H^2)^{1/2}$. k_s is the constant of linear spring and can be obtained by following the analysis in Chapter 3[192]. As a result, $k_s = \alpha \frac{B}{h^2}\sqrt{\frac{P_t}{E}}$, where B is the bending stiffness of 2-D sheet, E is Young's modulus, h is the thickness, P_t is the equivalent pressure of the driving forces, and α is a dimensionless parameter.

With the continuous deformation of 2-D sheets, the interactive binding energy will emerge and can be described by the energy in MSA, which is

$$E_{MSA} = \begin{cases} 0, L > L_0 \\ k_{MSA} L_0 (L_0 - L), L \leq L_0 \end{cases} \tag{5.4}$$

where k_{MSA} is the constant of the mechanical slider A and equals to the binding energy density γ_f of the 2-D sheet.

With the further evaporation of liquid, 2-D sheets will be deposited on the substrate and the adhesion energy between 2-D sheets and substrate will need to be considered. It reflects the influence of the substrate on the crumpling and assembling of 2-D sheets and can be defined as

$$E_{MSB} = \begin{cases} k_{MSB} L_0^2, R_c > L_0 \\ k_{MSB} L_0 R_c, R_c \leq L_0 \end{cases} \tag{5.5}$$

where k_{MSB} is the constant of mechanical slider B and equals to the binding energy density γ_{fs} between 2-D sheets and substrate.

In addition to the deformation energy E_{spring}, binding energy E_{MSA}, and adhesion energy E_{MSB}, the equivalent pressure P_t, which is the driving forces induced by liquid evaporation[192], will deform 2-D sheets and described by a potential energy E_p, which is

$$E_p = P_t \frac{\pi R_c^2 H}{3} \tag{5.6}$$

As a result, the total energy of the system is

$$E_{tot} = E_{spring} + E_{MSA} + E_{MSB} + E_p \tag{5.7}$$

$dE_{tot}/d(t/t_e) < 0$ is energy favorable of assembling 2-D sheets by liquid evaporation, where t_e is the real total evaporation time and t is the instantaneous time moment during liquid evaporation. $dE_{tot}/d(t/t_e)$ will increase as the evaporation continues, leading to a continues crumpling and assembling of 2-D sheets till to $dE_{tot}/d(t/t_e)$=0. When the assembling stops, the 2-D sheets will form a stable pattern due to the attractive van der Waals interaction among 2-D sheets (mechanical slider A) and between 2-D sheets and substrate (mechanical slider B). As an example, **Figure 5.4d** plots the variation of E_{spring},E_{MSA}, E_{MSB}, E_p and E_{tot} with the normalized evaporation time t/t_e for graphene sheets when θ_c^i=90°, θ_c^e=30°, R_c^i=150 nm, R_c^e=50 nm, A_t=48000 nm^2,$\gamma_{fs}/\gamma_f = 1$, and P_t=40 atm. With the liquid evaporation, L decreases. When $L \le L_0$, both E_{spring} and E_{MSA} (magnitude) increase due to the deformation and assembling of 2-D sheets. Both E_p and E_{MSB} decrease due to the decrease in liquid volume and contact radius. When $dE_{tot}/d(t/t_e)$=0, the assembling will stop and a stabilized deposited pattern of 2-D sheets can be obtained.

After complete evaporation of liquid, we can obtain the contact radius R_{cm} and height H_m of the assembled 2-D sheets. Further, the contact area is

$$A_{pr} = \pi R_{cm}^2 \tag{5.8}$$

And the aspect ratio is

$$\zeta = \frac{H_m}{2R_{cm}} \tag{5.9}$$

5.3 Computational Modeling and Methods

The large-scale coarse-grained molecular dynamics simulations are conducted to investigate the crumpling and assembling of 2-D sheets by liquid evaporation on a substrate and validate the theoretical analysis in Section 5.2. To increase the computational efficiency, the 2-D sheets are modeled by a 16:1 coarse-grained model of graphene, which has been validated in Section

3.3.1[192]. After that, the interaction of liquid molecules to graphene during liquid evaporation is replaced by an equivalent pressure P_t (**Figure 5.5**). If the graphene beads are exposed on the surface of the droplet, a constant force $F_p = P_t A_{bead}$ (A_{bead} is the area of graphene bead) pointing to the center of sphere of the droplet will be applied on the bead to provide a driving force for the crumpling and assembling of 2-D sheets.

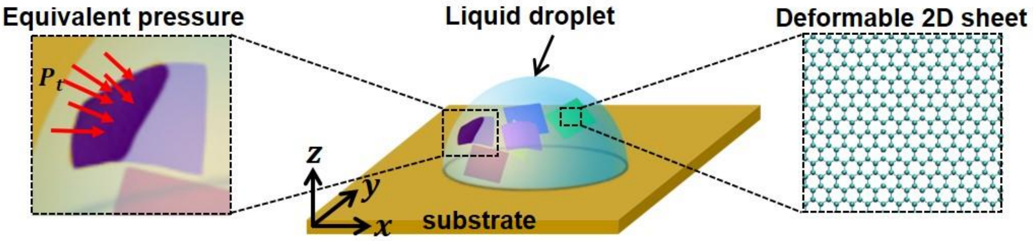

Figure 5.5. Simulation techniques for the crumpling and assembling of multiple 2-D sheets in a liquid droplet on the substrate. The 2-D sheet is a coarse-grained model of graphene with a coarse-graining scale 16:1. A constant force will be added on the beads of graphene if they are exposed on the surface of the droplet.

The substrate is modeled by a virtual plane (**Figure 5.5**), whose interaction with the 2-D sheet is modeled by a 12-6 L-J potential with potential well depth ϵ_{fs}, the parameter related to equilibrium distance σ=0.3629 nm, and cut-off radius 2.5σ. The binding energy density γ_{fs} between the 2-D sheet and the substrate is calculated by placing a 2-D sheet on the substrate (**Figure 5.6a**). The interactive van der Waals energy E_{vdW} between them is calculated after

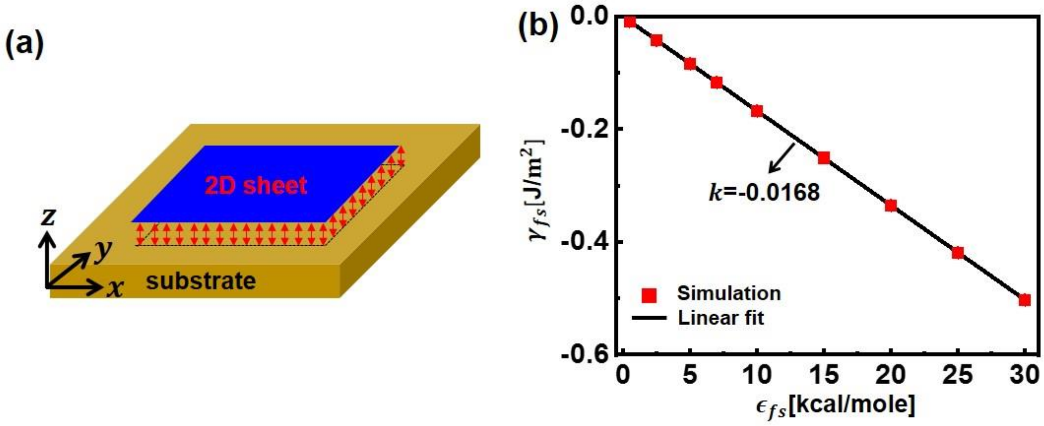

Figure 5.6. Calculation of the binding energy density between the 2-D sheet and the substrate in the simulation. (a) A 2-D sheet is placed on the substrate and their interaction is modeled by a 12-6 LJ potential. **(b)** Variation of the binding energy density γ_{fs} between 2-D sheet and substrate with the potential well depth ϵ_{fs} in the L-J potential.

the minimization of the system energy. The binding energy density can then be obtained via $\gamma_{fs} = E_{vdW}/A_g$, where A_g is the area of the 2-D sheet. By changing the values of potential well depth ϵ_{fs}, a one-to-one relationship between γ_{fs} and ϵ_{fs} can be obtained (**Figure 5.6b**). In the following simulation process, we can change the value of ϵ_{fs} to get certain γ_{fs}.

The evolution of liquid profile in the simulations is modeled by taking the liquid droplet on the substrate as a part of the whole sphere. **Figure 5.7** shows the 2-D schematics of the droplet. The origin of the coordinate system is on the substrate and the z axis is the axis of symmetry. The sphere has a radius R_d and its center is located at $(0, C_z)$ on the z-axis. For a given value of θ_c and R_c, we can get

$$R_d = \frac{R_c}{sin\theta_c} \tag{5.10}$$

and

$$C_z = \begin{cases} -(R_d^2 - R_c^2)^{\frac{1}{2}}, \theta_c \leq 90° \\ (R_d^2 - R_c^2)^{1/2}, \theta_c \leq 90° \end{cases} \tag{5.11}$$

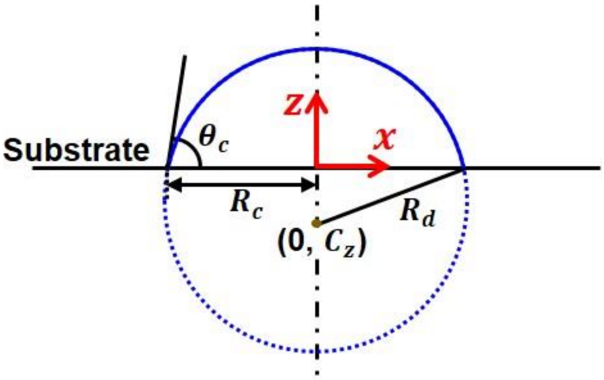

Figure 5.7. Schematics illustrate the position of the center C_z and radius R_d of a sphere. The liquid droplet on the substrate is a portion of the sphere and both its contact radius R_c and contact angle θ_c depend on C_z and R_d.

The simulation procedure consists of three steps: In the first step, the liquid droplet with contact angle θ_c^i and contact radius R_c^i is placed on the substrate. The initial position of graphene sheets is randomly distributed in the droplet. After that, the system is equilibrium at 300K and 1 atm for 1.0 ns with NVT ensemble under Noose/Hoover thermostat. In the second step, all the settings in the first step would remain the same except that the contact angle and contact radius of the virtual sphere change with time by following a well-defined function to mimic the evaporation process of the liquid droplet, which is $\theta_c = \theta_c^i + (\theta_c^e - \theta_c^i)(t_s - t_i)/t_e$, $(t_i < t_s < t_i + t_e)$, where t_s is the instantaneous time step during simulation, t_i is the time period required for the equilibrium of the system in the first step, and t_e is the time period for the droplet that changes from θ_c^i and R_c^i (initial contact angle and contact radius) to θ_c^e and R_c^e (final contact angle and contact radius). In the third step, the applied force F_p is removed at the end of evaporation. Another 2ns is performed under the NVT ensemble to monitor the final morphology of assembled graphene sheets and make sure it is stabilized.

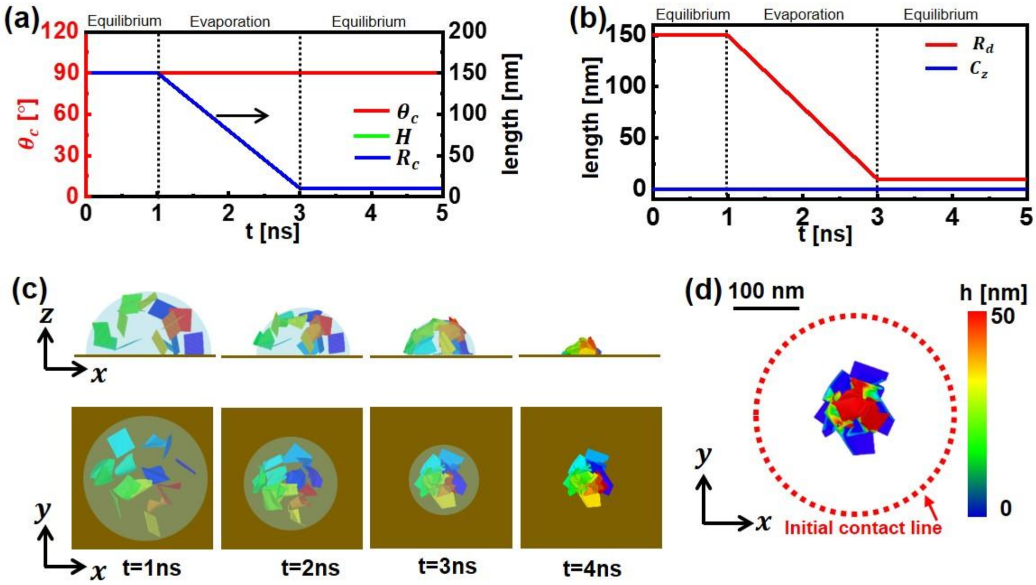

Figure 5.8. Variation of droplet profile and graphene morphology during the simulations when θ_c^i=90°, θ_c^e=90°, R_c^i=150 nm, R_c^e=10 nm, A_g^t=48000 nm^2, and P_t=40 atm (constant contact angle mode). (a) Variations of θ_c, H, and R_c with simulation time. **(b)** Variations of C_z and R_d with simulation time. **(c)** Snapshots from the side and top view in the simulations to show morphology evolutions of 2-D sheets during the liquid evaporation. **(d)** Morphology of the assembled 2-D sheets. The color bar indicates the height of the particles.

Figure 5.8a plots the variation of θ_c, R_c, and H with time during the simulations when θ_c^i=90°, θ_c^e=90°, R_c^i=150 nm, and R_c^e=10 nm (constant contact angle mode, route I in **Figure 5.2d**). **Figure 5.8b** plots the variation of R_d and C_z with time in correspondence to the variation of θ_c and R_c in Figure 5.8a. **Figure 5.8c** shows the side and top view of the snapshots during simulations and **Figure 5.8d** illustrates the top view of the final assembled pattern of graphene sheets with a color bar to indicate the height of graphene sheets.

Figure 5.9a plots the variation of θ_c, R_c, and H with time during the simulations when

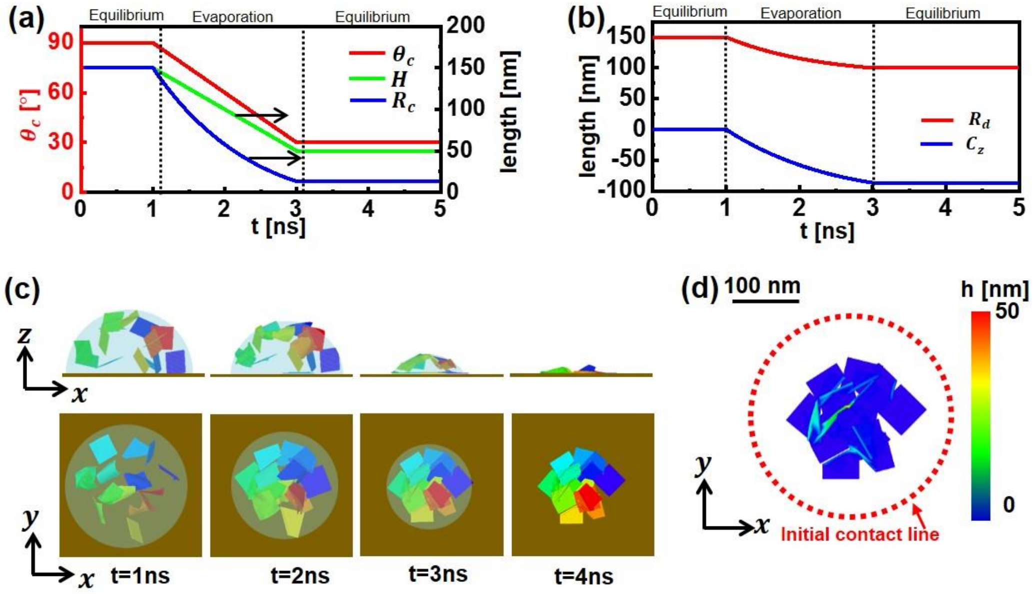

Figure 5.9. Variation of droplet profile and graphene morphology during the simulations when θ_c^i=90°, θ_c^e=30°, R_c^i=150 nm, R_c^e=50 nm, A_g^t=48000 nm^2, and P_t=40 atm (mixed mode). (a) Variations of θ_c, H, and R_c with simulation time. **(b)** Variations of C_z and R_d with simulation time. **(c)** Snapshots from the side and top view in the simulations to show morphology evolutions of 2-D sheets during the liquid evaporation. **(d)** Morphology of the assembled 2-D sheets. The color bar indicates the height of the particles.

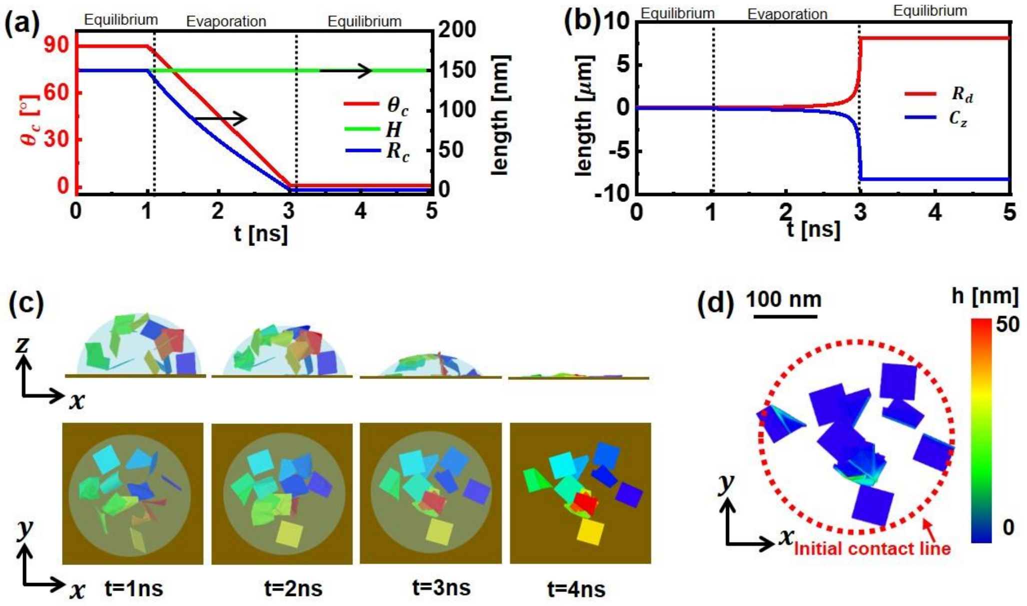

Figure 5.10. Variation of droplet profile and graphene morphology during the simulations when θ_c^i=90°, θ_c^e=1°, R_c^i=150 nm, R_c^e=150 nm, A_g^t=48000 nm^2, and P_t=40 atm (constant contact radius mode). (a) Variations of θ_c, H, and R_c with simulation time. **(b)** Variations of C_z and R_d with simulation time. **(c)** Snapshots from the side and top view in the simulations to show morphology evolutions of 2-D sheets during the liquid evaporation. **(d)** Morphology of the assembled 2-D sheets. The color bar indicates the height of the particles.

θ_c^i=*90*°, θ_c^e=*30*°, R_c^i=*150* nm, and R_c^e=*50* nm (mixed mode, route II in **Figure 5.2d**). **Figure 5.9b** plots the variation of R_d and C_z with time in correspondence to the variation of θ_c and R_c in Figure 5.9a. **Figure 5.9c** shows the side and top view of the snapshots during simulations and **Figure 5.9d** illustrates the top view of the final assembled pattern of graphene sheets with a color bar to indicate the height of graphene sheets.

Figure 5.10a plots the variation of θ_c, R_c, and H with time during the simulations when θ_c^i=*90*°, θ_c^e=*1*°, R_c^i=*150* nm, and R_c^e=*150* nm (constant contact radius mode, route III in **Figure 5.2d**). **Figure 5.10b** plots the variation of R_d and C_z with time in correspondence to the variation of θ_c and R_c in Figure 5.10a. **Figure 5.10c** shows the side and top view of the snapshots during simulations and **Figure 5.10d** illustrates the top view of the final assembled patterns of graphene sheets with a color bar to indicate the height of graphene sheets.

5.4 Contact Area and Aspect Ratio of Assembled Particles

As has been discussed in Section 5.2, both evaporation routes and interaction between graphene sheets and substrate could affect the final morphology of assembled graphene sheets. To illustrate the morphology evolution of assembled graphene sheets, simulations on a series of multiple graphene sheets under different evaporation routes and binding energy density between graphene sheets and substrate γ_{fs} are performed. **Figure 5.11** illustrates the assembled particles by 15 square graphene sheets with a size of 56.6 nm as a function of evaporation routes and normalized graphene-substrate binding energy density when the initial contact angle is kept at 90°. The top view of particles is shown and the height of particles is given to illustrate the local morphologies of particles. Along an evaporation route with higher κ^e/κ^i (route I, CCA) and on a substrate with lower γ_{fs}/γ_f, these multiple graphene sheets will experience assembly with very intensive deformation on individual graphene during evaporation, which is similar to the crumpling and assembling of graphene sheets in a free-standing liquid droplet. As a result, the assembled graphene sheets have a very small contact area with the substrate and higher height. Keep γ_{fs}/γ_f and decrease κ^e/κ^i (from route I to route III), the contact area will increase and the height will decrease. Similar results can also be observed by keeping evaporation route and increasing γ_{fs}/γ_f. With both lower κ^e/κ^i (route III, CCR) and higher γ_{fs}/γ_f, these graphene sheets will experience assembly with very limited deformation during evaporation. As a result, the assembled graphene sheets have a large contact area with the substrate and very low height.

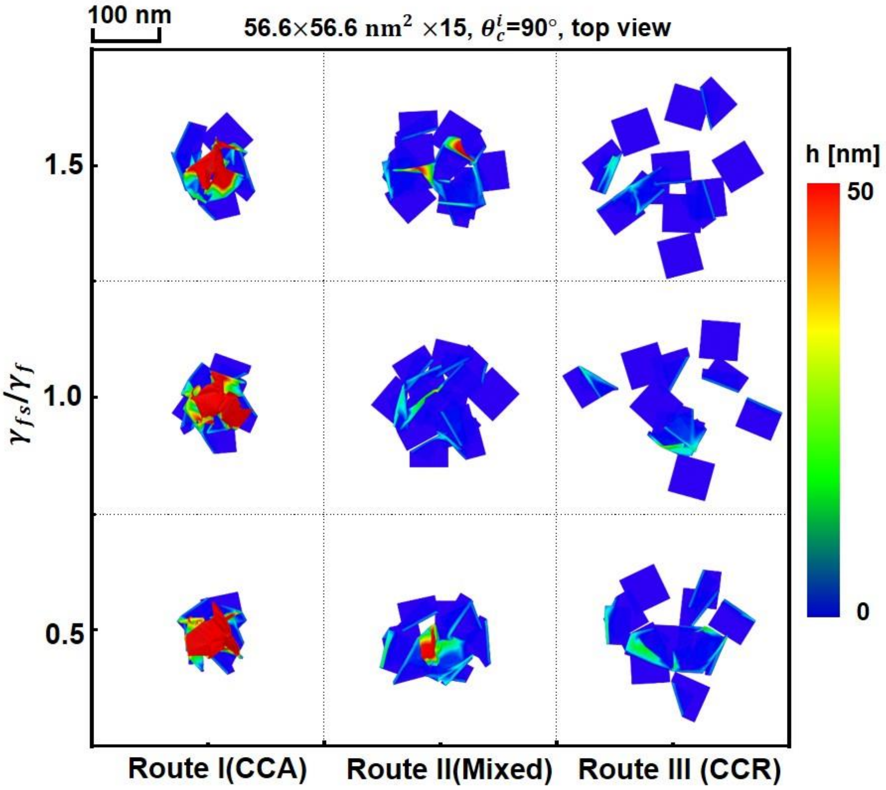

Figure 5.11. Top view of the assembled particles with the variation of evaporation route and binding energy density ratio. The initial contact angle is fixed at θ_c^i=90°. The color bar indicates the height of particles.

Figure 5.12 further illustrates the assembled particles as a function of evaporation routes and initial contact angles when the binding energy density is kept at γ_{fs}/γ_f=1. Same results can be observed by keeping the initial contact angle and decrease κ^e/κ^i (from route I to route III). At the same time, keeping the evaporation route (e.g. route I, CCA) and increasing the initial contact angle, these multiple graphene sheets will experience more intensive deformation during evaporation. As a result, the contact area of assembled particles will decrease and the height will increase. When $\theta_c^i = 180°$, the crumpling and assembling of graphene sheets will be independent of the substrate and the assembled particles will be the same as that fabricated by a free-standing droplet, which has been discussed in Chapter 3. When $\theta_c^i = 0°$, the assembling of graphene sheets will be independent of evaporation routes and the assembled particles will become uniformly deposited film on the substrate.

To quantitatively analyze the morphology of assembled particles and validate our theoretical analysis, **Figure 5.13** indicates the method to get the projected area A_{pr} and height H_m of the particles obtained from the simulations. To get A_{pr}, all the graphene beads are projected onto the $x-y$ plane and the center of mass of the particle is placed at the origin of the coordinate system (**Figure 5.13a**). Such projection is then be divided into n sectors. All the sectors share the same apex. The central angle of each sector can be obtained by $d\theta = 2\pi/n$ (**Figure 5.13a**). The distance of each bead to the apex in a single sector is calculated and the maximum value is selected, which corresponds to the outmost bead in the sector and the distance is denoted as R_{pr} (**Figure 5.13b**). Then we can get

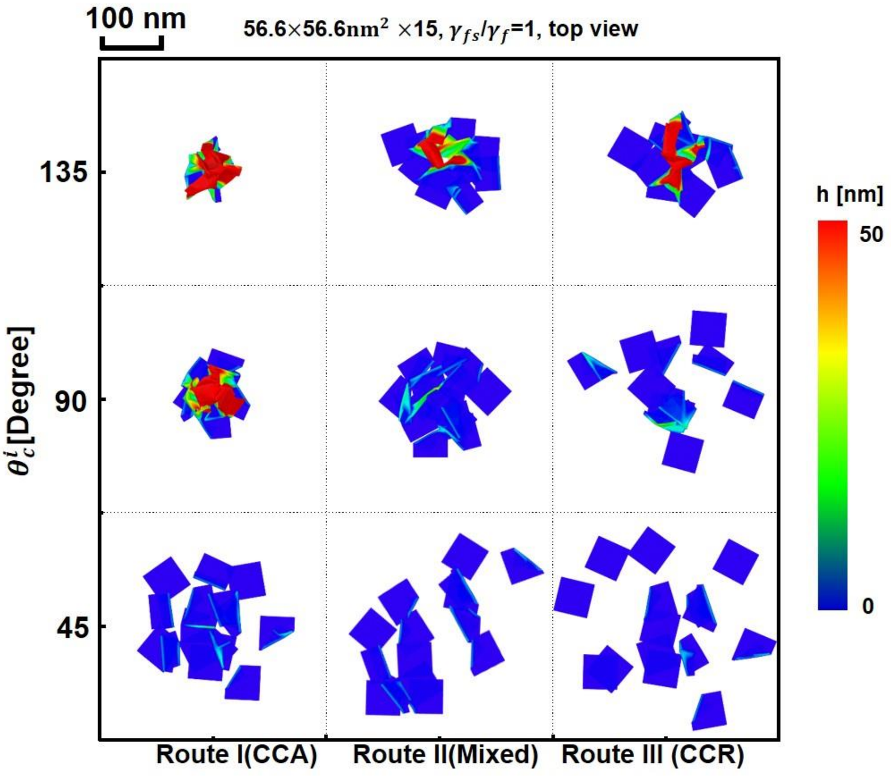

Figure 5.12. Top view of the assembled particles with the variation of evaporation route and initial contact angle. The binding energy density ratio is fixed at γ_{sg}/γ_g=1. The color bar indicates the height of particles.

$$A_{pr} = \frac{\pi}{n}\sum_{i=1}^{n}\left(R_{pr}^{i}\right)^2 \qquad (5.12)$$

After A_{pr} is obtained, the equivalent width d (**Figure 5.13b**) can be obtained by $d = 2\left(A_{pr}/\pi\right)^{1/2}$. Further, the particle can be mimicked by an oblique cone with width d and height H_m, where H_m is height of the assembled particle, and its aspect ratio is

$$\zeta = \frac{H_m}{d} \tag{5.13}$$

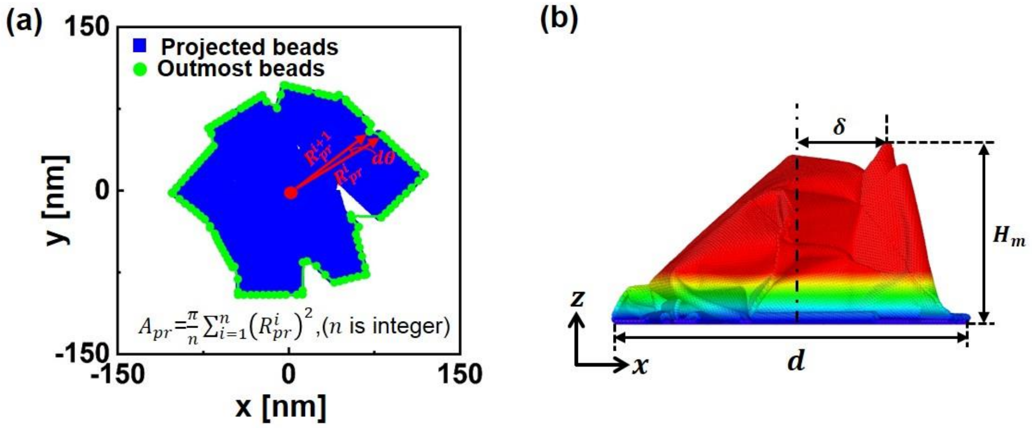

Figure 5.13. Methodology to characterize the morphology of assembled particles. (a) Top view to get the projected area of the particle. **(b)** Side view to get the height and aspect ratio of the particle.

After considering the synergistic effect of evaporation route and binding energy density, and incorporating the influence of initial contact angles, a unified parameter can be obtained to predict the morphologies of final assembled particles on the substrate, and it is

$$PU = g\left(\theta_c^i\right)\frac{\kappa^e/\kappa^i}{\gamma_{fs}/\gamma_f} \tag{5.14}$$

where $g\left(\theta_c^i\right) = \left[1 - cos\left(\theta_c^i\right)\right]^2\left[2 + cos\left(\theta_c^i\right)\right]$ is a dimensionless geometry to reflect the influences of initial contact angles. After this, **Figure 5.14a** gives the comparison of the normalized contact area A_{pr} / A_t between simulations and theoretical analysis. The experimental results are also included. Our theoretical predictions through Eq. (5.8) show remarkable agreement with both simulations and experimental results. The aspect ratio of assembled particles predicted by Eq. (5.9) also shows good agreement with the simulations, as is plotted in **Figure 5.14b.** The evaporation along route (I) experiences a much higher increase of surface curvature than other routes and generates particles with lower contact area and higher aspect ratio. On the contrary, the evaporation along route (III) experiences a much lower increase of surface curvature and generates particles with higher contact area and lower aspect

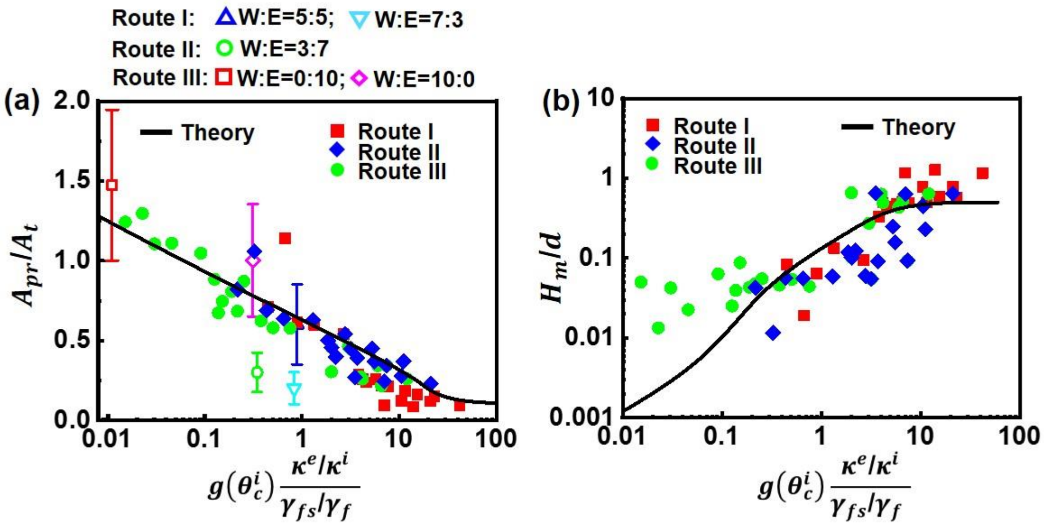

Figure 5.14. Comparison of the (a) projected area and (b) aspect ratio of particles between theoretical predictions and simulations. The experiment results are also included in (a) by evaporating 1μL graphene oxide solution in the water-ethanol mixture on Sylgard 184 10:1 PDMS film. W:E represents the volume ratio between water and ethanol in the mixture. The evaporation routes in experiments are also listed.

ratio. The significant differences among particles assembled along different evaporation routes further validate our evaporation route model and provide guidance to design particle morphologies by the liquid evaporation method.

5.5 Experimental Validation

To validate our theoretical predictions and verify our simulation results, evaporation experiments of a liquid droplet on a substrate are conducted by using graphene oxide (GO) solution in the water-ethanol mixture on different substrates (e.g. PDMS, Glass, VHB tape) at ambient condition. The concentration of GO is C=0.5 mg/mL and the volume of the droplet is V_d=1 μL. The droplet is small enough so that the influence of gravity on the profile of droplets can be neglected.

In the experiment, ramé-hart model 250 goniometer[217] (**Figure 5.15a**) was used to measure contact angle, contact radius, and height of droplet. A drop of GO solution was placed on the top side of a substrate (**Figure 5.15b**). The profile of droplets is recorded with the ramé-hart DROPimage software at a time interval of 10 seconds during the liquid evaporation process.

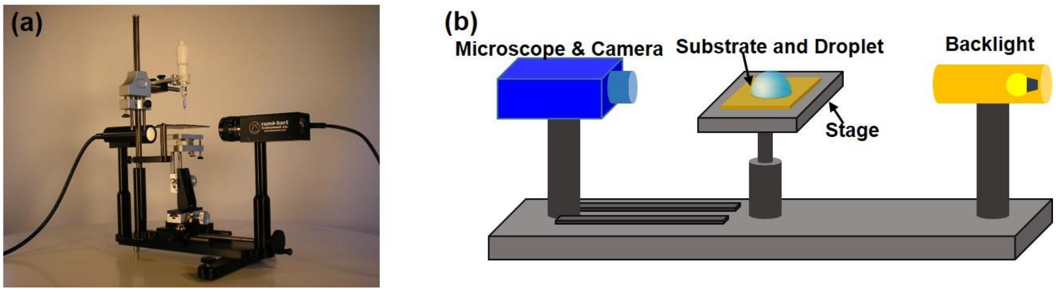

Figure 5.15. Equipment in the liquid evaporation experiment to measure contact angle, contact radius, and height of liquid droplet. (a) ramé-hart Model 250 Geniometer/Tensiometer with DROPimage Advanced[217]. **(b)** Schematics to show the measurement equipment.

Figure 5.16a shows snapshots of 1μL droplet with 0.5mg/mL GO in 70% water and 30% ethanol mixture on Sylgard 184 10:1 PDMS film during evaporation and the top view of the final deposited pattern. It can be observed from the snapshots that the contact radius is

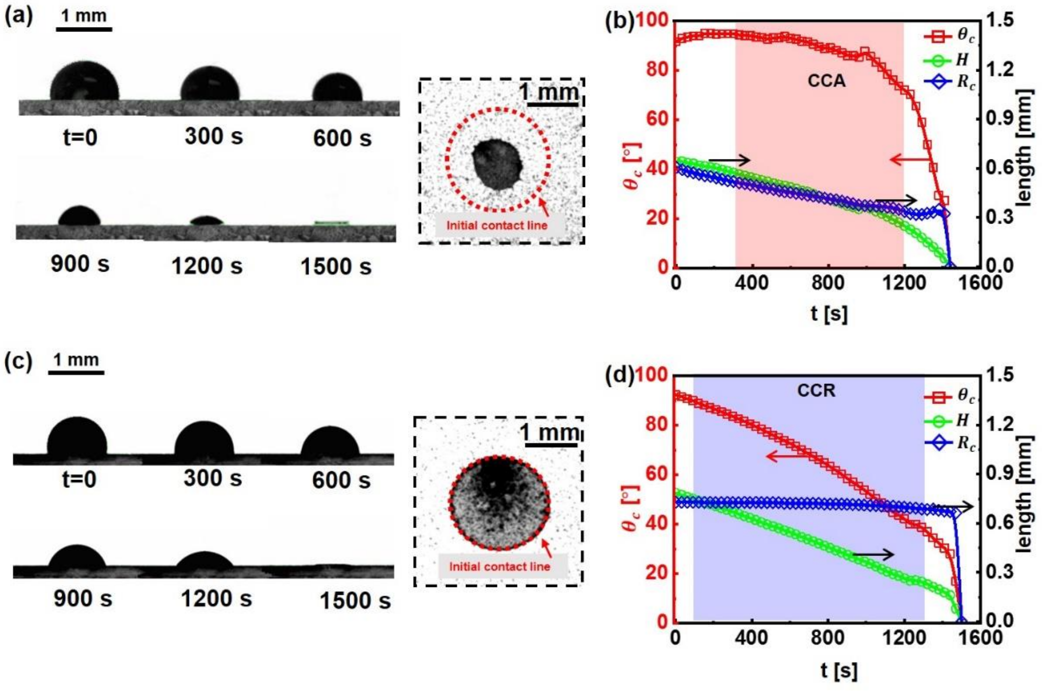

Figure 5.16. Profile evolution and deposited patterns of droplets contain GO suspension during liquid evaporation on a substrate. (a) Snapshots of 1μL droplet with 0.5mg/mL GO in 70% water and 30% ethanol mixture on Sylgard 184 10:1 PDMS film during evaporation and the top view of the final deposited pattern. The initial contact line is also shown. **(b)** Recorded contact angle θ_c, contact radius R_c, and height H of droplet during evaporation. A CCA mode can be obtained. **(c)** Snapshots of 1μL droplet with 0.5mg/mL GO in DI water on Sylgard 184 10:1 PDMS film during evaporation and the top view of the final deposited pattern. The initial contact line is also shown **(d)** Recorded contact angle θ_c, contact radius R_c, and height H of droplet during evaporation. A CCR mode can be obtained.

decreasing with liquid evaporation while the contact angle nearly does not change when t<1200s. As a result, the area of final deposited patterns is much smaller than the initial contact area. To compare the experimental results with our theoretical predictions and simulation results, the projected area A_{pr} is measured and is plotted in **Figure 5.14a**. Good agreement can be observed among theory, simulations, and experiments. This is further confirmed by the variation of contact angle θ_c, contact radius R_c, and height H with time during evaporation, where a CCA mode can be obtained when t<1200 s, as shown in **Figure 5.16b**.

Figure 5.16c shows snapshots of 1μL droplet with 0.5mg/mL GO in DI water on Sylgard 184 10:1 PDMS film during evaporation and the top view of the final deposited pattern. Unlike the droplet in **Figure 5.16a**, the contact angle keeps decreasing with liquid evaporation while the contact radius nearly does not change through the whole process. As a result, the area of final deposited patterns is nearly the same as the initial contact area. The CCR mode observed in **Figure 5.16d** further confirms this consistency.

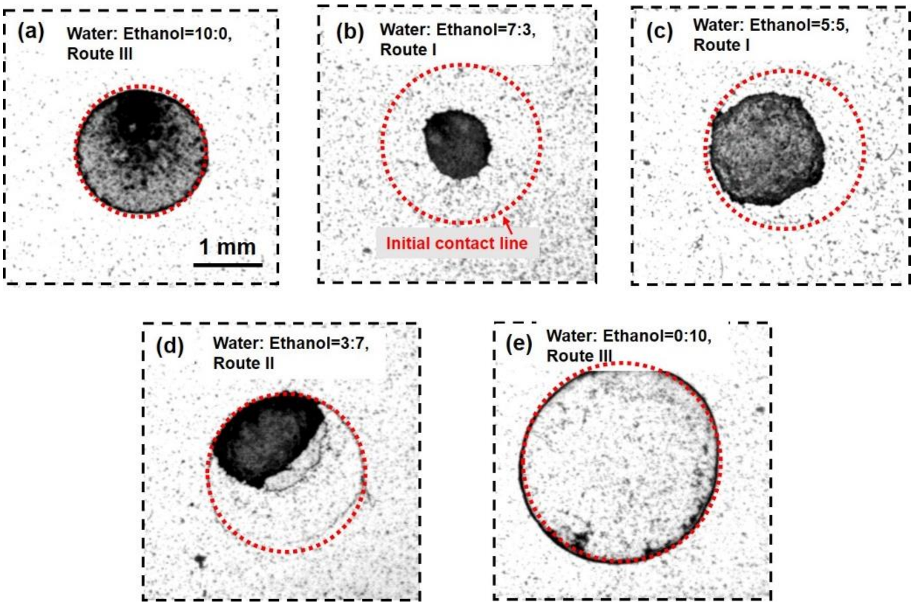

Figure 5.17. Final deposited patterns after complete evaporation of $1\mu L$ droplet contains graphene oxide in the water-ethanol mixtures on a Sylgard 184 10:1 PDMS film. The red dotted lines represent the initial contact lines before liquid evaporation. The evaporation route of the droplet during liquid evaporation for each pattern is also shown.

Figure 5.17 shows the final deposited patterns after complete liquid evaporation with 1 μL 0.5 mg/mL GO suspensions in the solution with different volume ratio between water and ethanol on a Sylgard 184 10:1 PDMS film. The initial contact line before evaporation occurs are also illustrated. The projected areas are calculated and are added in **Figure 5.14a**, which show good agreement with the theoretical predictions and simulation results.

5.6 Summary

We have proposed an evaporation route model to account for the influence of liquid profile evolution on the crumpling and assembling of 2-D deformable materials during liquid evaporation. The evolution of contact angle and contact radius before and after the liquid evaporation can all be described by the surface curvature of the droplet, which reflects the ability of the liquid to crumple and assembly the 2-D materials. The synergistic effect of the evaporation route and property of the substrate is further considered by a linear spring-mechanical slider model to quantitatively describe the crumpling and self-assembling of 2-D materials and adhesion on the substrate. The deformation of 2-D sheets is modeled by the energy stored in the linear spring connecting the three-phase contact line and apex of the droplet. A mechanical slider in parallel with the linear spring is introduced to take account of van der Waals binding energy in the overlapped parts of crumpled and assembled 2-D sheets. Another mechanical slider connecting the three-phase contact line and a fixed wall in parallel with the substrate is developed to describe the adhesion energy between 2-D sheets and the substrate. All of them are correlated with the profile of liquid droplet and the associated parameters are determined with the help of energy analysis. The energy competition among the linear springs and mechanical sliders are used to determine the final morphologies of assembled particles.

We have developed a coarse-grained molecular dynamics simulations method to validate the proposed theoretical model. The graphene sheet is selected and modeled by a 16:1 coarse-grained model to represent 2-D sheets. The liquid-induced driving force is replaced by an equivalent pressure to drive the crumpling and assembling of 2-D sheets. In the CGMD simulations, the droplet on the substrate is taken as a part of a whole sphere. The variation of contact angles and contact radius is achieved by formatting the position of center and radius of the sphere. Comprehensive CGMD simulations were performed to reveal the effect of evaporation route, film-substrate binding energy density, and initial contact angles on the morphology evolution of assembled particles.

We have also conducted an experimental investigation of liquid droplet evaporation on a substrate by utilizing graphene oxide solution in the water-ethanol mixtures. The evolution of contact angles, contact radius, and height of droplet during liquid evaporation is recorded. Different evaporation modes, like CCA and CCR mode can be obtained by changing the ratio between water and ethanol and different substrates. The morphologies of final deposited patterns in the experiments are characterized. The quantitative comparison of the morphologies among theoretical predictions, CGMD simulations, and experiments show good consistency.

Chapter 6 Conclusions and Future Work

6.1 Concluding Remarks

In this dissertation, we investigated the crumpling and assembling mechanism of low-dimensional nanomaterials under the liquid evaporation-induced driving forces and explored the morphologies and properties of the fabricated nanoparticles. We combined the theoretical analysis, computational simulations, and experimental investigations to elucidate the important role of mechanics in the extreme mechanics-driven nanomanufacturing of low-dimensional material-based 3-D architectures.

We start with the self-folding of a single free-standing 1-D nanofiber by liquid evaporation. We proposed a theoretical framework by considering the energy competition among liquid surface energy, solid-liquid interaction, deformation energy, and solid-solid interaction at overlap parts during evaporation. Based on this theory, two critical lengths of nanofiber, the elastocapillary length beyond which self-folding will continue by evaporation, and the critical self-folding length beyond which a stable folded pattern can be formed after complete evaporation of liquid, are obtained. Three typical energy favorable folded patterns of nanofiber, racket-like, spiral and helical patterns are identified. The effect of bending-induced stretching deformation, bending-induced local buckling deformation, and capillary flow-induced variation of cross-sections during evaporation are also discussed on the effect of self-folding and elucidated by introducing a cross-section factor of nanofibers.

Then, we extend the theoretical framework of a single 1-D nanofiber to describe the self-folding process of single graphene by liquid evaporation. Three representative geometries of graphene sheets, rectangular, circular, and triangular shapes, are studied. In addition to the critical elastocapillary length and critical self-folding length of graphene by liquid evaporation, a new critical length referred to as wet-capillary length, is given by considering the surface wettability of graphene. For different shapes of graphene (axial or central symmetry), the modes of deformation change, and eventually leads to various folded configurations, including 2-D “racket-like” for graphene with axial symmetry in geometry, and 3-D “cone-like” for graphene with central symmetry in geometry.

Further, we move to the crumpling and assembling of multiple 2-D materials in a free-standing liquid droplet by liquid evaporation. Firstly, an equivalent evaporation pressure model is developed to unify the driving force of crumpling and assembling 2-D materials by liquid evaporation. Secondly, guided by the continuum analysis of single 2-D sheet deformation on the surface of the liquid droplet, we propose a rotational spring-mechanical slider mechanics model to quantitatively describe the crumpling and self-assembling of 2-D material sheets suspended in liquid droplets. In this model, the rotational spring model is introduced to describe the out-of-plane large deformation of 2-D material sheets and the mechanical slider is developed to take account of van der Waal binding energy in overlaps of both self-folding deformation of individual sheets and self-assembly among multiple sheets. This model is used to understand the energy competition between crumpling and self-assembling deformation and predict the surface morphology and size of final assembled particles. Finally, we develop a 16:1 coarse-grained molecular dynamics (CGMD) model for graphene and also proposed a high-efficiency computational procedure to simulate solid-liquid interactions through a virtual spherical force field. We demonstrate that higher driving forces will promote the crumpling of individual 2-D sheet and hinder the inter-layer assembly among different sheets, generating the particles with higher surface ridge density. However, the overall sizes of particles are only a function of the total area of 2-D sheets in the particles and are independent of the magnitude of driving forces. The effect of geometric shape, number, size and area of 2-D material sheets on their evolution of energy and morphology during crumpling and assembling by liquid evaporation is also investigated and show a remarkable agreement among theoretical predictions, CGMD simulations, and experimental observations on both overall size and accessible area of assembled stable particle after the complete evaporation of liquid.

Inspired by the scalable accessible surface area and surface morphology of nanoparticles obtained from 2-D materials by liquid evaporation, we investigate the liquid evaporation-driven crumpling and assembling of CNTs/graphene hybrid nanomaterials in a free-standing droplet. Firstly, we theoretically demonstrate that the graphene will prefer to migrate and accumulate at the liquid/air interface while the CNTs stay inside the liquid droplet for their suspended liquid solution. As a result, the CNTs-encapsulated, crumpled graphene assembled composite nanoparticles could be formed by solution evaporation. Secondly, we combine the rotational spring-mechanical slider mechanics model of graphene with the mechanics model of packing of CNTs to predict the sizes, surface pore ratios, surface ridge density of fabricated particles. Finally, based on the structures and morphologies of the particles, we derive their accessible surface area, electrical conductivity, and stiffness. The presence of CNTs in the crumpled graphene particles could mitigate the inner structures and surface morphologies of particles significantly. When the mass fraction ratio of CNTs in the hybrid particles is lower, the particles tend to form a closed core-shell structure, with higher surface ridge density and lower accessible surface area. Increasing the mass fraction ratio of CNTs, the particles will become open-cell structures with lower surface ridge density and higher accessible surface area. By selecting the size and mass fraction of CNTs in the hybrid suspension before liquid evaporation, both the electrical conductivity, accessible surface areas, and mechanical strength of particles can be promoted.

Not limited to the evaporation of free-standing liquid droplets, we also include the liquid evaporation-driven crumpling and assembling of multiple 2-D nanomaterials on a substrate. Due to the existence of the substrate, the evaporation of liquid droplets presents different modes. Firstly, we propose an evaporation route model to unify the evolution of contact angle and contact radius during liquid evaporation by the surface curvature of the droplet. Secondly, the effect of the substrate is further considered by a linear spring-mechanical slider model to quantitatively describe the crumpling and self-assembling of 2-D materials and adhesion of 2-D materials on the substrate. The deformation of 2-D sheets is modeled by the energy stored in the linear spring connecting the three-phase contact line and apex of the droplet. A mechanical slider in parallel with the linear spring is introduced to take account of van der Waals binding energy in the overlapped parts of crumpled and assembled 2-D sheets. Another mechanical slider connecting the three-phase contact line and a fixed wall in parallel with the substrate is developed to describe the adhesion energy between 2-D sheets and the substrate. Finally, comprehensive coarse-grained molecular dynamics simulations is conducted to validate the proposed theoretical model. The variation of contact angles and contact radius are achieved by formatting the position of center and radius of the sphere. When the evaporation route has a higher increase of surface curvature and the substrate has a lower binding energy density with the 2-D materials, the assembled particle has a very small contact area with the substrate and higher height, which is similar to the particles obtained by evaporating a free-standing droplet. On the contrary, when the evaporation route has a lower increase of surface curvature and the substrate has a higher binding energy density with the 2-D materials, the assembled particle has a large contact area with the substrate and very low height, which is similar to the covering layer on the substrate. The quantitative comparison of the particle morphologies among theoretical predictions, CGMD simulations, and experiments is conducted and the results show good consistency with each other.

6.2 Recommendations for Future Work

The Manufacturing of low-dimensional nanomaterials with versatile structures and properties into functional 3-D architectures in a low-cost, high throughput fashion is always the top concern in the applications of low-dimensional nanomaterials, while the liquid evaporation-assisted manufacturing technique provides a facile route to address this challenge. The extreme mechanics proposed and elucidated in this thesis plays a leading role in this manufacturing process and is promised to achieve more breakthrough in broad view of nanomaterials and manufacturing techniques.

In addition to the homogeneous, pristine 1-D nanofiber and 2-D nanosheet being focused on in the current thesis, low-dimensional deformable nanomaterials that have functional groups[36, 218], defects[219, 220], and surface charge[221] are also desirable for the applications in functional devices. We have demonstrated that the mechanical properties and van der Waals interactions of low-dimensional materials are the key properties need to be considered and will govern the self-folding and assembling process during manufacturing. It is still an open and meaningful topic on how to incorporate the local inhomogeneous properties of low-dimensional nanomaterials in the theoretical models and computational modeling. It is also expected to control the structures and properties of fabricated 3-D architectures by designing the local properties and structures of low-dimensional materials before the liquid evaporation.

As discussed in Chapter 4, we investigate the crumpling and assembling mechanism of

CNTs/graphene hybrid suspensions during liquid evaporation, and the morphologies and performance of assembled particles can be significantly changed by manipulating the sizes and mass fraction ratio of CNTs. Inspired by such a 1-D/2-D mixture, the mixing of 0-D/1-D and 0-D/2-D materials, or the mixing of 2-D materials with different mechanical and van der Waals properties, such as graphene and molybdenum disulfide, is expected to generate more versatile properties of fabricated particles. At the same time, the development of fundamental mechanics theory which could incorporate the geometry mixture, soft-hard integration, and solid-liquid interaction would be a challenging topic with practical significance to pioneering the fabrication of novel architectures with unprecedented properties.

As discussed in Chapter 5, the existence of the substrate could significantly change the way of liquid evaporation and bring more possibilities to manipulate the morphologies of assembled particles. In addition to the planar and smooth substrate that has been focused on in this thesis, the substrate with local or overall non-zero curvature, surface morphologies, and patterning of surface wettability could largely change the profile as well as the evaporation process of a liquid droplet on it. Moreover, unlike the rigid substrate has no deformation during liquid evaporation, soft substrates will experience deformation either induced by the liquid or by external mechanical loadings and then influent the evaporation of liquid droplet on it. In the viewpoints of mechanics, it is an intriguing topic to develop the fundamental theoretical framework that could integrate the substrates with arbitrary surface properties and structures.

Beyond the properties of low-dimensional materials and substrates, the liquid evaporation-assisted manufacturing technique provides more possibilities to control the manufacturing process by external fields. For example, free-standing droplets of polar solution, such as water, is easier to deform under the electric field, which will generate ellipsoidal droplet instead of a perfect sphere[222]. As a result, the suspended low-dimensional materials will experience different driving forces with respect to the orientation of applied voltage. The morphologies and overall shapes of fabricated particles can then be controlled by the strength and direction of the applied electrical field. In addition to that, reorientation of liquid molecules and/or suspended materials under the external electric field will lead to polarization of the liquid-solid system and charge transfer within the droplet, which makes it possible to generate particles or surface protection films with preferred structures and properties. Moreover, in the electrospray technique, liquid droplets are generated by overcoming surface tension of liquid solution passing the nozzle through an applied high voltage between the nozzle and substrate and will be charged. During the flight of the sprayed droplets to the substrate, the charged droplets may rupture into numerous smaller ones with evaporation-induced volumetric shrinkage when the charge density residing on the droplet surface drastically exceeds the Rayleigh limit. This fission will limit a certain fractional amount of sheets before crumpling occurs, which in turn reduces the possibility of simple aggregation without crumpling. At the same time, this fission also provides a way to increase the resolution of printing, which is restricted by the size of nozzle in the traditional printing techniques. Therefore, the presence of electric fields is expected to further complicate this mechanism due to the surface charges of droplets. A comprehensive understanding and exploration of the underlying electro-hydrodynamic-induced mechanical deformation and assembly of low-dimensional materials may provide a new opportunity to manufacture low-dimensional materials-based 3-D porous particles. It may also lead to the development of new electrospray manufacturing techniques with the combined capability of producing 3-D porous particles and printing electronics devices with high sensitivities when the applied voltage is high enough.

Unlike to categorize the liquid droplet as “free-standing” and “on the substrate” and consider the evaporation of them separately in the manufacturing technique, the liquid evaporation is a successive process in 3D printing. During the flight of the sprayed droplets to the substrate, the solvent evaporation-induced capillary force will lead to self-assembly of the solid compositions inside the droplets, generating particles. If such evaporation is not complete, it will continue on the substrate. By carefully designing the nozzle-to-substrate distance, temperature field, and external fields in this manufacturing process, we can accurately manipulate the fraction of liquid evaporated during flight. Further, for the remaining evaporation process on the substrate, the temperature distribution of the substrate[223], vapor pressure[224], and applied voltage[225] can also be controlled to tune the morphologies of final assembled particles. This “Dual control” evaporation-assisted manufacturing technique is brand new and provides more maneuverability to obtain designated products in manufacturing. It also requires to combine the fundamental mechanics theory to describe the evaporation of “free-standing” and “on the substrate” seamlessly, which is challenging and fascinating.

Bibliography

1. Baughman, R.H., A.A. Zakhidov, and W.A. De Heer, *Carbon nanotubes--the route toward applications.* science, 2002. **297**(5582): p. 787-792.
2. Kotakoski, J., et al., *Toward two-dimensional all-carbon heterostructures via ion beam patterning of single-layer graphene.* Nano letters, 2015. **15**(9): p. 5944-5949.
3. Singh, S.K., M. Neek-Amal, and F. Peeters, *Electronic properties of graphene nano-flakes: energy gap, permanent dipole, termination effect, and Raman spectroscopy.* The Journal of chemical physics, 2014. **140**(7): p. 074304.
4. Li, L., et al., *Black phosphorus field-effect transistors.* Nature nanotechnology, 2014. **9**(5): p. 372.
5. Bonaccorso, F., et al., *Graphene photonics and optoelectronics.* Nature photonics, 2010. **4**(9): p. 611.
6. Novoselov, K.S., et al., *A roadmap for graphene.* nature, 2012. **490**(7419): p. 192-200.
7. Mak, K.F., et al., *Control of valley polarization in monolayer MoS 2 by optical helicity.* Nature nanotechnology, 2012. **7**(8): p. 494-498.
8. Yu, W.J., et al., *Highly efficient gate-tunable photocurrent generation in vertical heterostructures of layered materials.* Nature nanotechnology, 2013. **8**(12): p. 952.
9. Watanabe, K., T. Taniguchi, and H. Kanda, *Direct-bandgap properties and evidence for ultraviolet lasing of hexagonal boron nitride single crystal.* Nature materials, 2004. **3**(6): p. 404-409.
10. Zhi, C., et al., *Large‐scale fabrication of boron nitride nanosheets and their utilization in polymeric composites with improved thermal and mechanical properties.* Advanced Materials, 2009. **21**(28): p. 2889-2893.
11. Jiang, J.-W. and H.S. Park, *Negative poisson's ratio in single-layer black phosphorus.* Nature communications, 2014. **5**(1): p. 1-7.
12. Castellanos‐Gomez, A., et al., *Elastic properties of freely suspended MoS2 nanosheets.* Advanced Materials, 2012. **24**(6): p. 772-775.
13. Lee, C., et al., *Measurement of the elastic properties and intrinsic strength of monolayer graphene.* science, 2008. **321**(5887): p. 385-388.
14. Chen, S., et al., *Thermal conductivity of isotopically modified graphene.* Nature materials, 2012. **11**(3): p. 203-207.
15. Jo, I., et al., *Thermal conductivity and phonon transport in suspended few-layer hexagonal boron nitride.* Nano letters, 2013. **13**(2): p. 550-554.
16. Yan, R., et al., *Thermal conductivity of monolayer molybdenum disulfide obtained from temperature-dependent Raman spectroscopy.* ACS nano, 2014. **8**(1): p. 986-993.
17. Akinwande, D., et al., *A review on mechanics and mechanical properties of 2D materials—Graphene and beyond.* Extreme Mechanics Letters, 2017. **13**: p. 42-77.
18. Peigney, A., et al., *Specific surface area of carbon nanotubes and bundles of carbon nanotubes.* Carbon, 2001. **39**(4): p. 507-514.
19. Bao, H., et al., *Size-dependent elastic modulus of single-layer MoS2 nano-sheets.* Journal of Materials Science, 2016. **51**(14): p. 6850-6859.
20. Fan, X., X. Chen, and L. Dai, *3D graphene based materials for energy storage.*

Current Opinion in Colloid & Interface Science, 2015. **20**(5-6): p. 429-438.

21. Luo, J., H.D. Jang, and J. Huang, *Effect of sheet morphology on the scalability of graphene-based ultracapacitors.* ACS nano, 2013. **7**(2): p. 1464-1471.
22. Lim, T., et al., *Detection of chemicals in water using a three-dimensional graphene porous structure as liquid-vapor separation filter.* Nano Research, 2017. **10**(3): p. 971-979.
23. Sudeep, P.M., et al., *Covalently interconnected three-dimensional graphene oxide solids.* Acs Nano, 2013. **7**(8): p. 7034-7040.
24. Saththasivam, J., et al., *A Novel Architecture for Carbon Nanotube Membranes towards Fast and Efficient Oil/water Separation.* Sci Rep, 2018. **8**(1): p. 7418.
25. Diamant, H. and T.A. Witten, *Compression induced folding of a sheet: An integrable system.* Physical review letters, 2011. **107**(16): p. 164302.
26. Jin, L., A. Takei, and J.W. Hutchinson, *Mechanics of wrinkle/ridge transitions in thin film/substrate systems.* Journal of the Mechanics and Physics of Solids, 2015. **81**: p. 22-40.
27. Luo, J., et al., *Bulk nanostructured materials based on two-dimensional building blocks: a roadmap.* ACS nano, 2015. **9**(10): p. 9432-9436.
28. Cranford, S.W. and M.J. Buehler, *Packing efficiency and accessible surface area of crumpled graphene.* Physical Review B, 2011. **84**(20): p. 205451.
29. Tao, Y., et al., *Towards ultrahigh volumetric capacitance: graphene derived highly dense but porous carbons for supercapacitors.* Scientific reports, 2013. **3**: p. 2975.
30. Guan, K., et al., *Spray-evaporation assembled graphene oxide membranes for selective hydrogen transport.* Separation and Purification Technology, 2017. **174**: p. 126-135.
31. Zhou, Y., et al., *Three-dimensional crumpled graphene as an electro-catalyst support for formic acid electro-oxidation.* Journal of Materials Chemistry A, 2016. **4**(12): p. 4587-4591.
32. Liu, S., et al., *Crumpled graphene balls stabilized dendrite-free lithium metal anodes.* Joule, 2018. **2**(1): p. 184-193.
33. Deng, S. and V. Berry, *Wrinkled, rippled and crumpled graphene: an overview of formation mechanism, electronic properties, and applications.* Materials Today, 2016. **19**(4): p. 197-212.
34. Zhang, L., et al., *Porous 3D graphene-based bulk materials with exceptional high surface area and excellent conductivity for supercapacitors.* Scientific reports, 2013. **3**: p. 1408.
35. Li, H., et al., *Compressed porous graphene particles for use as supercapacitor electrodes with excellent volumetric performance.* Nanoscale, 2015. **7**(44): p. 18459-18463.
36. Zheng, Q., et al., *Effects of functional groups on the mechanical and wrinkling properties of graphene sheets.* Carbon, 2010. **48**(15): p. 4315-4322.
37. Warner, J.H., et al., *Rippling graphene at the nanoscale through dislocation addition.* Nano letters, 2013. **13**(10): p. 4937-4944.
38. Zhang, K. and M. Arroyo, *Understanding and strain-engineering wrinkle networks in supported graphene through simulations.* Journal of the Mechanics and Physics of

Solids, 2014. **72**: p. 61-74.

39. Ling, Y., et al., *Mechanically Assembled, Three-Dimensional Hierarchical Structures of Cellular Graphene with Programmed Geometries and Outstanding Electromechanical Properties.* ACS Nano, 2018.
40. Bao, W., et al., *Controlled ripple texturing of suspended graphene and ultrathin graphite membranes.* Nat Nanotechnol, 2009. **4**(9): p. 562-6.
41. Reddy, C.D. and Y.-W. Zhang, *Structure manipulation of graphene by hydrogenation.* Carbon, 2014. **69**: p. 86-91.
42. Warner, J.H., et al., *Rippling graphene at the nanoscale through dislocation addition.* Nano Lett, 2013. **13**(10): p. 4937-44.
43. Xu, B. and J.A. Rogers, *Mechanics-driven approaches to manufacturing—a perspective.* Extreme Mechanics Letters, 2016. **7**: p. 44-48.
44. Hao, W., et al., *Crumpled graphene ball-based broadband solar absorbers.* Nanoscale, 2018. **10**(14): p. 6306-6312.
45. Mao, S., et al., *A General Approach to One-Pot Fabrication of Crumpled Graphene-Based Nanohybrids for Energy Applications.* Acs Nano, 2012. **6**(8): p. 7505-7513.
46. Luo, J., et al., *Crumpled Graphene-Encapsulated Si Nanoparticles for Lithium Ion Battery Anodes.* J Phys Chem Lett, 2012. **3**(13): p. 1824-9.
47. Luo, J., et al., *Compression and aggregation-resistant particles of crumpled soft sheets.* ACS nano, 2011. **5**(11): p. 8943-8949.
48. Yang, J., et al., *A Highly Efficient Metal-Free Oxygen Reduction Electrocatalyst Assembled from Carbon Nanotubes and Graphene.* Adv Mater, 2016. **28**(23): p. 4606-13.
49. Parviz, D., et al., *Tailored Crumpling and Unfolding of Spray-Dried Pristine Graphene and Graphene Oxide Sheets.* Small, 2015. **11**(22): p. 2661-8.
50. Nie, Y., Y. Wang, and P. Biswas, *Mobility and Bipolar Diffusion Charging Characteristics of Crumpled Reduced Graphene Oxide Nanoparticles Synthesized in a Furnace Aerosol Reactor.* The Journal of Physical Chemistry C, 2017. **121**(19): p. 10529-10537.
51. Jiang, Y., et al., *Graphene Oxides in Water: Correlating Morphology and Surface Chemistry with Aggregation Behavior.* Environ Sci Technol, 2016. **50**(13): p. 6964-73.
52. Kavadiya, S., et al., *Crumpling of graphene oxide through evaporative confinement in nanodroplets produced by electrohydrodynamic aerosolization.* Journal of Nanoparticle Research, 2017. **19**(2).
53. Luo, J., J. Kim, and J. Huang, *Material processing of chemically modified graphene: some challenges and solutions.* Accounts of chemical research, 2013. **46**(10): p. 2225-2234.
54. Dou, X., et al., *Self-dispersed crumpled graphene balls in oil for friction and wear reduction.* Proceedings of the National Academy of Sciences, 2016. **113**(6): p. 1528-1533.
55. Zang, J., et al., *Stretchable and high-performance supercapacitors with crumpled graphene papers.* Sci Rep, 2014. **4**: p. 6492.
56. Ha, T., et al., *pH controlled synthesis of porous graphene sphere and application to supercapacitors.* Advanced Powder Technology, 2019. **30**(1): p. 18-22.

57. Chen, Z., et al., *Three-Dimensional Crumpled Graphene-Based Nanosheets with Ultrahigh NO2 Gas Sensibility.* Acs Applied Materials & Interfaces, 2017. **9**(13): p. 11819-11827.
58. Ramanathan T, et al., *Functionalized graphene sheets for polymer nanocomposites.* Nature Nanotechnology, 2008. **3**(6): p. 327-331.
59. Park, S.-H., et al., *Spray-Assisted Deep-Frying Process for the In Situ Spherical Assembly of Graphene for Energy-Storage Devices.* Chemistry of Materials, 2015. **27**(2): p. 457-465.
60. Choi, S.H., et al., *Rapid continuous synthesis of spherical reduced graphene ball-nickel oxide composite for lithium ion batteries.* Scientific Reports, 2014. **4**.
61. Chen, Y.-C., et al., *Structurally Deformed MoS2 for Electrochemically Stable, Thermally Resistant, and Highly Efficient Hydrogen Evolution Reaction.* Advanced Materials, 2017. **29**(44): p. 1703863.
62. Zhang, X., et al., *Evaporation-induced flattening and self-assembly of chemically converted graphene on a solid surface.* Soft Matter, 2011. **7**(19): p. 8745.
63. Wang, Y., et al., *Stitching chemically converted graphene on solid surfaces by solvent evaporation.* ACS Appl Mater Interfaces, 2012. **4**(12): p. 6443-9.
64. Lauga, E. and M.P. Brenner, *Evaporation-driven assembly of colloidal particles.* Physical review letters, 2004. **93**(23): p. 238301.
65. Vogel, N., et al., *Advances in colloidal assembly: the design of structure and hierarchy in two and three dimensions.* Chemical reviews, 2015. **115**(13): p. 6265-6311.
66. Matsumoto, T., et al., *Mechanical strain regulates endothelial cell patterning in vitro.* Tissue engineering, 2007. **13**(1): p. 207-217.
67. Ceccarelli, J., A. Cheng, and A.J. Putnam, *Mechanical strain controls endothelial patterning during angiogenic sprouting.* Cellular and molecular bioengineering, 2012. **5**(4): p. 463-473.
68. Liu, H., Y. Liu, and D. Zhu, *Chemical doping of graphene.* Journal of materials chemistry, 2011. **21**(10): p. 3335-3345.
69. Zhou, C., et al., *Modulated chemical doping of individual carbon nanotubes.* Science, 2000. **290**(5496): p. 1552-1555.
70. Sinnott, S.B., et al., *Model of carbon nanotube growth through chemical vapor deposition.* Chemical Physics Letters, 1999. **315**(1-2): p. 25-30.
71. Liu, J.-L. and X.-Q. Feng, *On elastocapillarity: A review.* Acta Mechanica Sinica, 2012. **28**(4): p. 928-940.
72. Chen, B., et al., *Binding energy of parallel carbon nanotubes.* Applied Physics Letters, 2003. **83**(17): p. 3570.
73. Zhou, W., et al., *Self-folding of single- and multiwall carbon nanotubes.* Applied Physics Letters, 2007. **90**(7): p. 073107.
74. Israelachvili, J. and R. Pashley, *The hydrophobic interaction is long range, decaying exponentially with distance.* Nature, 1982. **300**(5890): p. 341-342.
75. Israelachvili, J. and R. Pashley, *Measurement of the hydrophobic interaction between two hydrophobic surfaces in aqueous electrolyte solutions.* Journal of colloid and interface science, 1984. **98**(2): p. 500-514.

76. Meyer, E.E., K.J. Rosenberg, and J. Israelachvili, *Recent progress in understanding hydrophobic interactions.* Proceedings of the National Academy of Sciences, 2006. **103**(43): p. 15739-15746.
77. Wang, W.N., Y. Jiang, and P. Biswas, *Evaporation-Induced Crumpling of Graphene Oxide Nanosheets in Aerosolized Droplets: Confinement Force Relationship.* J Phys Chem Lett, 2012. **3**(21): p. 3228-33.
78. Tang, Z., et al., *Controllable crumpling of N-doped graphene induced by capillary force resistance.* RSC Advances, 2016. **6**(90): p. 87796-87801.
79. Gittens, G., *Variation of surface tension of water with temperature.* Journal of Colloid and Interface Science, 1969. **30**(3): p. 406-412.
80. Crandall, S.H., *An introduction to Mechanics of Solids*. 2012: Tata McGraw-Hill Education.
81. To, C.W.S., *Bending and shear moduli of single-walled carbon nanotubes.* Finite Elements in Analysis and Design, 2006. **42**(5): p. 404-413.
82. Ismail, A.E., G.S. Grest, and M.J. Stevens, *Capillary waves at the liquid-vapor interface and the surface tension of water.* J Chem Phys, 2006. **125**(1): p. 014702.
83. Laaksonen, A., R. McGraw, and H. Vehkamäki, *Liquid-drop formalism and free-energy surfaces in binary homogeneous nucleation theory.* The Journal of Chemical Physics, 1999. **111**(5): p. 2019-2027.
84. Walther, J.H., et al., *Carbon nanotubes in water: structural characteristics and energetics.* The Journal of Physical Chemistry B, 2001. **105**(41): p. 9980-9987.
85. Buehler, M.J., et al., *Self-Folding and Unfolding of Carbon Nanotubes.* Journal of Engineering Materials and Technology, 2006. **128**(1): p. 3.
86. Cohen, A.E. and L. Mahadevan, *Kinks, rings, and rackets in filamentous structures.* Proc Natl Acad Sci U S A, 2003. **100**(21): p. 12141-6.
87. Martel, R., H.R. Shea, and P. Avouris, *Rings of single-walled carbon nanotubes.* Nature, 1999. **398**(6725): p. 299-299.
88. Wang, Z.L., *ZnO nanowire and nanobelt platform for nanotechnology.* Materials Science and Engineering: R: Reports, 2009. **64**(3-4): p. 33-71.
89. Kong, X.Y. and Z.L. Wang, *Spontaneous polarization-induced nanohelixes, nanosprings, and nanorings of piezoelectric nanobelts.* Nano Letters, 2003. **3**(12): p. 1625-1632.
90. Bernaerts, D., et al., *Electron microscopy study of coiled carbon tubules.* Philosophical Magazine A, 1995. **71**(3): p. 605-630.
91. Annett, J. and G.L.W. Cross, *Self-assembly of graphene ribbons by spontaneous self-tearing and peeling from a substrate.* Nature, 2016. **535**(7611): p. 271-275.
92. Zhang, J., et al., *Free folding of suspended graphene sheets by random mechanical stimulation.* Phys Rev Lett, 2010. **104**(16): p. 166805.
93. Cranford, S., D. Sen, and M.J. Buehler, *Meso-origami: Folding multilayer graphene sheets.* Applied Physics Letters, 2009. **95**(12): p. 123121.
94. Fakhri, N., et al., *Diameter-dependent bending dynamics of single-walled carbon nanotubes in liquids.* Proc Natl Acad Sci U S A, 2009. **106**(34): p. 14219-23.
95. Schulman, R.D., et al., *Elastocapillary bending of microfibers around liquid droplets.* Soft Matter, 2017. **13**(4): p. 720-724.

96. Krishnan, A., et al., *Young's modulus of single-walled nanotubes.* Physical Review B, 1998. **58**(20): p. 14013.
97. Chen, F. and P.E. Smith, *Simulated surface tensions of common water models.* J Chem Phys, 2007. **126**(22): p. 221101.
98. Vega, C. and E. de Miguel, *Surface tension of the most popular models of water by using the test-area simulation method.* J Chem Phys, 2007. **126**(15): p. 154707.
99. Liu, Q., Y. Gao, and B. Xu, *Liquid evaporation-driven folding of graphene sheets.* Applied Physics Letters, 2016. **108**(14): p. 141906.
100. Zhao, J., et al., *Coarse-grained potentials of single-walled carbon nanotubes.* Journal of the Mechanics and Physics of Solids, 2014. **71**: p. 197-218.
101. Chen, H., et al., *Energy dissipation capability and impact response of carbon nanotube buckypaper: A coarse-grained molecular dynamics study.* Carbon, 2016. **103**: p. 242-254.
102. Plimpton, S., *LAMMPS user's manual.* Sandia National Laboratory, 2005.
103. Liu, Q. and B. Xu, *Actuating Water Droplets on Graphene via Surface Wettability Gradients.* Langmuir, 2015. **31**(33): p. 9070-9075.
104. Zhao, J., et al., *Binding energy and mechanical stability of two parallel and crossing carbon nanotubes.* Proceedings of the Royal Society A: Mathematical, Physical and Engineering Science, 2015. **471**(2180): p. 20150229.
105. Mark, P. and L. Nilsson, *Structure and dynamics of the TIP3P, SPC, and SPC/E water models at 298 K.* The Journal of Physical Chemistry A, 2001. **105**(43): p. 9954-9960.
106. Plimpton, S., *Fast parallel algorithms for short-range molecular dynamics.* Journal of computational physics, 1995. **117**(1): p. 1-19.
107. Wang, G.F., X.Q. Feng, and S.W. Yu, *Surface buckling of a bending microbeam due to surface elasticity.* Europhysics Letters (EPL), 2007. **77**(4): p. 44002.
108. Wang, G.-F. and X.-Q. Feng, *Surface effects on buckling of nanowires under uniaxial compression.* Applied Physics Letters, 2009. **94**(14): p. 141913.
109. Vodenitcharova, T. and L.C. Zhang, *Mechanism of bending with kinking of a single-walled carbon nanotube.* Physical Review B, 2004. **69**(11).
110. Lourie, O., D. Cox, and H. Wagner, *Buckling and collapse of embedded carbon nanotubes.* Physical Review Letters, 1998. **81**(8): p. 1638.
111. Cao, G. and X. Chen, *Buckling of single-walled carbon nanotubes upon bending: Molecular dynamics simulations and finite element method.* Physical Review B, 2006. **73**(15).
112. Lestringant, C., et al., *Buckling of an Elastic Ridge: Competition between Wrinkles and Creases.* Phys Rev Lett, 2017. **118**(16): p. 165501.
113. Mylvaganam, K., T. Vodenitcharova, and L.C. Zhang, *The bending-kinking analysis of a single-walled carbon nanotube—a combined molecular dynamics and continuum mechanics technique.* Journal of Materials Science, 2006. **41**(11): p. 3341-3347.
114. Li, B., et al., *Mechanics of morphological instabilities and surface wrinkling in soft materials: a review.* Soft Matter, 2012. **8**(21): p. 5728.
115. Wang, C.G., et al., *Buckling behavior of carbon nanotubes under bending: From ripple to kink.* Carbon, 2016. **102**: p. 224-235.
116. Yakobson, B.I., C. Brabec, and J. Bernholc, *Nanomechanics of carbon tubes:*

instabilities beyond linear response. Physical review letters, 1996. **76**(14): p. 2511.

117. Hoberg, T.B., E. Verneuil, and A.E. Hosoi, *Elastocapillary flows in flexible tubes.* Physics of Fluids, 2014. **26**(12): p. 122103.
118. Liu, Y. and B.I. Yakobson, *Cones, pringles, and grain boundary landscapes in graphene topology.* Nano Lett, 2010. **10**(6): p. 2178-83.
119. Lu, Q. and R. Huang, *Excess energy and deformation along free edges of graphene nanoribbons.* Physical Review B, 2010. **81**(15).
120. Patra, N., B. Wang, and P. Král, *Nanodroplet activated and guided folding of graphene nanostructures.* Nano letters, 2009. **9**(11): p. 3766-3771.
121. Roman, B. and J. Bico, *Elasto-capillarity: deforming an elastic structure with a liquid droplet.* J Phys Condens Matter, 2010. **22**(49): p. 493101.
122. Li, M., et al., *Capillary Origami Inspired Fabrication of Complex 3D Hydrogel Constructs.* Small, 2016. **12**(33): p. 4492-500.
123. de Gennes, P.G., *Wetting: statics and dynamics.* Reviews of Modern Physics, 1985. **57**(3): p. 827-863.
124. Alben, S., B. Balakrisnan, and E. Smela, *Edge effects determine the direction of bilayer bending.* Nano Lett, 2011. **11**(6): p. 2280-5.
125. Werder, T., et al., *On the water− carbon interaction for use in molecular dynamics simulations of graphite and carbon nanotubes.* The Journal of Physical Chemistry B, 2003. **107**(6): p. 1345-1352.
126. Zhang, Y., Q. Liu, and B. Xu, *Self-Folding Mechanics of Surface Wettability Patterned Graphene Nanoribbons by Liquid Evaporation.* Journal of Applied Mechanics, 2017. **85**(2): p. 021006-021006-9.
127. Rivetti, M. and A. Antkowiak, *Elasto-capillary meniscus: pulling out a soft strip sticking to a liquid surface.* Soft Matter, 2013. **9**(27): p. 6226.
128. Bueno, J., et al., *Three-dimensional dynamic simulation of elastocapillarity.* Meccanica, 2017.
129. Meng, X., et al., *Mechanics of self-folding of single-layer graphene.* Journal of Physics D: Applied Physics, 2013. **46**(5): p. 055308.
130. Plimpton, S., P. Crozier, and A. Thompson, *LAMMPS-large-scale atomic/molecular massively parallel simulator.* Sandia National Laboratories, 2007. **18**.
131. Stuart, S.J., A.B. Tutein, and J.A. Harrison, *A reactive potential for hydrocarbons with intermolecular interactions.* The Journal of chemical physics, 2000. **112**(14): p. 6472-6486.
132. Brenner, D.W., et al., *A second-generation reactive empirical bond order (REBO) potential energy expression for hydrocarbons.* Journal of Physics: Condensed Matter, 2002. **14**(4): p. 783.
133. Werder, T., et al., *On the water− carbon interaction for use in molecular dynamics simulations of graphite and carbon nanotubes.* The Journal of Physical Chemistry B, 2003. **107**(6): p. 1345-1352.
134. Okuyama, K. and I. Wuled Lenggoro, *Preparation of nanoparticles via spray route.* Chemical Engineering Science, 2003. **58**(3): p. 537-547.
135. Deegan, R.D., et al., *Capillary flow as the cause of ring stains from dried liquid drops.* Nature, 1997. **389**(6653): p. 827-829.

136. Nikolayev, V.S., et al., *Experimental evidence of the vapor recoil mechanism in the boiling crisis.* Phys Rev Lett, 2006. **97**(18): p. 184503.
137. Schmatko, T., H. Hervet, and L. Leger, *Friction and Slip at Simple Fluid-Solid Interfaces: The Roles of the Molecular Shape and the Solid-Liquid Interaction.* Physical Review Letters, 2005. **94**(24).
138. Paulsen, J.D., et al., *Optimal wrapping of liquid droplets with ultrathin sheets.* Nat Mater, 2015. **14**(12): p. 1206-9.
139. Hure, J. and B. Audoly, *Capillary buckling of a thin film adhering to a sphere.* Journal of the Mechanics and Physics of Solids, 2013. **61**(2): p. 450-471.
140. Liu, Q. and B. Xu, *Two- and three-dimensional self-folding of free-standing graphene by liquid evaporation.* Soft Matter, 2018. **14**(29): p. 5968-5976.
141. Vincenti, W.G. and C.H. Kruger, *Introduction to physical gas dynamics*. Vol. 246. 1965: Wiley New York.
142. Thomson, W., *4. On the equilibrium of vapour at a curved surface of liquid.* Proceedings of the Royal Society of Edinburgh, 1872. **7**: p. 63-68.
143. Huang, X., et al., *Coordinated buckling of thick multi-walled carbon nanotubes under uniaxial compression.* Nano Research, 2010. **3**(1): p. 32-42.
144. Hibbeler, R., *Mechanical properties of materials.* Mechanics of Materials, 8th Edition, Prentice Hall, 2011: p. 81-117.
145. Sugden, S., *VI.—The variation of surface tension with temperature and some related functions.* Journal of the Chemical Society, Transactions, 1924. **125**: p. 32-41.
146. Freire, M.G., et al., *Surface tensions of imidazolium based ionic liquids: Anion, cation, temperature and water effect.* Journal of Colloid and Interface Science, 2007. **314**(2): p. 621-630.
147. Chen, F. and P.E. Smith, *Simulated surface tensions of common water models*. 2007, AIP.
148. Liu, Q. and B. Xu, *A unified mechanics model of wettability gradient-driven motion of water droplet on solid surfaces.* Extreme Mechanics Letters, 2016. **9**: p. 304-309.
149. Tocci, G., L. Joly, and A. Michaelides, *Friction of water on graphene and hexagonal boron nitride from ab initio methods: very different slippage despite very similar interface structures.* Nano Lett, 2014. **14**(12): p. 6872-7.
150. Hu, H. and R.G. Larson, *Analysis of the microfluid flow in an evaporating sessile droplet.* Langmuir, 2005. **21**(9): p. 3963-3971.
151. Kim, J., et al., *Visualizing graphene based sheets by fluorescence quenching microscopy.* Journal of the American Chemical Society, 2009. **132**(1): p. 260-267.
152. Vliegenthart, G.A. and G. Gompper, *Forced crumpling of self-avoiding elastic sheets.* Nat Mater, 2006. **5**(3): p. 216-21.
153. Zhou, Y., et al., *Mechanics of nanoscale wrinkling of graphene on a non-developable surface.* Carbon, 2015. **84**: p. 263-271.
154. King, H., et al., *Elastic sheet on a liquid drop reveals wrinkling and crumpling as distinct symmetry-breaking instabilities.* Proceedings of the National Academy of Sciences, 2012. **109**(25): p. 9716-9720.
155. Zhang, Q. and J. Yin, *Spontaneous buckling-driven periodic delamination of thin films on soft substrates under large compression.* Journal of the Mechanics and Physics of

Solids, 2018. **118**: p. 40-57.
156. Oshri, O., F. Brau, and H. Diamant, *Wrinkles and folds in a fluid-supported sheet of finite size.* Phys Rev E Stat Nonlin Soft Matter Phys, 2015. **91**(5): p. 052408.
157. Brau, F., et al., *Wrinkle to fold transition: influence of the substrate response.* Soft Matter, 2013. **9**(34): p. 8177.
158. Diamant, H. and T.A. Witten, *Compression induced folding of a sheet: an integrable system.* Phys Rev Lett, 2011. **107**(16): p. 164302.
159. Holmes, D.P. and A.J. Crosby, *Draping films: a wrinkle to fold transition.* Phys Rev Lett, 2010. **105**(3): p. 038303.
160. Ciarletta, P., *Wrinkle-to-fold transition in soft layers under equi-biaxial strain: A weakly nonlinear analysis.* Journal of the Mechanics and Physics of Solids, 2014. **73**: p. 118-133.
161. Zhu, W., et al., *Structure and electronic transport in graphene wrinkles.* Nano Lett, 2012. **12**(7): p. 3431-6.
162. Cerda, E., et al., *Conical dislocations in crumpling.* Nature, 1999. **401**(6748): p. 46.
163. Matan, K., et al., *Crumpling a thin sheet.* Phys Rev Lett, 2002. **88**(7): p. 076101.
164. Mora, T. and A. Boudaoud, *Thin elastic plates: On the core of developable cones.* EPL (Europhysics Letters), 2002. **59**(1): p. 41.
165. Faber, J.A., A.F. Arrieta, and A.R. Studart, *Bioinspired spring origami.* Science, 2018. **359**(6382): p. 1386-1391.
166. Haberman, R., *Applied partial differential equations with Fourier series and boundary value problems*. 2012: Pearson Higher Ed.
167. Mendoza-Sanchez, B. and Y. Gogotsi, *Synthesis of Two-Dimensional Materials for Capacitive Energy Storage.* Adv Mater, 2016. **28**(29): p. 6104-35.
168. Qin, Z., et al., *The mechanics and design of a lightweight three-dimensional graphene assembly.* Science advances, 2017. **3**(1): p. e1601536.
169. Gonzalez, M. and A.M. Cuitiño, *A nonlocal contact formulation for confined granular systems.* Journal of the Mechanics and Physics of Solids, 2012. **60**(2): p. 333-350.
170. Vogel, N., et al., *Advances in colloidal assembly: the design of structure and hierarchy in two and three dimensions.* Chem Rev, 2015. **115**(13): p. 6265-311.
171. Hsu, M.F., et al., *Self-assembled shells composed of colloidal particles: fabrication and characterization.* Langmuir, 2005. **21**(7): p. 2963-2970.
172. Ruiz, L., et al., *A coarse-grained model for the mechanical behavior of multi-layer graphene.* Carbon, 2015. **82**: p. 103-115.
173. Gillis, P.P., *Calculating the elastic constants of graphite.* Carbon, 1984. **22**(4-5): p. 387-391.
174. Plimpton, S., P. Crozier, and A. Thompson, *LAMMPS-large-scale atomic/molecular massively parallel simulator.* Sandia National Laboratories, 2007. **18**: p. 43.
175. Holyst, R., et al., *Evaporation of freely suspended single droplets: experimental, theoretical and computational simulations.* Rep Prog Phys, 2013. **76**(3): p. 034601.
176. Yang, H., et al., *Assembling of graphene oxide in an isolated dissolving droplet.* Soft Matter, 2012. **8**(44): p. 11249.
177. Ortolani, L., et al., *Folded graphene membranes: mapping curvature at the nanoscale.* Nano Lett, 2012. **12**(10): p. 5207-12.

178. Liang, H., S.T. Acton, and D.S. Weller. *Content-aware neuron image enhancement*. in *2017 IEEE International Conference on Image Processing (ICIP)*. 2017. IEEE.
179. Ma, X., M.R. Zachariah, and C.D. Zangmeister, *Crumpled nanopaper from graphene oxide.* Nano Lett, 2012. **12**(1): p. 486-9.
180. Cranford, S.W. and M.J. Buehler, *Packing efficiency and accessible surface area of crumpled graphene.* Physical Review B, 2011. **84**(20).
181. Luo, J., et al., *Graphene oxide nanocolloids.* Journal of the American Chemical Society, 2010. **132**(50): p. 17667-17669.
182. Zhang, L., et al., *Size-controlled synthesis of graphene oxide sheets on a large scale using chemical exfoliation.* Carbon, 2009. **47**(14): p. 3365-3368.
183. Shenoy, V.B., et al., *Edge-stress-induced warping of graphene sheets and nanoribbons.* Phys Rev Lett, 2008. **101**(24): p. 245501.
184. Shenoy, V.B., C.D. Reddy, and Y.-W. Zhang, *Spontaneous curling of graphene sheets with reconstructed edges.* Acs Nano, 2010. **4**(8): p. 4840-4844.
185. Chen, X., C. Yi, and C. Ke, *Bending stiffness and interlayer shear modulus of few-layer graphene.* Applied Physics Letters, 2015. **106**(10): p. 101907.
186. Ye, Z., et al., *Role of wrinkle height in friction variation with number of graphene layers.* Journal of Applied Physics, 2012. **112**(11): p. 116102.
187. Wu, L., et al., *DLVO interactions of carbon nanotubes with isotropic planar surfaces.* Langmuir, 2013. **29**(12): p. 3976-88.
188. Gudarzi, M.M., *Colloidal Stability of Graphene Oxide: Aggregation in Two Dimensions.* Langmuir, 2016. **32**(20): p. 5058-68.
189. Liu, Q. and B. Xu, *Two-and three-dimensional self-folding of free-standing graphene by liquid evaporation.* Soft matter, 2018. **14**(29): p. 5968-5976.
190. Liu, Q. and B. Xu, *Liquid-Evaporation-Assisted Self-Folding of One-Dimensional Nanomaterials.* The Journal of Physical Chemistry C, 2018. **122**(5): p. 3078-3090.
191. Sun, T., et al., *Hydrophobic silica aerogel reinforced with carbon nanotube for oils removal.* Journal of Porous Materials, 2014. **21**(6): p. 967-973.
192. Liu, Q., J. Huang, and B. Xu, *Evaporation-driven crumpling and assembling of two-dimensional (2D) materials: A rotational spring–mechanical slider model.* Journal of the Mechanics and Physics of Solids, 2019. **133**: p. 103722.
193. Lu, W.B., et al., *A cohesive law for interfaces between multi-wall carbon nanotubes and polymers due to the van der Waals interactions.* Computer Methods in Applied Mechanics and Engineering, 2008. **197**(41-42): p. 3261-3267.
194. Purohit, P.K., J. Kondev, and R. Phillips, *Mechanics of DNA packaging in viruses.* Proc Natl Acad Sci U S A, 2003. **100**(6): p. 3173-8.
195. Kim, J., et al., *Graphene oxide sheets at interfaces.* Journal of the American Chemical Society, 2010. **132**(23): p. 8180-8186.
196. Kim, D.H., Y.S. Yun, and H.-J. Jin, *Difference of dispersion behavior between graphene oxide and oxidized carbon nanotubes in polar organic solvents.* Current Applied Physics, 2012. **12**(3): p. 637-642.
197. Zhao, P. and G. Shi, *Study of Poisson's ratios of graphene and single-walled carbon nanotubes based on an improved molecular structural mechanics model.* Structural Longevity, 2011. **5**(1): p. 49-58.

198. Tersoff, J., *Contact resistance of carbon nanotubes.* Applied Physics Letters, 1999. **74**(15): p. 2122-2124.
199. Buldum, A. and J.P. Lu, *Contact resistance between carbon nanotubes.* Physical Review B, 2001. **63**(16): p. 161403.
200. Bodkhe, S., et al., *One-step solvent evaporation-assisted 3D printing of piezoelectric PVDF nanocomposite structures.* ACS applied materials & interfaces, 2017. **9**(24): p. 20833-20842.
201. Goh, G.L., et al., *Sessile droplets containing carbon nanotubes: a study of evaporation dynamics and CNT alignment for printed electronics.* Nanoscale, 2019. **11**(22): p. 10603-10614.
202. Erbil, H.Y., *Evaporation of pure liquid sessile and spherical suspended drops: a review.* Adv Colloid Interface Sci, 2012. **170**(1-2): p. 67-86.
203. Yu, H.Z., et al., *Evaporation of water microdroplets on self-assembled monolayers: from pinning to shrinking.* Chemphyschem, 2004. **5**(7): p. 1035-8.
204. Brutin, D. and V. Starov, *Recent advances in droplet wetting and evaporation.* Chem Soc Rev, 2018. **47**(2): p. 558-585.
205. Zhang, X., et al., *Evaporation of sessile water droplets on superhydrophobic natural lotus and biomimetic polymer surfaces.* Chemphyschem, 2006. **7**(10): p. 2067-70.
206. Brutin, D., B. Sobac, and C. Nicloux, *Influence of Substrate Nature on the Evaporation of a Sessile Drop of Blood.* Journal of Heat Transfer, 2012. **134**(6).
207. Xu, J., J. Xia, and Z. Lin, *Evaporation-induced self-assembly of nanoparticles from a sphere-on-flat geometry.* Angew Chem Int Ed Engl, 2007. **46**(11): p. 1860-3.
208. Nguyen, T.A.H., M.A. Hampton, and A.V. Nguyen, *Evaporation of Nanoparticle Droplets on Smooth Hydrophobic Surfaces: The Inner Coffee Ring Deposits.* The Journal of Physical Chemistry C, 2013. **117**(9): p. 4707-4716.
209. Chen, Y., et al., *On the Effect of Substrate Viscoelasticity on the Evaporation Kinetics and Deposition Patterns of Nanosuspension Drops.* Langmuir, 2020.
210. Armstrong, S., et al., *Pinning-Free Evaporation of Sessile Droplets of Water from Solid Surfaces.* Langmuir, 2019. **35**(8): p. 2989-2996.
211. Erbil, H.Y., G. McHale, and M. Newton, *Drop evaporation on solid surfaces: constant contact angle mode.* Langmuir, 2002. **18**(7): p. 2636-2641.
212. Chen, X., et al., *Evaporation of droplets on superhydrophobic surfaces: Surface roughness and small droplet size effects.* Physical review letters, 2012. **109**(11): p. 116101.
213. Semenov, S., et al., *Evaporation of sessile water droplets: Universal behaviour in presence of contact angle hysteresis.* Colloids and Surfaces A: Physicochemical and Engineering Aspects, 2011. **391**(1-3): p. 135-144.
214. Schönfeld, F., et al., *Evaporation dynamics of sessile liquid drops in still air with constant contact radius.* International Journal of Heat and Mass Transfer, 2008. **51**(13-14): p. 3696-3699.
215. Wang, F.-C. and H.-A. Wu, *Pinning and depinning mechanism of the contact line during evaporation of nano-droplets sessile on textured surfaces.* Soft Matter, 2013. **9**(24): p. 5703.
216. Tan, H., et al., *Porous supraparticle assembly through self-lubricating evaporating*

colloidal ouzo drops. Nat Commun, 2019. **10**(1): p. 478.
217. http://www.ramehart.com/250.htm.
218. Park, S.K., Q. Mahmood, and H.S. Park, *Surface functional groups of carbon nanotubes to manipulate capacitive behaviors.* Nanoscale, 2013. **5**(24): p. 12304-12309.
219. Arca, F., et al., *Steric Interference in Bilayer Graphene with Point Dislocations.* Nanomaterials, 2019. **9**(7): p. 1012.
220. Warner, J.H., et al., *Dislocation-driven deformations in graphene.* Science, 2012. **337**(6091): p. 209-212.
221. Zhang, X., et al., *Surface Charge Transfer Doping of Low‐Dimensional Nanostructures toward High‐Performance Nanodevices.* Advanced Materials, 2016. **28**(47): p. 10409-10442.
222. Macky, W., *Some investigations on the deformation and breaking of water drops in strong electric fields.* Proceedings of the Royal Society of London. Series A, Containing Papers of a Mathematical and Physical Character, 1931. **133**(822): p. 565-587.
223. Dunn, G., et al., *The strong influence of substrate conductivity on droplet evaporation.* Journal of Fluid Mechanics, 2009. **623**: p. 329-351.
224. Malinowski, R., et al., *Dynamic Control of Particle Deposition in Evaporating Droplets by an External Point Source of Vapor.* J Phys Chem Lett, 2018. **9**(3): p. 659-664.
225. Taylor, G.I., *Disintegration of water drops in an electric field.* Proceedings of the Royal Society of London. Series A. Mathematical and Physical Sciences, 1964. **280**(1382): p. 383-397.